Convective Cloud and Rainfall Processes Over the Maritime Continent: Simulation and Analysis of the Diurnal Cycle

by

Rebecca L. Gianotti

B. E. (Environmental Engineering), University of Western Australia (2003)
B. A. (Asian Studies), University of Western Australia (2003)
M. Environmental Management, University of Queensland (2006)
M. S. (Civil and Environmental Engineering), Massachusetts Institute of Technology (2008)

Submitted to the Department of Civil and Environmental Engineering
in partial fulfillment of the requirements for the degree of

Doctor of Philosophy in the Field of Hydrology

at the

MASSACHUSETTS INSTITUTE OF TECHNOLOGY

February 2013

Signature of Author: _____
Department of Civil and Environmental Engineering
November 16, 2012

Certified by: _____
Elfatih A. B. Eltahir
Professor of Civil and Environmental Engineering
Thesis Supervisor

Accepted by: _____
Heidi M. Nepf
Chair, Departmental Committee for Graduate Students

Convective Cloud and Rainfall Processes Over the Maritime Continent: Simulation and Analysis of the Diurnal Cycle

by
Rebecca L. Gianotti

Submitted to the Department of Civil and Environmental Engineering
on November 16, 2012, in partial fulfillment of the requirements for the degree of
Doctor of Philosophy in the Field of Hydrology

ABSTRACT

The Maritime Continent experiences strong moist convection, which produces significant rainfall and drives large fluxes of heat and moisture to the upper troposphere. Despite the importance of these processes to global circulations, current predictions of climate change over this region are still highly uncertain, largely due to inadequate representation of the diurnally-varying processes related to convection. In this work, a coupled numerical model of the land-atmosphere system (RegCM3-IBIS) is used to investigate how more physically-realistic representations of these processes can be incorporated into large-scale climate models. In particular, this work improves simulations of convective-radiative feedbacks and the role of cumulus clouds in mediating the diurnal cycle of rainfall.

Three key contributions are made to the development of RegCM3-IBIS. Two pieces of work relate directly to the formation and dissipation of convective clouds: a new representation of convective cloud cover, and a new parameterization of convective rainfall production. These formulations only contain parameters that can be directly quantified from observational data, are independent of model user choices such as domain size or resolution, and explicitly account for subgrid variability in cloud water content and non-linearities in rainfall production. The third key piece of work introduces a new method for representation of cloud formation within the boundary layer. A comprehensive evaluation of the improved model was undertaken using a range of satellite-derived and ground-based datasets, including a new dataset from Singapore's Changi airport that documents diurnal variation of the local boundary layer height.

The performance of RegCM3-IBIS with the new formulations is greatly improved across all evaluation metrics, including cloud cover, cloud liquid water, radiative fluxes and rainfall, indicating consistent improvement in physical realism throughout the simulation. This work demonstrates that: (1) moist convection strongly influences the near surface environment by mediating the incoming solar radiation and net radiation at the surface; (2) dissipation of convective cloud via rainfall plays an equally important role in the convective-radiative feedback as the formation of that cloud; and (3) over parts of the Maritime Continent, rainfall is a product of diurnally-varying convective processes that operate at small spatial scales, on the order of 1 km.

Thesis Supervisor: Elfatih A. B. Eltahir
Title: Professor of Civil and Environmental Engineering

Acknowledgements

For most people, it takes a village to raise a thesis. For me, the production of this thesis felt like the effort of a small island nation rather than a village, and I am grateful to all those who have offered guidance and support over the years of its creation.

Firstly, I am incredibly thankful to my advisor, Fatih. I have the attention span of a hyperactive small child, so keeping me on task is much like herding cats. I am grateful to Fatih for managing to keep me focused enough to finish this PhD. But much more than just directing my activity, I have learned a great deal from Fatih about science and about being a scientist. Throughout this process we had so many conversations about how the world works, thinking about what we see in the environment and how what we intuitively understand as scientists might translate into model-speak. I really valued this approach of first understanding what we're trying to achieve, and then thinking about what physically makes sense with respect to model representation. His knowledge of hydrologic and atmospheric science enabled many a roadblock to be surmounted, and I will always be grateful to have had the opportunity to learn from him.

I have received valuable input and advice from a number of people. My wonderful committee members – Jeremy Pal, Charles Harvey and Tieh Yong Koh – provided invaluable feedback on the development of this research. I am so grateful that they put up with the infrequent and long distance meetings, and the logistical and technical nightmares involved with maintaining a committee in three different time zones. My thanks also go to Kerry Emanuel for several useful discussions on convection and convective parameterization schemes, and to Dongfeng Zhang for her work and assistance with RegCM3.

I am very grateful to other members of the Eltahir group and Parsons Laboratory for their technical assistance and helpful suggestions. Marc Marcella and Jonathan Winter were instrumental in my learning of RegCM3, and Marc in particular is owed a great debt of thanks for his help with coding and that loveable little beast known as ferret. At the risk of excluding someone, many thanks also go to Mohamed Siam, Teresa Yamana, Anjuli Jain, Noriko Endo, Osama Mekki Seidahmed, Marie-Estelle Demory, Ryan Knox and Gautam Bisht for fruitful discussions and debates during research meetings and help with data acquisition and analysis.

An organisation only runs as well as its administrators. The Parsons Laboratory is a magnificent place to work in large part because of the wonderful staff who support it. I am very grateful to Gayle Sherman, Sheila Frankel, Jim Long, Joanne Batziotegos and Vicki Murphy for all their work in supporting me and all the students of this great building, and for being the friendly backbone of a warm, welcoming workplace. Many thanks also to the administrators of the Civil and Environmental Engineering department – especially Kris Kipp, Jeanette Marchoki, Pat Dixon and Patty Glidden – who do a great job of looking after vast numbers of students with a smile (no matter how many times I ask for favours!).

I have travelled to Singapore a number of times over the course of this PhD. I am very grateful to the staff and other researchers of SMART and CENSAM for their efforts in ensuring I had somewhere to stay and work while in Singapore and for making me feel welcome in an environment that often felt incredibly foreign, despite its familiarity.

Particular thanks go to Regina Chan, Adiana Abdullah and Carol Tong for coordinating the logistics of my travels; to Joo Siong Sim and Ifan for making sure my Singapore-based computer was functional; and to Alex Cobb and Laure Gandois for providing some much-needed friendship and good times while in Singapore.

I would never have been able to undertake a PhD without external funding sources. I am incredibly grateful for funding provided by the MIT Presidential Fellowship, the Singapore National Research Foundation (NRF), through the Singapore-MIT Alliance for Research and Technology (SMART) Center for Environmental Sensing and Modeling (CENSAM), and by the MIT Martin Family Society of Fellows for Sustainability.

And now for the people who are central to my life, without whom this thesis would not exist and I would be a far lesser human being.

A debt of thanks that can never be repaid goes to my extended family, especially the members of RUMHED, for their unconditional love and support and for never doubting that I was capable of undertaking and completing this degree. Everything builds from you guys.

To Kate, Bec, Bec, Gin, Sarah, Ellie, Amy and Sarah Jane – thank you for being such wonderful individuals and the best collection of girlfriends in existence. You encourage me, keep me in line, make me laugh and inspire me. That we are able to maintain such close ties despite the distance between us speaks to how much I value your presence in my life.

Thank you also to Matt, Ben and Ryan for being great friends and allowing me to steal away so much time with your wives.

To the current and former members of the Parsons Laboratory and your lovely partners – thank you for your friendship and for creating an unrivalled work environment. I doubt I will ever again work with such a talented, inspiring and warm-hearted group of people.

Thank you to the wonderful members of MIT's *Komaza* magazine and Engineers Without Borders, especially Helen D'Couto and Bina Choi. Being part of your teams was an invaluable experience for me. These activities were more than side projects – they were inspirational and incredibly satisfying. I am so grateful to have had the opportunity to work and learn with such energetic and compassionate people.

To Matt – thank you for the creative distractions, the inspiration for future endeavours, and much-needed breaks from the university environment. Someday very soon there will be a piece of film with both of our names on it.

To Mary – thank you for sharing this transitional period of life with me, providing levity and laughs and a great sounding board for bouncing ideas. How comforting it is to know I have a kindred spirit across the ocean.

To Checka – thank you for your inspirational gratitude, joy and amazing (and irreplaceable) yoga instruction. You will be sorely missed.

Finally, to Gaj – my sounding board, live-in therapist, occasional punching bag, head cheerleader, MATLAB guru, baggage handler, travel buddy, handyman, partner-in-crime, beer brewer, lover and best friend – this thesis is for you as much as it is for me.

Table of Contents

List of Figures

List of Tables

Chapter 1: Introduction

History teaches us that simulation without understanding can be perilous, and is in any case intellectually empty.

- Kerry Emanuel

1.1 Motivation

The Maritime Continent region is home to approximately 375 million people. It is the portion of Southeast Asia comprising Malaysia, Indonesia, Brunei Darussalam, Singapore, East Timor and the Philippines, approximately bounded by 90°E – 140°E and 10°S – 10°N (Figure 1-1). It contains thousands of islands, ranging in size from tens to thousands of kilometers, with steep topographic gradients: the two highest peaks in the region are 4884 m in the Indonesian province of Irian Jaya (western New Guinea) and 4100 m in the Malaysian province of Sabah (northeastern Borneo). The islands are interspersed by segments of ocean with depths varying from as little as 50 m in parts of the South China Sea to as much as 5000 m in the Pacific and Indian Ocean basins. Few regions of the world contain such dramatic geographic variability in relatively small spatial scales as the Maritime Continent.

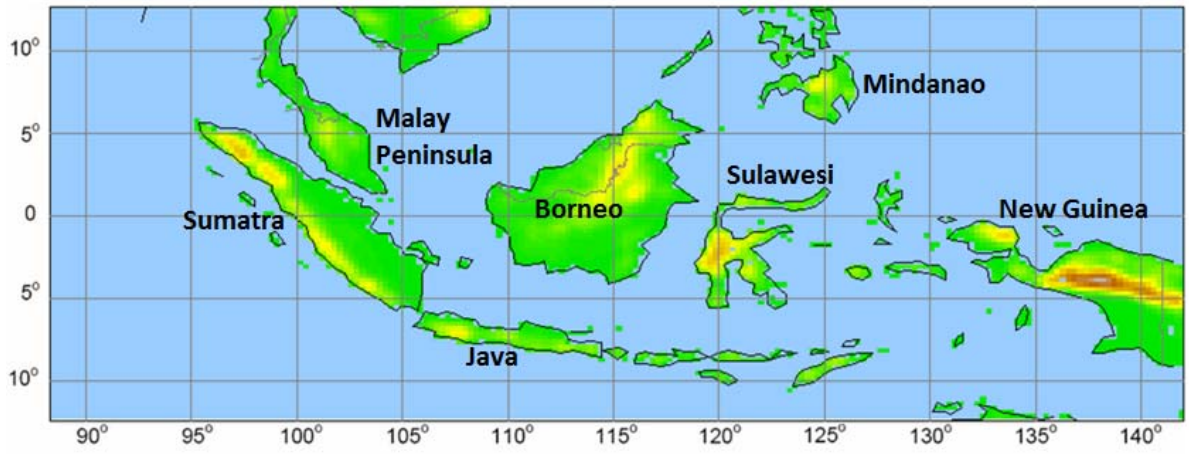

Figure 1-1. Approximate boundary and major islands of the Maritime Continent region. The color gradient indicates relative topographic gradients over the islands.

Rainfall is generally very high over this region, with annual precipitation totals of about 2700 mm. The Maritime Continent is located at the western edge of the oceanic

'warm pool', where sea surface temperatures are approximately 30^{o}C year round, and the rising branch of the Pacific Ocean's Walker circulation. During the months of December-February, the region also lies within the Intertropical Convergence Zone (ITCZ) and it is influenced by both the South Asian and East Asian monsoons, associated with seasonal movement of the ITCZ. Therefore the large-scale conditions influencing this region are generally conducive to strong convection.

It has long been known that convective storms over the tropics are responsible for significant inputs of heat and moisture to the upper troposphere, due to large releases of latent heat and the production of dense clouds that shield from radiative cooling (Ramage 1968). Given the importance of convective processes in the Maritime Continent to global rainfall and circulation processes, accurate simulation of the climate of this region is critical for simulations of both regional and global circulations (Neale and Slingo 2003).

However, current predictions of climate change over the Maritime Continent still contain a high degree of uncertainty. The Fourth Assessment Report of the Intergovernmental Panel on Climate Change ('the IPCC report') noted that, although the performance of regional climate models has improved significantly over many parts of the world, simulations over the Southeast Asian region still demonstrate significant variation in projected impacts from climate change (Christensen *et al.* 2007), indicating that the mechanisms driving rainfall in this region are still not adequately understood or represented in climate models. The IPCC report also noted that local impacts of climate change are likely to vary significantly within Southeast Asia due to the region's complex topography and oceanic influences (Christensen *et al*. 2007).

Southeast Asia has been identified as a region highly vulnerable to climate variability, due to its long coastlines, high concentration of people and economic activity in coastal areas, heavy reliance on agriculture and natural resources, and variable adaptive capacity (Nitivattananon *et al.* 2013). Particular sources of projected risk are increases in diarrhoeal disease, associated with floods and droughts, and epidemics of malaria, dengue and other vector-borne diseases (Cruz *et al.* 2007). These human health risks are all strongly dependent on local and regional climatic and hydrologic conditions. We therefore have a

critical need to improve our ability to simulate processes related to rainfall over the Maritime Continent.

1.2 Background

The diurnal cycle of rainfall and temperature is one of the strongest modes of variability in the climate of the Maritime Continent (Yang and Slingo 2001, Kitoh and Arakawa 2005). Specific studies undertaken to better understand the diurnal cycle over the Maritime Continent include the Island Thunderstorm Experiment (ITEX; e.g. Keenan *et al.* 1989, Simpson *et al.* 1992), the Maritime Continent Thunderstorm Experiment (MCTEX; Keenan *et al.* 2000), the Tropical Oceans-Global Atmosphere Coupled Ocean-Atmosphere Response Experiment (TOGA-COARE; e.g. Liberti *et al.* 2001), and the Tropical Warm Pool-International Cloud Experiment (TWP-ICE; May *et al.* 2008). These studies used detailed site-specific data obtained primarily from ground-based radar and meteorological stations or ocean buoys. In more recent years, satellite-based observations have provided a more spatially coherent picture of the diurnal rainfall cycle over the region (e.g. Hall and Vonder Haar 1999, Sorooshian *et al.* 2002, Nesbitt and Zipser 2003, Mori *et al.* 2004, Janowiak *et al.* 2005, Ichikawa and Yasunari 2006, Yang and Smith 2006). In particular, the diurnal cycles of convection and rainfall propagation have been well described for the islands of Sumatra (Mori *et al.* 2004, Sakurai *et al.* 2005, Wu *et al.* 2009b), Borneo (Ichikawa and Yasunari 2006, Hara *et al.* 2009, Wu *et al.* 2009a), New Guinea (Zhou and Wang 2006, Ichikawa and Yasunari 2008) and the Malay Peninsula (Joseph *et al.* 2008).

The dominant diurnal signal over the Maritime Continent has been attributed to local insolation-driven instability and circulations initiated by differential responses to insolation (e.g. Saito *et al.* 2001, Yang and Slingo 2001, Slingo *et al.* 2003, Qian 2008). Land-sea breeze circulations are the most well-known of these and have been studied extensively (e.g. Neumann and Mahrer 1974, Baker *et al.* 2001, Zhou and Wang 2006). The smaller heat capacity of the land surface compared to the ocean causes differential radiative heating during the daytime, creating a much larger diurnal temperature variation over land than over ocean. The comparatively lower pressure over land produces a sea breeze in the late morning to early afternoon, which initiates convection over land-ocean boundaries. Similar

circulations are created by differential heating between mountain and lowland areas. Convective cells are observed to aggregate into mesoscale convective systems (MCSs) in areas of strong convergence, particularly over mountains, leading to prolonged rainfall overnight. Over flat areas, convection can also be initiated or enhanced by the collision of two sea breezes, as shown by Joseph *et al.* (2008) over the southern Malay Peninsula and by Qian (2008) over Java. These circulations and other diurnal processes will be discussed further later in this thesis.

Generally, more daily total rainfall falls over land than over ocean, because the larger diurnal variations in land surface temperature create greater low-level instability (Neale and Slingo 2003). But the timing and magnitude of the diurnal rainfall cycle varies significantly by the relative size of an island or body of water and the proximity to a coastline. Mountainous areas of the larger islands are observed to produce more rainfall than the flat coastal areas; coastal ocean areas generally exhibit significantly higher diurnal variations in rainfall than the open ocean. It is thought that much of the variability observed over the oceans within the Maritime Continent may be related to MCSs that start over land then move away over the oceans with the land breeze (Liberti *et al.* 2001, Saito *et al.* 2001, Mori *et al.* 2004, Ichikawa and Yasunari 2008). Gravity waves initiated by land-based convection are also thought to be a mechanism for propagation of rainfall over coastal oceans (Yang and Slingo 2001, Mori *et al.* 2004). Zhou and Wang (2006) showed that offshore propagation of rainfall near New Guinea results from a combination of land breezes and gravity waves forced by deep convection over the steep mountains of the island. This propagation of convection will also be discussed further later in this thesis.

Various studies have shown that global climate models (also general circulation models; GCMs) struggle to accurately reproduce the observed climate over the Maritime Continent region, with land areas having either a wet bias (e.g. Dai and Trenberth 2004, coupled model in Martin *et al.* 2006) or a dry bias (e.g. Yang and Slingo 2001, atmosphere-only model in Martin *et al.* 2006), usually accompanied by underestimation of rainfall over the oceans (e.g. Collier and Bowman 2004, Neale and Slingo 2003). It has been suggested that the source of these errors includes poor representation of the diurnal cycle of

convection over land and the complex circulation patterns generated by land-sea contrasts (Martin *et al.* 2006), in part because the coarse resolution of GCMs is insufficient to physically represent the processes that occur over the subgrid-scale islands within the Maritime Continent (Hahmann and Dickinson 2001, Neale and Slingo 2003).

Failure to accurately simulate rainfall processes has flow-on effects to simulation of the land surface hydrology. It was suggested by Dai and Trenberth (2004) that GCMs will also fail to capture nonlinear processes impacting the diurnal cycle of land surface hydrology, such as the different partitioning of rainfall into evaporation and runoff that occurs when rainfall is simulated during the daytime rather than night-time. Indeed, simulation of the diurnal rainfall cycle is notoriously problematic for GCMs, with the most common error being the early occurrence of daily peak precipitation around midday in simulations, about 4-6 hours ahead of observations (e.g. Yang and Slingo 2001, Collier and Bowman 2004, Dai and Trenberth 2004). Therefore it seems apparent that accurate representation of precipitation over the Maritime Continent can only be achieved by a model that can adequately capture processes occurring at scales of 10-100 km.

However, relatively few studies using regional climate models (RCMs), typically run at resolutions of tens of kilometers, have been conducted over the Maritime Continent. The previous studies suggest that systemic problems exist with regard to the simulation of diurnal, small-scale processes within large-scale climate models.

Francisco *et al.* (2006) applied Regional Climate Model (RegCM, maintained at the International Center for Theoretical Physics) to simulation of monsoonal rainfall over the Philippines. In general, the model could reproduce the observed monsoonal rainfall patterns well, but its performance depended strongly on the choice of forcing boundary conditions and the ocean flux scheme (Francisco *et al.* 2006). As a result, different combinations of forcing fields and flux parameterizations provided good simulation of rainfall and made it difficult to determine which model user choices were the most appropriate.

Wang *et al.* (2007) used Regional Climate Model (developed at the International Pacific Research Center) to simulate the diurnal cycle over the Maritime Continent. Those authors found that the model could reasonably reproduce the diurnal cycle, with afternoon

rainfall maxima over land areas and night-time maxima over ocean areas, but with a time shift that was about 2-4 hours too early compared with satellite observations. The authors found some improvement in model performance by changing the value of the convective entrainment / detrainment rate (Wang *et al.* 2007).

Joseph *et al.* (2008) used the Coupled Ocean / Atmosphere Mesoscale Prediction System (COAMPS) with nested domains to simulate rainfall and flow fields around the Malay Peninsula on 23 April 2002. The model reproduced observations reasonably well, but with a cold bias over land during the daytime and a rainfall peak too early in the day by about an hour (Joseph *et al.* 2008).

Qian (2008) used Regional Climate Model Version 3 coupled to Biosphere Atmosphere Transfer Scheme Version 1e to simulate the diurnal rainfall cycle over the island of Java, Indonesia. The model system was able to reproduce the diurnal cycle reasonably well, but again the timing of the rainfall peak was too early in the day (Qian 2008).

Previous studies have shown consistent error in simulations by GCMs and RCMs over the Maritime Continent region. However, the literature is scarce on detail as to the precise nature of these errors and how they might be addressed. It is often said that models are the laboratories of climate scientists: tools that provide better understanding of the myriad of physical processes occurring in this extremely large and complex system. But the use of these tools relies on a solid grasp of both the processes we wish the model to simulate and the design and intention of the model itself. The latter point has become increasingly important as GCMs and RCMs have grown in size and complexity, incorporating the work of multitudes of scientists spanning a wide variety of specialist fields. To improve our simulations of the existing climate and our projections of future climate variability, we need to better understand both the natural world and our tools for studying it.

1.3 Thesis Structure

This thesis investigates diurnal processes related to convection over the Maritime Continent region. It aims to better understand why large-scale climate models fail to capture these processes and how more physically-realistic simulations might be achieved. In

particular, this work is concerned with the convective-radiative feedback and the role of cumulus clouds in mediating the diurnal cycle of rainfall.

Chapter 2 provides a description of the coupled model system used in this work and assesses its performance with regard to simulation of the existing climate of the Maritime Continent region, particularly rainfall.

Chapter 3 more closely investigates simulation of the near surface environment. It describes modifications made to improve simulation of the planetary boundary layer height, non-convective clouds within the planetary boundary layer and surface turbulent heat fluxes. The simulated boundary layer height over Singapore is compared to a dataset obtained specifically for this study.

Chapter 4 describes a new method for parameterizing convective cloud fraction, which relies on observed climatologies of cloud water content and accounts for subgrid variability in cloud cover. It is shown that the new method provides the necessary convective-radiative feedback that was previously absent in the model.

Chapter 5 describes a new method for parameterizing the conversion of cloud droplets into rainfall within large-scale climate models. The new method is constrained by observations of cloud droplets, distributions of cloud water content, and climatological rainfall intensity. It is shown that this method can significantly improve the simulation of both the diurnal-scale processes and mean climate of the Maritime Continent.

Chapter 6 explores the spatial variability of the diurnal rainfall cycle over the Maritime Continent. Behavior over the larger islands is explored in more detail with a view to isolating the specific processes that cannot be captured with a large-scale climate model.

Chapter 7 explores the influence of El Niño and La Niña events on convective rainfall and the diurnal cycle at both the regional and sub-regional scale. It is shown that the improved version of the model capably reproduces the interannual variability observed across the region.

Chapter 8 summarizes the conclusions that can be drawn from this work and provides recommendations for future studies.

Additional information is provided in an appendix for the interested reader.

Chapter 2: Model Description and Assessment

The work presented in this thesis investigates the diurnal cycle of convective processes over the Maritime Continent using the Regional Climate Model Version 3 (RegCM3) coupled to the land surface models Biosphere Atmosphere Transfer Scheme Version 1e (BATS1e) and Integrated Biosphere Simulator (IBIS). The first task when commencing work with a climate model, before it can be used as an experimental tool, is to evaluate its ability to reproduce observations of the existing climate. To that end, this chapter provides a description of the coupled model system and evaluates its performance over the Maritime Continent, with particular attention paid to the simulation of rainfall.

RegCM3-BATS1e has previously shown good results in simulating the large-scale rainfall patterns caused by the monsoon systems over tropical West Africa, South America and South Asia (Pal *et al.* 2007). Therefore it is also expected to show good performance in simulating the large-scale dynamics over the Maritime Continent. RegCM3-BATS1e has been used over Java (Qian 2008) and an earlier version has been used over the Philippines (Francisco *et al.* 2006), but a detailed investigation of the model's performance over the Maritime Continent as a whole and with respect to diurnal and spatial variability in rainfall has yet to be undertaken. In addition, the RegCM3-IBIS model system is untested over the Maritime Continent.

2.1 Model Description

Regional Climate Model (RegCM) was originally developed at the National Center for Atmospheric Research (NCAR) and is now maintained by the International Center for Theoretical Physics (ICTP). It is a three-dimensional, hydrostatic, compressible, primitive equation, σ-coordinate regional climate model. The dynamical core of RegCM3 is based on the hydrostatic version of the Pennsylvania State University / NCAR Mesoscale Model Version 5 (MM5; Grell *et al*. 1994) and employs NCAR's Community Climate Model Version 3 (CCM3) atmospheric radiative transfer scheme (described in Kiehl *et al.* 1996). Planetary

boundary layer dynamics follow the non-local formulation of Holtslag *et al*. (1990) and Holtslag and Boville (1993). Ocean surface fluxes are handled by Zeng's bulk aerodynamic ocean flux parameterization scheme (Zeng *et al*. 1998), where sea surface temperatures are prescribed. The Subgrid Explicit Moisture Scheme (SUBEX) is used to handle large-scale, resolvable, non-convective clouds and precipitation (Pal *et al*. 2000). Finally, three different convective parameterization schemes are available for representation of non-resolvable rainfall processes (Giorgi *et al*. 1993): Kuo (Anthes 1977), Grell (Grell 1993) with Fritsch-Chappell (Fritsch and Chappell 1980) or Arakawa-Schubert (Grell *et al*. 1994) closures, and Emanuel (Emanuel 1991, Emanuel and Živković-Rothman 1999). Further details of the developments and description of RegCM3 are available in Pal *et al*. (2007).

To represent the land surface physics, RegCM3 comes coupled to the land surface scheme BATS1e (described in Dickinson *et al*. 1993). BATS1e uses a one-layer canopy with two soil layers and one snow layer to perform eight major tasks, including: calculation of soil, snow or sea-ice temperature in response to net surface heating; calculation of soil moisture, evaporation and surface and groundwater runoff; calculation of the plant water budget, including foliage and stem water storage, intercepted precipitation and transpiration; and calculation of foliage temperature in response to energy-balance requirements and consequent fluxes from the foliage to canopy air (Dickinson *et al.* 1993). Additional modifications have been made to BATS1e to account for the subgrid variability of topography and land cover as described in Giorgi *et al*. (2003).

Winter *et al.* (2009) coupled RegCM3 to an additional land surface scheme – IBIS (described in Foley *et al*. 1996). IBIS contains four modules, operating at different time steps, and includes a two-layer canopy with six soil layers and three snow layers. The four modules simulate processes associated with the land surface (surface energy, water, carbon dioxide and momentum balance), vegetation phenology (winter-deciduous and drought-deciduous behavior of specific plant types in relation to seasonal climatic conditions), carbon balance (annual carbon balance as a function of gross photosynthesis, maintenance respiration and growth respiration), and vegetation dynamics (time-dependent changes in vegetation cover

resulting from changes in net primary productivity, carbon allocation, biomass growth, mortality and biomass turnover for each plant functional type) (Foley *et al.* 1996).

2.2 Experimental Design

Simulations were begun at 1 July 1997 and ended 31 December 2001. The first 6 months of output were ignored for spin-up. The remaining simulation years (1998-2001) were used for model evaluation and were chosen for maximal overlap between the datasets used for lateral boundary conditions and observational comparison, described below.

The model domain (Figure 2-1) was centered along the equator at 115^{o}E, used a normal Mercator projection and spanned 95 grid points meridionally and 200 grid points zonally, with a horizontal resolution of 30 km. This resolution was chosen to allow for representation of most of the islands within the domain, and the concomitant diurnal processes, but without sacrificing too much computational speed. The simulations used 18 vertical sigma levels, from the ground surface up to the 50 mb level.

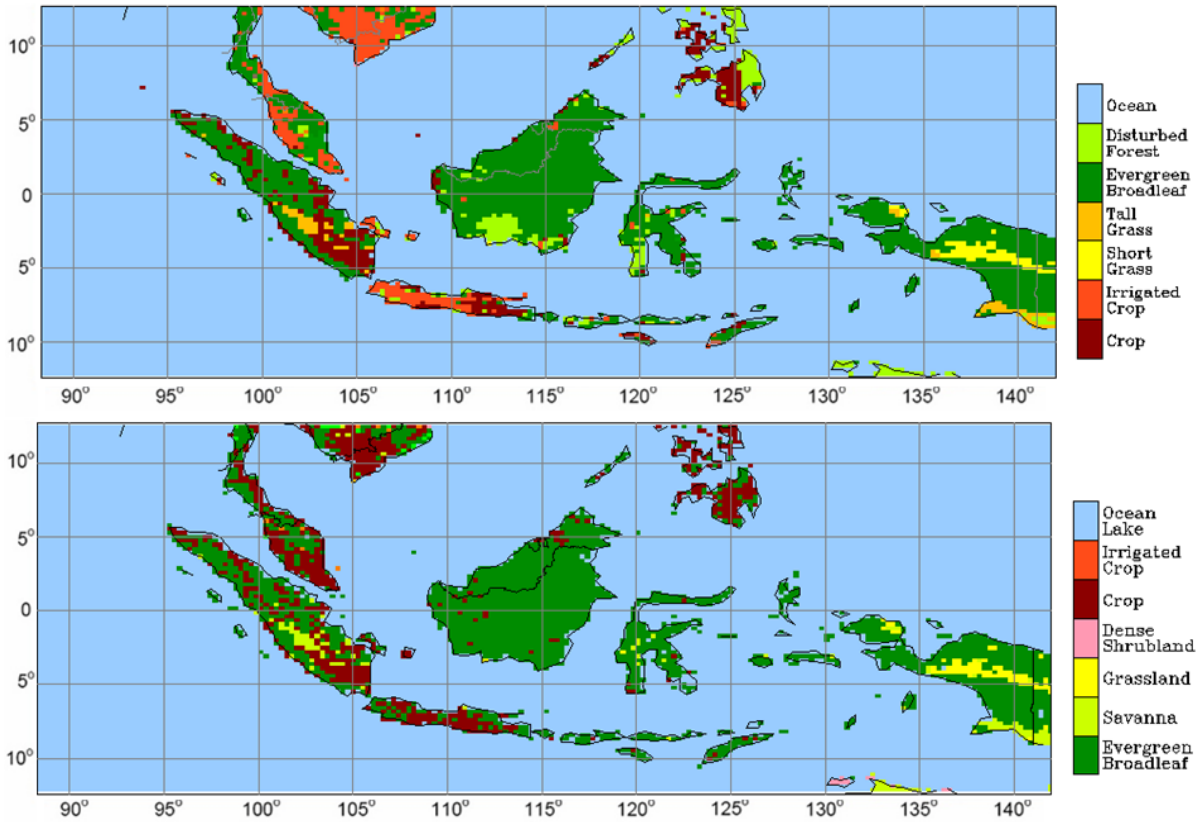

Figure 2-1. Model domain showing the land use classification (top) from GLCC used for BATS1e and (bottom) from Ramankutty (1999) used for IBIS.

In all simulations presented, the land surface scheme was run every 120 seconds, twice the model time step. A small time step was necessary because of the relatively high resolution used and to ensure convergence in areas with significant convective activity.

Sea surface temperatures (SSTs) were prescribed using the National Ocean and Atmospheric Administration (NOAA) optimally interpolated SST (OISST) dataset, which is available at 1^{o} x 1^{o} resolution and at a weekly timescale (Reynolds *et al*. 2002). Topographic information for both RegCM3-BATS1e and RegCM3-IBIS was taken from the United States Geological Survey's Global 30 arc second elevation dataset (GTOPO30), aggregated to 10 arc minutes (United States Geological Survey 1996).

For RegCM3-BATS1e, vegetation cover information was taken from the United States Geological Survey's Global Land Cover Characterization (GLCC) database (United States Geological Survey 1997), at 10 minute resolution. Soil properties were automatically assigned according to vegetation type.

For RegCM3-IBIS, vegetation biomes were based on the potential global vegetation dataset of Ramankutty (1999), modified to include two extra biomes for inland water and ocean as described in Winter *et al.* (2009). The vegetation biomes were used in conjunction with two climatology datasets to populate each grid cell with plant functional types: 1) the monthly mean climatology of temperature (New *et al.* 1999) and 2) the minimum temperature ever recorded at a location minus the average temperature of the coldest month (Bartlein 2000). Soil properties, such as albedo and porosity, were determined based on the relative proportions of clay and sand in each grid cell. Sand and clay percentages were taken from the Global Soil Dataset, which has a spatial resolution of 5 minutes (Global Soil Data Task, International Geosphere-Biosphere Programme, Data and Information System 2000). In all simulations presented, RegCM3-IBIS was run with static vegetation only.

Soil moisture, soil temperature and soil ice content were initialized in RegCM3-IBIS using the output from a global 0.5^{o} x 0.5^{o} resolution 20-year offline simulation of IBIS as described in Winter *et al.* (2009).

For most simulations, the European Centre for Medium-range Weather Forecasts (ECMWF) 40-year Re-Analysis (ERA40) dataset (Uppala *et al.* 2005), available September

1957 to August 2002, was used to force the boundaries and was obtained from the ECMWF data server. For comparison purposes, two simulations with RegCM3-BATS1e were also forced with lateral boundary conditions taken from the National Center for Environmental Prediction (NCEP) / National Center for Atmospheric Research (NCAR) Reanalysis 2 product (hereafter referred to as NNRP2) (Kanamitsu *et al.* 2002). The exponential relaxation technique of Davies and Turner (1977) was used with both datasets. All model output analysis presented here excludes a border region of width 5 grid cells to account for the effects of boundary interpolation.

To evaluate the sensitivity of the model to the choice of convective parameterization scheme, simulations were run using three of the options available with RegCM3: the Grell scheme using both the Arakawa-Schubert and Fritsch-Chappell closures and the Emanuel scheme. Over the tropics, the Kuo scheme has consistently shown poor simulation of rainfall and is not considered an appropriate scheme for use in this region (e.g. Slingo *et al.* 1994, Jenkins 1997), so it was not included in this study. The Grell scheme with Fritsch-Chappell closure and the Emanuel scheme were also used to test the influence of the lateral boundary conditions and land surface scheme.

A total of seven simulations are presented in this assessment. All model parameters were left at default values. The different characteristics of these simulations are summarized in Table 2-1. Throughout the remainder of this chapter, the names shown in Table 2-1 will be used to reference each simulation.

Table 2-1. Characteristics of simulations used in the assessment. The names are used to reference each simulation within the text.

Simulation Name	Convection Scheme	Boundary Conditions	Land Surface Scheme
GFC	Grell with F-C	ERA40	BATS1e
EMAN	Emanuel	ERA40	BATS1e
GAS	Grell with A-S	ERA40	BATS1e
GFCNCEP	Grell with F-C	NNRP2	BATS1e
EMANNCEP	Emanuel	NNRP2	BATS1e
GFCIBIS	Grell with F-C	ERA40	IBIS
EMANIBIS	Emanuel	ERA40	IBIS

2.2.1 A Note on the Choice of Convection Scheme and Boundary Conditions

Climate model performance is generally highly sensitive to the choice of lateral boundary conditions and convective parameterization scheme. In this assessment, preference is given equally to the Grell convection scheme with Fritsch-Chappell closure and to the Emanuel convection scheme, while the ERA40 forcing boundary conditions are favored over the NNRP2. Explanations for these preferences are provided here.

Previous evaluations of the ERA40, NNRP1 (the first NCEP-NCAR reanalysis product) and NNRP2 products have identified their relative strengths and weaknesses. Representation of the Intertropical Convergence Zone (ITCZ) is much stronger and closer to observations in ERA40 than NNRP1, as evidenced by the locations and magnitudes of rainfall (Janowiak *et al.* 1998, Trenberth and Guillemot 1998), atmospheric water vapor (Trenberth and Guillemot 1998), and diabatic heating and cooling (Chan and Nigam 2009). ERA40 also shows a stronger Walker circulation over the Pacific basin than NNRP1 and more closely follows the seasonal movement of the ITCZ and monsoonal rainfall (Chan and Nigam 2009). Both NNRP1 and NNRP2 have poor representation of interannual variability in water vapor, and representation of the El Niño-Southern Oscillation is better in ERA40 than in NNRP1 or NNPR2 (Sudradjat *et al.* 2005).

The amplitude of diabatic heating in ERA40 is too high, indicating over-representation of convection, and precipitation from ERA40 is generally higher than that obtained from satellite observations (Chan and Nigam 2009). However, the variability and spatial patterns of water vapor in ERA40 are similar to observations (Sudradjat *et al.* 2005). NNRP1 has significant dry biases in the tropics, particularly over the oceanic tropical convergence zones (Trenberth and Guillemot 1998) and over the Maritime Continent (Newman *et al.* 2000). The dry bias in NNRP1 appears to be stronger than the wet bias in ERA40 (Chan and Nigam 2009, Newman *et al.* 2000). This dry bias in NNRP1 does not seem to have been fixed in NNRP2, since Sudradjat *et al.* (2005) showed that NNRP2 still contains a dry bias in atmospheric water vapor over the Maritime Continent and western Pacific warm pool.

Therefore, while both reanalysis products contain deficiencies, it is considered that the ERA40 product contains better representation of the dynamics over the tropics and the Maritime Continent than NNRP2.

Previous studies have demonstrated that the convective parameterization schemes have different strengths and weaknesses. The Kuo parameterization is a bulk scheme in which rainfall is calculated as a fraction of the moisture convergence within each vertical column. As mentioned above, this type of convection scheme is not considered appropriate for simulating tropical convection and thus has not been investigated here.

The Grell and Emanuel schemes are both mass flux schemes that implement convective adjustment in accordance with the quasi-equilibrium assumption, in which the time scale over which convection removes instability created by large-scale forcing is very small compared to the time scale of the large-scale forcing. The Grell scheme treats clouds as two steady-state circulations: an updraft and a downdraft. No mixing occurs between the cloud and the environment except at the top and bottom of the circulations, with no entrainment or detrainment along the edges of the cloud. By contrast, the Emanuel scheme assumes that mixing within clouds is highly episodic and inhomogeneous, and considers convective fluxes based on an idealized model of sub-cloud-scale updrafts and downdrafts.

Davis *et al.* (2009) showed that the Grell scheme with both the Arakawa-Schubert (A-S) and Fritsch-Chappell (F-C) closures underestimated convective rainfall over tropical land areas, while over the ocean the Grell scheme with F-C closure overestimated and Grell with A-S closure underestimated convective rainfall. The Emanuel scheme was found to overestimate total rainfall over both land and ocean, but provided the most realistic partitioning of convective and stratiform rainfall, as well as better spatial distribution of convective rainfall (Davis *et al.* 2009). Pal *et al.* (2007) showed that simulations using the Emanuel scheme over the West African monsoon overestimated precipitation over the wettest areas, while Jenkins (1997) showed that the Grell scheme over West Africa underestimated summer season precipitation. Over South America, the Grell scheme has been shown to underestimate the magnitude of both precipitation and temperature, while the Emanuel scheme performs reasonably well in simulating the distribution of precipitation

over the continent and its adjacent oceans (Pal *et al.* 2007). Over Korea and East Asia, work by Im *et al.* (2008) and Singh *et al.* (2006) showed that the Emanuel scheme was better able to simulate the monsoon circulations and the timing and amplitude of rainfall compared to the Grell scheme. However, the Emanuel scheme consistently overestimated rainfall volumes, while the Grell scheme tended to overestimate winter season precipitation and underestimate summer season precipitation (Im *et al.* 2008).

Therefore neither the Grell nor Emanuel scheme has consistently provided better simulation over the tropics in studies to date, prohibiting an *a priori* choice of appropriate parameterization scheme.

2.2.2 Comparison Datasets

To assess the performance of RegCM3-BATS1e and RegCM3-IBIS, model precipitation output was compared primarily to data from the Tropical Rainfall Measuring Mission (TRMM) Multisatellite Precipitation Analysis (TMPA) 3B42 product (described in Huffman *et al.* 2007), referenced in this work simply as TRMM. The TRMM product is available from January 1998 to the present day, and was considered the most appropriate dataset for use in this study because it is available across the Maritime Continent at 3-hourly temporal and 0.25^{o} x 0.25^{o} spatial resolution, making it one of the highest resolution datasets available over this region.

Huffman *et al.* (2007) showed that TRMM produced good matching in the rainfall histogram compared to radar observations at Kwajelein, in the Republic of the Marshall Islands. When comparing time series of precipitation estimates from TRMM to observations obtained from buoys in the western Pacific Ocean, Huffman *et al.* (2007) also noted that the two datasets agreed on the occurrence of most precipitation events, despite some differences in sampling.

To confirm that TRMM would be suitable for use in this study, its precipitation estimates were compared to those from the meteorological station at Changi Airport, on the island of Singapore. Hourly rainfall observations were obtained for the period 0000 local time (LT) 1 January 1998 to 2400 LT 31 December 2001. The hourly data were aggregated into 3-hourly time periods to match the temporal resolution of TRMM. Figure 2-2 shows the

comparison between the histogram using the 3-hourly aggregated Changi station data and the TRMM land grid point closest to the island of Singapore, averaged for the period 1998-2001. The lowest rainfall intensity bin of less than 0.0417 mm hr^{-1} represents zero rainfall, since TRMM is not capable of detecting rainfall at intensities below 1 mm day^{-1}. Figure 2-2 shows that there is very good agreement in the histograms between the two datasets, and importantly the match at both ends of the histogram is very close.

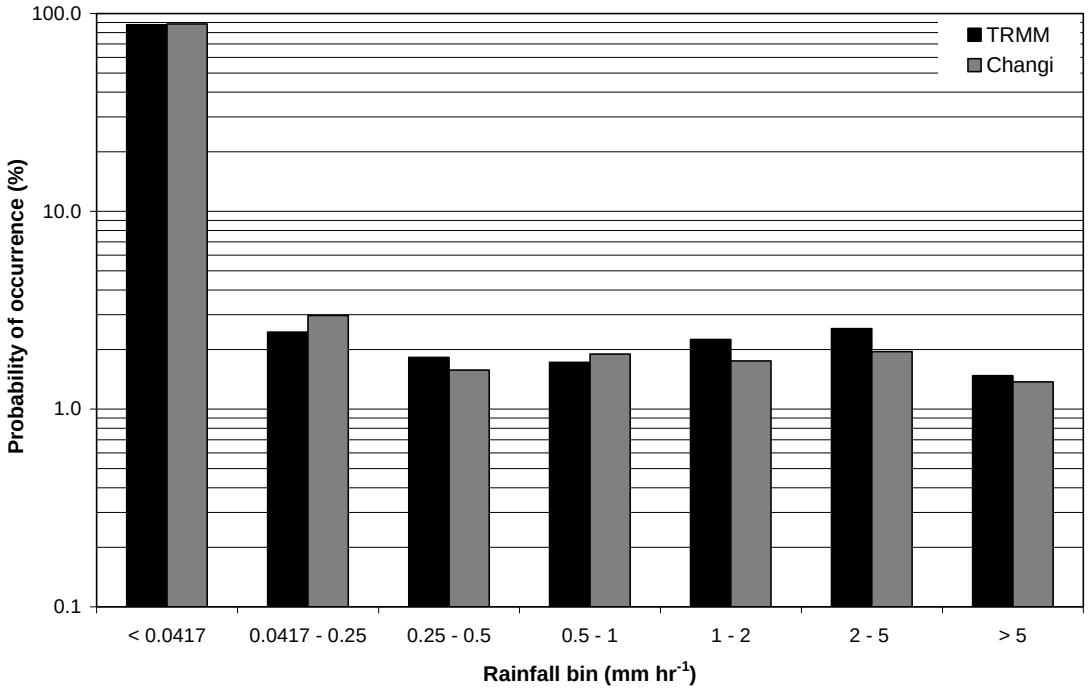

Figure 2-2. Rainfall histogram, with rainfall intensities in mm hr^{-1}, over Singapore for period 1998-2001: comparison between TRMM (black) and Changi meteorological station (grey), shown on log-linear axes.

Figure 2-3 shows the diurnal cycle of rainfall using the same two datasets, averaged over the period 1998-2001. The time stamp for the aggregated Changi station data is offset from the TRMM time stamp by 0.5 hours. This is because the timestamp for the center of the given 3-hourly averaging window used for the TRMM product is on the hour, while for the Changi dataset the center of the given hourly data window is on the half hour. Again there is very good agreement in the two datasets in terms of the general shape and magnitude of the curve. Figure 2-3 shows that the daily peak in TRMM lags slightly behind the Changi station data. However, with the 3-hour data interval of TRMM, it is impossible to

say exactly how large the lag is between the datasets. TRMM does contain a wet bias, with an average daily rainfall rate of 7.4 mm day^{-1} compared to 6.8 mm day^{-1} from the Changi data. Also the peak daily rainfall rate in TRMM, occurring around 4 pm, is approximately 0.2 mm hr^{-1} higher than the Changi station data. Despite this bias, it is considered that the TRMM dataset compares well enough to the Changi station data to be suitable for use in this assessment, especially given the difference in resolution between these two datasets.

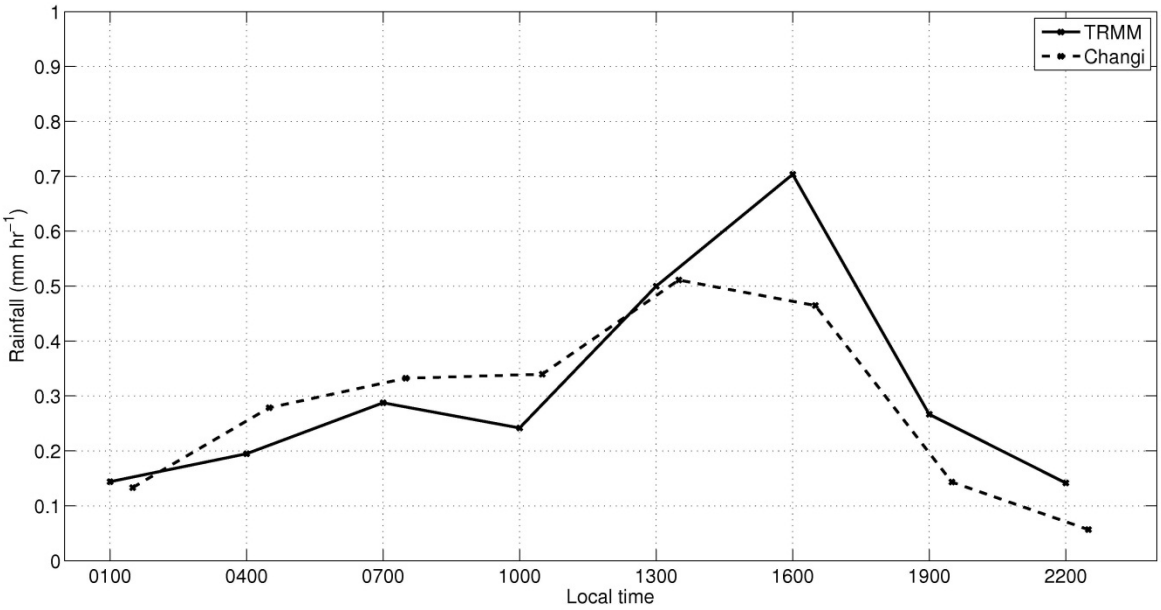

Figure 2-3. Average diurnal cycle of rainfall (in mm hr^{-1}) over Singapore for period 1998-2001: comparison between TRMM (solid line) and Changi meteorological station (dashed line).

2.3 Simulation Results

The two simulations chosen as the comparative basis for all other simulations are the Grell scheme with Fritsch-Chappell closure (GFC) and the Emanuel scheme (EMAN) used with the ERA40 boundary conditions and BATS1e land surface scheme. Analysis of these two simulations will be presented first.

2.3.1 GFC and EMAN

Figure 2-4 presents the rainfall histogram for TRMM compared to the GFC and EMAN simulations. The histogram has been constructed by splitting the domain with a land-ocean mask (excluding the boundary edges) to elucidate differences in model performance over

different surface types. The lowest rainfall intensity bin, equivalent to less than 1 mm day^{-1}, is used to represent dry periods.

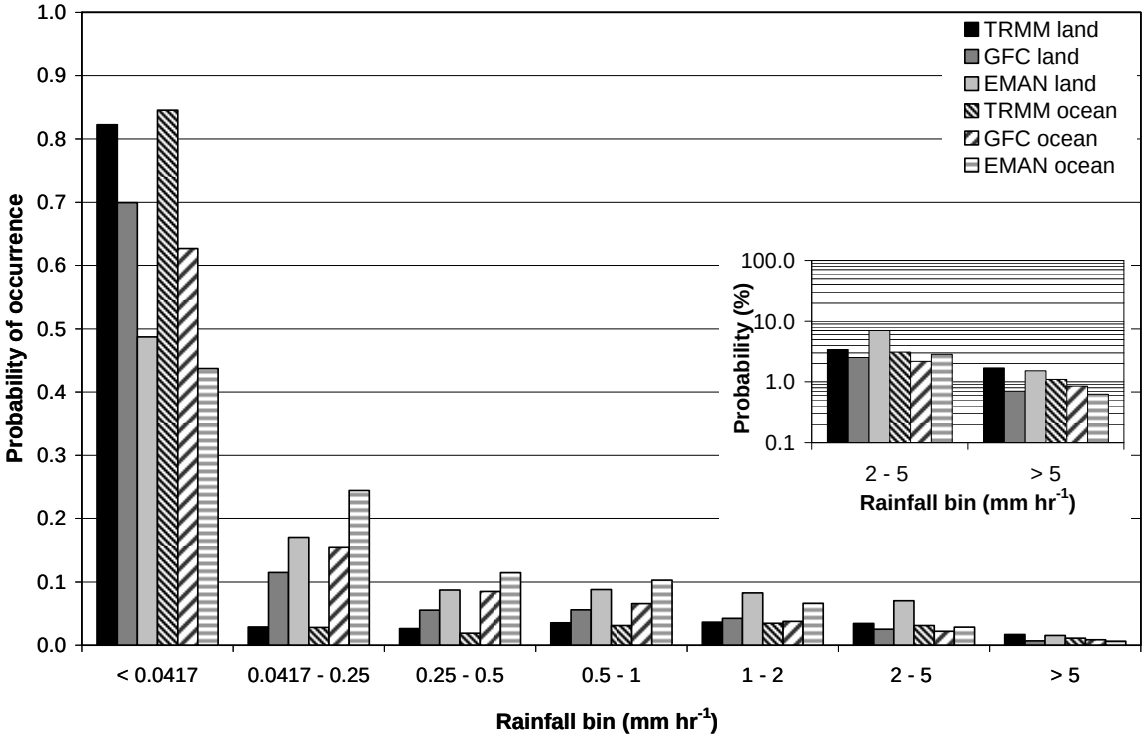

Figure 2-4. Rainfall histogram, with rainfall intensities in mm hr^{-1}, over Maritime Continent for period 1998-2001: comparison between TRMM and the GFC and EMAN simulations. All rainfall bins are shown on linear axes, with the inset panel also showing the highest-intensity rainfall bins on log-linear axes to allow for easier visualization of the tail end of the histogram.

Figure 2-4 shows that both simulations contain significant errors in the rainfall histogram, particularly with respect to the simulated frequency of dry periods and low intensity rainfall (the first and second rainfall bins, respectively). The first rainfall bin shows the proportion of time that the observations / simulations record no rainfall, so the proportion of time with non-zero rainfall can be found by taking the difference between 100% and the value in the first rainfall bin (this will be equal to the sum of the remaining rainfall bins).

The magnitude of error is larger in EMAN than in GFC. Over land, EMAN simulates non-zero rainfall nearly 3 times as frequently as TRMM (non-zero rainfall occurs 51% of the time in EMAN but only 17% of the time in TRMM), while GFC simulates non-negligible

rainfall nearly twice as frequently as TRMM (non-zero rainfall occurs 30% of the time in GFC). Figure 2-4 also shows that both GFC and EMAN simulate low intensity rainfall, less than 0.25 mm hr^{-1}, over land about 10 times more frequently than recorded in TRMM. Over ocean, the errors in the frequency of dry periods and low intensity rainfall are even worse than over land in both simulations.

The model errors in the low intensity end of the rainfall histogram could be physically understood as the model simulating frequent drizzle, while the observational data suggests less frequent bursts of rainfall. Figure 2-5 illustrates this difference: it shows the time series of rainfall over the location of Singapore for the first 2 months of the analysis period, January to February 1998. The simulated rainfall time series for EMAN (not shown here) is qualitatively similar to GFC, but with more pronounced errors. While there are differences between TRMM and Changi in the magnitude and exact timing of rainfall, the datasets agree on the general inter-storm period and order of magnitude of rainfall events. By contrast, GFC simulates much higher frequency of rainfall with relatively low intensities.

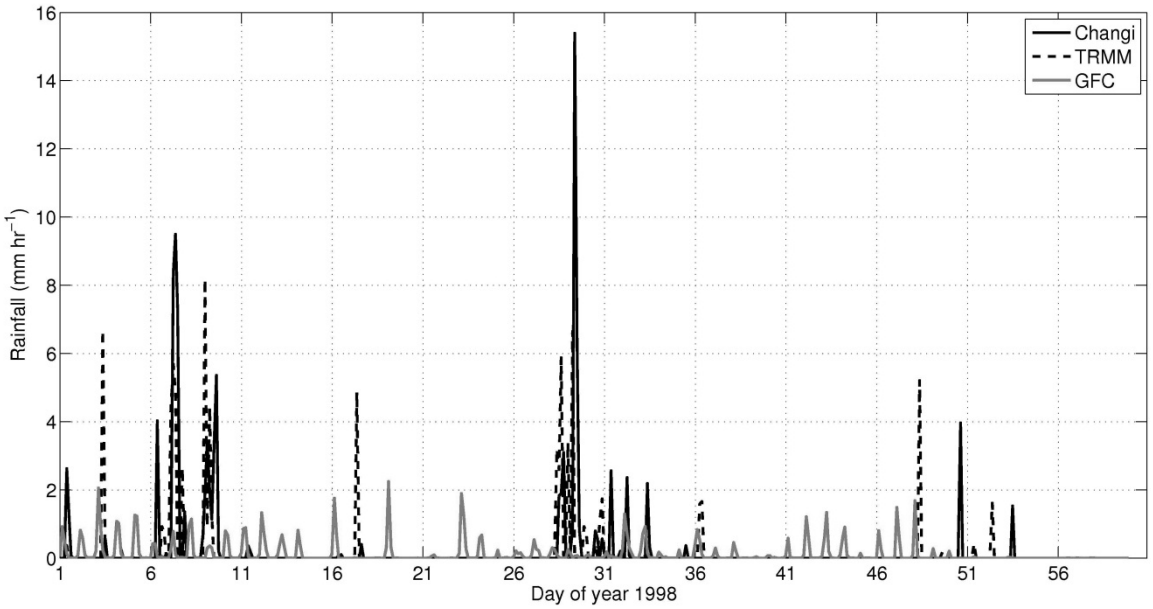

Figure 2-5. Time series of rainfall (in mm hr^{-1}) over Singapore for period January – February 1998. The short time interval allows the nature of the model error to be illustrated.

In the medium rainfall intensity range of 0.25-2 mm hr^{-1}, Figure 2-4 shows that both GFC and EMAN simulate rainfall over both land and ocean with higher frequency than

TRMM, though the errors are smaller for GFC than for EMAN. For rainfall of intensity 2-5 mm hr^{-1}, GFC simulates rainfall with similar frequency to TRMM. EMAN simulates similar frequency of rainfall to TRMM over ocean, but overestimates rainfall frequency at this intensity over land. For high intensity rainfall of greater than 5 mm hr^{-1}, Figure 2-4 shows that GFC simulates rainfall with less frequency than TRMM over both land and ocean. EMAN simulates rainfall of high intensity at about the same frequency as TRMM over land, but with less frequency than TRMM over ocean.

Figure 2-6, Figure 2-7 and Figure 2-8 illustrate the spatial difference in rainfall over land and ocean through representation of the average diurnal cycle, with each 3-hourly averaging window over 24 hours represented by one panel in each figure. Figure 2-6 shows the average diurnal cycle for 1998 to 2001 from TRMM. The diurnal movement of rainfall between land and ocean is very clear. Rainfall over land begins in the late afternoon (around 1600 LT mid-domain), builds into the evening (until about 2200 LT mid-domain) and dissipates by early morning (around 0400 LT mid-domain). Over ocean the rainfall begins late at night (around 2200 LT mid-domain), builds in the morning (until about 0400 LT mid-domain) and dissipates by early afternoon (around 1300 LT mid-domain).

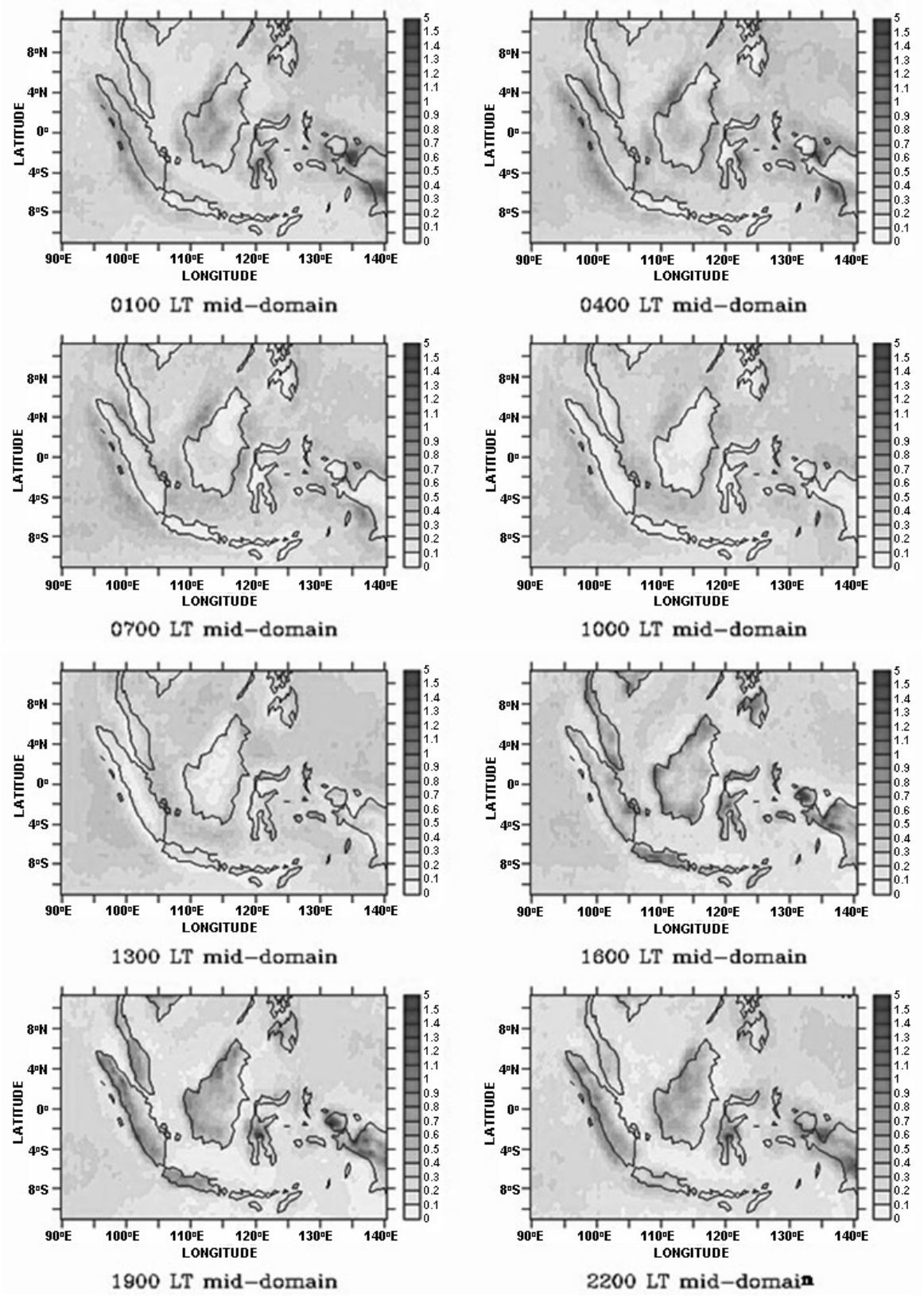

Figure 2-6. Diurnal cycle of rainfall from TRMM. Local time for the center of the domain is given at the bottom of each panel. Each panel represents the average rainfall rate in mm hr^{-1} (shown by the color scale bar) over a 3-hour period centered at the given time, averaged over the period 1998-2001.

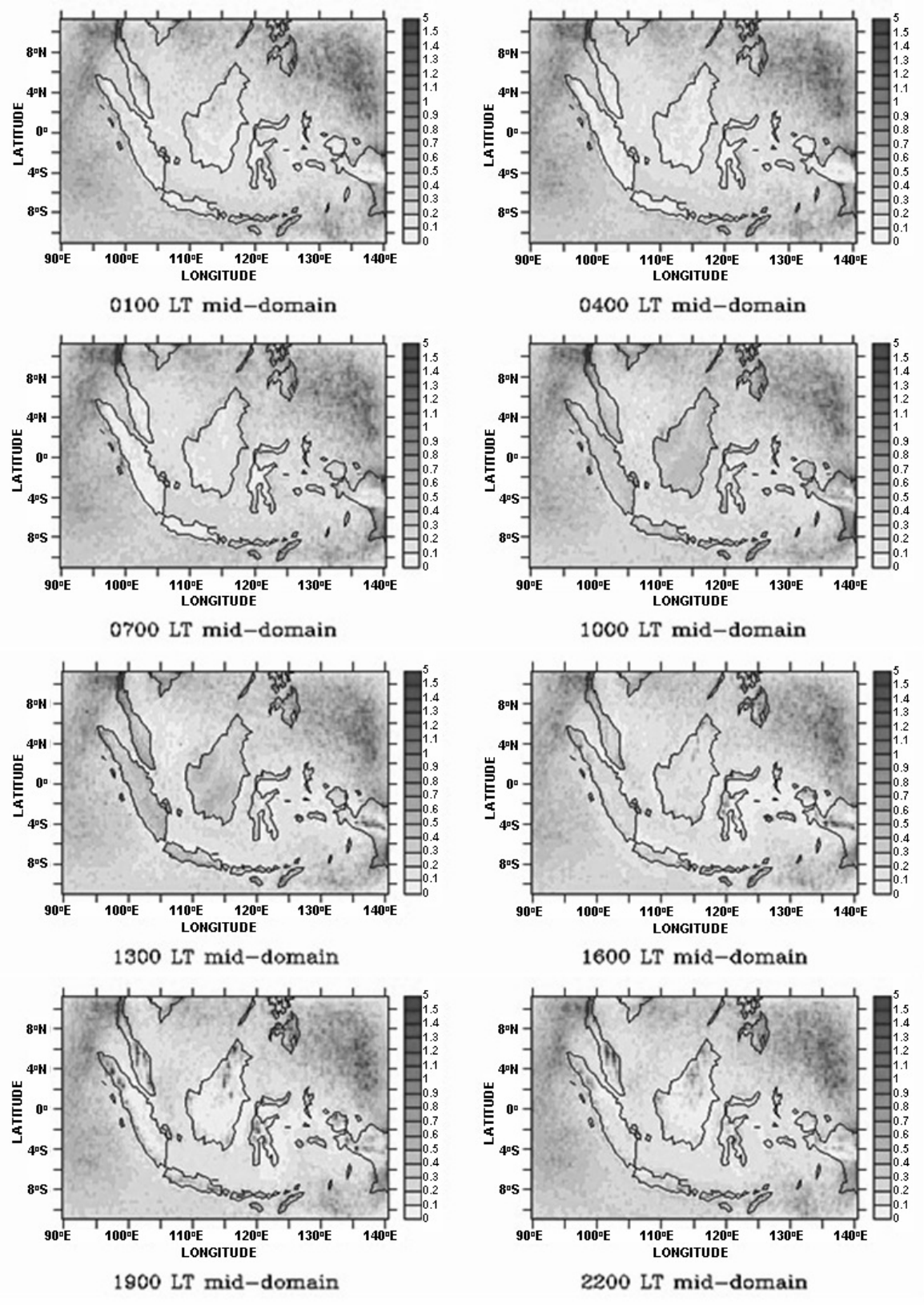

Figure 2-7. As for Figure 2-6 but for the GFC simulation.

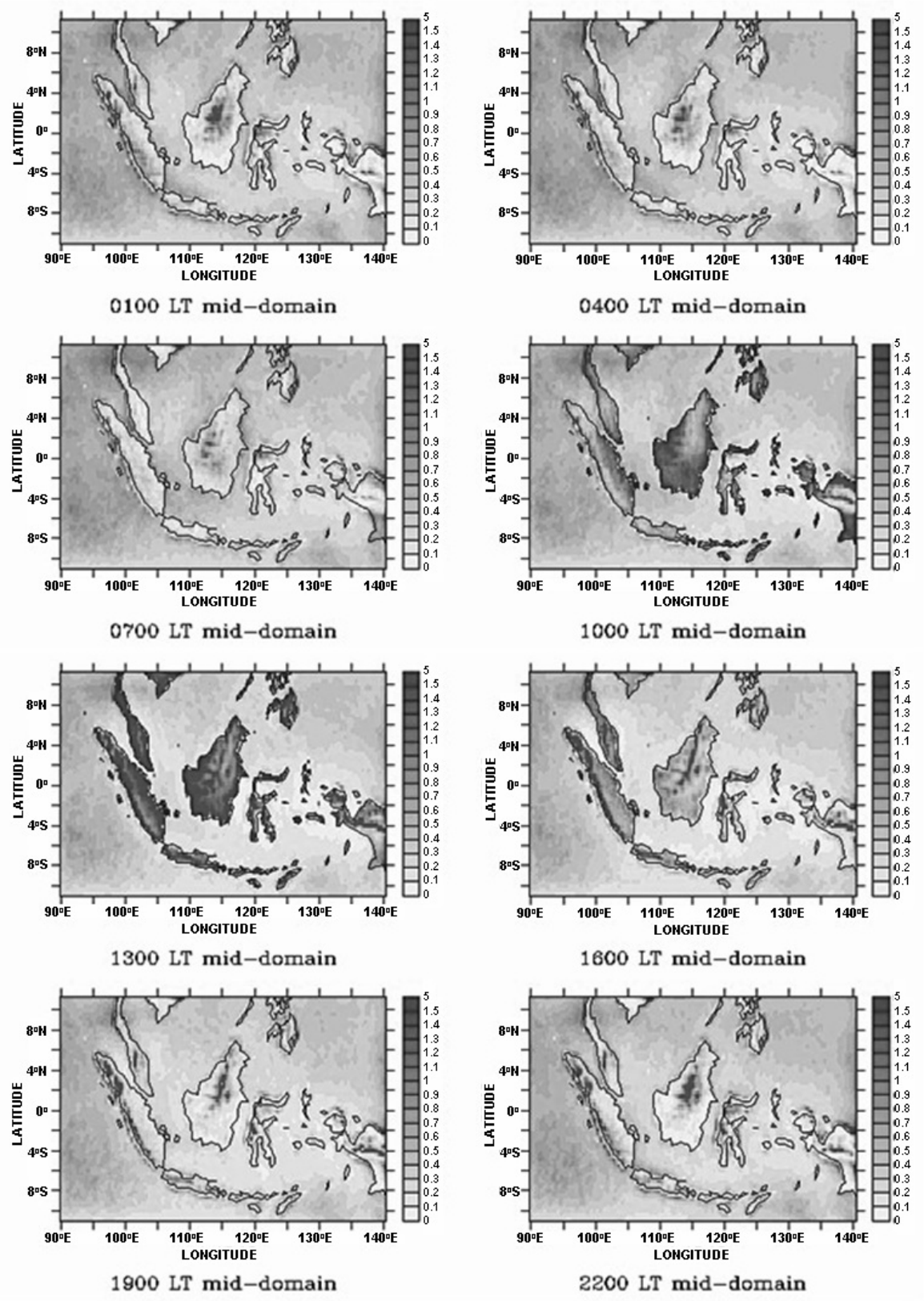

Figure 2-8. As for Figure 2-6 but for the EMAN simulation.

Figure 2-7 and Figure 2-8 show the average diurnal cycle of rainfall from GFC and EMAN respectively. In both simulations, the model capably simulates a diurnal signal of rainfall over land, with rainfall building in the late morning and prolonged rainfall over some mountainous areas in the evening. However, there are several errors to note in both simulations. In GFC, the magnitude of the rainfall peak over land is not as great as in TRMM, while the magnitude of rainfall over ocean is skewed relative to TRMM: the enclosed ocean in the center of the domain shows a negligible diurnal signal and very little total rainfall, but the open ocean areas in the corners of the domain receive more rainfall than most of the land areas. In EMAN, the rainfall over land is significantly greater than in TRMM, although the simulated oceanic rainfall is generally better in EMAN than in GFC. In both simulations, the diurnal rainfall peak over land arrives about 6 hours too early compared to TRMM.

Table 2-2 presents the average total rainfall, separately for land and ocean, for TRMM and the model simulations. In GFC there is a dry bias over land and a wet bias over ocean. Figure 2-7 shows that this bias occurs over the more open ocean areas towards the edges of the domain. EMAN presents a very significant wet bias over land, with nearly twice the amount of rainfall as TRMM, and also contains a wet bias over ocean.

Table 2-2 also shows the relative partitioning of total rainfall into convective and large-scale (stratiform) rain. Observations of the different fractions were taken from Mori *et al.* (2004), who used the 2A25, 2A12 and 2B31 TRMM products to describe the convective versus stratiform rainfall split over Indonesia for the period 1998-2000. The observations show that in general the majority of rainfall in this region results from convection, with a slightly higher proportion of convective rainfall over land than over ocean.

Table 2-2 shows that both GFC and EMAN simulate more convective than large-scale rainfall, over both land and ocean, but exhibit some error. Over land, GFC underestimates both the convective rainfall fraction and the magnitude of convective rainfall. Over ocean, GFC simulates the convective-large-scale rainfall split reasonably well, with some overestimation of each type of rainfall. Over land, EMAN simulates the convective-large-scale rainfall split reasonably well but significantly overestimates the volumes of each type.

Over ocean, EMAN significantly overestimates the convective rainfall fraction, with underestimation of the large-scale rainfall volume.

The remaining simulations in Table 2-2 will be discussed in the following sections.

Table 2-2. Average daily rainfall (in mm day^{-1}) over land and ocean over period 1998-2001 for each simulation presented in this assessment, with TRMM values shown for comparison.

Product / Simulation	Land Average			Ocean Average		
	Total	Convective	Large-scale	Total	Convective	Large-scale
TRMM	*8.7*	*5.5 (63%)*	*3.2 (37%)*	*7.0*	*4.0 (57%)*	*3.0 (43%)*
GFC	7.7	4.2 (54%)	3.5 (46%)	8.8	4.8 (54%)	4.0 (46%)
EMAN	16.3	9.6 (59%)	6.7 (41%)	8.3	6.4 (77%)	1.9 (23%)
GAS	5.7	1.1 (20%)	4.6 (80%)	6.0	1.2 (20%)	4.8 (80%)
GFCNCEP	4.7	2.2 (46%)	2.5 (54%)	2.3	1.1 (48%)	1.2 (52%)
EMANNCEP	8.7	6.4 (73%)	2.3 (27%)	2.5	2.2 (87%)	0.3 (13%)
GFCIBIS	8.5	3.7 (43%)	4.8 (57%)	6.7	3.6 (53%)	3.1 (47%)
EMANIBIS	14.9	8.8 (59%)	6.1 (41%)	7.3	5.8 (79%)	1.5 (21%)

Figure 2-9 shows the average diurnal cycle of rainfall separately for land and ocean for each of the convection schemes used in this study. Over land, the daily peak rainfall rate occurs around 7 pm in TRMM but around midday in GFC and EMAN, as was suggested by Figure 2-6, Figure 2-7 and Figure 2-8. Over ocean, both GFC and EMAN simulate the average diurnal cycle of rainfall reasonably well compared to TRMM. The peak rainfall rate in both simulations occurs at approximately the same time as TRMM, in the early morning. The diurnal amplitude of rainfall over ocean is also well represented in GFC and EMAN.

Discussion of the other simulations shown in Figure 2-9 is contained in the following sections.

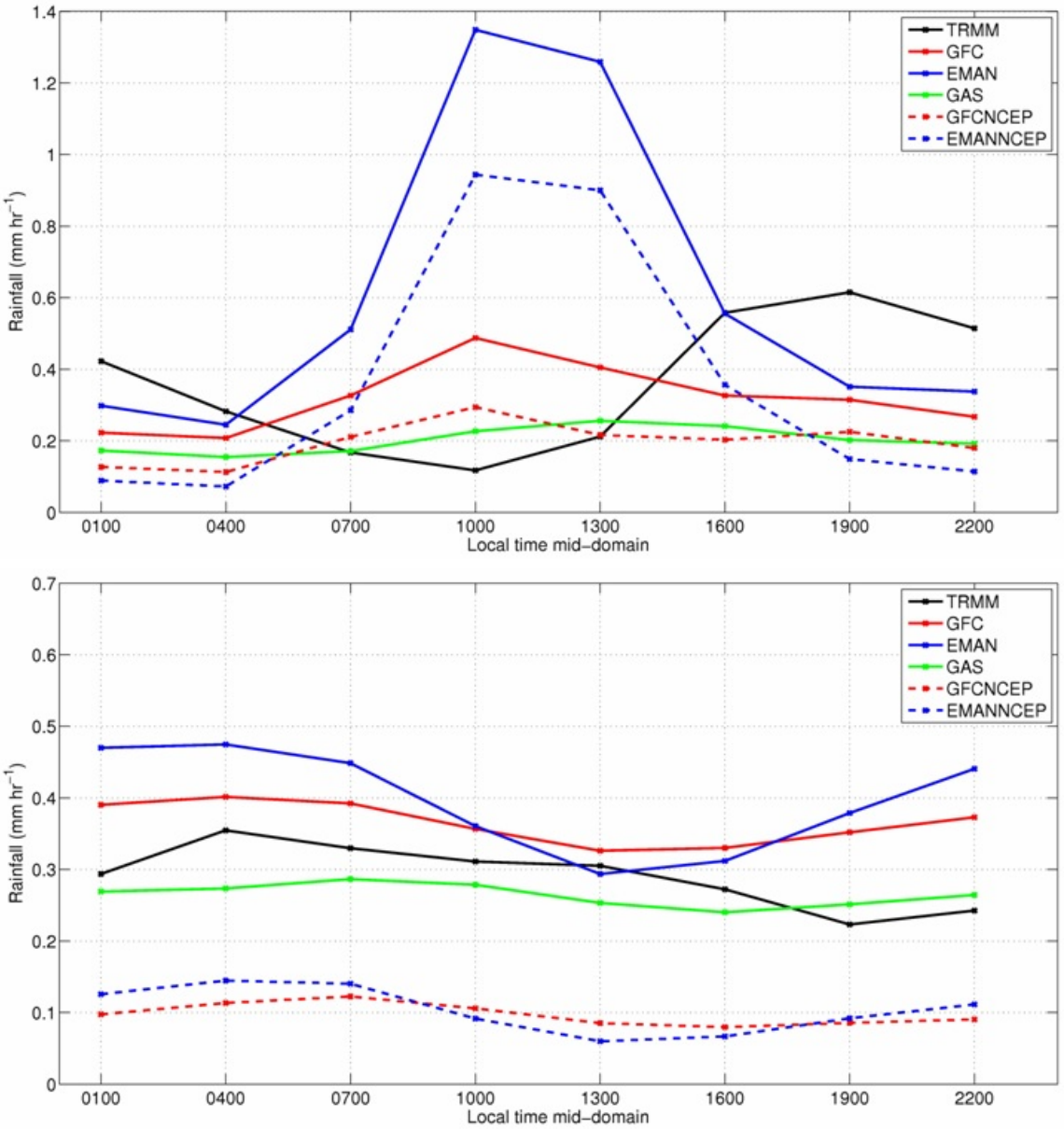

Figure 2-9. Average diurnal cycle of rainfall (in mm hr^{-1}) over period 1998-2001: comparison between TRMM, the GFC (red) and EMAN (blue) simulations using ERA40 (solid lines) and NCEP (dashed lines), and the GAS simulation (green). All simulations use the BATS1e land surface scheme. (a) Upper panel shows average of land cells within the domain; (b) lower panel shows average of ocean cells.

2.3.2 Convection Scheme Comparison

Figure 2-9 shows the simulated diurnal cycle of rainfall from the GAS simulation. The rainfall histogram for this simulation contained values midway between the EMAN and GFC

histograms, and so for brevity it is not shown here. Table 2-2 presents the average daily rainfall over land and ocean for the GAS simulation.

The results show that the GAS simulation presents a dry bias over both land and ocean, and the bias is worse over land than that presented by GFC. The amount of convective rainfall simulated by GAS is severely underestimated over both land and ocean, such that the majority of the total rainfall results from the large-scale scheme in the GAS simulation rather than from the convection scheme. The timing of the diurnal cycle in GAS compares well to observations, although the amplitude of the cycle is much smaller in GAS than in TRMM.

2.3.3 Lateral Boundary Conditions Comparison

Simulations using both the Grell with Fritsch-Chappell closure and Emanuel schemes were run using NNRP2 instead of ERA40, to test the model's sensitivity to lateral boundary conditions. These simulations are termed GFCNCEP and EMANNCEP; descriptions are given in Table 2-1. Figure 2-9 shows the average diurnal rainfall cycle for the GFCNCEP and EMANNCEP simulations compared to TRMM and the GFC and EMAN simulations. Average daily rainfall values over land and ocean are presented in Table 2-2.

Figure 2-9 shows that both GFCNCEP and EMANNCEP simulate a diurnal rainfall cycle over land and ocean with generally the same shape and timing as their respective comparison simulations, GFC and EMAN. Both GFCNCEP and EMANNCEP contain the same timing error of an early daily rainfall peak over land. However, the magnitude of rainfall is significantly impacted by the choice of boundary conditions. Using NNRP2 instead of ERA40 reduced the rainfall in GFC by 40% over land, worsening the dry bias that this scheme presents over land. The rainfall in EMAN was reduced by nearly 50% over land, virtually eliminating the wet bias that this scheme presents over land and producing a rainfall volume that matches TRMM. Over ocean, the impact of using NNRP2 was even greater, reducing the rainfall simulated by both GFC and EMAN by at least 70% and producing significant dry biases. The NCEP simulations exhibit similar errors to the previous simulations with regard to the convective rainfall fraction: GFCNCEP exhibits underestimation of the convective rainfall fraction, while EMANNCEP overestimates the convective fraction, with particularly bad error

over the ocean. The rainfall histogram as simulated by GFCNCEP and EMANNCEP (not shown for brevity) showed some improvement compared to GFC and EMAN, but still contained significant error in the simulation of dry periods and low intensity rainfall, and significantly worsened the error in underestimation of high intensity rainfall.

2.3.4 Land Surface Scheme Comparison

Finally, simulations using IBIS were run as an alternative to BATS1e, to test the sensitivity of the model performance to the underlying land surface scheme. These simulations are termed GFCIBIS and EMANIBIS; descriptions are given in Table 2-1.

Figure 2-10 shows the rainfall histogram just for the land grid cells. There are some small differences between the simulations using BATS1e and IBIS that vary depending on the convection scheme. With GFCIBIS, the errors in the frequency of dry periods and low intensity rainfall are slightly less than in GFC: the frequency of dry periods increases from 70% in GFC to 72% in GFCIBIS compared to 82% in TRMM, while the frequency of low intensity rainfall decreases from 12% in GFC to 11% in GFCIBIS compared to 3% in TRMM. Thus the histogram for GFCIBIS is a closer match to TRMM than for GFC. By contrast, EMANIBIS produces worse error than EMAN: the frequency of dry periods decreases from 49% in EMAN to 45% in EMANIBIS, and the frequency of low intensity rainfall increases from 17% in EMAN to 19% in EMANIBIS. However, the differences between GFC and GFCIBIS or between EMAN and EMANIBIS are smaller than the differences between TRMM and any of the individual simulations.

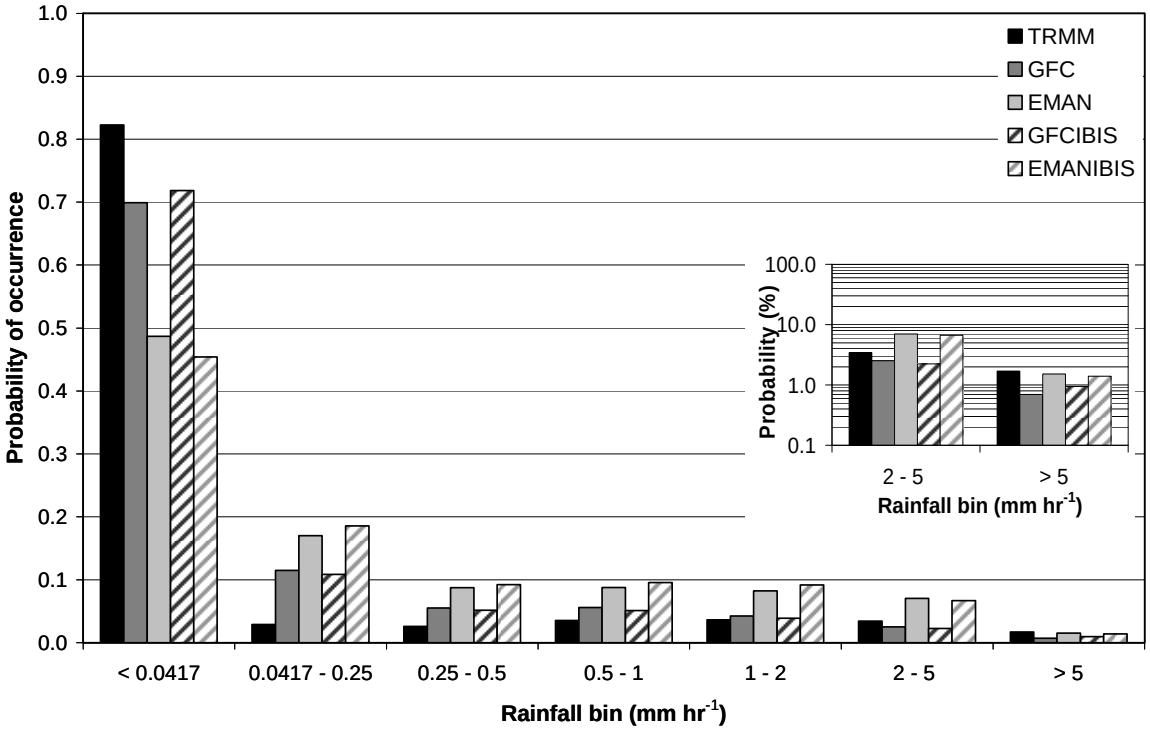

Figure 2-10. Rainfall histogram, with rainfall intensities in mm hr^{-1}, comparing TRMM and the simulations using GFC and EMAN with both BATS1e and IBIS for period 1998-2001. Results are shown only for land cells. All rainfall bins are shown on linear axes, with the inset panel also showing the highest-intensity rainfall bins on log-linear axes.

Figure 2-11 shows the average diurnal rainfall cycle for the GFCIBIS and EMANIBIS simulations compared to TRMM and to the GFC and EMAN simulations. Average daily rainfall values over land and ocean are presented in Table 2-2. The results show that the total rainfall over land in GFCIBIS is improved compared to GFC, with a very close match to TRMM. However, Table 2-2 indicates that the partitioning of rainfall in this simulation contains significant error, with 20% underestimation of the convective fraction and compensatory overestimation of the large-scale fraction. Over ocean, GFCIBIS simulates both the rainfall volumes and convective-large-scale split very well compared to observations. Over land, EMANIBIS suffers from similar problems as EMAN, with severe overestimation of both convective and large-scale rainfall. Over ocean, EMANIBIS simulates the total rainfall volume very well but significantly overestimates the convective rainfall fraction.

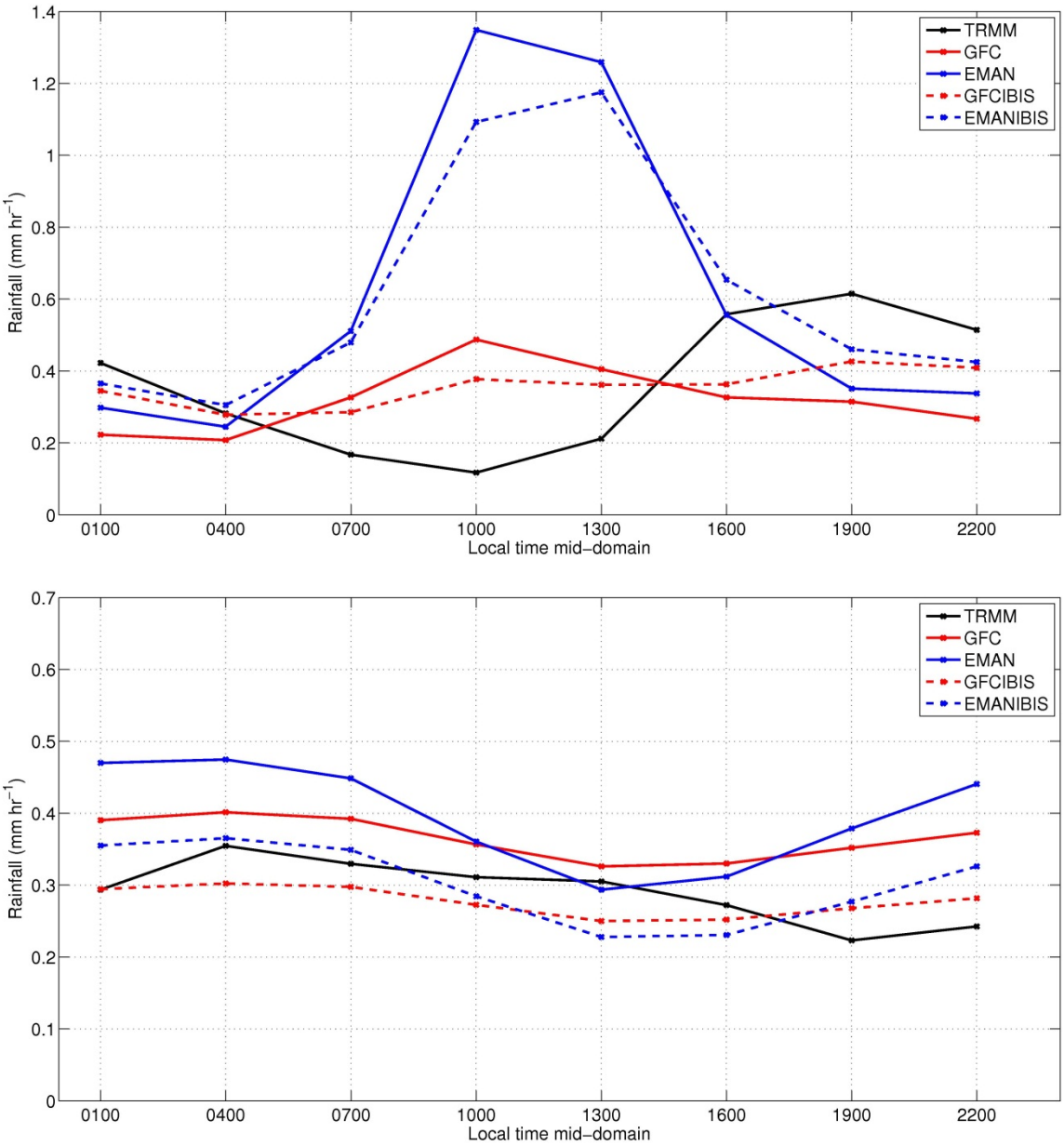

Figure 2-11. Average diurnal cycle of rainfall (in mm hr^{-1}) over period 1998-2001: comparison between TRMM and the GFC (red) and EMAN (blue) simulations using BATS1e (solid lines) and IBIS (dashed lines). (a) Upper panel shows average of land cells within the domain; (b) lower panel shows average of ocean cells.

Over land, Figure 2-11 shows that the timing of the diurnal rainfall cycle in GFCIBIS is significantly changed relative to GFC, with the daily rainfall peak occurring in the late evening with a closer match to TRMM. This is due to the decrease in convective rainfall with GFCIBIS compared to GFC: convective rainfall occurs primarily during the afternoon, concomitant

with the incoming solar radiation, while large-scale rainfall occurs mostly at night in the simulations (not shown). The diurnal amplitude of the rainfall cycle is poor in GFCIBIS, with amplitude of only 0.125 mm hr^{-1} compared to 0.5 mm hr^{-1} in TRMM. The general shape and timing of the diurnal rainfall cycle is unchanged between EMAN and EMANIBIS, exhibiting error with an early and overestimated daily rainfall peak, although EMANIBIS produces a smaller daily rainfall peak than EMAN and reduces the wet bias.

Over ocean, the shape and timing of the diurnal rainfall cycle are relatively unchanged both between GFC and GFCIBIS and EMAN and EMANIBIS. For both convection schemes, IBIS results in less rainfall than BATS1e, producing a small dry bias in GFCIBIS and leaving a small wet bias in EMANIBIS.

To further investigate the differences between the BATS1e and IBIS simulations, the components of the surface energy flux were determined; average daily values are presented in Table 2-3. Net radiation is defined as the sum of surface absorbed (incoming minus reflected/emitted) shortwave and longwave radiation.

Table 2-3. Simulated average daily land surface energy fluxes and evapotranspiration components over period 1998-2001. Units are listed in notes below the table.

Simulation	R_N	LH	SH	ET	T	GE	I
GFC	154	117	37	4.0	2.0	0.7	1.3
EMAN	149	153	-2	5.3	1.2	0.7	3.4
GFCIBIS	143	104	36	3.6	2.1	0.4	1.0
EMANIBIS	143	134	6	4.6	1.6	0.6	2.4

R_N = Net radiation absorbed at surface (W m^{-2}), LH = latent heat flux away from surface (W m^{-2}), SH = sensible heat flux away from surface (W m^{-2}), ET = total evapotranspiration (mm day^{-1}), T = transpiration (mm day^{-1}), GE = ground evaporation (mm day^{-1}), I = interception loss (mm day^{-1}).

The net radiation at the land surface is higher in GFC than in GFCIBIS. The majority of the radiation is removed from the land surface via latent heat flux in both GFC and GFCIBIS, though GFC has a higher value of latent heat flux to compensate for a higher net radiation, while the sensible heat flux values are almost the same between the two simulations. The net radiation at the land surface is almost the same in EMAN and EMANIBIS, but the breakdown of net radiation is significantly different between the two simulations. In EMAN,

almost all the radiation at the land surface is removed via latent heat flux, with the latent heat flux being so strong as to create a negative net sensible heat flux, i.e. net flux downward towards the surface. By contrast in EMANIBIS, while the majority of the net radiation is still removed by latent heat flux, some radiation is also removed from the surface via sensible heat flux.

Since the large majority of surface-absorbed radiation is removed via latent heat flux in all four of these simulations, it is possible that overestimation of evapotranspiration (ET) contributes to the observed errors in simulated rainfall. This potential source of error was investigated by looking at each simulated component of ET: transpiration from foliage, evaporation from ground surfaces (either beneath the canopy or from patches of bare ground), and interception loss (evaporation directly from wetted vegetation surfaces). Average daily values of each ET component from GFC, EMAN, GFCIBIS and EMANIBIS are also presented in Table 2-3.

In both GFC and GFCIBIS, the largest contributor to the total ET is transpiration, with interception loss constituting a smaller fraction in both simulations. It is interesting that interception loss decreases from GFC to GFCIBIS even though total rainfall over land increases. This is likely due to the shift in timing of the rainfall cycle, shown in Figure 2-11. The decrease in midday rainfall reduces the amount of water available for direct evaporation from the wet canopy during the daytime, when the net radiation is highest. Ground evaporation is the smallest component of ET, representing only a small fraction of total ET in both Grell simulations.

The ET component breakdown results are quite different for the Emanuel scheme simulations. Total ET is higher in both EMAN and EMANIBIS than in the Grell simulations, and with both Emanuel simulations the largest contributor to the total ET is interception loss. The partitioning between interception loss and transpiration is therefore reversed between the GFC and EMAN simulations. This result can be understood in terms of the much higher volumes of rainfall simulated by both Emanuel scheme simulations and the peak rainfall occurring at midday in both of these simulations, concomitant with the peak radiation and

therefore leading to high evaporation rates from the wetted canopy. Ground evaporation is again the smallest component of ET in both EMAN and EMANIBIS.

To compare these results to observations, Table 2-4 presents measured values of ET, interception loss and transpiration from field studies conducted at various locations across the Maritime Continent. These studies suggest that the average observed ET is approximately 3.5 mm day^{-1}. Hence simulated total ET is too high in all simulations presented here except GFCIBIS.

Table 2-4. Measured values of ET, interception loss and transpiration (in mm day^{-1}) from field studies.

Study Location	Total ET (mm day^{-1})	Interception Loss	Transpiration (mm day^{-1})	Reference
Forests, northern Sumatra	3.4-3.9			Wild and Hall 1982
Lowland tropical rainforest, western Java	4.1	1.6 mm day^{-1} (21% of total rain)	2.4-2.6	Calder *et al.* 1986
Montane forests, Sabah, Borneo	1.9-2.5		0.85-2.1	Bruijnzeel *et al.* 1993
Brunei, northwest Borneo		1.3 mm day^{-1} (18% of total rain)		Dykes 1997
Unlogged and logged forests, Kalimantan, Borneo		unlogged: 0.7 mm day^{-1} (11% of rain), logged: 0.6 mm day^{-1} (6% of rain)		Asdak *et al.* 1998
Lowland forest, Malaysia and Indonesia	3.2-3.4			Goh 2003
Forest, Sarawak, Borneo			2.9-3.5	Kumagai *et al.* 2004
Lowland tropical forest, Borneo		0.6 mm day^{-1} (8.5% of rain) – 0.8 mm day^{-1} (12% of rain)		Manfroi *et al.* 2006
Heath and evergreen rain forest, Kalimantan, Borneo		17% of rain		Vermimmen *et al.* 2007

Table 2-4 shows that the average observed value of interception loss is approximately 1.2 mm day^{-1}, while for transpiration the average observed value is about 2.4 mm day^{-1}. Hence the interception loss simulated by GFC and GFCIBIS is close to observations, but interception loss simulated by EMAN and EMANIBIS is too high. The

simulated transpiration rates are about 0.4 mm day^{-1} too low in GFC and GFCIBIS and 1 mm day^{-1} too low in EMAN and EMANIBIS.

2.4 Discussion

The simulations presented here have demonstrated three errors in the rainfall histogram as simulated by both the RegCM3-BATS1e and RegCM3-IBIS model systems: 1) large underestimation of dry periods; 2) large overestimation of low intensity rainfall; 3) small underestimation of high intensity rainfall. These errors indicate that the model simulates very frequent drizzle, particularly over the ocean, while observations show less frequent bursts of rainfall. It is noted that the magnitude of the error in reproducing the observed frequency of high intensity rainfall is relatively small, certainly smaller than the error in reproducing the observed frequency of low intensity rainfall. However, since high intensity rainfall has such a significant impact on surface hydrology, and therefore its accurate simulation is crucial for studies of land use change, it is considered that the histogram errors documented here are all significant.

These errors persist, to a greater or lesser degree, regardless of the choice of convective parameterization scheme, land surface scheme or lateral boundary conditions. The Grell convection scheme with Fritsch-Chappell closure used in conjunction with the IBIS land surface scheme presented the smallest magnitude of error in the rainfall histogram compared to the other simulations presented here, but still contained substantial error. In results not shown here, the histogram errors also persisted when the horizontal resolution was increased to use 15 km grid cells instead of 30 km, the model domain was increased to twice the extent of the current domain in each direction (bounded approximately by 70^{o}E – 160^{o}E and 20^{o}N – 20^{o}S), and 29 vertical layers were used instead of 18, indicating that the errors are not merely artifacts of the experimental design.

This assessment has also documented error in the volume of rainfall simulated over both land and ocean. The presence of either a wet or dry bias and the magnitude of this bias were shown to be highly dependent on model user choices. In particular, changing the convection scheme and/or lateral boundary conditions can significantly impact the results. The Grell convection scheme with Fritsch-Chappell closure generally showed the smallest

magnitude bias of the convection schemes tested here, although it must be noted that the Grell scheme generally underestimates the proportion of rainfall that is created by convection over land. The large-scale rainfall tends to compensate for this underestimation, such that the total rainfall volume matches well to observations. Despite the Emanuel scheme's more sophisticated treatment of mixing and entrainment processes, which might lead one to expect better results over regions with significant convection, this scheme did not show good performance over the Maritime Continent, with very large error in the rainfall histogram and a significant wet bias over land. The convective rainfall fraction was very large, indicating that much of the overestimation in total rainfall was created by convection.

Both the Grell and Emanuel schemes suffered from error in the timing of the diurnal rainfall cycle, with a daily peak that was 6-9 hours too early compared to TRMM. It is noted that the diurnal cycle in TRMM presented a lag relative to the Changi station data, and therefore it is possible that the actual daily rainfall peak occurs earlier over the Maritime Continent in general than indicated by TRMM. However, it can still be said that the simulated diurnal cycle is too early.

This assessment agrees with previous work that the ERA40 dataset is much wetter over the Maritime Continent than NNRP2. Over land, NNRP2 may lead to reasonable simulation of the diurnal rainfall cycle over some locations and with certain model configurations. For example, Qian (2008) showed that RegCM3-BATS1e using the Emanuel scheme with the NNRP2 lateral boundary conditions showed good performance in simulating the diurnal rainfall cycle over the island of Java. However, the general wet bias in the Emanuel scheme and dry bias in NNRP2 means that the two used in combination could produce the correct volume of rainfall for the wrong reasons. This study shows that NNRP2 produces a general dry bias over ocean areas, and with any convection scheme except Emanuel it also produces a dry bias over land areas. Therefore it is considered that the NNRP2 dataset is too dry for this region and less suitable for use as lateral boundary conditions than the ERA40 dataset.

This study indicates that the primary driver for the observed errors in the model is within the atmospheric part of the model system and not the land surface scheme, since the errors in the rainfall histogram were similar when using either BATS1e or IBIS. Also, it is noted that when simulated rainfall volumes are closer to observations (such as comparing the Grell scheme results to the Emanuel scheme), the simulated surface fluxes and ET components are also closer to observations. This suggests that the errors in surface fluxes are the result of errors in rainfall and not the cause. Since the partitioning between transpiration and interception loss is highly dependent on the fractional canopy area that is wet versus dry, which in turn depends on how frequently the canopy intercepts rainfall, it is easy to understand that this partitioning matches more closely to observations when simulated rainfall volumes are more realistic. The better performance of the simulations using IBIS compared to BATS1e suggests that there is some influence of the land surface scheme on the simulated rainfall, but this effect is comparatively small.

The errors documented here are not unique to RegCM3. For example, Dai and Trenberth (2004) showed that the NCAR Community Climate System Model GCM simulated precipitation greater than 1 mm day^{-1} occurring at least 80% of the time over the Maritime Continent, with greater frequency of lower intensity rainfall compared to observations. Wang *et al.* (2007) documented simulation errors in the phase of the diurnal cycle of rainfall over this region, as described previously. Stephens *et al.* (2010) showed that the frequency of occurrence of global oceanic precipitation in several GCMs, including the ECMWF, CAM and the UK Met Office GCM, was significantly overestimated compared to observations, even when the resolution of the observations was significantly degraded. In their study, only a cloud-resolving model was able to simulate the observed incidence of global precipitation (Stephens *et al.* 2010). Therefore the results presented here indicate that GCMs and RCMs experience the same difficulties in simulating the climate of the Maritime Continent, and it is not simply a matter of resolution or a specific user choice that is at fault. Rather there is a more fundamental issue at the root of these simulation errors in large-scale models.

Given that convection is the major source of rainfall in both the observations and simulations presented here, the model errors are likely to stem from the same problem:

convective rainfall is initiated too frequently. There are two steps to activating convective adjustment in GCMs and RCMs: establishing threshold criteria for triggering convection, and creating sufficient environmental conditions to meet those criteria. Consequently it is considered that there are two main avenues to pursue, to identify the origin of the errors documented in this assessment.

The first avenue of investigation is simulation of the lower atmosphere. This region determines the conditions that can precede or prohibit convection. It is also influenced by convective activity through the production of cumulus clouds, which absorb and reflect incoming radiation and produce rainfall, cooling and moistening the surface environment and thereby inhibiting further convection. Therefore accurate simulation of the lower atmosphere is critical for establishing the necessary pre-conditioning for convective adjustment within large-scale climate models.

The remainder of this thesis will pursue this avenue of investigation in two parts:

1. simulation of the planetary boundary layer region, the processes that drive the diurnal rise and fall of the boundary layer height and the location of the lifted condensation level with respect to the top of the boundary layer (i.e. the role of the near surface environment in forcing convection); and
2. simulation of the cloud cover that results from convective activity and the production of convective rainfall (i.e. the feedback of convective activity on the near surface environment and subsequent convection).

Simulation of the boundary layer and near surface environment will be investigated in Chapter 3. The simulation of convective cloud cover is covered in Chapter 4 and the production of convective rainfall from that cloud cover is investigated in Chapter 5.

The second suggested avenue of investigation is with regard to the nature of the threshold criteria for triggering convection. Presently, the convection schemes in RegCM3 (and many other RCMs) contain threshold criteria that are essentially uniform in time and space and are meant to represent the mean behavior of an ensemble of convective cells. These schemes were originally made for use in a model with a coarse resolution, such that a single grid cell could be expected to contain an ensemble of individual convective cells.

However, a single grid cell in an RCM simulation might only hold one or a few convective cells. Therefore the effect of using a uniform threshold criterion is essentially to impose the mean behavior of many convective cells onto every convective cell within an RCM domain.

It seems likely that both spatial and temporal variability in convection need to be incorporated into the RegCM3 model system to improve model performance. This problem has been identified and reviewed by Neelin *et al*. (2008) among others, and the current literature indicates ongoing work to incorporate stochasticity into the triggering of convective activity as one method of introducing the necessary variability. This thesis will not explore the issue of subgrid variability in convective triggering, but it is recommended that future developments on this subject be incorporated into the RegCM3 model system.

There may also be other methods for limiting the onset of convection. For example, Chow *et al.* (2006) found that the Emanuel convection scheme produced too much rainfall over East Asia during the Asian summer monsoon, particularly over the South China Sea region. The model performance was improved by applying convection suppression criteria in the form of a relative vorticity threshold, whereby the convection was shut down when the low-level flow was anticyclonic and stronger than a given threshold value (Chow *et al.* 2006). Peng *et al.* (2004) used the Emanuel scheme within the Navy Operational Global Atmospheric Prediction System (NOGAPS). Those authors found errors in under-prediction of high intensity rainfall and too much light intensity rainfall, with a systematic wet bias. Improvement in the performance of NOGAPS was achieved when treatment of the mixing cloud mass flux was altered such that the flux depended on the undiluted air parcel buoyancy itself, rather than the buoyancy gradient (Peng *et al*. 2004). Improvements in simulated precipitation were also made when the updraft source level was changed, from the level of maximum moist static energy to the level that results in the greatest virtual temperature difference between the parcel and environmental air at the corresponding lifting condensation level, which maximizes the parcel buoyancy (Peng *et al.* 2004).

This thesis will not investigate such conditions on convective activity but notes that it could be explored in future work.

Chapter 3: Diurnal Cycle of the Planetary Boundary Layer

Chapter 2 identified that the primary error within the RegCM3 model system lies with the simulation of convective processes. Diagnosing the exact source(s) of this error is extremely difficult, because convective rainfall (all rainfall, in fact) is not a state variable but rather represents the net result of many different and interacting processes. These include: the onset of a convective updraft, condensation within a cloud, mixing and entrainment within the cloud, conversion of cloud droplets to raindrops, and evaporation of rainfall within the downdraft before reaching the surface. Therefore errors in the simulation of surface rainfall could be considered an integral of errors in all the processes necessary to produce that rainfall.

Convection motion is initiated primarily within the planetary boundary layer (PBL) region. The PBL is the part of the troposphere that is both affected by the characteristics of the surface and responds to surface forcings on time scales of an hour or less (Stull 1988). All diurnal variability in the lower atmosphere is derived from processes originating at the surface, which responds to the diurnal cycle of incoming solar radiation with a similar diurnal cycle of turbulent heat fluxes (latent and sensible), particularly over land. These fluxes are responsible for the turbulent eddies that mix the lower atmosphere, stimulating growth of the PBL and creating the instability that triggers moist convection. The onset of convection also feeds back to the surface through the creation of cumulus clouds, which shield the surface from incoming solar radiation, and the production of rainfall, which cools and moistens the surface. Moist convection therefore both responds to and influences conditions in the near surface environment.

The main characteristics of the PBL throughout the course of a day are illustrated in Figure 3-1. These characteristics are pronounced over land surfaces, compared to ocean surfaces, because of the strong diurnal variability in turbulent fluxes of latent and sensible heat that result from the limited heat capacity of the land.

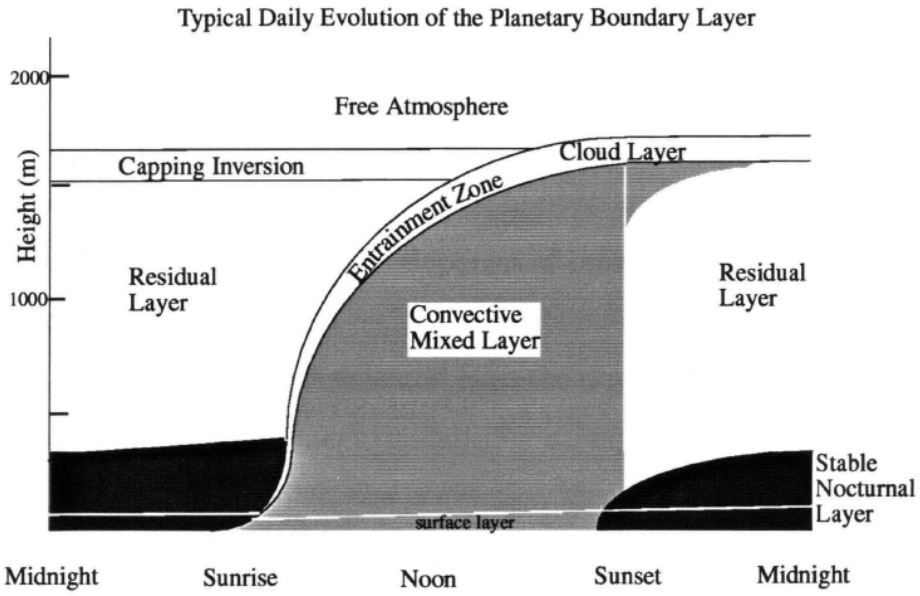

Figure 3-1. Typical daily boundary layer (BL) evolution in a high pressure region over land. The three major parts of the BL are a turbulent convective mixed layer, a less-turbulent residual layer containing former mixed layer air, and a nocturnal stable BL of sporadic turbulence. The mixed layer can be further subdivided into a cloud layer and a subcloud layer (Figure 1.1 from Findell 2001, based on Stull 1988).

3.1 Planetary Boundary Layer Height

Large-scale climate models (global, GCMs, and regional, RCMs) must parameterize turbulent transport within the PBL region. The role of parameterization schemes is to describe the evolution of thermodynamic properties due to the exchange of heat, water vapor and momentum at the earth's surface and entrainment of air from above the PBL. A key variable in these parameterization schemes is definition of the PBL height. However, to the best of this author's knowledge, the simulated PBL height within RegCM3 has not been evaluated against observational data. In general, simulations of PBL height are rarely evaluated within climate models (Seidel *et al.* 2012).

The PBL height is particularly important in relation to the lifted condensation level (LCL). The LCL represents the elevation at which a moist air parcel being lifted adiabatically reaches saturation, and thus the convective cloud base could be expected to form at about the height of the LCL. If the atmosphere was conditionally unstable, and the level of free convection (LFC) coincided with the LCL, then air that was lifted to the LCL could be expected to undergo moist convection, potentially producing rainfall. Since it can be assumed that any

air parcel lifted from near the surface could reach the top of the daytime mixed PBL, it is possible for a moist air parcel to be lifted to saturation and trigger convection if the PBL height is greater than the LCL. Therefore the simulated PBL height is critical for the triggering of convection, and some modeling studies have indeed shown a very sensitive response of precipitation to the depth of the mixed PBL (e.g. Cha *et al.* 2008).

It was noted in initial simulations using RegCM3 that the PBL height over land was very high given the generally humid environment of the Maritime Continent. Figure 3-2 shows the diurnal cycle of PBL height simulated by the default version of RegCM3-IBIS (as described in Chapter 2) using both the Grell with Fritsch-Chappell and Emanuel convection schemes, averaged over the period 1998-2001 for land cells within the domain. The LCL simulated by each scheme is also shown for comparison.

The PBL height is only shown here over land because the ocean surface shows limited diurnal variability in PBL depth, since the fixed SSTs drive nearly constant turbulent heat fluxes. Chapter 2 also indicated that model error with respect to convection was worse over land than over ocean, so behavior over land surfaces is of particular interest.

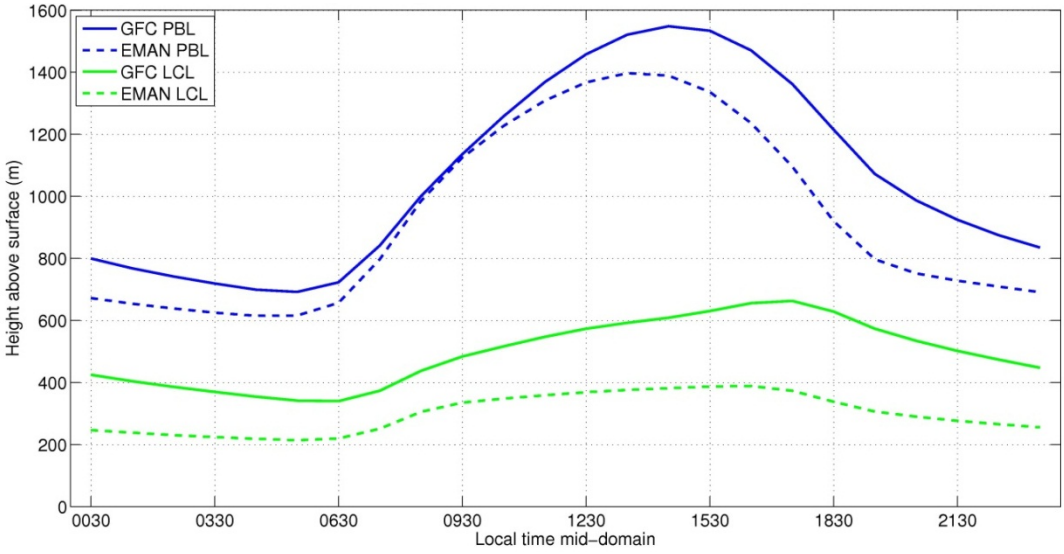

Figure 3-2. Average diurnal cycle of PBL height and elevation of LCL (both in m) over land cells for period 1998-2001 as simulated by RegCM3-IBIS using the Grell Fritsch-Chappell and Emanuel convection schemes.

Figure 3-2 shows that over land, with both convection schemes, the average PBL height is always greater than the average LCL. This suggests that the initiation of convection

in the model is not limited by the ability of a moist air parcel to reach a level of saturation. In particular, it is noted that the average night-time PBL is quite high – the average minimum is 600 m above the land surface.

Several measurements have been made of the nocturnal and early morning PBL height over sub-tropical and mid-latitude locations. Benkley and Schulman (1979) showed that the early morning PBL height was about 330 m over a smooth, flat Illinois site. Koracin and Berkowicz (1988) showed that the nocturnal PBL height was approximately 180 m over central Illinois, using data obtained through the Electric Power Research Institute (EPRI) Plume Model Validation and Development (PMVD) Project. Tombrou *et al.* (1998) presented rawinsonde data that showed a mean nocturnal PBL height of about 350 m over Helliniko airport near Athens, Greece. Contini *et al.* (2008) showed that the nocturnal PBL height was about 300 m based on data collected from a meteorological station in Lecce, Italy. These datasets suggest that the nocturnal PBL simulated by RegCM3 over land is too high.

3.1.1 Observations of PBL Height over Singapore

To sample the PBL height over the Maritime Continent region, a new dataset was acquired from Changi Airport, Singapore. Radiosonde data were obtained by Singapore's National Environment Agency at 8 am, 11 am, 2 pm and 8 pm local time (LT) over the period 1 October to 23 November 2010, pending airport traffic. In total, 35 soundings were taken at 8 am LT, 28 soundings at 11 am LT, 29 soundings at 2 pm LT and 34 soundings at 8 pm LT. Temperature, relative humidity, dew point temperature, wind direction and wind speed measurements were recorded at 2 second intervals from the surface to a maximum elevation of 25-30 km, during an ascent that took 60-90 minutes.

The radiosonde data were used to calculate vertical profiles of the potential temperature and water vapor mixing ratio. Since potential temperature is a conserved quantity for all dry adiabatic processes, and the PBL region is approximately adiabatic, potential temperature should remain approximately constant throughout the PBL. In addition, water vapor should be well-mixed over the depth of the PBL. Therefore the region over which potential temperature and mixing ratio are approximately constant can be taken as the estimated PBL depth.

Figure 3-3 and Figure 3-4 show, respectively, the vertical profiles of potential temperature and water vapor mixing ratio in the lowest 3 km of the atmosphere as recorded by the Changi airport radiosonde, separated for each of the four times of day when measurements were made. The PBL height can be qualitatively estimated from these figures using the region of approximately constant potential temperature and water vapor mixing ratio as the mixed PBL depth, as shown in Table 3-1.

Table 3-1. PBL height (in m) over Changi airport estimated qualitatively from radiosonde data using depth of constant potential temperature (theta) and water vapor mixing ratio.

PBL height (m)	8 am LT	11 am LT	2 pm LT	8 pm LT
Constant mixing ratio	300	600	700	300
Constant theta	0	900	900	200

(a)

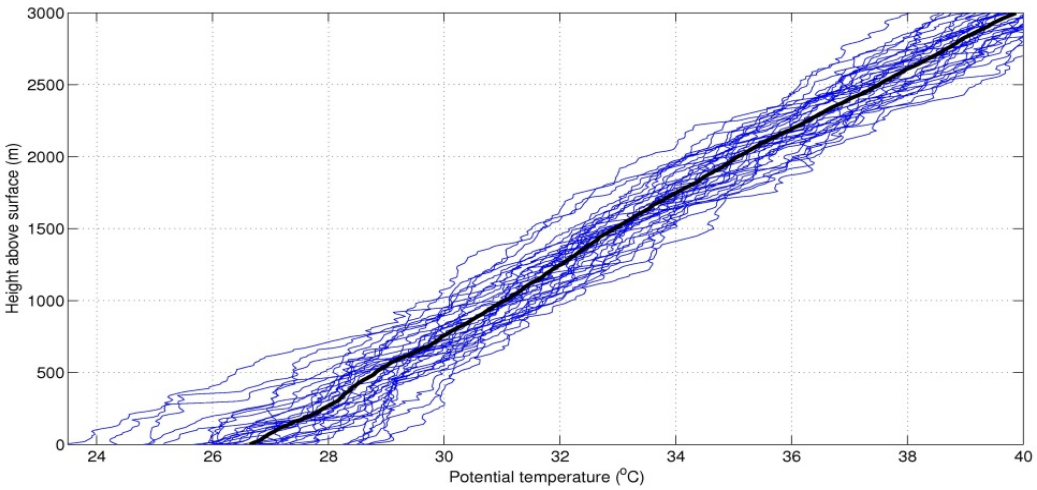

(b)

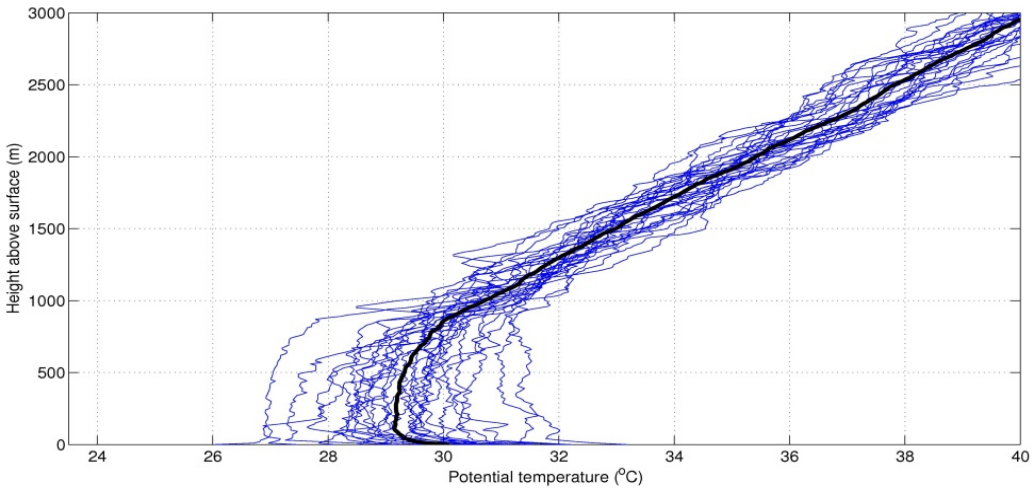

(c)

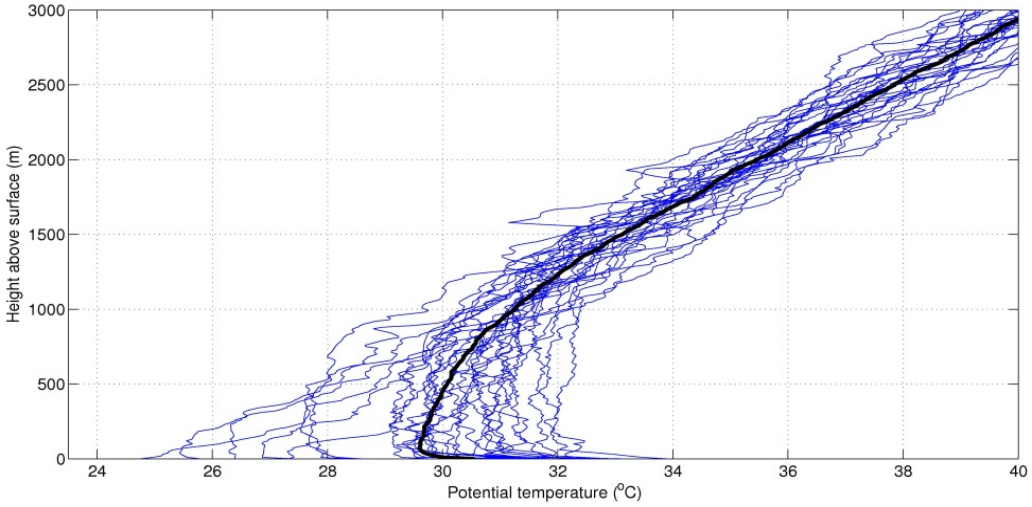

(d)

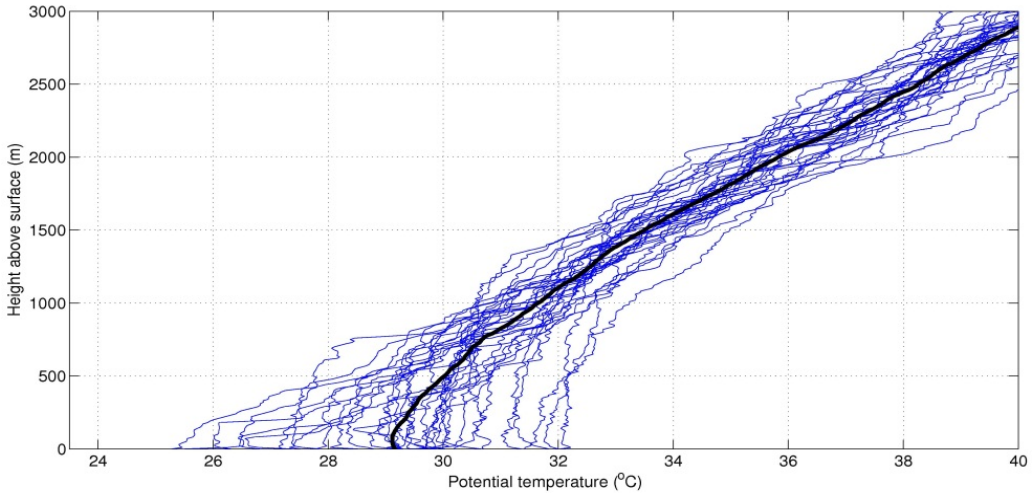

Figure 3-3. Profiles of potential temperature (in ^{o}C) for lowest 3 km of atmosphere from Changi airport radiosonde data, 1 October – 23 November 2010. (a) 8 am LT; (b) 11 am LT; (c) 2 pm LT; (d) 8 pm LT. Blue lines show individual soundings; black line shows mean profile.

(a)

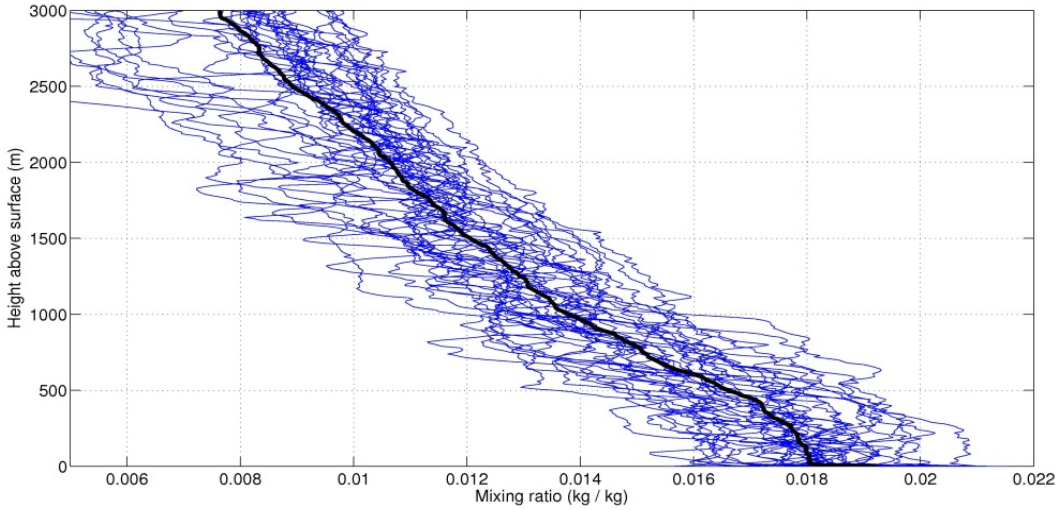
Height above surface (m)
Mixing ratio (kg / kg)
0
500
1000
1500
2000
2500
3000
0.006
0.008
0.01
0.012
0.014
0.016
0.018
0.02
0.022

(b)

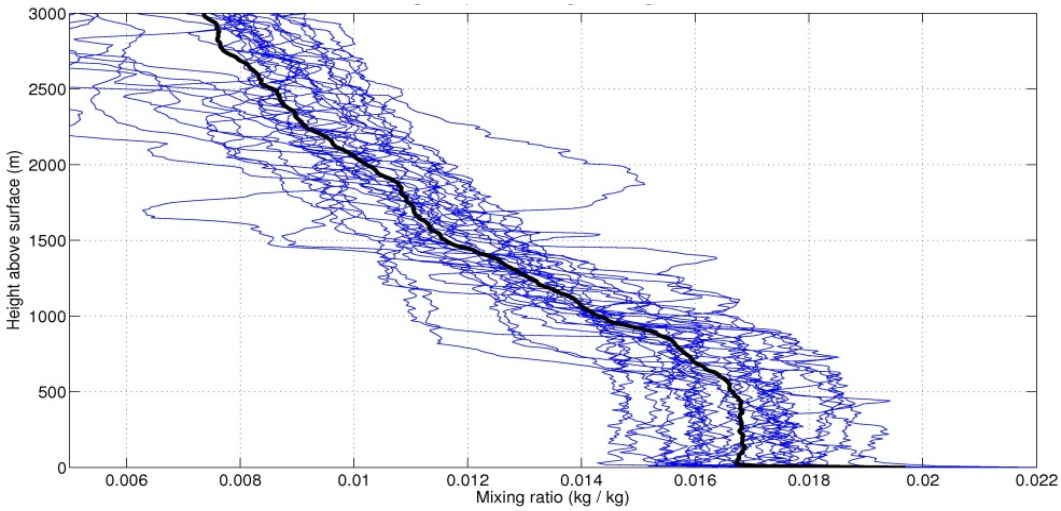
Height above surface (m)
Mixing ratio (kg / kg)
0
500
1000
1500
2000
2500
3000
0.006
0.008
0.01
0.012
0.014
0.016
0.018
0.02
0.022

(c)

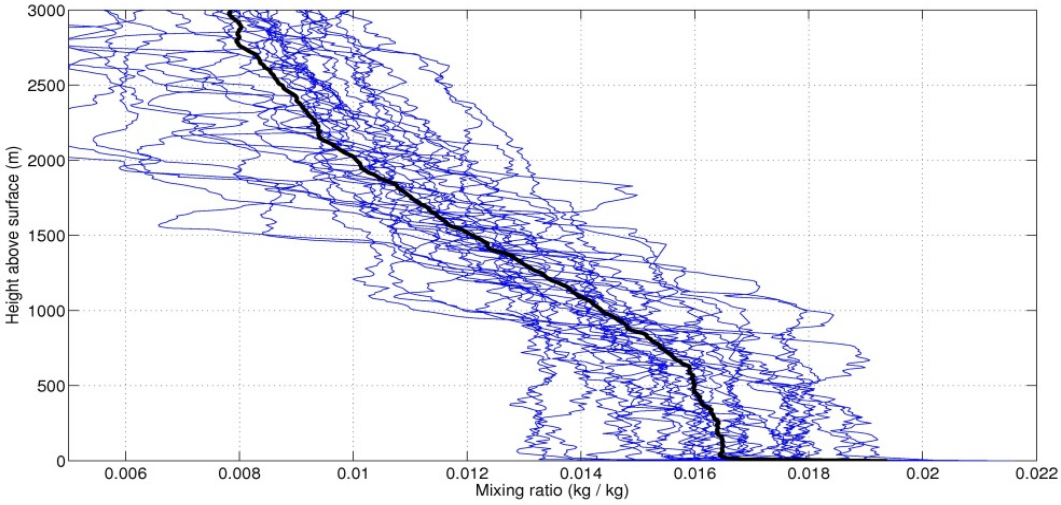
Height above surface (m)
Mixing ratio (kg / kg)
0
500
1000
1500
2000
2500
3000
0.006
0.008
0.01
0.012
0.014
0.016
0.018
0.02
0.022

(d)

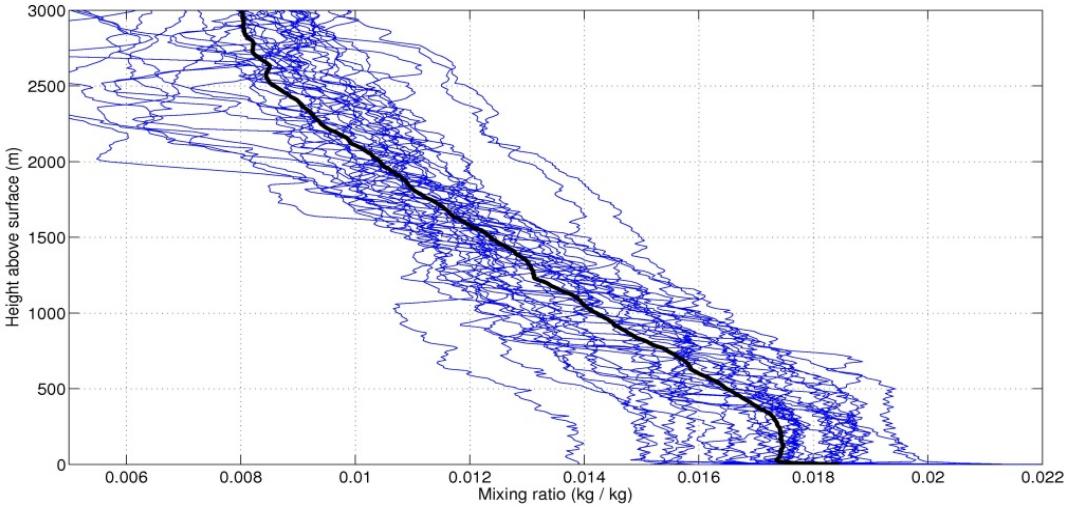

Figure 3-4. Profiles of water vapor mixing ratio (in kg/kg) for lowest 3 km of atmosphere from Changi airport radiosonde data, 1 October – 23 November 2010. (a) 8 am LT; (b) 11 am LT; (c) 2 pm LT; (d) 8 pm LT. Blue lines show individual soundings; black line shows mean profile.

To provide a more quantitative estimate, the PBL height was calculated as the elevation at which the gradient of potential temperature ($\Delta\theta$ / Δz) exceeded 0.005 K m^{-1}, in accordance with condition 1 of Heffter (1980). To remove noise in the radiosonde data due to the 2-second sampling interval, a moving-average window of 100 m depth was calculated before estimating the vertical gradient in potential temperature. Table 3-2 shows statistics of the calculated PBL height from all the profiles shown in the figures above. Note that, due to the averaging window used, the minimum height returned with this algorithm is 90 m.

Table 3-2. PBL height (m) over Singapore estimated from radiosonde data using condition 1 of Heffter (1980).

PBL height (m)	8 am LT	11 am LT	2 pm LT	8 pm LT
Mean	225	811	731	676
Maximum	810	1340	1540	1750
Minimum	90	90	90	90
Standard deviation	201	295	464	503

The actual PBL height over Singapore is likely to be somewhere between these qualitative and quantitative estimates. Hence the PBL height used for comparison to the model output was taken to be 250 m at 8 am, 800 m at 11 am, 750 m at 2 pm and 500 m at

8 pm. The estimated PBL height at 8 am is consistent with the early morning and nocturnal PBL data presented by Benkley and Schulman (1979), Koracin and Berkowicz (1988), Tombrou *et al.* (1998) and Contini *et al.* (2008). It is noted that the observations from Changi airport were collected over a limited time period, and there may be some variability in PBL height associated with seasonal or interannual conditions that is not captured by these measurements. However, these data are the only measurement of PBL height recorded over the Maritime Continent (to the best of this author's knowledge) and therefore they provide an invaluable metric against which to assess the simulated PBL height.

It must be remembered that a meteorological station represents a point-scale measurement, while a model grid cell represents the average condition over a much larger area (30 km in the simulations presented here). Hence comparison between the Singapore data and the model must be made carefully. Figure 3-5 compares the physical geography of the Malay Peninsula region, indicating the island of Singapore at the southern end of this Peninsula, and the model domain with 30 km resolution. The resolution of the model domain results in loss of some of the smaller islands, and the location of Singapore is approximated as the southern-most grid cell of the simulated Peninsula. Changi airport, where the soundings were taken, is located on the east coast of Singapore.

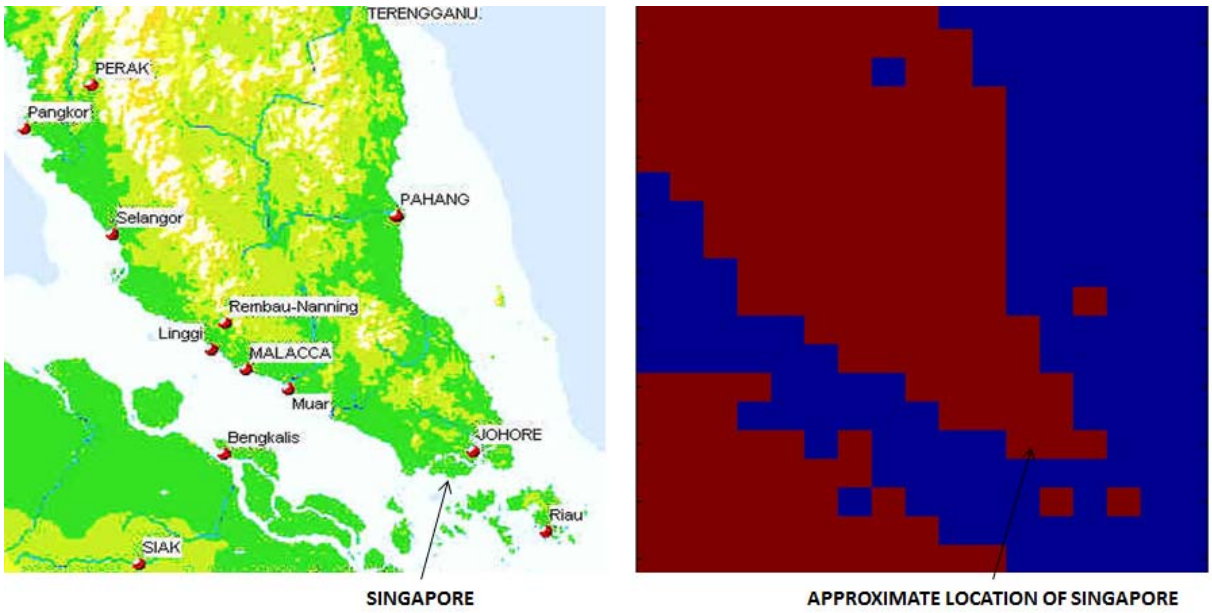

Figure 3-5. Comparison between (left) geography of Malay Peninsula and (right) model domain with 30 km grid cells.

When choosing which model grid cell(s) to compare to the Changi airport sounding data, the measured wind speed and direction can be used to determine the source of the conditions recorded by the sounding, and hence which grid cells have the most appropriate representation of those conditions. For example, if wind is recorded in a southerly or easterly direction at Changi airport, the sounding will measure conditions originating from the ocean, while winds recorded from the north or west will measure conditions more typical of the land.

To assess the impact of wind speed and direction on the PBL height, the wind profiles were analyzed from the same soundings used to calculate the PBL height. Table 3-3 shows the mean wind speed and direction for each time of day, averaged over different depths starting at the surface (i.e. the depths represent the lowest X m of the atmosphere). The estimated PBL height is shown for comparison. A wind direction of 0 degrees signifies wind coming from the north; direction is calculated clockwise from north.

Table 3-3. Mean wind speed (in m s^{-1}) and direction (in deg) measured by Changi Airport soundings.

	8 am LT		11 am LT		2 pm LT		8 pm LT	
PBL height	250 m		800 m		750 m		500 m	
Averaging Depth	Direction (deg)	Speed (m s^{-1})	Direction (deg)	Speed (m s^{-1})	Direction (deg)	Speed (m s^{-1})	Direction (deg)	Speed (m s^{-1})
1000 m	251	4.9	251	4.2	244	4.6	251	4.0
500 m	260	3.8	246	3.6	237	4.2	243	3.3
250 m	295	2.8	242	3.2	233	4.0	243	2.9
100 m	313	1.8	241	2.7	229	3.4	246	2.3

Table 3-3 shows that there is little diurnal variability in either wind direction or wind speed when averaged over the lowest 1000 m. The mean wind is from the southwest at about 4.5 m s^{-1}. As the averaging depth is made shallower and brought closer to the surface, the wind directions and speeds exhibit increasing diurnal variability. At lower elevations, the early morning winds are westerly but weaker, while the afternoon winds are more southerly and stronger. This pattern is consistent with a land-sea breeze circulation, which is known to be a strong feature in this region. Singapore's National Environment Agency notes that the climatology of the October-November period (when the soundings were taken) is

characterized by an inter-monsoon transition phase with winds that are typically light and variable, interacting with the sea breeze.

Therefore the wind data suggest that a land grid cell from the model is likely the most appropriate comparison to the observations at 8 am. But throughout the rest of the day, either an ocean grid cell or an average of land and ocean grid cells should provide the most appropriate comparison.

Figure 3-6 compares the estimated PBL height from the Changi airport soundings to simulated values from the default version of RegCM3-IBIS using both the Grell with Fritsch-Chappell and Emanuel convection schemes (model output is averaged over the period 1998-2001, taken from the simulations described in Chapter 2). The figure shows the PBL height simulated for a land grid cell, at the approximate location of Singapore at the southern end of the Malay Peninsula, and for the ocean grid cell immediately adjacent. The average value for the PBL height at each time of day is denoted by the star markers for the Changi data and by the dashed lines for the model output. The vertical bars indicate the observed and simulated variability of the PBL height at each time of day, and are calculated using the unbiased estimator for the standard deviation.

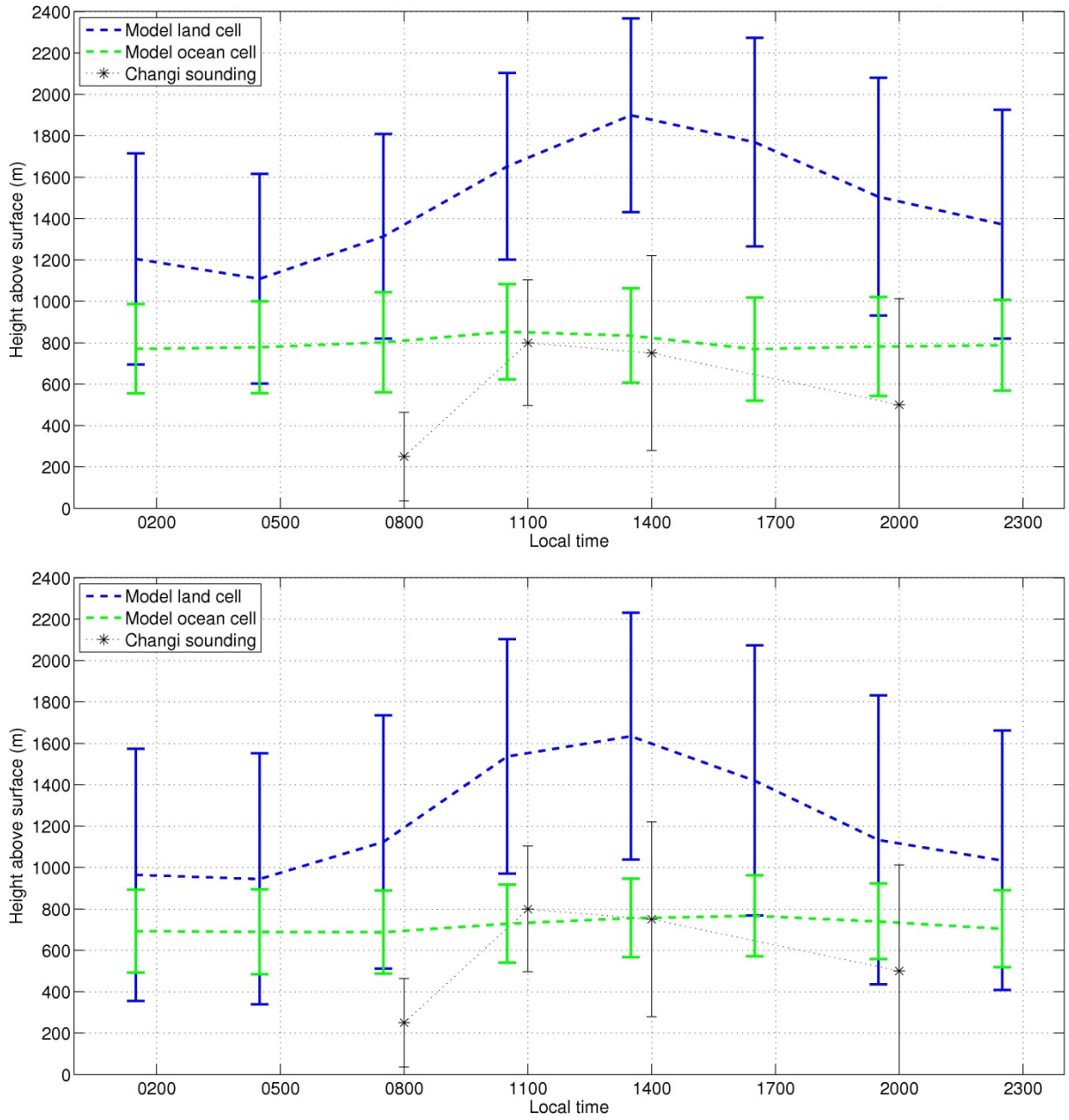

Figure 3-6. Diurnal PBL height (in m) over or near Singapore, simulated by the (top) Grell Fritsch-Chappell and (bottom) Emanuel convection schemes using either a land (blue) or ocean (green) grid cell to represent Singapore, compared to the PBL height estimated from the Changi soundings (black stars; dotted lines are shown to interpolate between the measurement times). The vertical bars signify one standard deviation of each sample set and illustrate the variability in the simulated and observed PBL height.

Figure 3-6 indicates that the simulated PBL height over the land grid cell nearest to Singapore is substantially higher than the height estimated from the Changi airport

soundings. It was suggested that the land grid cell should be the most appropriate comparison to observations in the early morning, when winds are light and westerly. However, the simulated early morning PBL height over land is about 800 m higher than observations, confirming that the simulated PBL in RegCM3 does not collapse appropriately at night. During the day, Figure 3-6 indicates that the simulated PBL over the nearby ocean is substantially lower than over land and is a much closer match to the observations.

To address the issue with the nocturnal PBL height, two modifications were made to the simulated PBL within RegCM3.

3.1.2 Modifications to Simulated Planetary Boundary Layer Height

RegCM3 uses the non-local diffusion scheme developed by Holtslag *et al.* (1990) and Holtslag and Boville (1993) (hereafter referred to as 'the Holtslag scheme') to parameterize the properties and dynamics of the PBL.

Calculation of Critical Richardson Number

The Holtslag scheme calculates the eddy diffusivity between model layers (i.e. turbulent fluxes) and non-local transport of temperature and water vapor across the PBL (i.e. large-scale eddies due to deep, dry convective plumes that can transport air parcels counter to the local gradient). These calculations require specification of the PBL height, *h*, which is solved iteratively from a bulk value of the critical Richardson number, Ri_c:

$$Ri_c = \frac{(g/\theta_{v0})(\theta_{vh}-\theta_{v0})h}{u_h^2+v_h^2} \quad (3\text{-}1)$$

where Ri_c = 0.25, *g* = gravitational acceleration, θ_v = virtual potential temperature, *u* = zonal wind component, *v* = meridional wind component and *h* = PBL height. The subscript *0* corresponds to the near surface value.

In the Holtslag scheme, the bulk Richardson number *Ri* is calculated over the level closest to the surface and subsequent higher levels. Once the bulk *Ri* exceeds the critical value, the value of PBL height *h* is derived with a linear interpolation between the layer with $Ri > Ri_c$ and the layer with $Ri < Ri_c$.

Calculation of the PBL height using the bulk Richardson number is usually found to be satisfactory in unstable conditions, but it can sometimes create very deep boundary layers, especially when surface wind speeds are high (Vogelezang and Holtslag 1996). If the simulated PBL is too deep, there will be too much mixing and transport from the PBL upwards into the conditionally unstable cloud layer, which has implications for the convection scheme (Vogelezang and Holtslag 1996). This result was shown by Cha *et al.* (2008) to significantly impact simulation of rainfall in the East Asian monsoon.

To achieve better simulation of the PBL height in neutral and stable conditions, Vogelezang and Holtslag (1996) revised the Holtslag scheme. In the revised scheme, the bulk critical Richardson number, Ri_c, is a function of the wind shear over the depth of the PBL and the surface friction velocity:

$$Ri_c = \frac{(g/\theta_{vs})(\theta_{vh}-\theta_{vs})(h-z_s)}{(u_h-u_s)^2+(v_h-v_s)^2+bu_*^2} \quad (3\text{-}2)$$

where Ri_c = 0.25, g = gravitational acceleration, θ_v = virtual temperature, u = zonal wind component, v = meridional wind component, h = PBL height, z = elevation of model layer, b = 100, u_* = surface frictional velocity, and the subscript s = model layer 20-80 m above the surface.

Vogelezang and Holtslag (1996) showed that the revised scheme was more generally applicable than the original scheme, being suitable for stable and neutral conditions as well as unstable conditions. Those authors found that the midday (unstable) PBL height was unaffected but the night-time (stable) PBL height was lower with the revised scheme. Therefore this revision to the Holtslag scheme was incorporated into RegCM3.

Depth of Night-time Boundary Layer

It was noted that the PBL height, within both the original Holtslag scheme and the revised version, is constrained by a minimum threshold as follows:

$$PBL_{min} = \frac{0.07u_*}{f} \quad (3\text{-}3)$$

where u_* = surface frictional velocity and f = Coriolis parameter. The value of f is constrained such that f_{min} = 2.546 x 10^{-5} sec^{-1}, which is the value at 10^o latitude. None of the Holtslag scheme authors cite a reference for this specific equation, but presumably it comes from the work of Koracin and Berkowicz (1988). This minimum threshold in RegCM3 is used as a way to estimate the height of the night-time PBL.

During the daytime, the mixed PBL develops as a result of both convective and mechanical mixing. The height of this PBL is shown schematically as the convective mixed layer in Figure 3-1. After the convective response to daytime solar radiation subsides, turbulence decays in the formerly well-mixed layer. The resulting layer of air is usually referred to as the residual layer (see Figure 3-1) because its initial mean state variables are the same as those in the recently-decayed mixed layer (Stull 1988). At night, the residual layer is disconnected from the surface by the stable layer that grows upward from the surface (see Figure 3-1) due to radiative cooling. The residual layer is therefore unaffected by turbulent transport of surface-related properties and is usually not considered to be part of the boundary layer (Stull 1988). The nocturnal stable layer is still turbulently mixed but has substantially different properties from the daytime mixed layer, since only mechanical mixing is active at night (Benkley and Schulman 1979) and the turbulence tends to be weaker and sporadic (Stull 1988). Typical magnitudes for the height of the nocturnal stable layer range from near zero to over 1000 m, but are usually within the range 100-500 m (Stull 1988).

Models such as RegCM3 that parameterize the mixed PBL do so in order to distinguish the free atmospheric flow from the near-surface boundary region. The Holtslag scheme, and others like it, do not explicitly resolve the details of the different parts of the boundary region that develop with a diurnal cycle – there is no defined residual layer, and there is no distinct representation of a stable layer that develops from the ground upwards beneath the residual layer. Instead, the model attempts to separate a layer that is mixed, in which the conditions are affected by turbulent transport, from a free atmosphere experiencing laminar flow, in which large-scale advection and diffusion are the modes of

transport. The critical Richardson number, as in equation (3-2), is often used to indicate the transition from turbulent to laminar flow.

As opposed to the daytime mixed PBL, which has a clearly defined top, the nocturnal stable layer has a poorly-defined top that blends into the residual layer (Stull 1988). Tombrou *et al.* (1998) noted that, "although a lot of studies have been devoted to [the height of the nocturnal PBL], there is still confusion in the definition of its upper boundary and thus the determination of its depth." The modeling challenge then is how to estimate the depth of a near-surface layer at night that experiences turbulent but not convective mixing.

Models have adopted a variety of approaches to estimate the nocturnal PBL. The first to be developed were diagnostic equations that assume an equilibrium stable layer depth. Although the nocturnal PBL is rarely actually in steady state, when synoptic variations are not too rapid and there is no strong momentum and heat exchange between the boundary layer and the rest of the troposphere, a quasi-equilibrium state can be considered to apply (Tombrou *et al.* 1998). Later research led to the development of rate-based equations, in which the nocturnal PBL tends to adjust towards an equilibrium state with a prescribed response time (Stull 1988). Over ten versions of rate equations are available in the literature. None of the diagnostic or rate-based expressions can be said to yield the best result (Stull 1988).

Diagnostic expressions are arguably the most commonly-used within models and several types have been proposed, including the version currently used within RegCM3. The nocturnal PBL depths estimated for mid-latitude regions that were noted previously (from the work of Tombrou *et al.* 1998, Contini *et al.* 2008 and others) were all the result of fitting observational data to a variety of diagnostic relationships. One of the most well-known pioneering expressions for the computation of the nocturnal PBL height was developed by Zilitinkevich (1972):

$$PBL_h = c\left(\frac{u_* L}{f}\right)^{1/2} \tag{3-4}$$

where PBL_h = nocturnal PBL height, c = parameter usually set to 0.4 to fit data, u_* = friction velocity, L = Obukhov length and f = Coriolis parameter.

This expression assumes that the fluid within the nocturnal PBL exists as an Ekman layer – a steady but turbulent boundary layer located within a stratified rotating fluid. The height of this layer is proportional to the rotational height scale for neutral conditions (where the steady turbulence regime is governed by the friction velocity and the Coriolis parameter) (Tombrou *et al.* 1998). With the Zilitinkevich (1972) expression, the effects of rotation remain crucial for the stable boundary layer depth even in the limiting case of very strong stability (Tombrou *et al.* 1998).

The expression used in RegCM3 to estimate the nocturnal PBL height was recommended by Koracin and Berkowicz (1988) based on fitting parameters to their Illinois dataset. The form of this equation was first proposed by Yu (1978) and assumes that the nocturnal PBL height is proportional to the neutral Ekman layer but not directly dependent on stability, in contradiction to the expression of Zilitinkevich (1972). It is also based on the vertical profile of the mean velocity and its physical basis is that the only parameters governing the steady turbulence regime in a perfectly neutral boundary layer are the friction velocity, u_*, and the Coriolis parameter, f, so that u_*/f is the only length scale that can be composed out of the two. Therefore the Ekman layer depth and the depth of the turbulence should be quite close. This equation is believed to be valid for neutral and stable conditions (Koracin and Berkowicz 1988).

Over mid-latitudes, the Ekman layer may be a reasonable estimate of the separation between the free-atmospheric laminar flow and the near-surface turbulent flow. However, the Ekman layer is the region of a fluid where the flow is the result of a balance between an applied pressure gradient, Coriolis forces and turbulent drag. Therefore it is unlikely to be a good approximation for the nocturnal stable layer over the tropics, given that the effect of Coriolis forces becomes negligible and the fluid does not experience geostrophic flow. In fact, it was noted by Vogelezang and Holtslag (1996) that the minimum constraint applied to the PBL height within their scheme is only applicable outside the tropics, even though it is applied over all potential model domains within RegCM3. Over the tropical belt 10^oS to

10^{o}N, i.e. the model domain used in this work, the minimum PBL constraint results in $PBL_{min} \geq 2749u_{*}$. Hence if the friction velocity is of magnitude 0.1-1 m s^{-1} (which tests showed it frequently is over this domain), the PBL cannot collapse below a height of about 500 m, as shown in Figure 3-2. Therefore the estimated nocturnal PBL height currently used within RegCM3 is considered inappropriate for use over the tropical region being studied in this work.

Unfortunately, an appropriate expression is not readily available for estimating the stable nocturnal PBL depth near the equator within a parameterized PBL scheme. All of the diagnostic relationships for the nocturnal PBL height that this author found were dependent upon geostrophic flow in a rotating fluid. In the absence of a definitive expression for the nocturnal PBL height over the tropics, the simplest reasonable expression was sought for implementation into RegCM3.

Stull (1988) provides examples of different methods used for estimating the depth of the nocturnal PBL. It could be defined as being the lowest height where (Stull 1988):

- the wind becomes maximum, signifying the level of the nocturnal jet;
- the lapse rate is isothermal ($\Delta T / \Delta z = 0$), indicating the inversion top;
- the lapse rate is adiabatic ($\Delta \theta / \Delta z = 0$), indicating the top of the stable layer, consistent with condition 1 of Heffter (1980);
- the turbulent kinetic energy becomes zero or a small portion of its surface value, signifying the top of the turbulent layer;
- the shear stress becomes zero or a small fraction of its surface value, signifying the top of the stress layer;
- the wind becomes geostrophic, indicating the bottom of the free atmosphere;
- sodar returns disappear, indicating the top of the layer with temperature fluctuations.

Analysis of the Changi airport sounding data (presented in Table 3-2) showed that the gradient of potential temperature ($\Delta \theta / \Delta z$) often exceeded 0.005 K m^{-1} at very low elevations in the early morning, resulting in an estimated PBL height of less than 100 m. This indicates that the lapse rate over Singapore frequently becomes adiabatic very close to the

surface at night. Hence if the adiabatic lapse rate method listed above by Stull (1988) was used over Singapore, it would suggest a very shallow nocturnal PBL.

Therefore the minimum threshold on the PBL height was changed to z_s, the elevation of the lowest model layer. In RegCM3, this layer takes a height of around 40 m. Note that this threshold does not require the night-time PBL height be as low as 40 m; it simply removes the previous constraint that was a function of the Coriolis parameter, allowing the PBL to collapse at night. Sensitivity tests showed that the exact magnitude of the minimum PBL height used within RegCM3 did not significantly impact the results as long as the value was on the order of 200 m or less, so it does not appear that 40 m is a limiting constraint.

Admittedly, this method is not a physically-based expression for estimating the nocturnal PBL depth over the tropics. But it is considered reasonable to use the lowest model layer elevation for constraining the minimum PBL height in this work, given the temperature sounding data described above. However, it is likely that the nocturnal stable layer over the Maritime Continent will be shallower than other tropical regions due to the presence of significant cloud cover and a substantial vegetated canopy, both of which limit night-time radiative cooling. Therefore the lowest model layer may not be an appropriate constraint on the nocturnal stable PBL height over other tropical regions. Future work in this field may elucidate a more definitive scaling relationship (i.e. a diagnostic expression) for the tropics or another method of calculation that is more appropriate, for example derived from the rate of radiative cooling or one of the methods noted by Stull (1988).

3.2 Boundary Layer Clouds

Cumulus and stratocumulus clouds can form near the top of the mixed PBL, as shown schematically in Figure 3-1. These boundary layer clouds are most commonly observed over subtropical marine regions, particularly off the western coasts of the American continents, and are known to play a crucial role in climate sensitivity (Bachiochi and Krishnamurti 2000, McCaa and Bretherton 2004, Bony and Dufresne 2005). This has been the motivation for several field campaigns – including the First International Satellite Cloud Climatology Project (ISCCP) Regional Experiment (FIRE; Albrecht *et al*. 1988), the Atlantic Stratocumulus Transition Experiment (ASTEX; Albrecht *et al*. 1995), the East Pacific Investigation of Climate

(EPIC) model (Bretherton *et al*. 2004), the Second Dynamics and Chemistry of Marine Stratocumulus field study (DYCOMS-II; Stevens *et al*. 2003), and Rain in Shallow Cumulus over the Ocean (RICO; Rauber *et al*. 2007) – as well as extensive modeling activity (e.g. Krueger *et al*. 1995, Bretherton *et al*. 1999, Svensson *et al*. 2000, McCaa and Bretherton 2004) (as summarized in Karlsson *et al.* 2010).

In the Fourth IPCC Assessment Report (Christensen *et al*. 2007), cloud feedbacks were identified as a primary reason for differences between models, with the shortwave impact of boundary-layer and mid-level clouds making the largest contribution. But their simulation has remained problematic for large-scale climate models (e.g. Bachiochi and Krishnamurti 2000, Bony and Dufresne 2005). Most commonly, coupled GCMs underestimate the presence of low-level marine stratus cloud cover (e.g. Frey *et al*. 1997).

A key feature of these boundary layer clouds is their location near the top of the mixed PBL, hence the commonly-used terms 'cloud-topped boundary layer' and 'stratocumulus-capped boundary layer'. Within the mixed PBL region, turbulent eddies are very effective at removing gradients of any active or passive quantity within that turbulent flow (Benkley and Schulman 1979), such that conserved variables such as potential temperature and humidity are nearly constant with height within the mixed PBL (Stull 1988). It is therefore expected that condensate (cloud liquid water) would be similarly well-mixed within this region. Hence if condensate were to form within a model layer inside the mixed PBL, for example in the case of early morning fog, it would be expected to mix over the PBL depth, such that cloudiness would be relatively uniform over the well-mixed region.

Variable cloud cover within the mixed PBL region was noted in initial simulations using RegCM3. Figure 3-7 and 3-8 show the diurnal cycle of cloud cover simulated by the default version of RegCM3-IBIS (as described in Chapter 2) using both the Grell and Emanuel convection schemes, averaged over the period 1998-2001 separately for land and ocean cells.

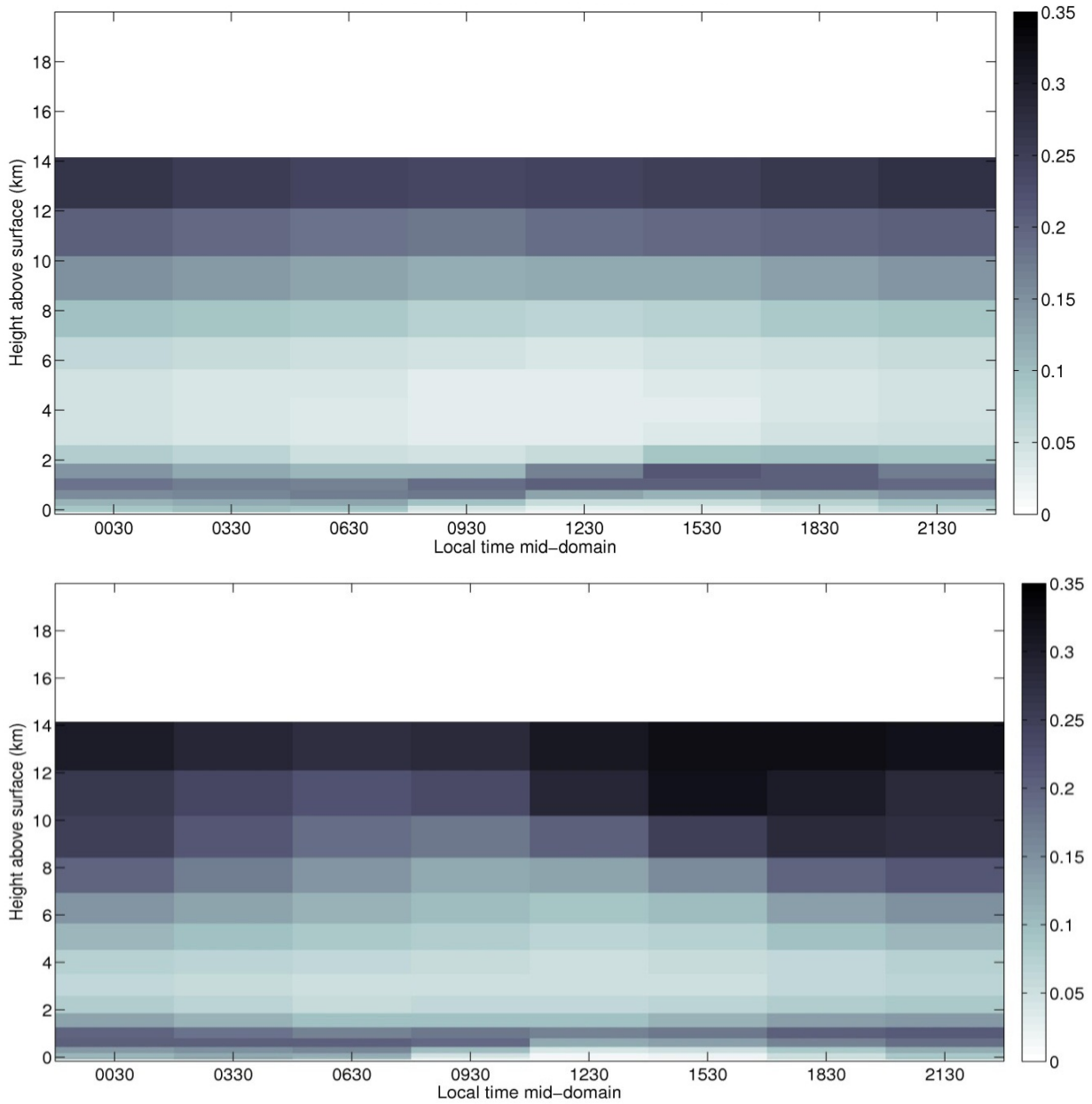

Figure 3-7. Diurnal cycle of cloud cover averaged over land grid cells within the model domain for the period 1998-2001, using the default RegCM3-IBIS with the Grell (top) and Emanuel (bottom) convection schemes. Color bar indicates fractional coverage of grid cell. The x-axis labels indicate the time of the middle of each 3-hour output window, with respect to local time in the center of the model domain. To represent the y-axis on a linear scale, the vertical extent of each model layer was assigned a single value of cloud cover, as provided by the model output. In reality, a smoother profile with less abrupt vertical variability would be expected.

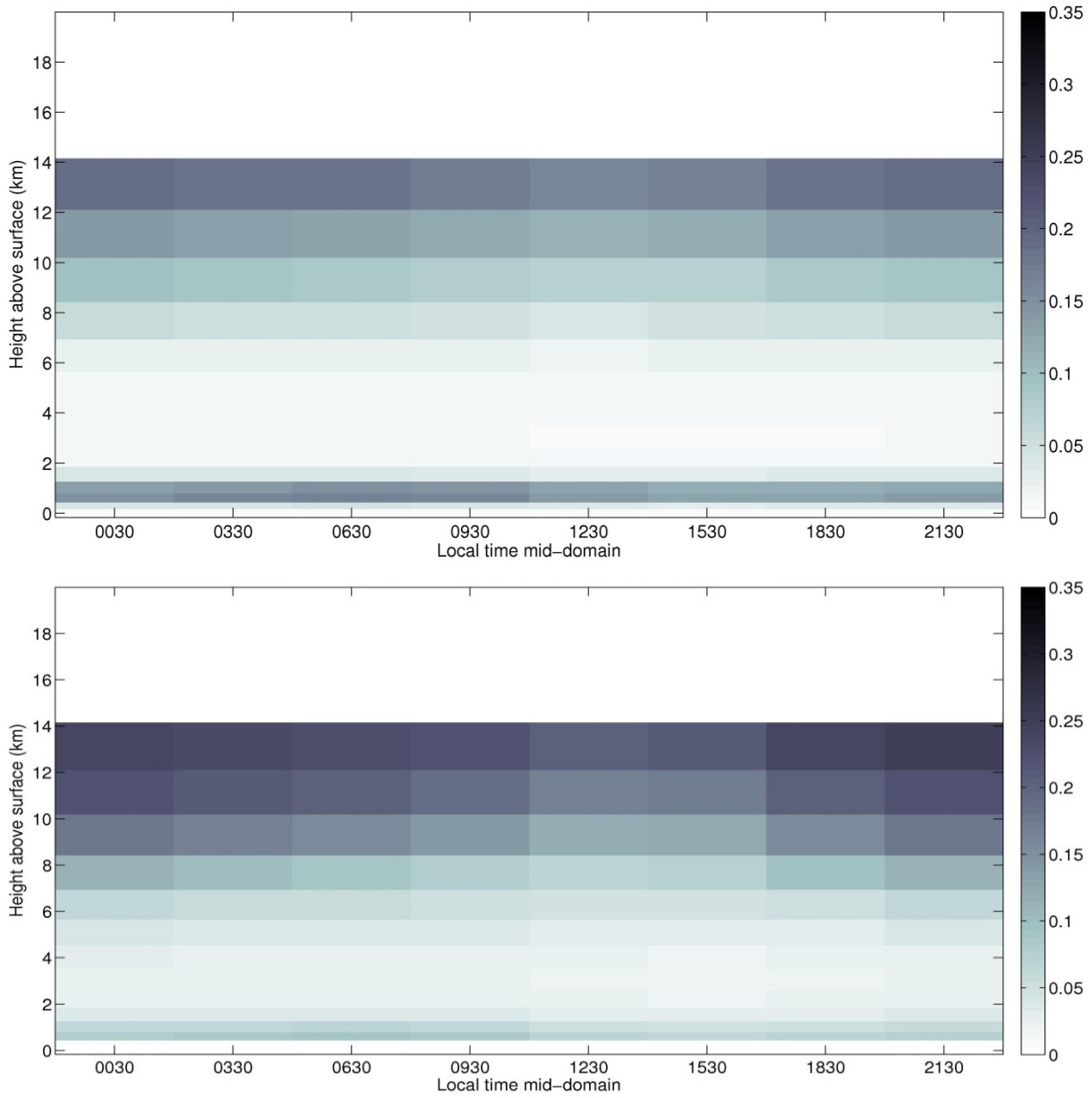

Figure 3-8. As for Figure 3-7 but for ocean grid cells.

Over ocean grid cells, the model simulates a thin layer of clouds at approximately 500 m elevation, similar to the marine boundary layer clouds commonly observed and consistent with the cloud base shown for the Pacific Ocean by Wang *et al*. (2011). But considerable cloud cover is simulated over land grid cells at very low elevations, in many instances all the way down to the surface. This very low cloud is particularly concerning since it was shown in Figure 3-2 that the average simulated LCL reaches a minimum of about

400 m over land, indicating that the simulated atmosphere should be cloud-free at least below this elevation. To the best of this author's knowledge, assessment of this low-level cloud cover simulated over land by RegCM3 has not been published in the literature.

However, a tunable parameter exists within RegCM3 that prevents low-level clouds from being radiatively-active, such that they produce rainfall but do not absorb or reflect radiation. The existence of this model parameter suggests that low-level cloud cover has previously identified as a problem within the model but was not adequately addressed.

One published work was found that alludes to use of this parameter. Sun *et al*. (1999) used RegCM2 to simulate rainfall-generation processes over eastern Africa. Part of that work included specifying the cloud base level with respect to the radiation transfer scheme. No further details were given in that work, but this author considers it likely that specifying the cloud base involved tuning the parameter governing the elevation of radiatively-active clouds. Sun *et al.* (1999) found that model performance was improved with respect to wind shear and rainfall when the lowest three model layers were designated cloud-free, instead of just the lowest model layer (the parameter default setting). This work, although somewhat vague, suggests that the simulation of clouds within the PBL can have a significant impact and that RegCM3 may simulate erroneous low cloud cover.

There are indications that other models may exhibit similar issues with cloud cover within the PBL.

Bachiochi and Krishnamurti (2000) placed constraints on the formation of stratus clouds within the PBL in the Florida State University coupled ocean-atmosphere model. In their case, the goal was to increase the fractional cloud cover over subtropical ocean regions by making the cloud cover a function of the simulated PBL height and ground wetness (Bachiochi and Krishnamurti 2000). Additionally, the cloud fraction was set to zero if the relative humidity at either the level defining the PBL top or the model level just below the PBL top was less than 80% (Bachiochi and Krishnamurti 2000). The new cloud fraction was found to greatly improve the cloud amount over the eastern ocean basin, with subsequent improvement in the representation of surface solar radiation fluxes, low-level winds and thermal structure (Bachiochi and Krishnamurti 2000).

In the work of Smith (1990), which is the basis for cloud simulation in the Hadley Centre's Global Environment Model (HadGEM1; Martin *et al.* 2006), the PBL was permitted to exist within the lowest 3 vertical model layers (out of a total of 11 layers; i.e. it could go no higher than the third layer). A threshold relative humidity value was imposed on the simulation of resolvable (non-convective) cloud, which varied over the PBL: a threshold value of 0.925 was required in the lowest 2 model layers while a value of 0.85 was required in all other model layers. This variable threshold restricts the formation of cloud within the PBL except in the layer directly beneath the PBL top, where capping stratocumulus cloud is observed to exist. The use of a higher threshold within the PBL is suggestive of an attempt to reduce very low cloud cover.

In NCAR's Community Atmosphere Model Version 4.0 (CAM4.0; Neale *et al.* 2010), the simulation of stratus clouds over marine areas was altered relative to previous versions of the model to improve the simulation of subtropical marine stratocumulus cloud. In CAM4.0, stratus cloud over oceans is assumed to be located in the model layer directly beneath the strongest stability jump between 750 mb and the surface (Neale *et al.* 2010), where stability is defined by the gradient in potential temperature. This location represents the model layer below the inversion that signifies the top of the PBL. If no two layers present a potential temperature difference greater than 0.125 K mb^{-1}, no cloud is diagnosed (Neale *et al.* 2010). This limitation would effectively restrict the formation of cloud over ocean grid cells within well-mixed boundary layers.

A more physically-based method was sought to address the issue of excessive cloud cover simulated within the PBL by RegCM3.

3.2.1 New Simulation of Non-convective Clouds Within the PBL

In RegCM3, cloud fraction within a grid cell can be created by both convective and large-scale (i.e. resolvable, non-convective) processes. Each type of cloud fraction is calculated independently of the other and then the larger of the two values is taken as the grid-cell cloud fraction and used for calculations of radiative transfer. Almost all of the low-level cloud cover shown in Figure 3-7 is large-scale.

Large-scale cloud fraction, $FC_{L\text{-}S}$, is calculated by the SUBEX routine (Pal *et al*. 2000) as a function of the average grid cell relative humidity, based on the work of Sundqvist (1988):

$$FC_{L-S} = 1 - \sqrt{1 - \frac{\mathrm{RH} - \mathrm{RH}_{\min}}{\mathrm{RH}_{\max} - \mathrm{RH}_{\min}}} \tag{3-5}$$

where RH_{min} = threshold RH (relative humidity) required for cloud formation and RH_{max} = maximum value that RH can take. In RegCM3, the default values are RH_{max} = 1.01, RH_{min} = 0.8 over land and RH_{min} = 0.9 over ocean. This formula is applied to each grid volume (uniformly in the vertical dimension of a grid cell), such that each model layer has a separate calculation of $FC_{L\text{-}S}$.

To address the overestimation of low-level large-scale clouds within the mixed PBL layer in RegCM3, a constraint was placed on the SUBEX routine such that clouds were not permitted to form within the PBL unless the bulk saturation, calculated over the depth of the PBL, exceeded a specified threshold, as follows:

$$RH_{bulk} = \frac{q_{bulk}}{q_{s,bulk}} \tag{3-6}$$

where RH_{bulk} = bulk measure of relative humidity;

$$q_{bulk} = \sum_{z_s}^{z_{PBL}} q(z) \tag{3-7}$$

where q_{bulk} = bulk measure of water vapor mixing ratio over the PBL depth, $q(z)$ = grid-mean water vapor mixing ratio at elevation z, z_{PBL} = PBL height as calculated by the modified Holtslag PBL scheme described above, z_s = elevation of lowest model layer;

$$q_{s,bulk} = \sum_{z_s}^{z_{PBL}} q_s\,(z) \tag{3-8}$$

where $q_{s,bulk}$ = bulk measure of saturation mixing ratio over the PBL depth, $q_s(z)$ = grid-mean saturation mixing ratio at elevation z; and

$$FC_{L-S}(z) = 0 \; if \; RH_{bulk} < \; RH_T \qquad for \; z_s < z < \; z_{PBL} \qquad (3\text{-}9)$$

where $FC_{L\text{-}S}(z)$ = large-scale fractional cloud cover at elevation z and RH_T = threshold bulk relative humidity. The threshold bulk relative humidity, RH_T, was assigned a value of 0.9, which is consistent with the value of RH_{min} used for general calculation of the large-scale fractional cloud cover.

Note that this condition was placed only on the formation of large-scale cloud cover, and not convective, since most of the low cloud cover was simulated at night-time when convection is not active.

3.3 Modifications to Surface Fluxes

Three other minor model modifications were made to improve the representation of surface fluxes within the RegCM3-IBIS system. These modifications were made to the Zeng ocean surface flux scheme, the simulation of soil heat flux within IBIS and the depth of rainfall intercepted by the canopy in IBIS.

3.3.1 Modified Ocean Surface Roughness Length

There are two options available with RegCM3 for parameterizing the turbulent fluxes of latent and sensible heat over ocean surfaces: an algorithm used with BATS and the bulk aerodynamic scheme of Zeng *et al.* (1998, hereafter termed 'the Zeng scheme'). The BATS algorithm uses standard Monin-Obukhov similarity relations to compute the fluxes with no special treatment of convective and very stable conditions, with a constant roughness length. This algorithm is substantially inferior to the Zeng scheme, which describes all stability conditions and includes a gustiness velocity to account for the additional flux induced by boundary layer-scale variability. Therefore the Zeng scheme has been used in all simulations presented in this thesis.

The Zeng scheme was validated against data from the TOGA-COARE study (Zeng *et al.* 1998) and is similar to the bulk algorithm (COARE Version 2.5) derived by Fairall *et al.* (1996) using data from the TOGA-COARE experiment under weak to moderate wind conditions (i.e. less than 12 m s^{-1}). In both the Zeng scheme and COARE algorithm, the ocean surface roughness length z_o is calculated by:

$$z_o = z_{ch}\frac{u_*^2}{g} + 0.11\frac{\nu}{u_*} \tag{3-10}$$

In the Zeng scheme, the parameter z_{ch} is a constant value: z_{ch} = 0.013. However, Fairall *et al.* (2003) presented updates to the COARE algorithm (COARE Version 3.0), in which z_{ch} varies to account for higher wind speeds:

$$z_{ch} = \begin{cases} 0.011 & for\ U \leq 10\ m\ s^{-1} \\ 0.011 + \frac{0.007(U-10)}{8} & for\ 10 < U \leq 18\ m\ s^{-1} \\ 0.018 & for\ U > 18\ m\ s^{-1} \end{cases} \tag{3-11}$$

where U = wind speed at 10 m above the surface.

This version of the z_{ch} calculation is more generally applicable than the constant value used within the Zeng scheme, and therefore it was implemented into the Zeng flux scheme in RegCM3.

3.3.2 Modified Soil Thermal Conductivity

The IBIS land surface scheme (Foley *et al.* 1996) is based on the LSX model (Thompson and Pollard 1995), which in turn was built upon the BATS model of Dickinson *et al.* (1986). In this scheme, heat is diffused linearly between the soil layers in which the soil thermal conductivity and heat capacity are derived from de Vries (1963).

The calculation for soil thermal conductivity ignores the component of total soil heat flux that results from empty pore space (i.e. air) within the soil matrix, as though the soil were always fully saturated. Soils within the Maritime Continent region are likely to be at

least partly saturated for a large proportion of time, given the high volume of rainfall experienced in this region. But the impact of the empty pore space on the calculation of thermal conductivity may prove important when using this model in other contexts, and thus the calculation was modified accordingly.

The existing calculation for thermal conductivity, *C*, within IBIS is:

$$C = C_{dry} 0.56^{\rho_w} 2.24^{\rho_i} \tag{3-12}$$

where C_{dry} = dry soil conductivity (W m^{-1} K^{-1}), ρ_w = volumetric water content (kg kg^{-1}), ρ_i = volumetric ice content (kg kg^{-1}), 0.56 = (conductivity of water/conductivity of air) and 2.24 = (conductivity of ice/conductivity of air), where:

$$C_{dry} = 0.3 f_{sand} + 0.265 f_{silt} + 0.25 f_{clay} \tag{3-13}$$

where f_{sand}, f_{silt} and f_{clay} are the fraction of sand, silt and clay, respectively, in the soil at a given grid point and the coefficients represent the thermal conductivity of those soil constituents.

The calculation of thermal conductivity was modified within IBIS such that:

$$C = C_{dry}^{1-\varphi} 0.01^{\varphi} 0.56^{\rho_w} 2.24^{\rho_i} \tag{3-14}$$

where φ = porosity of soil and 0.01 = approximate thermal conductivity of air (W m^{-1} K^{-1}). This modification is consistent with the representations of thermal conductivity in unsaturated soils described by Farouki (1981) and Verseghy (1991).

3.3.3 Modified Canopy Interception

The final minor modification to the model was to alter the canopy scheme within IBIS to reduce the amount of intercepted canopy storage, i.e. the depth of rainfall that can accumulate on canopy leaves and stems before dripping through to the ground floor. This

change was made because it was noticed that the partitioning of total evapotranspiration into transpiration and interception loss as simulated by the model was biased too heavily towards interception loss when compared to observations, as described in Section 2.3. Hence the amount of intercepted rainfall was reduced by decreasing the canopy storage by 30%.

3.4 Impact of Changes to Simulation of the Near Surface Environment

All of the changes described above were implemented into the RegCM3-IBIS model system. The performance of the modified model was assessed using the Grell Fristch-Chappell and Emanuel convection schemes over the simulation period 1998-2001. Only the IBIS land surface scheme was used, since it shows better simulation of the surface fluxes (see Section 2.3) than BATS1e, and its two-layer canopy is a more reasonable representation of the tropical forest within the Maritime Continent region than the one-layer canopy of BATS1e. Only the ERA40 reanalysis was used for lateral boundary conditions, since it produces much better simulations than the NNRP2 (see Section 2.3). Simulations were begun at 1 July 1997 and ended 31 December 2001. The first 6 months of output were ignored to allow for spin-up. The domain, land cover classifications, lateral and initial boundary conditions and SSTs were all the same as described in Chapter 2.

Several datasets were used for comparison to the model.

To evaluate the new simulation of low cloud cover, the model results were compared to the International Satellite Cloud Climatology Project (ISCCP) Stage D2 product, made available by NASA. This product provides the fractional cloud cover at three different elevations: high (50-440 mb), middle (440-680 mb) and low (680-1000 mb), at 280 km resolution and monthly timescales. Data was averaged over the period 1998-2001 to compare to the model. The model output was aggregated to the same horizontal grid as the ISCCP data for a direct comparison. To match up the vertical resolution, the model output was aggregated in the vertical assuming random overlap of clouds between layers. Model layers 2-8 (roughly 760-1000 mb) were used for the low clouds to evaluate the change made to simulation of clouds within the PBL.

Solar radiation is compared to the NASA/GEWEX (Global Energy and Water Cycle Experiment)'s Surface Radiation Budget (SRB) dataset Release 3.0, made available by the NASA Langley Research Center Atmospheric Sciences Data Center. This data set is available at 3-hourly intervals on a 1^{o} x 1^{o} global grid. The data was interpolated to the model domain for direct comparison to simulation output.

Observations of latent heat flux over land are taken from direct observations of evapotranspiration (ET) in the Maritime Continent region, as described in Table 2-4. Over ocean, latent and sensible heat flux observations are from the Woods Hole Oceanographic Institute (WHOI) Global Dataset of Ocean Evaporation. The WHOI observations of latent and sensible heat flux compare well with data collected during the TOGA COARE experiment (Webster *et al.* 1996, Weller and Anderson 1996, Lau and Sui 1997, Sui *et al.* 1997, Emanuel and Živković-Rothman 1999).

Rainfall observations are taken from the TRMM 3B42 product, as described in Chapter 2. Convective and stratiform rainfall fractions are taken from Mori *et al.* (2004), as described in Chapter 2.

3.4.1 Planetary Boundary Layer Height

Figure 3-9 and Figure 3-10 show the average diurnal cycle of the new PBL height compared to the original PBL height and the LCL. Only the default value of the LCL is shown since there was negligible change in the simulated LCL with the PBL height modifications.

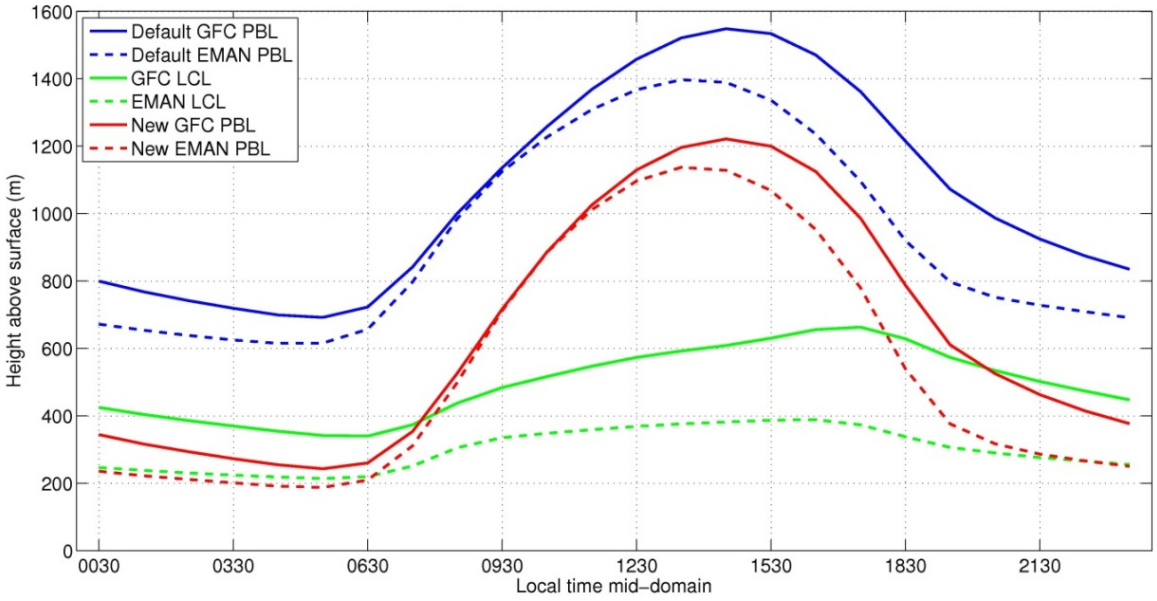

Figure 3-9. Average diurnal cycle of original PBL height (blue), new PBL height (red) and elevation of LCL (green) (all in m above surface) over land cells within the model domain for the period 1998-2001, using RegCM3-IBIS with both the Grell with Fritsch-Chappell closure (GFC, solid line) and Emanuel (EMAN, dashed line) convection schemes.

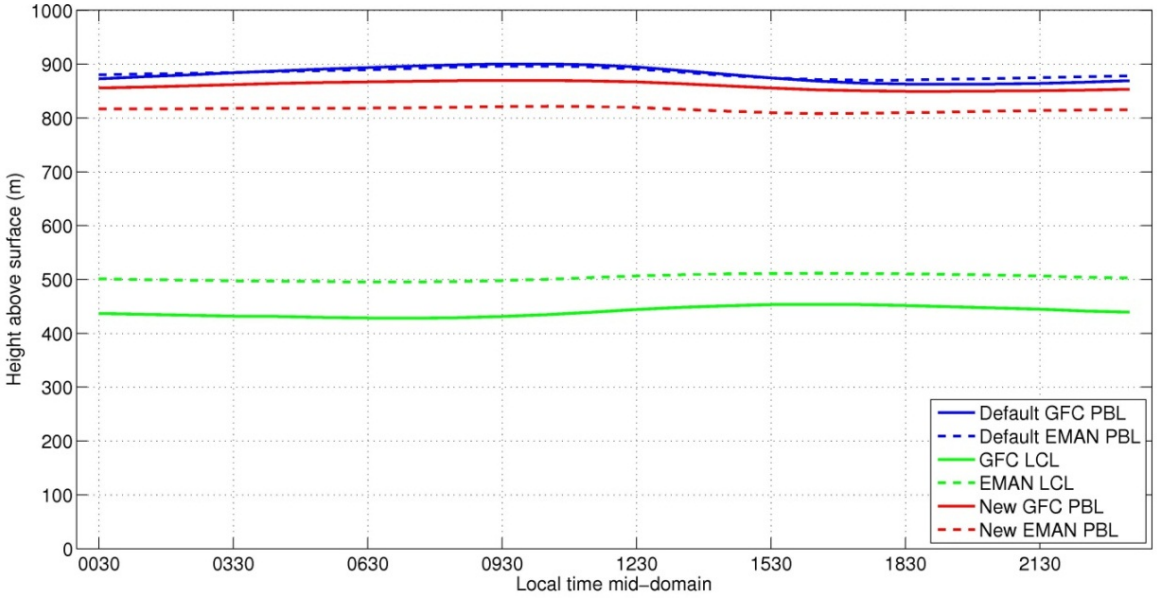

Figure 3-10. Average diurnal cycle of original PBL height (blue), new PBL height (red) and elevation of LCL (green) (all in m above surface) over ocean cells within the model domain for the period 1998-2001, using RegCM3-IBIS with both the Grell with Fritsch-Chappell closure (GFC, solid line) and Emanuel (EMAN, dashed line) convection schemes.

The new PBL height over land is significantly lower than the old one, on average by 400-500 m. This results in the average PBL height dropping to about 200 m at night, an elevation that is more consistent with the collapse of the daytime mixed layer and consistent with the early morning and nocturnal PBL datasets described previously. Hence this result shows the strong influence of the original minimum constraint placed on the PBL height. Figure 3-9 also shows that the new PBL height drops below the elevation of the LCL at night and in the early morning, which would limit night-time convection.

The new PBL height over ocean changes very little with the new modifications, decreasing by less than 100 m throughout the day and remaining substantially higher than the LCL. Turbulent heat fluxes exhibit very little diurnal variability over ocean due to the imposed weekly-mean SST, and hence the simulated PBL height should not be expected to collapse at night in the way that it does over land.

Figure 3-11 shows the average diurnal cycle of the PBL height simulated by the modified PBL scheme within RegCM3, comparing a land grid cell to an ocean grid cell as the approximate location of Singapore as described previously for Figure 3-6. The estimated PBL height from the Changi radiosonde data is shown for comparison, and vertical bars denote the observed and simulated variability as described for Figure 3-6. Table 3-4 summarizes the approximate height of the simulated PBL at the times corresponding to the Changi radiosonde data.

Table 3-4. PBL height (in m) comparison between Changi sounding estimate and values simulated using new PBL modifications, over land and ocean model grid cells.

PBL height (m)	8 am LT	11 am LT	2 pm LT	8 pm LT
Changi sounding estimate	250	800	750	500
Grell Fritsch-Chappell – land grid cell	382	990	1375	800
Grell Fritsch-Chappell – ocean grid cell	674	708	704	655
Emanuel – land grid cell	249	959	1180	456
Emanuel – ocean grid cell	680	726	754	758

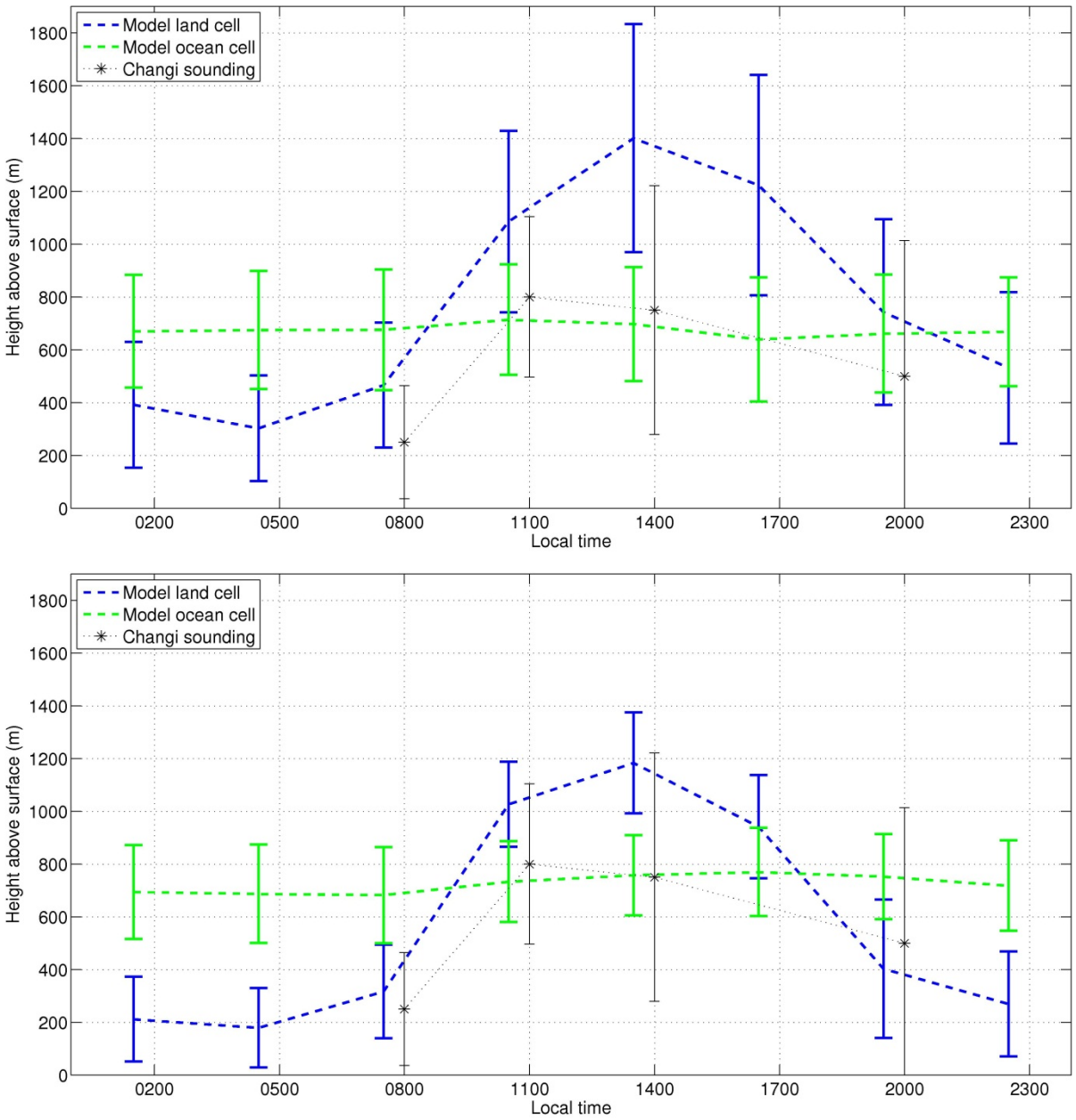

Figure 3-11. Diurnal PBL height (in m) over or near Singapore, simulated by the (top) Grell Fritsch-Chappell and (bottom) Emanuel convection schemes using either a land (blue) or ocean (green) grid cell to represent Singapore, compared to the PBL height estimated from the Changi soundings (black stars; dotted lines are shown to interpolate between the measurement times). The vertical bars signify one standard deviation of each sample set and illustrate the variability in the simulated and observed PBL height.

The results show that the modifications made to the PBL scheme significantly improve the simulated PBL height over Singapore. The new PBL scheme captures the low

PBL height that is shown in the observations in the morning and evening, which was significantly overestimated in the default scheme. If a land grid cell is an appropriate comparison to the Changi sounding data in the early morning and evening, and an ocean grid cell is the appropriate comparison during the daytime as discussed earlier, then the Emanuel scheme in particular provides a good match to the observed PBL height. These results indicate that the new PBL scheme results in a much more physically-realistic PBL simulation.

3.4.2 Low Cloud Cover

Figure 3-12 and Figure 3-13 show the diurnal cycle of cloud cover using the Grell Fritsch-Chappell and Emanuel schemes, respectively, averaged over the period 1998-2001 for land and ocean grid cells.

Note that these figures show the presence of cloud cover up to about 16.5 km elevation in the new simulations, but cloud cover was only present to about 14 km in the default simulations (Figure 3-7 and Figure 3-8). In the default version of RegCM3, no radiatively-active cloud cover or cloud liquid water are permitted to exist in the top two model layers. This limits the existence of radiatively-active clouds to about 14 km above the surface. However, the troposphere attains its maximum depth over the Maritime Continent and clouds are observed at altitudes up to 17 km. It was noted from Figure 3-7 and Figure 3-8 that the abrupt truncation of high cloud cover at 14 km seemed unphysical. Therefore in the modified simulations presented below, cloud cover and cloud liquid water have been permitted to exist within the second-most top model layer (they are still restricted in the top model layer). Although this change affected the depth and extent of the high cloud cover, sensitivity tests showed that it did not affect the low cloud cover.

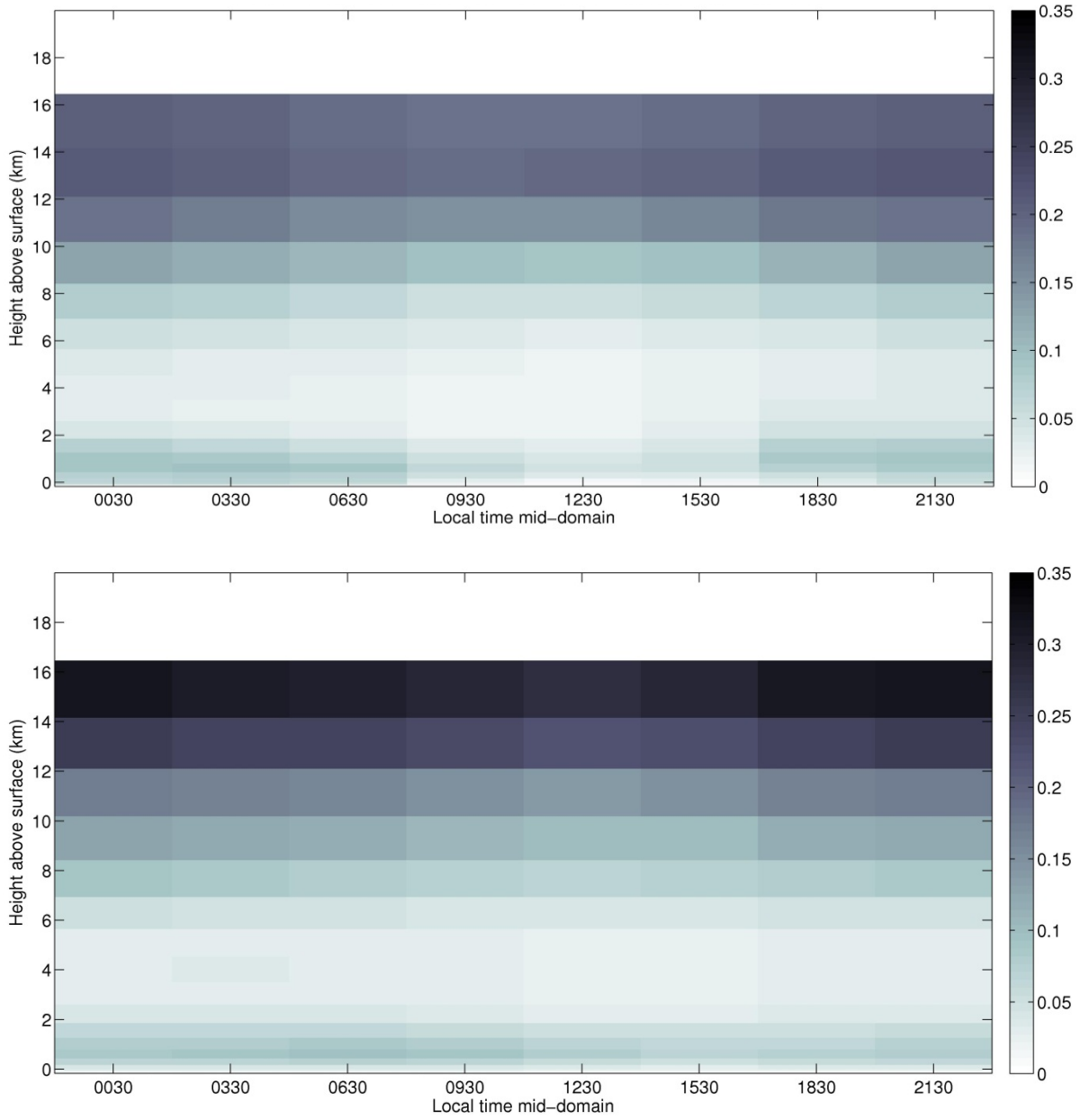

Figure 3-12. Diurnal cycle of cloud cover incorporating changes to cloud fraction, averaged for period 1998-2001 using Grell Fritsch-Chappell convection scheme for land (top) and ocean (bottom) grid cells. Color bar indicates fractional coverage of grid cell. The x-axis labels indicate the time of the middle of each 3-hour output window, with respect to local time in the center of the model domain. To represent the y-axis on a linear scale, the vertical extent of each model layer was assigned a single value of cloud cover, as provided by the model output. In reality, a smoother profile with less abrupt vertical variability would be expected.

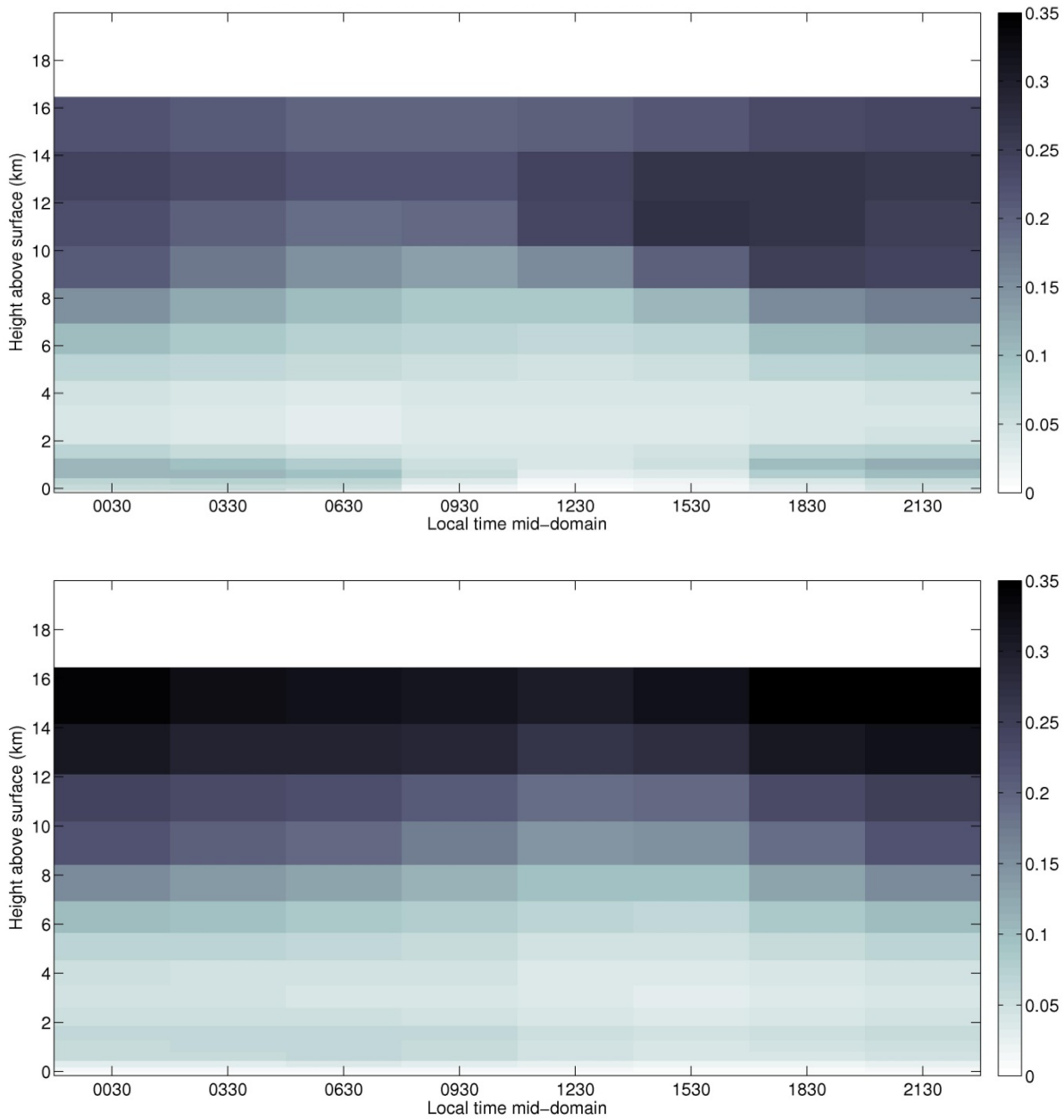

Figure 3-13. As for Figure 3-12 but using the Emanuel convection scheme.

Figure 3-12 and Figure 3-13 show that the new simulation of clouds within the PBL significantly reduced the simulated low cloud cover at all times of the day. The impact is particularly noticeable during the daytime with the Grell scheme and at night with the Emanuel scheme, when the schemes respectively produce the greatest extent of low cloud cover.

Figure 3-14 shows the difference in low cloud cover between the ISCCP data and the simulated results, using both the Grell Fritsch-Chappell and Emanuel convection schemes.

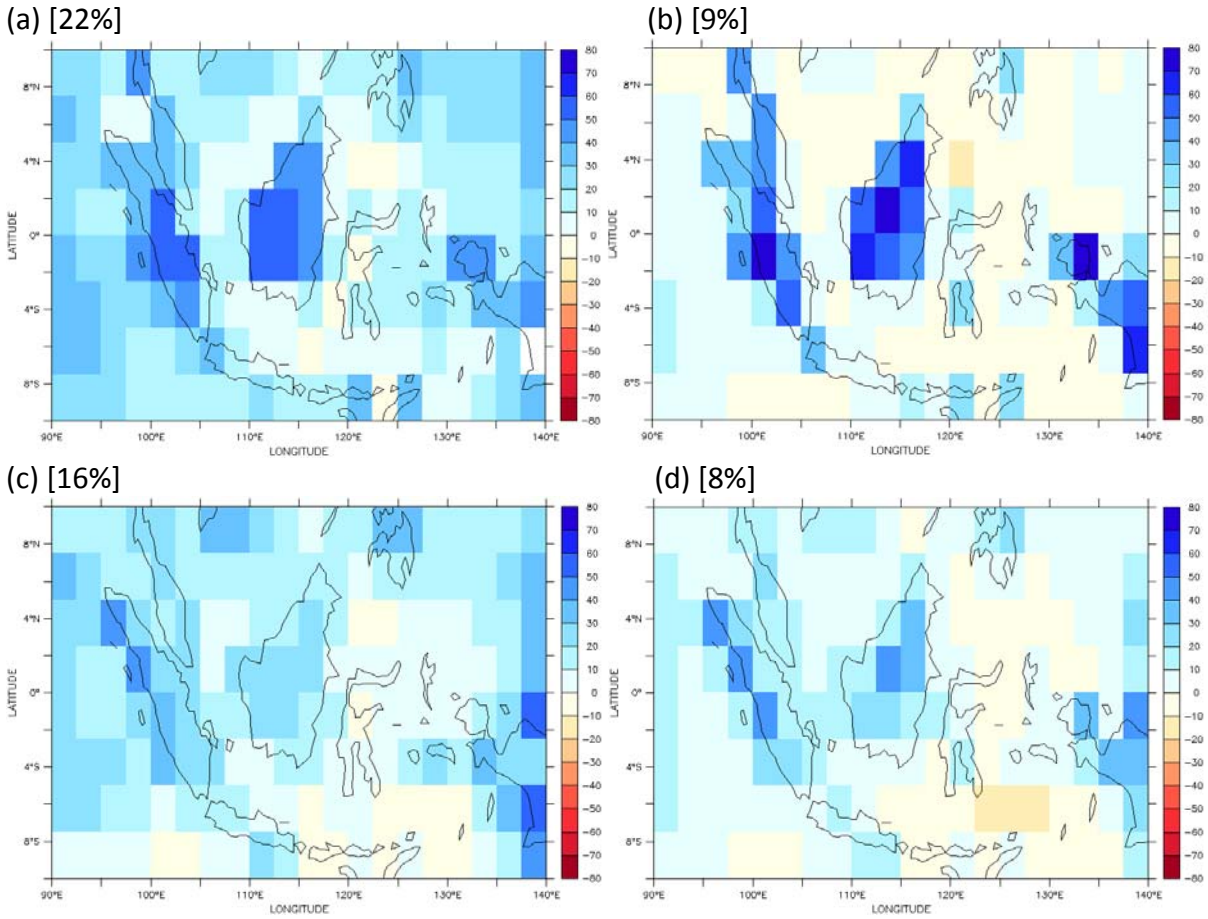

Figure 3-14. Average low cloud fraction for 1998-2001: simulation minus ISCCP data for (a) Grell Fritsch-Chappell with default clouds, (b) Emanuel scheme with default clouds, (c) Grell scheme with new PBL cloud cover and (d) Emanuel scheme with new PBL cloud cover. Domain-averaged error (model – ISCCP cloud fraction) is shown in parentheses. Color bar indicates fractional coverage of grid cell.

Figure 3-14 shows that the modified simulations with both the Grell Fritsch-Chappell and Emanuel convection schemes overestimate the extent of low cloud cover over land, but the bias is smaller with the new simulation of PBL cloud cover than in the default version of the model. Therefore it is considered that the new simulation represents an improvement over the default version of simulated cloud cover within RegCM3.

3.4.3 Radiative and Turbulent Heat Fluxes

Table 3-5 shows the average daily fluxes of radiation and turbulent heat with respect to the surface, averaged separately for land and ocean grid cells. Observations are compared to the default model, the model modified with just the new PBL height calculation, and the model modified with all the changes described in this chapter.

Table 3-5. Average daily surface radiative and turbulent heat fluxes (all in W m^{-2}) over period 1998-2001 for simulations using the default and modified model.

LAND

Simulation	SW_{dn}	SW_{abs}	Surface albedo	Planetary albedo	LW_{dn}	LW_{up}	R_N	LH	SH
Observations	202	170	16%	48%	411	452	129	95	34
Grell F-C default	225	194	14%	45%	411	464	141	104	36
Grell F-C – only PBL height change	217	187	14%	45%	411	458	140	100	41
Grell F-C modified (all changes)	257	222	13%	44%	401	459	164	118	48
Emanuel default	213	183	14%	50%	416	457	141	134	6
Emanuel – only PBL height change	214	184	14%	50%	419	458	144	126	19
Emanuel modified (all changes)	238	204	14%	49%	409	456	157	137	21

OCEAN

Simulation	SW_{dn}	SW_{abs}	Surface albedo	Planetary albedo	LW_{dn}	LW_{up}	R_N	LH	SH
Observations	220	206	6%	45%	420	467	158	108	10
Grell F-C default	264	247	6%	40%	414	473	188	129	12
Grell F-C – only PBL height change	262	246	6%	40%	413	473	186	132	16
Grell F-C modified (all changes)	261	245	6%	43%	413	473	184	128	15
Emanuel default	257	241	6%	45%	418	473	186	126	4
Emanuel – only PBL height change	265	248	6%	45%	417	473	192	116	6
Emanuel modified (all changes)	252	235	6%	49%	420	473	182	118	7

Notes on Table 3-5: SW_{dn} = shortwave (solar) radiation incident at the surface, SW_{abs} = net absorbed shortwave radiation at the surface, LW_{dn} = longwave radiation incident at the surface, LW_{up} = longwave radiation emitted from surface, R_N = net radiation absorbed at surface, LH = latent heat flux

away from surface, SH = sensible heat flux away from surface. Surface albedo is the ratio of solar radiation reflected by the surface to the incoming solar radiation (i.e. SW_{up} / SW_{dn}). RegCM3 does not output the outgoing solar radiation at the top of atmosphere so planetary albedo is calculated as (1 – OLR / SW_{TOA}), where OLR = outgoing longwave radiation, since all insolation at the top of atmosphere (SW_{TOA}) will be either reflected (due to albedo) or absorbed and re-emitted as longwave radiation, assuming no net gain in energy over the period used for simulation.

Table 3-5 shows that the default model with both convection schemes significantly overestimates the amount of incoming solar radiation (insolation) and net absorbed solar radiation at the earth's surface, particularly over ocean surfaces. This overestimation occurs despite good simulation of the planetary albedo, especially with the Emanuel scheme. Hence this result suggests that there are compensating deficiencies in the simulation of cloud cover that combine to produce adequate albedo but do not absorb as much of the solar radiation as observed. Chapter 4 will demonstrate that the model overestimates the coverage of high cloud cover but underestimates the daytime convective cloud cover lower in the atmosphere. This combination of errors was also shown by Lin and Zhang (2004) using the NCAR Community Atmosphere Model Version 2 (CAM2).

Reducing the PBL height improved insolation by a small amount over land with the Grell scheme. This is because the reduction in PBL height led to less convection, even though Table 3-6 will show that there was no reduction in convective rainfall. This is due to the manner in which convective mass flux is calculated within the Grell scheme, which will be discussed in Chapter 5. Less convection led to increased moisture build-up in the lower atmosphere, which created more large-scale clouds in the 1 km immediately above the surface that prevented insolation from reaching the surface.

By contrast, reducing the PBL height over land had negligible impact on insolation with the Emanuel scheme, even though Table 3-6 will show that this change did impact the convective rainfall. This is because the convective mass flux with the Emanuel scheme, although reduced by the shallower PBL depth, is still very strong. There was a large vertical transport of moisture away from the surface, leaving little moisture at lower levels to be converted into large-scale cloud. Despite the strong convection, the poor representation of

convective clouds in RegCM3 results in little convective cloud cover and will be discussed at length in Chapter 4.

With both schemes, reducing the PBL height over land changed the partitioning of turbulent heat fluxes due to a reduction in rainfall, with less LH and more SH.

Over ocean, the modification to PBL height had negligible impact on insolation with the Grell scheme since the PBL height did not actually change much (see Figure 3-10). Since no other changes were made to the ocean, it is likely that the difference in LH to SH partitioning that results with the PBL height modification is due to a difference in low-level wind speeds, possibly as a result of changing dynamics over nearby islands.

The PBL modification worsened the error over the ocean with the Emanuel scheme, even though the actual change to the PBL was only on the order of 100 m (see Figure 3-10). Triggering of the Emanuel scheme is apparently very sensitive to the PBL height, so even this small reduction in PBL height was sufficient to reduce convection with this scheme (as shown in Table 3-6). The reduction in convection enabled more moisture to build up in the lower 1 km of the atmosphere, which was converted into large-scale cloud, but reduced cloud cover in the region 1-8 km above the surface because of the reduced vertical transport of moisture. This reduction in large-scale cloud in the middle atmosphere is the cause of increased insolation. Again, the change in LH to SH partitioning over ocean with the Emanuel scheme is likely due to interactions with nearby islands.

When the new simulation of PBL clouds and the addition of clouds in the second-highest model layer were included, the overestimation bias in insolation was worsened considerably over land with both convection schemes. This is due to the reduction in low-level cloud cover, which is also indicated by the reduction in longwave radiation down to the surface. This difference is especially significant considering that the new high clouds reduced insolation; the impact of the reduction in PBL clouds was far greater than the addition of new high clouds. The overestimation of insolation propagates into error in the absorbed shortwave radiation and net radiation at the surface, and subsequently into increased fluxes of LH and SH over land.

Over ocean, the changes to cloud cover had the opposite impact – the reduction in low PBL clouds was smaller in magnitude than the addition of new high cloud, with the net result of less insolation reaching the ocean surface.

The impact of changes to the ocean surface roughness length, soil heat flux and canopy interception are imperceptible in the modified simulations, since the changes due to the PBL height and cloud cover swamp any signal from the difference in surface fluxes.

Over both land and ocean, the model simulates longwave radiation reasonably well – mean daily values of longwave radiation both down to the surface and up from the surface are within about 10 W m^{-2} (about 3% error) of the observations. The flux of longwave radiation has a muted diurnal cycle (i.e. very small diurnal amplitude) and the model generally matches well to the observed cycle (not shown).

Table 3-5 shows that the model simulates the surface and planetary albedos reasonably well over both land and ocean. The Grell scheme tends to underestimate the planetary albedo slightly and the Emanuel scheme slightly overestimates it. This is due to the respective differences between the schemes in convective strength, which create differences in the moisture transported aloft and transformed into large-scale cloud cover at high altitudes.

The error in the simulated mean daily insolation is primarily due to an overestimation of the early and mid-afternoon radiation, as shown in Figure 3-15 and Figure 3-16 below. These figures compare the default model to the version with all modifications made in this chapter. The peak insolation is overestimated by about 100-200 W m^{-2} over land and by 200 W m^{-2} over ocean. It is also noted that the early morning insolation is underestimated by the model, so that in general the shape of the diurnal cycle of insolation is weighted more heavily towards the afternoon in the model compared to the observations.

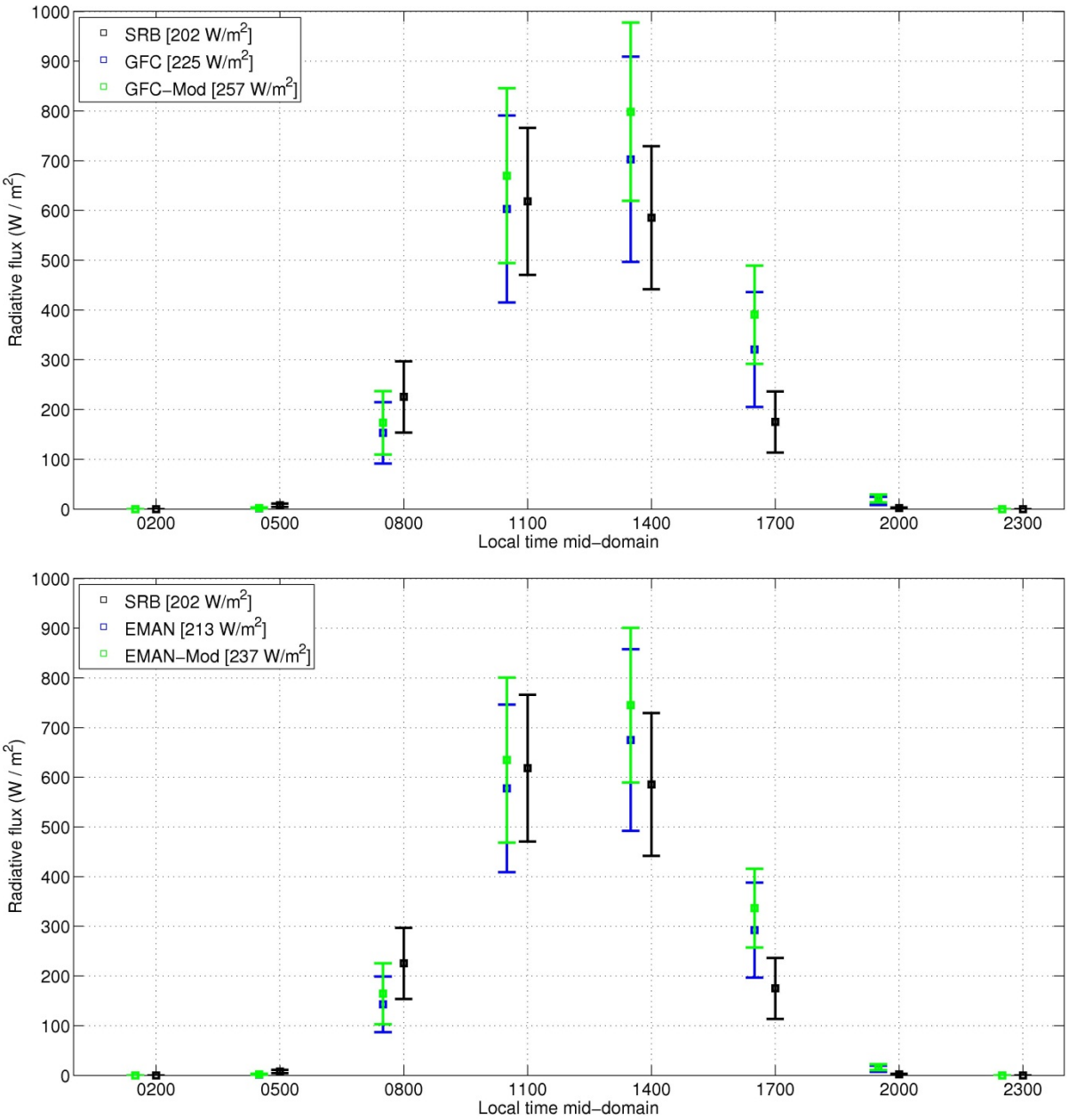

Figure 3-15. Diurnal cycle of incoming solar radiation (in W m^{-2}) averaged over land for period 1998-2001 for SRB observations and simulations using (top) Grell with Fritsch-Chappell and (bottom) Emanuel convection schemes, comparing the default version to the modified (-Mod) version. Square symbol indicates the mean value; error bars indicate +/- 1 standard deviation.

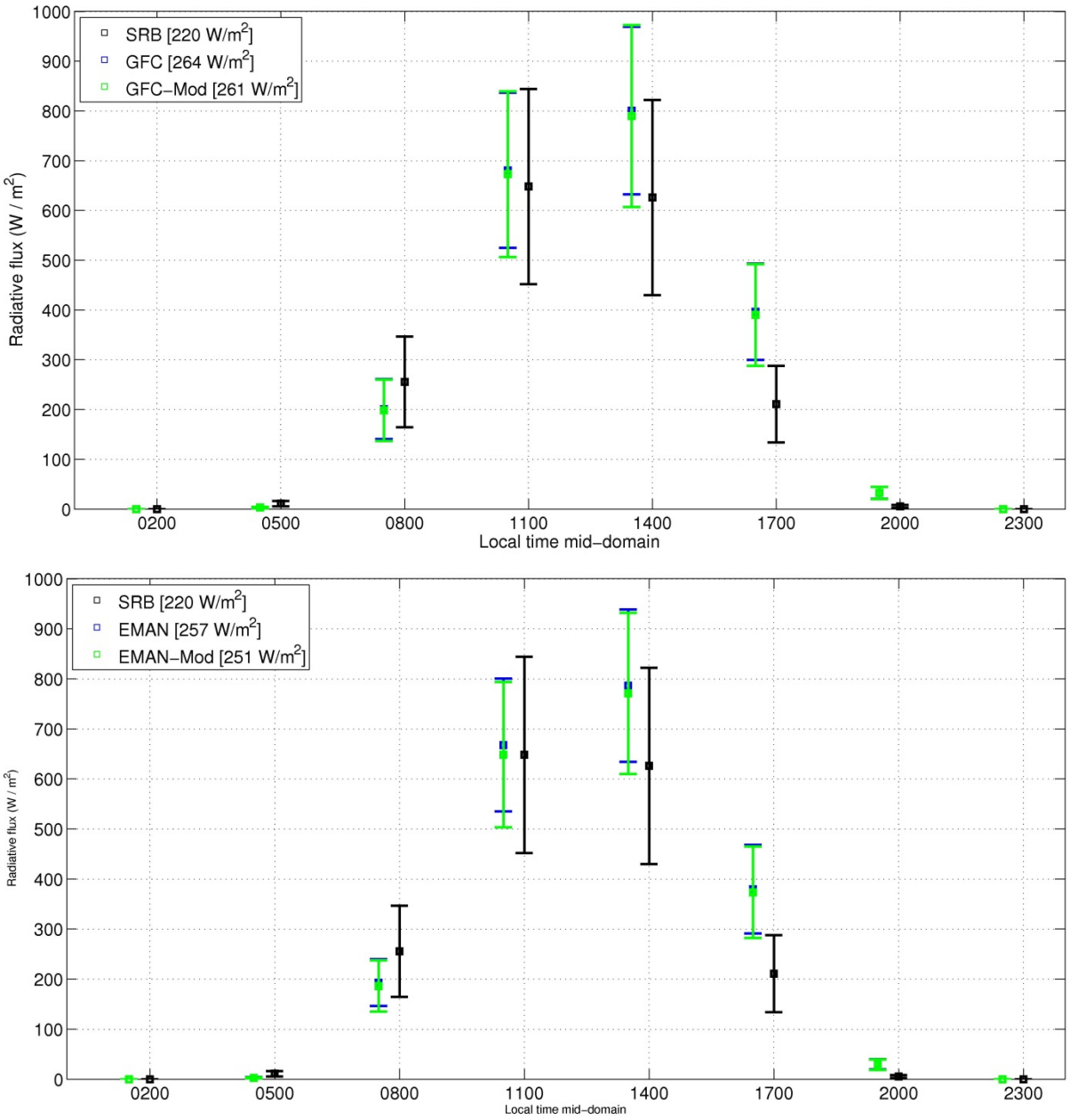

Figure 3-16. Diurnal cycle of incoming solar radiation (in W m^{-2}) averaged over ocean for period 1998-2001 for SRB observations and simulations using (top) Grell with Fritsch-Chappell and (bottom) Emanuel convection schemes, comparing the default version to the modified (-Mod) version. Square symbol indicates the mean value; error bars indicate +/- 1 standard deviation.

3.4.4 Rainfall

Table 3-6 shows the average daily rainfall over the period 1998-2001 separately for land and ocean, including the relative convective and large-scale rainfall fractions.

Table 3-6. Average daily rainfall (in mm day^{-1}) over land and ocean over period 1998-2001 for simulations with default and modified versions of the model.

Product / Simulation	Land Average			Ocean Average		
	Total	Convective	Large-scale	Total	Convective	Large-scale
TRMM	*8.6*	*5.4 (63%)*	*3.2 (37%)*	*7.0*	*4.0 (57%)*	*3.0 (43%)*
Grell F-C default	8.5	3.7 (43%)	4.8 (57%)	6.7	3.8 (56%)	2.9 (44%)
Grell F-C – only PBL height change	7.5	3.8 (51%)	3.7 (49%)	6.8	4.6 (68%)	2.2 (32%)
Grell F-C modified (all changes)	10.9	4.4 (40%)	6.5 (60%)	8.5	4.1 (48%)	4.4 (52%)
Emanuel default	14.9	11.9 (80%)	3.0 (20%)	7.2	6.2 (86%)	1.0 (14%)
Emanuel – only PBL height change	13.4	7.8 (58%)	5.6 (42%)	5.4	4.1 (75%)	1.3 (25%)
Emanuel modified (all changes)	16.8	9.9 (59%)	6.9 (41%)	6.7	3.8 (57%)	2.9 (43%)

Table 3-6 confirms that the lower PBL height led to less convection with the Emanuel scheme, over both land and ocean. This reduction in convection increased the fraction of time in which no rainfall occurred, as shown in Figures 3-19 and 3-20. There was also less convection with the Grell scheme, but due to the nature of the convective mass flux calculation in this scheme there was actually a small increase in rainfall. This will be discussed further in Chapter 5. The changes to large-scale rainfall over land are a reflection of the changes to convective rainfall. When convective rainfall is reduced with the Emanuel scheme, leaving more residual moisture, large-scale rainfall is increased. Conversely, large-scale rainfall decreases with the Grell scheme as convective rainfall increases and removes moisture from the atmosphere. The impact of the lower PBL height on rainfall over the ocean is similar to that over land.

When the changes to cloud cover were incorporated, the two convection schemes exhibited similar changes to rainfall. Over land, the reduction in PBL cloud cover led to increased insolation and therefore increased low-level instability and increased convective rainfall, while the increase in high cloud cover led to an increase in large-scale rainfall. Over ocean, the change to high cloud cover was sufficient to reduce the insolation, thereby reducing convective rainfall, while also increasing large-scale rainfall.

With both convection schemes, the net result of all the modifications made in this chapter is an improvement in the simulation of convective rainfall compared to TRMM, over both land and ocean – increasing it with the Grell scheme and decreasing it with the Emanuel scheme. However, the modifications also led to significant increases in large-scale rainfall with both schemes compared to the default model, which produced an overestimation bias and worsened the total rainfall compared to TRMM.

The average diurnal cycles of rainfall over land and ocean are shown in Figure 3-17 and Figure 3-18 below, comparing the default model to the version with all modifications presented in this chapter.

Over land, the modified simulations did not appreciably change the timing or general shape of the diurnal cycle. With both schemes, the reduction in low level cloud led to a small increase in convective rainfall during the middle of the day. This improved the daytime peak with the Grell Fritsch-Chappell scheme but worsened the bias with the Emanuel scheme. With the Emanuel scheme, the reduction in daytime convection due to the lower PBL height can be seen in the morning and evening (approximately 5-9 pm). With both schemes, the increase in large-scale rainfall due to increased high cloud cover is noticeable from about 10 pm until the early morning.

Over the ocean, Figure 3-18 shows that the simulated shape of the diurnal rainfall cycle is unchanged with the new modifications using both the Grell Fritsch-Chappell and Emanuel schemes. In general, both schemes show reasonably good simulation of the diurnal rainfall cycle compared to TRMM over the ocean.

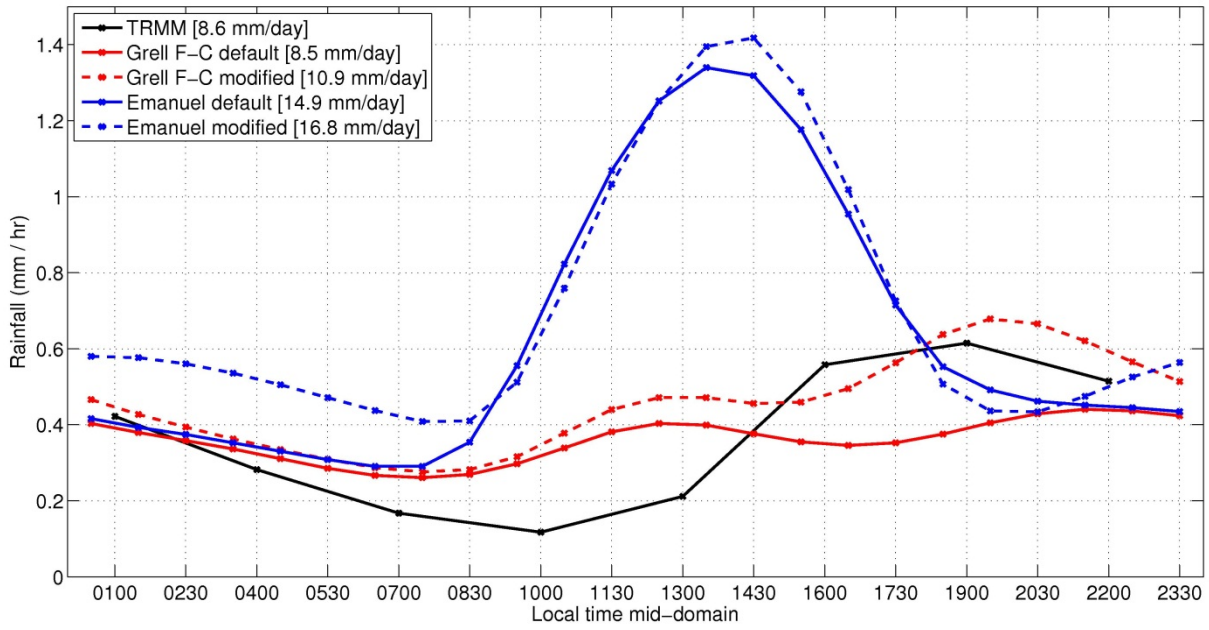

Figure 3-17. Diurnal cycle of rainfall (in mm hr^{-1}) averaged over land for period 1998-2001, comparing default simulations to the modified version of the model.

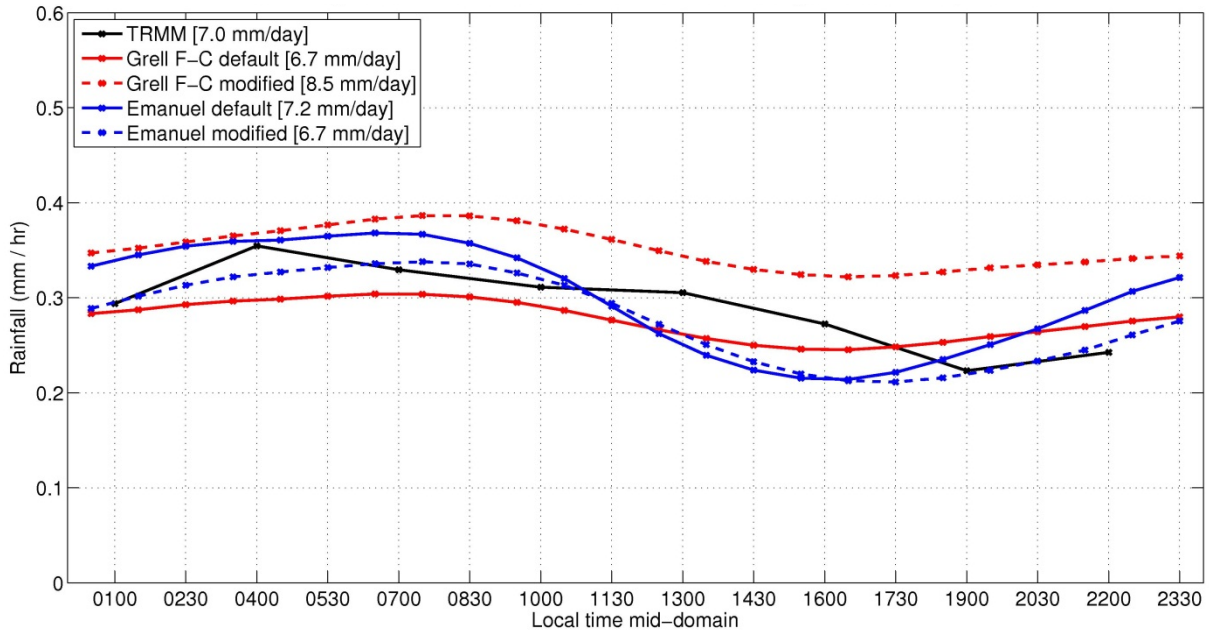

Figure 3-18. Diurnal cycle of rainfall (in mm hr^{-1}) averaged over ocean for period 1998-2001, comparing default simulations to the modified version of the model.

Finally, the impact on the rainfall histogram is shown in Figures 3-19 and 3-20. The changes to non-raining times (intensity less than 0.0417 mm hr^{-1}) reflect the changes to convective rainfall described above. Increases in convective rainfall worsened the histogram,

while decreases in convective rainfall improved the histogram. However, in both cases, the changes were small compared to the magnitude of the error with respect to TRMM.

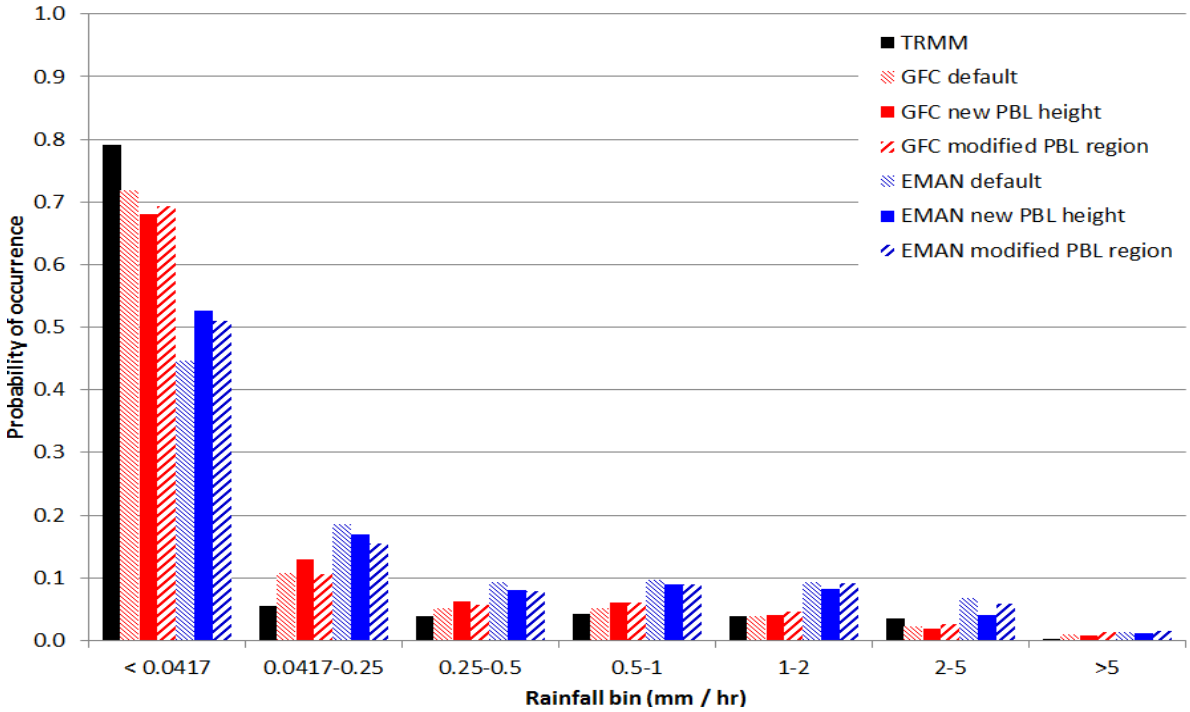

Figure 3-19. Rainfall histogram, with rainfall intensities in mm/hr, averaged over land grid cells for period 1998-2001, comparing TRMM to simulations using Grell with Fritsch-Chappell (GFC) and Emanuel (EMAN) convection schemes. 'Modified PBL region' refers to all modifications made in Chapter 3.

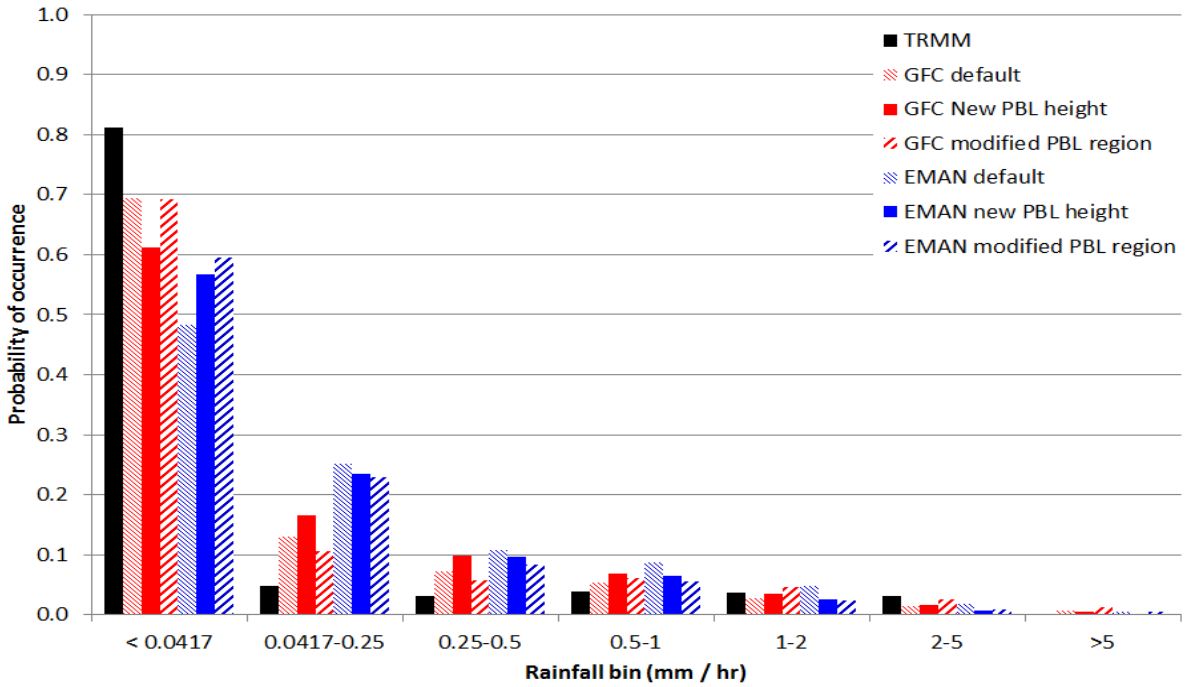

Figure 3-20. Rainfall histogram as in Figure 3-19 but averaged over ocean grid cells.

3.5 Summary

This chapter has shown that changes to the near surface environment can affect the simulation of both convective and large-scale rainfall. The modifications made here had positive impacts on the simulation of convective rainfall with both convection schemes.

However, the modifications were not sufficient to address the errors that were identified in the previous sections with regard to the diurnal rainfall cycle and rainfall histogram. This result by itself would suggest that another factor is influencing the pre-conditions for convection that has not been affected by the modifications to the PBL region made thus far. The simulated errors with respect to solar radiation indicate that this factor lies in attenuation of incoming solar radiation, most likely due to poor representation of cloud cover.

This chapter has investigated the response of the surface to the incoming radiation that is received, a response that helps to trigger convection. Chapter 4 will investigate how this radiation is impacted by the presence of convective activity and will seek to improve the simulation of convective cloud cover and its impact on the incoming solar radiation.

Chapter 4: On the Simulation of Convective Cloud Fraction

Cumulus convection influences large-scale atmospheric dynamics not only through diabatic heating and vertical transports of heat and moisture, but also through the interaction of cumulus clouds with radiation (Tiedtke 1988). The strong interaction of clouds with both shortwave and longwave radiation alters the distribution of surface and atmospheric heating, which in turn drives the atmospheric motion that is responsible for cloud formation, including the variability associated with atmospheric convection (Bergman and Salby 1996), creating a convective-radiative feedback. Therefore clouds serve both as indicators of atmospheric motion and as contributors to atmospheric and ocean dynamics.

The role that clouds play in the climate system is shown schematically in Figure 1 from Arakawa (2004), and their impact on the global radiation budget is illustrated in Figure 1 from Trenberth *et al*. (2009), both reproduced below. The role of clouds in the radiation budget is especially strong over the Maritime Continent, illustrated by the observed planetary albedo of 45-48% over this region (Table 3-5) compared to the global mean planetary albedo of around 30% (Figure 4-2 below).

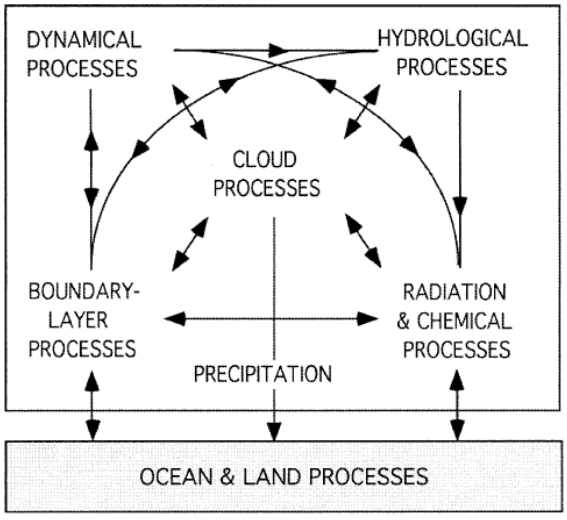

Figure 4-1. Interactions between various processes in the climate system, showing the key role played by clouds (Figure 1 in Arakawa 2004).

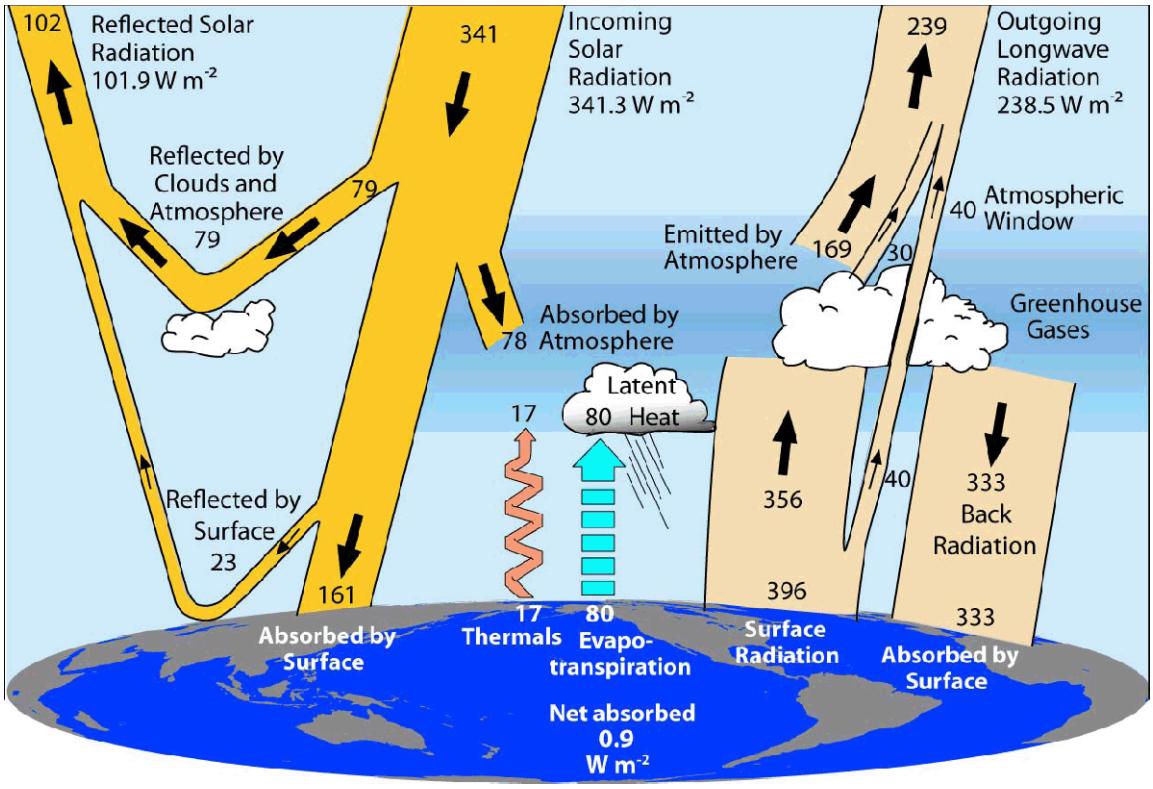

Figure 4-2. Global annual mean energy fluxes (in W m^{-2}) over the period March 2000 – May 2004 (Figure 1 taken from Trenberth *et al*. 2009).

Despite significant improvements over recent decades in the ability of large-scale models to reproduce the existing climate and its sensitivity, the representation of clouds remains extremely problematic. In the Fourth IPCC Assessment Report (Christensen *et al.* 2007), cloud feedbacks were identified as a primary reason for differences between models, with the shortwave impact of boundary-layer and mid-level clouds making the largest contribution. The uncertainties that exist with regard to cloud processes are illustrated in Figure 2 of Arakawa (2004), reproduced below. These uncertainties are a major cause for concern, since models predict different responses of clouds to global warming and it is not yet possible to determine which estimates of the climate change cloud feedbacks are the most reliable (Christensen *et al*. 2007).

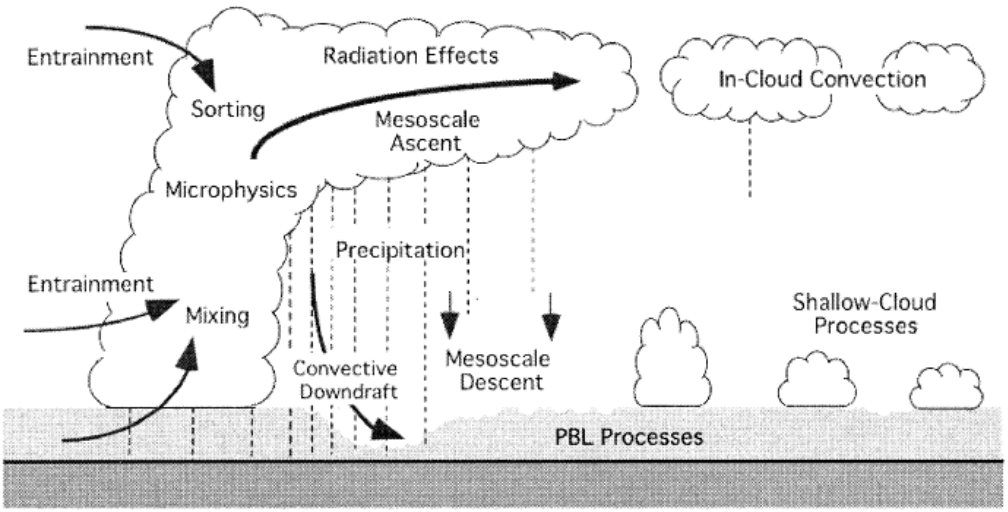

Figure 4-3. Cloud and associated processes for which major uncertainties in formulations exist (Figure 2 from Arakawa 2004).

Few studies have been undertaken to evaluate the performance of large-scale climate models with respect to cloud cover and radiative fluxes over the tropics. A few relevant works are summarized here to provide a comparison to the performance of RegCM3 over the Maritime Continent. The models all show significant errors with regard to simulation of radiative fluxes and cloud cover.

Lin and Zhang (2004) evaluated cloud climatology and the cloud radiative forcing at the top of the atmosphere as simulated by the NCAR Community Atmospheric Model Version 2 (CAM2). It was shown that the model overestimated total cloud amount in the western Pacific Ocean, Maritime Continent and central Africa, but paradoxically simulated reasonable cloud radiative forcing at the top of the atmosphere (Lin and Zhang 2004). It was shown that the model contained compensatory deficiencies: excessive high clouds and deficient middle-top clouds compensated for errors in longwave forcing, while excessive optically thick clouds and deficient optically medium clouds compensated for errors in shortwave forcing (Lin and Zhang 2004). Importantly, the authors noted that the general lack of middle- and low-top optically intermediate and thin clouds was associated with the inability of the model convection to produce clouds (Lin and Zhang 2004).

Kothe and Ahrens (2010) evaluated the monthly radiation budget over West Africa as simulated by eight different RCMs, which contributed to the European Union project

ENSEMBLES. It was shown that most of the models generally underestimated surface net shortwave radiation in ocean areas and in parts of the Intertropical Convergence Zone and overestimated cloud fraction, especially over ocean and in the equatorial region. It was noted that the strong under- and overestimations of surface net shortwave radiation in summer seemed to be connected to the strong over- and underestimations of cloud fraction in the same regions (Kothe and Ahrens 2010). Errors in cloud fraction accounted for more than 20% of the radiative flux errors over land and more than 40% over ocean (Kothe and Ahrens 2010).

Li and Zhou (2010) evaluated the performance of RegCM3 coupled to the Hybrid Coordinate Ocean Model (HYCOM) in a 20-year simulation of the present climate over East Asia. It was found that the coupled model resulted in a 2^{o}C cold bias in sea surface temperature (SST) just south of Japan, partly due to underestimation of the net shortwave radiation simulated at the sea surface. To keep the simulated SST close to observations, a heat flux adjustment for solar radiation had to be made. With this adjustment, the coupled model was shown to reproduce the main features of East Asian circulations reasonably well (Li and Zhou 2010). It is possible, even probable, that the underestimation of shortwave radiation in the model was due to errors in the simulation of cloud coverage and/or cloud liquid water path, since the absorption and reflection of shortwave radiation plays such a significant role in regulating net shortwave radiation at the surface. However, the authors did not present an evaluation of the simulated cloud water content or cloud coverage so any inferences about shortwave radiation are only a guess on this author's part.

GCMs and RCMS must parameterize the processes associated with convective clouds, since they occur on a scale much smaller than a large-scale climate model is capable of resolving. The first order objective is to accurately simulate the presence or absence of clouds, i.e. the cloud fraction. This chapter summarizes the current state of practice with regard to the simulation of convective cloud fraction, discusses the deficiencies in current methods in large-scale models, including RegCM3, and presents a new parameterization of convective cloud fraction that is tested within RegCM3-IBIS.

4.1 Review of Existing Parameterization Methods for Convective Cloud Fraction

One of the most important problems in any numerical simulation is the representation (or 'parameterization') of physical processes that occur on space and/or time scales too small to be explicitly simulated by the model. Differences in parameterization methods are a primary reason why climate model results differ (Christensen *et al.* 2007). Simulation of convective clouds in GCMs and RCMs is limited by the need to parameterize the sub-grid scale convective activity and by the use of grid-averaged properties. Typically, a diagnostic value of the grid-averaged cloud liquid water is simulated based on the water vapor and saturation mixing ratios within the grid cell. That single value is then used for representation of the cloud water content within the grid cell, without regard to the natural variability in cloud density that can occur on the scale of a model grid cell (typically 30 km – 200 km).

It was noted by Arakawa (2004) that there was no need to determine the fractional cloud cover for the 'classical objectives' of cumulus parameterization, which were to evaluate the vertical distributions of cumulus heating and moistening. Therefore representations of convective cloud fraction in large-scale climate models have historically been extremely simple or neglected altogether. A good review of large-scale model representations of cloud fractional cover and cloud microphysical processes, up to the mid-1990s, can be found in Fowler *et al.* (1996).

In their seminal work describing a convective parameterization scheme based on quasi-equilibrium theory, Arakawa and Schubert (1974) assumed that the fractional area (FC) covered by active cumulus updrafts is negligibly small, i.e. FC << 1, and thus provided no calculation of the convective cloud cover. The only interaction between convection and cloudiness was provided via detrainment of convective cloud water at the top of cumulus towers, which could be incorporated into the stratiform cloud cover. This method has been adopted by several GCMs (e.g. the Colorado State University GCM, Fowler *et al.* 1996).

But fractional cloud cover is required for the 'non-classical objectives' of cumulus parameterization described by Arakawa (2004), which include the interactions of convection

with radiation. However, very few formulations for convective cloud fraction have been developed to explicitly model this type of cloudiness within large-scale climate models.

Convective cloud cover in the model described by Sundqvist *et al*. (1989) is given by:

$$b = \xi \tau F_{cu} \tag{4-1}$$

where τ = characteristic time scale for convection, $\xi = \xi_0 f(\sigma)$ = quantity resulting from Kuo's assumption and closure relation, a modification of the Kuo parameterization scheme presented in Sundqvist (1988), while

$$\mathrm{F_{cu}} = \frac{1+\frac{\sigma_B - \sigma_T}{0.3}}{1+2.5\xi\tau}(1 + \mathrm{U}) \tag{4-2}$$

where σ_B = sigma vertical coordinate at cloud base, σ_T = sigma vertical coordinate at cloud top, U = grid-scale relative humidity. F_{cu} is a parameter function that (i) increases b as the cloud depth increases, (ii) increases b as the relative humidity increases, and (iii) prevents b from approaching unity when ξ is large (Sundqvist *et al*. 1989). In the Sundqvist *et al*. (1989) parameterization, if the top level of a convective cloud has a temperature of -20°C or less, the condensation at that level is treated as stratiform to allow representation of a convective anvil.

Tiedtke (1993) considered convective clouds to be condensates produced in cumulus updrafts and detrained into the environmental air. The sources of convective cloud water content, S_{cv}, and convective cloud cover, $S(a)_{cv}$, were described by:

$$S_{cv} = \frac{D_u}{\rho} l_u \tag{4-3-a}$$

$$S(a)_{cv} = (1 - a)\frac{D_u}{\rho} \tag{4-3-b}$$

where D_u = detrainment of mass, l_u = specific content of cloud water content in updrafts, α = cloudy area, ρ = density of cloudy air. The factor $(1 - \alpha)$ appears because updraft air is assumed to detrain simultaneously into cloud-free air as well as into already existing clouds, ensuring realistic limits at zero cloud cover (updraft air detrains only into clear air) and at cloud cover 1 (all updraft air detrains into existing clouds) (Tiedtke 1993). The detrainment D_u is obtained from the cumulus parameterization for the updraft mass flux.

In testing, the simulated convective cloud cover using the Tiedtke scheme was shown to reproduce some of the observed global cloud characteristics, e.g. a cloudy maximum over the Intertropical Convergence Zone (ITCZ) and minima over the subsidence regions of Australia, North Africa, South Africa and South America. However, significant errors in the amount of fractional cloud cover were noted. High cloud amount was significantly overestimated over the tropics, including the Maritime Continent region, while low and mid-level clouds were underestimated (Tiedtke 1993).

The Tiedtke (1993) method is used in the European Centre for Medium-range Weather Forecasts (Jakob and Klein 1999) and Geophysical Fluid Dynamics Laboratory (Donner *et al.* 2011) GCMs, among others.

While both the Sundqvist *et al*. (1989) and Tiedtke (1993) formulations link convective cloud fraction to attributes of the convective motion, neither scheme captures the effects of subgrid variability in convective activity (i.e. variations in updraft mass flux and cloud liquid water that are small in scale relative to the size of a model grid cell) on cumulus cloud formation.

Other methods used by GCMs are similarly simplistic. In the Max Planck Institute's ECHAM5 (Roeckner *et al*. 2003), the fractional area occupied by a convective cloud ensemble is a function of the difference in elevation between the detrainment level and top of the cloud. Roeckner *et al*. (2003) noted that the treatment of convective cloud cover in the ECHAM5 model is arbitrary, stating "there is no particular reason for choosing this particular function". In the Hadley Center's HadGEM1 (Martin *et al*. 2006), convective cloud fraction is diagnosed from the logarithm of the total water flux and applied as a constant value

between cloud base and top. In NCAR's CAM4.0 (Neale *et al*. 2010), convective cloud fraction is a linear function of the logarithm of the convective mass flux.

Bony and Emanuel (2001) have provided the only example this author could find of an attempt to explicitly link the subgrid variability in convective cloud water content and cloud fraction to convective activity. Their approach was to consider that the convection parameterization scheme should predict the in-cloud water content, while a statistical cloud scheme should predict how this cloud water is spatially distributed within the domain. Condensed water is produced at the subgrid scale by cumulus convection and at the large scale by supersaturation. This scheme therefore makes no distinction between convective and stratiform clouds, but instead accounts for all types of clouds that may be associated with cumulus convection (Bony and Emanuel 2001). The total cloud fraction is obtained from:

$$f = \int_{q_s}^{\infty} P(q_t) dq_t \qquad (4\text{-}4)$$

where f = cloud fraction, q_s = saturation mixing ratio, q_t = total water content (vapor and condensate) and $P(q_t)$ = probability density function (PDF) that describes the subgrid variability around the mean of q_t.

The PDF chosen was of a generalized lognormal form, which requires determination of the first three statistical moments (mean, variance and skewness coefficient) of the subgrid-scale fluctuations of the total water mixing ratio (Bony and Emanuel 2001). If there is no subgrid-scale variability within the domain, the parameterization becomes equivalent to an all-or-nothing large-scale saturation scheme (Bony and Emanuel 2001).

While this scheme is certainly an improvement upon previous attempts, there are two issues with its practical implementation in a large-scale climate model. Firstly, it is computationally expensive, due to its dependence on the first three statistical moments of the PDF and evaluation of the error function resulting from the integral in (4-4). Secondly, it lumps together all the condensate within a grid cell, but most GCMs and RCMs require a separate large-scale cloud fraction for calculation of the non-convective rainfall and potentially for specification of different cloud optical properties within the radiative transfer

scheme. This scheme is therefore not optimally suited for the structure of current large-scale climate models and, to the best of this author's knowledge, it has not yet been implemented in any of the commonly used GCMs or RCMs.

Examples of the treatment of convective cloud cover in selected current large-scale models are shown in Table 4-1 below.

Table 4-1. Method for treatment of convective cloud fraction in selected large-scale climate models.

Model	Treatment of Convective Cloud Cover
ECHAM5 (Max Planck Institute; Roeckner *et al.* 2003)	Model assumes the presence of a convective cloud ensemble, with updrafts and downdrafts in steady state. Fractional area of each individual updraft is constant with height except where it detrains. The spectrum of clouds detraining at different levels is given by: $$\sigma(z) = \sigma_0 cos\left(\frac{\pi(z - z_d)}{2(z_t - z_d)}\right)$$ where $\sigma(z_d) = \sigma(z_t) = \sigma_0$ = constant, z_d = detrainment level, z_t = highest possible cloud level.
HadGEM1 (Hadley Center; Martin *et al.* 2006)	Convective cloud fraction diagnosed empirically from linear relation with the logarithm of total water flux. Cloud fraction constant with height within a model grid box and applied as a constant value between cloud base and top. To represent convective anvils: cloud fraction is increased linearly with height above the freezing level to the cloud top (represents the anvil) and decreased to a constant value below the freezing level (represents the convective tower).
CAM4.0 (National Center for Atmospheric Research; Neale *et al.* 2010)	Three types of cloud are diagnosed: low-level marine stratus (C_{st}), convective cloud (C_{cir}) and layered cloud (C_c). Convective cloud fraction is related to the updraft mass flux in the deep and shallow cumulus schemes according to: $C_{shallow} = 0.04*\ln(1.0 + 500*M_{c,shallow})$ $C_{deep} = 0.1*\ln(1.0 + 500*M_{c,deep})$ where M_c = convective mass flux. Parameters are constant in time and space.
GFDL (NOAA Geophysical Fluid Dynamics Laboratory AM2/LM2; Rotstayn *et al* 2000, Tiedtke 1993)	Convective cloud cover parameterized according to Tiedtke (1993): $$S_{cv} = \frac{D_u}{\rho} l_u, S(a)_{cv} = (1 - a)\frac{D_u}{\rho}$$ where D_u = convective detrainment as calculated by the convective mass flux scheme, l_u = specific content of cloud water content in updrafts, a = cloudy area, ρ = density of cloudy air.
NASA GISS GCM (Yao and Del Genio 1999)	Convection scheme of Del Genio and Yao (1993). A fraction of the condensate from deep convection detrains into the environment. The detrained condensate then combines with any anvil cloud water generated by large-scale cloud formation in the same grid box. Cloud cover of anvil clouds in the absence of large-scale cloud is $10C_m$, where C_m is the ratio of convective mass to grid-box air mass. Cloud cover for the non-anvil portion of convection is C_m.
ECMWF (European Centre for Medium-Range Forecasts; Jakob and Klein 1999)	Convection and convective clouds are parameterized as in Tiedtke (1993), as described above for the GFDL model.

4.2 Existing Parameterization of Convective Cloud Fraction in RegCM3

The existing treatment of convective cloud cover in RegCM3 is simplistic and fairly arbitrary. The horizontal fractional cover of convective cloud, FC_{cnv}, within each grid cell is calculated according to:

$$FC_{cnv} = 1 - 0.75^{1/N} \tag{4-5}$$

where N = number of model layers between cloud top and cloud base, which is determined by the convection scheme.

There is no available reference for this formulation. It is assumed that the cloud fraction within a grid column is distributed randomly in space between model layers. Within each layer, clouds fill the grid cell uniformly in the vertical direction. The relationship is constant in time and space, and is used for each of the convection schemes available for use within RegCM3. Figure 4-4 illustrates the implications of the default formulation for convective cloud cover in RegCM3.

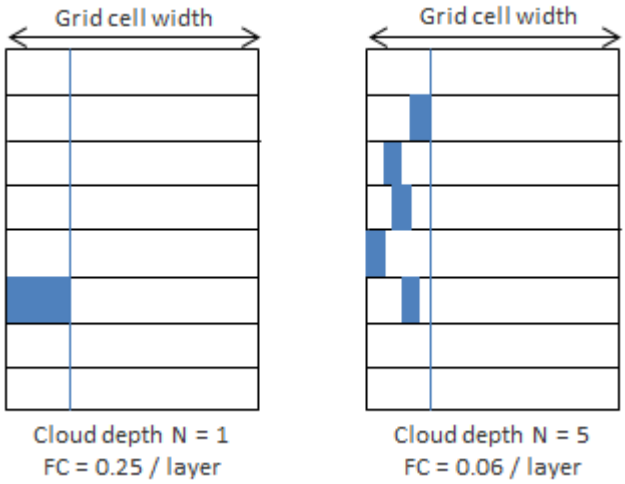

Figure 4-4. Schematic illustration of default calculation of convective cloud fraction within RegCM3. Left: the cloud fraction resulting from a simulated cloud that occupies one model layer. Right: the cloud fraction resulting from a simulated cloud that occupies five model layers.

The existing formulation in RegCM3 is problematic because it has no physical basis, arbitrarily restricts the cloud cover to a maximum extent of 0.25, regardless of model

resolution, and requires that each vertical layer within a column experiencing convective motion have the same fractional cloud cover. The cloud fraction is completely independent of the amount of simulated cloud liquid water (CLW). It does not allow clouds to vary their extent in the vertical in response to changes in CLW resulting from rainfall, evaporation and turbulent mixing within the column. The formulation also results in the unrealistic outcome that stronger convection produces smaller fractional cloud cover per grid cell than weaker convection, since deeper convective motion will result in a larger value of N and consequently smaller FC_{cnv} per layer.

Additionally, RegCM3 assigns a uniform value of the within-cloud CLW that is not physically realistic: 0.3 g m^{-3} for the Grell or Kuo convection schemes and 0.05 g m^{-3} for the Emanuel scheme. No distinction is made between CLW over land and over ocean. However, it has been observed that convective clouds contain CLW contents of around 1 g m^{-3} (e.g. Rogers and Yau 1989, Emanuel 1994, Rosenfeld and Lensky 1998), with some variation between maritime and continental clouds (shown in Section 4.3). Therefore the CLW parameters assigned in RegCM3 are considerably smaller than observations, particularly in the case of the Emanuel convection scheme, and do not show the appropriate spatial variability.

The impact of the existing representation of convective cloud cover can be examined by looking again at Figure 3-7, 3-8, 3-12 and 3-13. These figures showed the diurnal cycle of cloud cover using both the Grell and Emanuel convection schemes over land and ocean, for the default version of the model and with the modifications to the PBL.

Over land, simulation with the Emanuel scheme exhibits a distinct diurnal cycle in high cloud cover, with more cloud generated in the late afternoon and night-time, which is the product of daytime convection. Convective updrafts transport moisture into the upper atmosphere, where it detrains and is then added to the large-scale water vapor content. The increase in humidity is converted by the SUBEX routine into large-scale cloud cover. The simulation of high large-scale clouds at night is consistent with observations over the Maritime Continent, in which convective anvils and mesoscale convective systems (which can be thought of as a hybrid of convective and non-convective rainfall) persist throughout

the night over the islands (e.g. Ichikawa and Yasunari 2006, Ichikawa and Yasunari 2008). A diurnal signature is hard to discern with the Grell scheme since the daytime convection is much weaker and less moisture is transported aloft than with the Emanuel scheme.

The default Grell simulation produces low cloud cover in the afternoon, concomitant with convective activity, but it was discerned that this cloud is almost entirely large-scale cloud cover produced by the SUBEX routine and not convective cloud. Since convective mass flux is relatively weak with the Grell scheme, compared to the Emanuel scheme, some residual moisture builds up in the lower atmosphere during the day as a result of turbulent surface fluxes, which the SUBEX routine converts into cloud cover. But when the new simulation of large-scale clouds within the PBL is imposed, Figure 3-12 shows that much of the afternoon cloud disappears.

The cloud cover shown in Figures 3-12 and 3-13 is noticeable for lacking an appropriate representation of low and middle cloud cover associated with daytime convection. Specifically, lower atmosphere cloud is actually at a minimum when convective activity is strongest, in the early afternoon. This is due to the default convective cloud cover formulation in RegCM3. Cloud depth with the Emanuel scheme can be quite large – up to 10 layers – resulting in a cloud fraction of only 3% per model layer during the afternoon when convection is at its strongest. Even with the Grell scheme, a cloud depth of 5 layers is commonly simulated, resulting in a convective cloud fraction of around 5%.

Therefore these results illustrate the unphysical outcome that results from the default version of convective cloud fraction in RegCM3. Convection, although responsible for producing rainfall and transporting moisture aloft to form large-scale clouds, does not play a significant role in the formation of low and mid-level cloud cover. Strong convection, which in reality would produce thick clouds that block insolation, instead leads to less cloud and more insolation than weak convection. The model is missing an appropriate convective-radiative feedback.

4.3 A New Parameterization for Convective Cloud Fraction

To address the deficiencies in the current formulation of convective cloud fraction in RegCM3, a new formulation was developed. The ideas that form the basis of this work come

from Eltahir and Bras (1993), who developed a method to calculate the fractional coverage of rainfall in large-scale climate models based on observations of average rainfall intensity.

Eltahir and Bras (1993) compiled data from a number of convective storms in the tropics, subtropics and mid-latitudes to show that the relationship between rainfall volume and storm area is close to being linear. It was shown that the same relationship can be used to infer the storm area from the rainfall volume simulated by a climate model, if the average rainfall intensity at a given location is known from observations (Eltahir and Bras 1993). Similarly, a relationship can be derived that uses the CLW simulated by a climate model to infer the fractional area covered by a convective cloud, as follows.

When convective cloud forms over some fraction *FC* of a large area, in this case the grid cell of a large-scale climate model (GCM or RCM, where the size of the grid cell is much larger than the scale of an individual cumulus cloud), the distribution of CLW over that grid cell can be described by the following mixed distribution:

$$g_{CLW} = FC f_{CLW} + (1 - FC)\delta(CLW - 0) \quad (4\text{-}6)$$

where g_{CLW} = CLW over the total area, *FC* = fractional area of the grid cell covered with cloud, δ = Dirac delta function, and f_{CLW} = conditional probability density function (PDF) of the CLW within the cloud, given that CLW is greater than zero.

At this stage, no assumptions are made about the form of the PDF f_{CLW}. The observed form of f_{CLW} has been fitted to a lognormal distribution (Foster *et al*. 2006) and to a Weibull distribution (Iassamen *et al.* 2009), but this current work does not require the PDF to be explicitly specified. It is assumed that the mean of f_{CLW} is invariant in time. This assumption seems reasonable given that observations of CLW in convective clouds typically fall within a limited range, as shown in Table 4-2. The assumption of temporal invariance in the mean of f_{CLW} is an idealization and it is possible that the real mean will vary between cloud systems at the same location. The mean of the conditional PDF f_{CLW} is denoted by CLW_{clim} and may be geographically variable, taking a different value over land and ocean.

Table 4-2. Observations of cloud liquid water content used to calculate new convective cloud fraction.

Cumulus Cloud Type	Value	Location / Description	Reference
Continental	0.1 – 3 g m^{-3}	Java, Indonesia, influenced by land-derived aerosols	Rosenfeld and Lensky 1998
	1 g m^{-3}	Montana, USA	Rogers and Yau 1989
Maritime	0.25 – 1.3 g m^{-3}	Kwajalein Atoll, western Pacific Ocean	Rangno and Hobbs 2005
	0.4 – 1.2 g m^{-3}	Eastern Australian coast, warmer than freezing, 2000 – 10 000 ft deep	Warner 1955

The expected value of CLW, *E(CLW)*, over a model grid cell is given by:

$$E(CLW) = \int_{CLW=0}^{\infty} CLW\, g_{CLW}\, dCLW$$
$$= (1 - FC)0 + FC \int_{CLW=0^+}^{\infty} CLW\, f_{CLW}\, dCLW = CLW_{clim} FC \tag{4-7}$$

which implies that:

$$FC = \frac{E(CLW)}{CLW_{clim}} \tag{4-8}$$

The expected value of CLW, *E(CLW)*, can be taken as the simulated grid-average value of CLW, which is a prognostic variable in most large-scale climate models and will hereafter be denoted as $\overline{CLW}$. This leads to an expression for the fractional area of a model grid cell that is covered by convective cloud, FC_{cnv}:

$$FC_{cnv} = \frac{\overline{CLW}}{CLW_{clim}} \tag{4-9}$$

The observations in Table 4-2 suggest that $CLW_{clim} \approx 1.2$ g m^{-3} over land and $CLW_{clim} \approx 0.7$ g m^{-3} over ocean. It is noted that these values of CLW_{clim} are chosen from within an observed range; there is some flexibility in the choice of these values that could be explored by the model user.

The new formulation has three major advantages over the existing representation of convective cloud cover in RegCM3:

1. the simulated cloud cover is linked explicitly to the simulated CLW and is also tied to physically-observed CLW;
2. it recognizes the subgrid variability in CLW that exists in reality and should be accounted for in the model; and
3. only one parameter requires specification to implement this function into RegCM3: CLW_{clim}, which can be taken from observational data, making it easy to implement consistently across different convection schemes.

The new formulation is therefore more physically realistic than the existing scheme in RegCM3 and it is independent of specific model user decisions, like model domain and grid cell resolution.

Both Xu and Randall (1996) and Bony and Emanuel (2001) have noted that local, cloud-scale microphysical processes (such as transformations between water species) should be formulated within models in terms of the local concentrations, rather than grid-cell averaged concentrations. To the first order, these local concentrations are equal to the grid-cell averaged concentrations divided by the cloud amount (Xu and Randall 1996; Bony and Emanuel 2001). The formulation for convective cloud cover presented here is consistent with this reasoning. It is also conceivable that the same formulation could be applied to represent the fractional coverage within a grid cell of different hydrometeor species (e.g. liquid raindrops, ice crystals, graupel), should they be simulated separately within a given model's microphysical parameterization.

4.4 Performance of New Parameterization for Convective Cloud Fraction

Simulations were run using RegCM3-IBIS to test the impact of the new convective cloud cover. The new formulation for FC_{cnv}, using CLW_{clim} = 1.2 g m^{-3} for land and CLW_{clim} = 0.7 g m^{-3} for ocean, replaced the existing function for FC_{cnv}. These values for CLW_{clim} were also used to replace the default values of within-cloud CLW (which were 0.3 g m^{-3} for the Grell scheme and 0.05 g m^{-3} for the Emanuel scheme). Domain set up, initial and boundary conditions were identical to those described in Chapters 2 and 3.

Datasets used for comparison include the TRMM rainfall products, SRB radiative fluxes, turbulent LH and SH fluxes and ISCCP cloud cover, described in Chapters 2 and 3. When comparing the model output of fractional cloud cover to the ISCCP, the model output was aggregated in the vertical assuming random overlap of clouds between layers, using layers 2-8 (roughly 760-1000 mb) for the low clouds, layers 9-12 (roughly 450-700 mb) for the middle clouds, and 13-17 (roughly 100-400 mb) for the high clouds.

CLW simulated by the model was compared to observations taken from the CloudSat Radar-Only Cloud Water Content Product Version 2 (2B-CWC-RO; Austin 2007). CloudSat is a NASA Earth Sciences System Pathfinder mission and flies as part of the A-Train constellation of satellites. The satellite produces 1.3 km-wide swaths and repeats the same track every 16 days. Cloud water content profiles are available with a vertical resolution of approximately 240 m, beginning in 2006. CloudSat retrievals are performed separately for the liquid and ice phases and then combined to obtain a composite profile. However, RegCM3 only simulates the cloud liquid water content at all elevations. Therefore the single model output of cloud liquid water profile is compared to the combined CloudSat liquid and ice profile.

The CloudSat product is not available as a gridded product. Therefore to directly compare the model to the observations, two 1^{o} x 1^{o} boxes were chosen – over central Borneo and over the western Pacific Ocean. The Pacific Ocean grid box was chosen as representative of a maritime environment with limited influence of the regional islands (compared to the South China Sea, for example). Unfortunately, the CloudSat swaths do not pass over the island of Singapore, so that location could not be chosen for comparison to the other Singapore-based datasets used in this thesis. Therefore a mountainous region of Borneo was chosen as representative of a large island that experiences all the observed land-based dynamics of this region. Model output and satellite swath data were averaged to produce mean cloud water profiles for each box. The range of available data for 2006-2011 from CloudSat was screened and only the pixels with good quality data flags were used. The satellite flies over the model domain within two defined windows: a ‘daytime’ window of 11 am-2:30 pm and a ‘night-time’ window of 11 pm-2:30 am. An average profile was calculated for each flyover window over the 2006-2011 period. A total of 23,000 pixels within the 1^{o} x

1^{o} box were used for analysis, of which 8000 were during the day and 15,000 were at night. Similarly, a time-averaged profile was calculated from the model output for the simulation period 1998-2001, using the output times corresponding to the flyover windows. Although the two analysis periods do not overlap, it is considered that the average profile of cloud water should be similar enough between these periods to merit a qualitative comparison.

It is very important to note that the CloudSat data is only from satellite overpasses in which there was no precipitation recorded, since the presence of any significant precipitation violates the assumptions of the retrieval algorithms (Austin 2007). However, RegCM3 generates convective cloud water only when the convection scheme is activated, which is more than likely to produce rainfall. Therefore it is impossible to separate the model output of cloud water into raining and non-raining times if simulated convective cloud water is desired. Hence the simulated CLW is likely to be biased towards higher values than would be expected if only non-raining CLW values were used.

4.4.1 Cloud Fraction

The time-mean horizontal fractional cloud cover simulated by RegCM3-IBIS for the period 1998-2001 is compared to the ISCCP data in Figure 4-5, Figure 4-6 and Figure 4-7 for the low, mid-level and high cloud categories respectively. The figures compare the default version of the RegCM3-IBIS model, modified version of the model (including all changes made in Chapter 3) and model with new FC_{cnv} as described in this chapter (including all changes made in Chapter 3), for both the Grell with Fritsch-Chappell (GFC) and Emanuel convection schemes (EMAN).

The default simulations (GFC and EMAN) and the simulations modified as in Chapter 3 (GFC-Mod and EMAN-Mod) all overestimate low cloud cover compared to ISCCP. The bias is smaller with the modified simulations compared to the default ones due to the new simulation of large-scale cloud formation within the PBL region, as described in Chapter 3. Average middle cloud fraction shows a small underestimation by the default and modified simulations, and again the modified simulations improve upon the default ones by reducing the underestimation bias. High cloud cover is overestimated by all the default and modified simulations, although with very small bias in the default simulation using GFC.

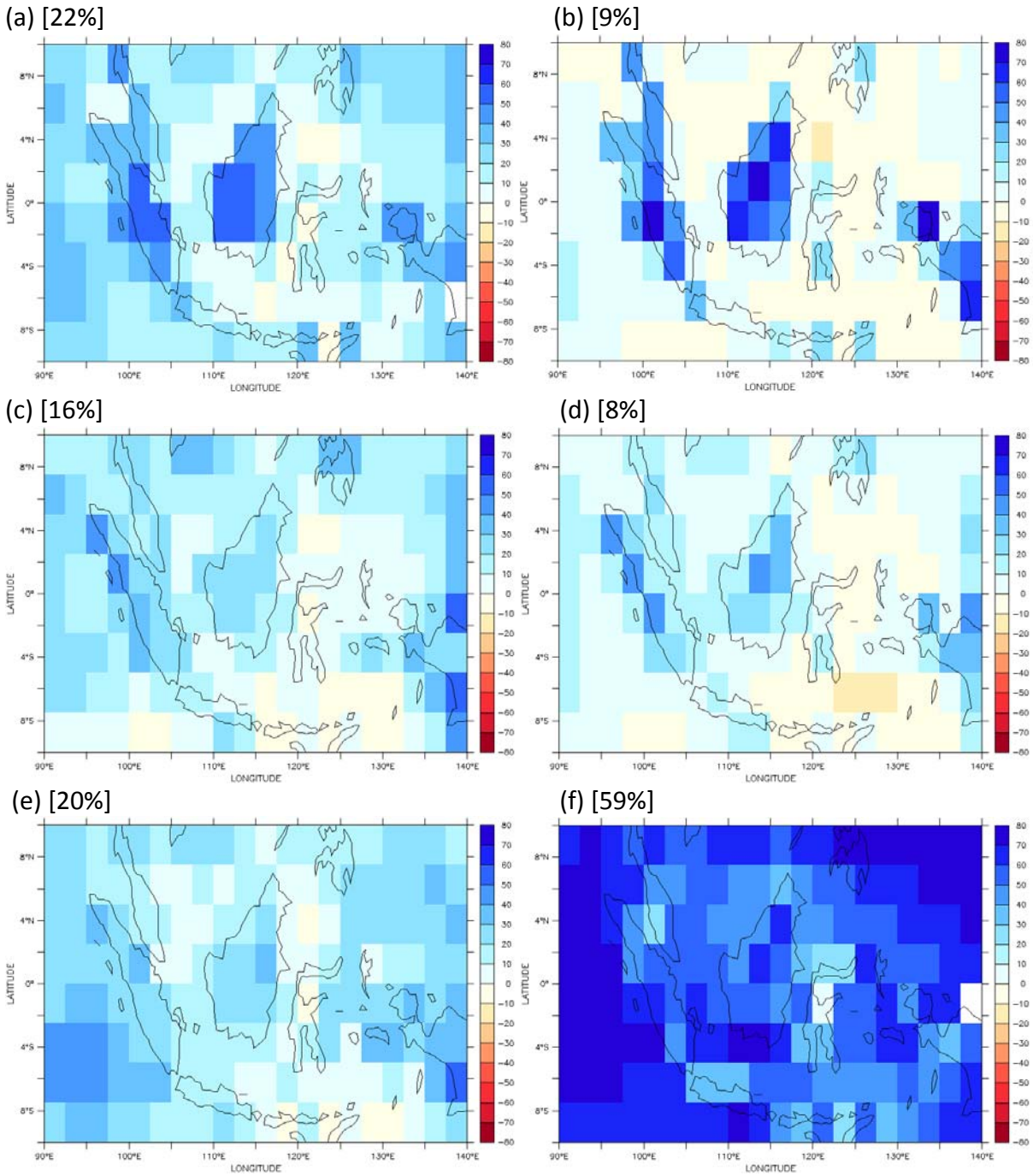

Figure 4-5. Average low cloud fraction for 1998-2001: simulation minus ISCCP data for (a) GFC (default model), (b) EMAN (default model), (c) GFC-Mod (as in Chapter 3), (d) EMAN-Mod (as in Chapter 3), (e) GFC-New (with new FC_{cnv}) and (f) EMAN-New (with new FC_{cnv}). Domain-averaged error (model – ISCCP cloud fraction) is shown in parentheses. Color bar indicates fractional coverage of grid cell.

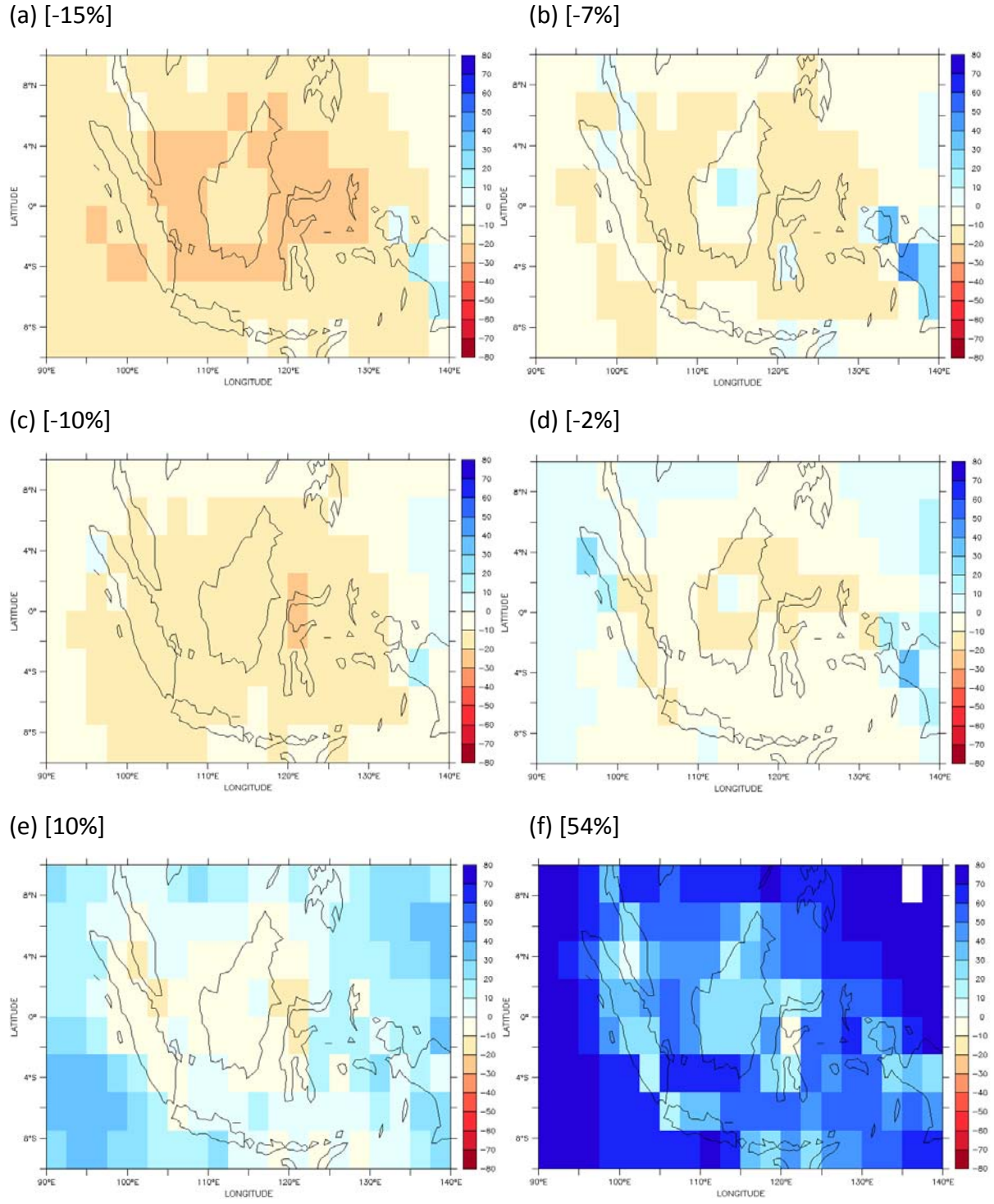

Figure 4-6. Average middle cloud fraction for 1998-2001: simulation minus ISCCP data for (a) GFC (default model), (b) EMAN (default model), (c) GFC-Mod (as in Chapter 3), (d) EMAN-Mod (as in Chapter 3), (e) GFC-New (with new FC_{cnv}) and (f) EMAN-New (with new FC_{cnv}). Domain-averaged error (model – ISCCP cloud fraction) is shown in parentheses. Color bar indicates fractional coverage of grid cell.

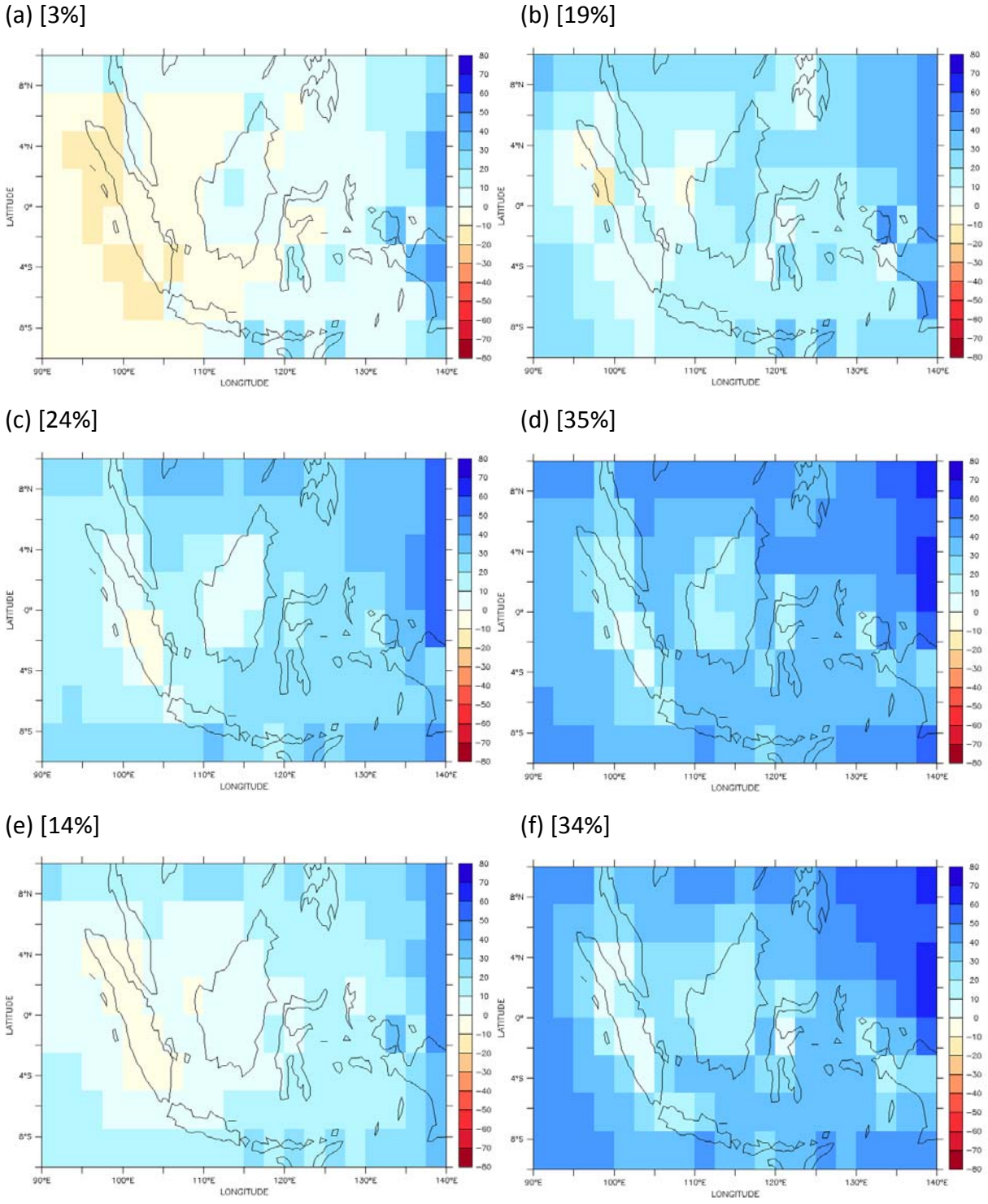

Figure 4-7. Average high cloud fraction for 1998-2001: simulation minus ISCCP data for (a) GFC (default model), (b) EMAN (default model), (c) GFC-Mod (as in Chapter 3), (d) EMAN-Mod (as in Chapter 3), (e) GFC-New (with new FC_{cnv}) and (f) EMAN-New (with new FC_{cnv}). Domain-averaged error (model – ISCCP cloud fraction) is shown in parentheses. Color bar indicates fractional coverage of grid cell.

In the default and modified simulations, the Emanuel scheme shows less error in cloud fraction at low and middle levels but worse error at high levels than the Grell scheme. This is due to the nature of RegCM3's default formulation for convective cloud cover. The Emanuel scheme produces stronger convective updraft mass flux than the Grell scheme, resulting in a deeper cloud and therefore smaller FC_{cnv} per model layer. The Emanuel scheme also transports more moisture to the upper atmosphere, which translates into more cloud produced by the SUBEX scheme at high altitudes.

The figures show that the new convective cloud cover formulation had substantially different impacts with the two convection schemes.

With the Grell Fritsch-Chappell scheme, low cloud cover increased by about 4% and high cloud cover decreased by about 10%, while middle cloud cover increased by about 20%. This removed the previous underestimation bias at middle levels compared to ISCCP and instead created an overestimation bias of the same magnitude.

In stark contrast, the new simulation using the Emanuel scheme results in significant increases of about 50% in cloud fraction across the model domain, producing a substantial overestimate of cloud cover compared to the ISCCP data. High cloud cover did not change significantly, retaining a significant overestimation bias compared to ISCCP.

These results highlight that the Emanuel scheme produces much more CLW, as the result of a stronger convective mass flux, than the Grell scheme. Hence when the simulated CLW is used to calculate the convective cloud cover, the Emanuel scheme produces much greater fractional cloud area than the Grell scheme. That the cloud cover with the Grell scheme did not change as much in the new simulation as with the Emanuel scheme suggests that the default formulation for cloud cover in RegCM3 had been a relatively reasonable estimate for the cloud cover produced by the Grell scheme.

To look at the vertical cloud structure with higher resolution, Figure 4-8 and Figure 4-9 show the mean diurnal cycle of the cloud cover profile over land for the period 1998-2001, respectively for the Grell Fritsch-Chappell and Emanuel schemes, and Figure 4-10 and Figure 4-11 show the same profiles for ocean.

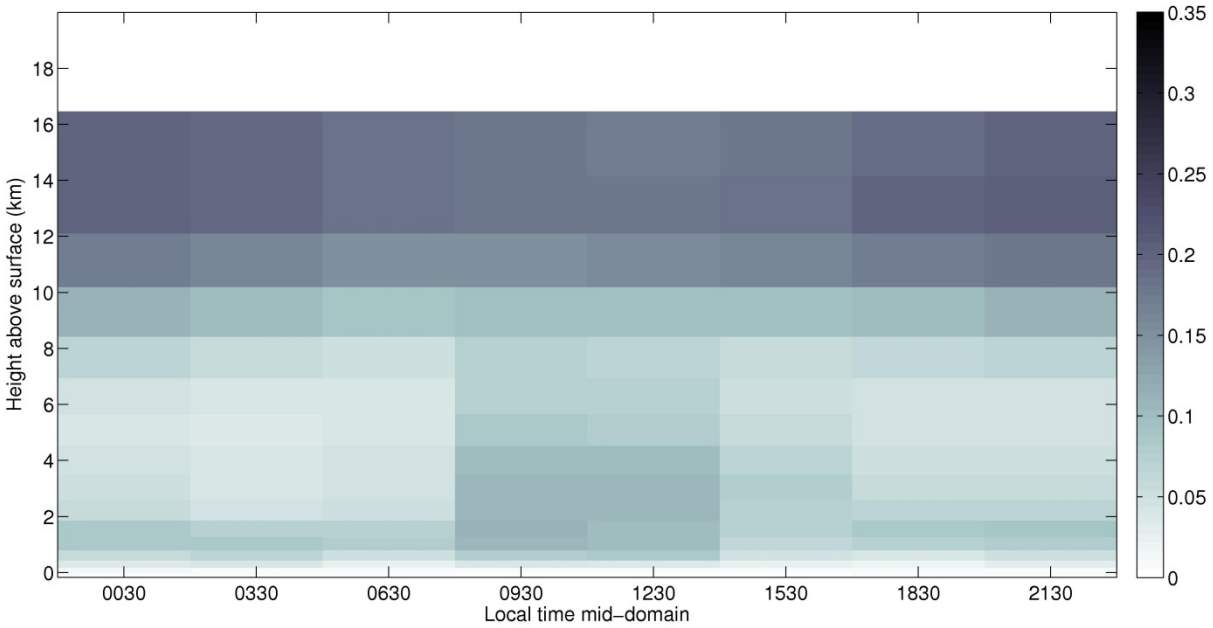

Figure 4-8. Average diurnal cycle of cloud cover over land 1998-2001 using Grell Fritsch-Chappell scheme with new convective cloud fraction and modifications from Chapter 3. Color bar indicates fractional coverage of grid cell.

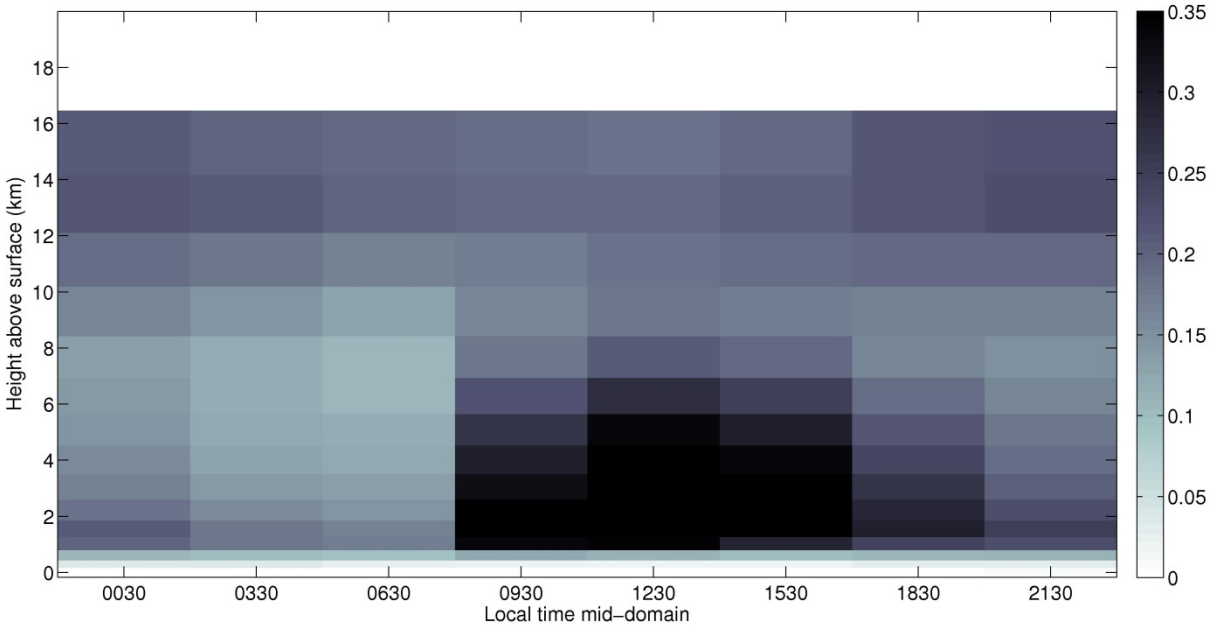

Figure 4-9. Average diurnal cycle of cloud cover over land 1998-2001 using Emanuel scheme with new convective cloud fraction and modifications from Chapter 3. Color bar indicates fractional coverage of grid cell.

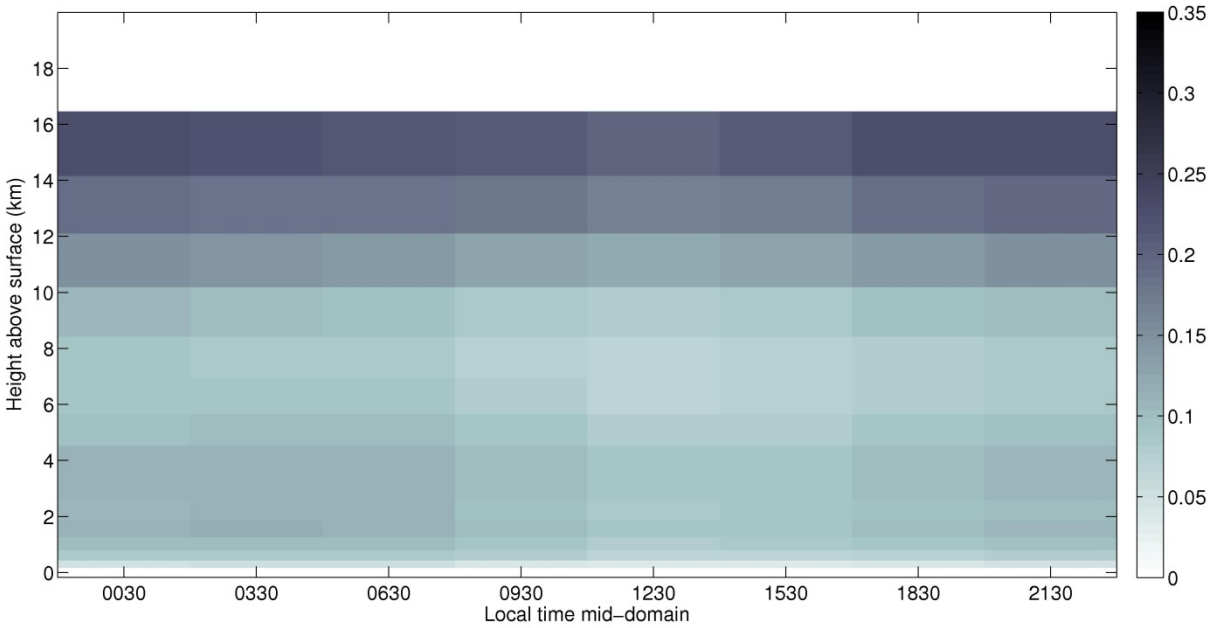

Figure 4-10. Average diurnal cycle of cloud cover over ocean 1998-2001 using Grell Fritsch-Chappell scheme with new convective cloud fraction and modifications from Chapter 3. Color bar indicates fractional coverage of grid cell.

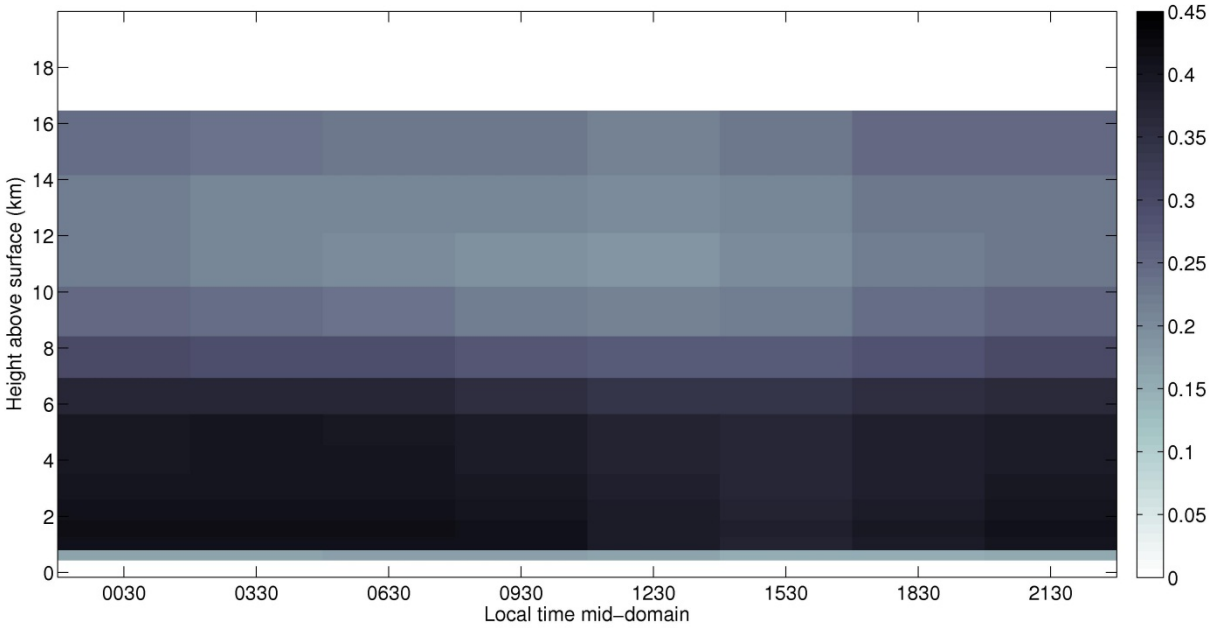

Figure 4-11. Average diurnal cycle of cloud cover over ocean 1998-2001 using Emanuel scheme with new convective cloud fraction and modifications from Chapter 3. Color bar indicates fractional coverage of grid cell. Note the change to the color bar range.

These figures illustrate the substantial changes made to the vertical structure of cloud cover compared to the cloud cover presented in Chapter 3.

Over land, the presence of convective motion is clearly visible, with cloud simulated in the 9:30 am – 3:30 pm window approximately 2-8 km above the surface. This cloud is in the precise location that we would expect to see cumulus clouds resulting from daytime convection, indicating that the new formulation is working as intended. The cloud is significantly denser and more prolonged when using the Emanuel scheme than the Grell scheme, which can be attributed to the stronger convective updrafts and greater volumes of condensate produced with the Emanuel scheme. Although there was only a modest change to time-averaged cloud cover over land with the Grell scheme, Figure 4-8 shows that the diurnal timing of the cloud cover shifted significantly from a maximum at night to a maximum in the afternoon with the new convective cloud cover.

Over ocean, both simulations still exhibit a very muted diurnal cycle of cloud cover, similarly to the previous simulations. The new simulation with the Grell Fritsch-Chappell scheme shows a small increase in the low-to-mid-level cloudiness throughout the day compared to the previous simulation. The new simulation with the Emanuel scheme shows a significant increase in cloudiness throughout the lower half of the atmosphere, which again can be attributed to the stronger convective flux associated with this scheme.

4.4.2 Cloud Water Content

Figure 4-12 and Figure 4-13 compare the simulated CLW to the cloud water content measured by CloudSat for the central Borneo and western Pacific Ocean grid boxes. Note that the CLW profiles plotted for each simulation represent the radiatively-active CLW, i.e. the CLW 'seen' by the radiation scheme within RegCM3. The simulations designated GFC-Mod and EMAN-Mod refer to those presented in Chapter 3, containing modifications to the PBL region. The default simulations are not shown since they are very similar to the simulations GFC-Mod and EMAN-Mod.

(a)

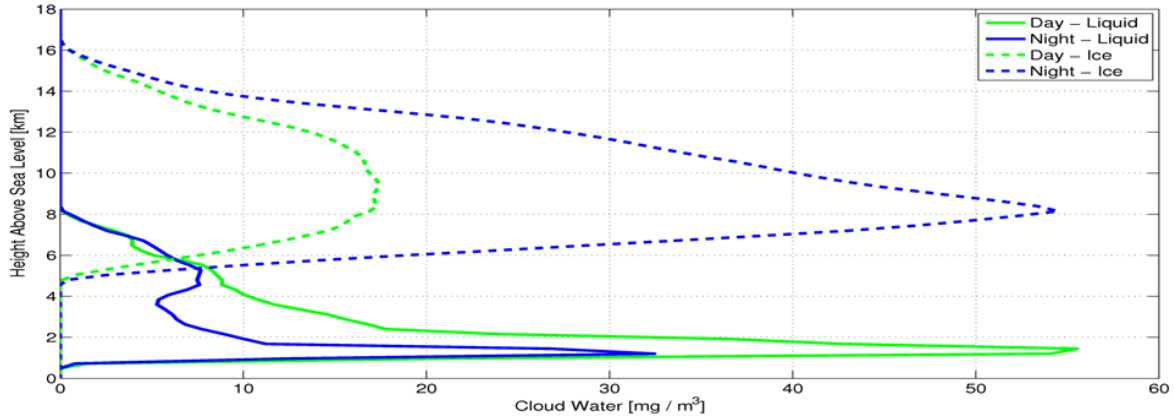
Day – Liquid
Night – Liquid
Day – Ice
Night – Ice
Height Above Sea Level [km]
Cloud Water [mg / m3]

(b)

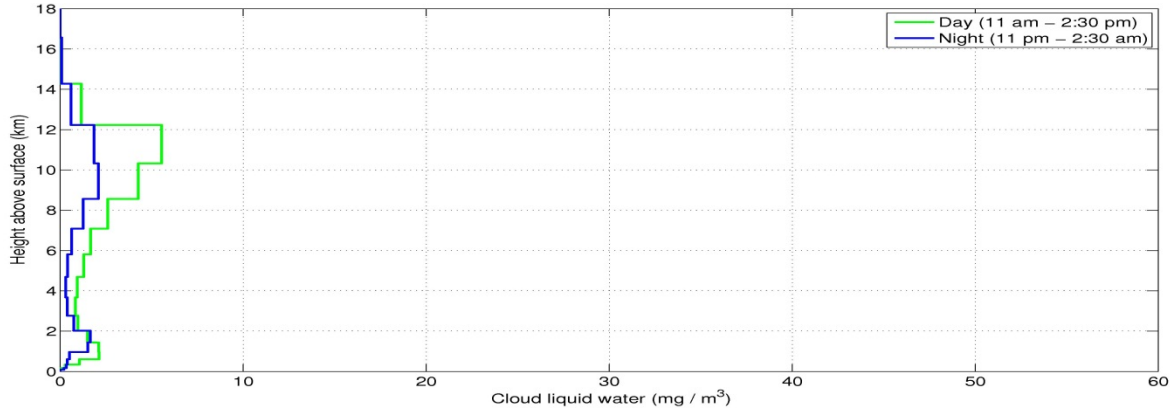
Day (11 am – 2:30 pm)
Night (11 pm – 2:30 am)
Height above surface (km)
Cloud liquid water (mg / m3)

(c)

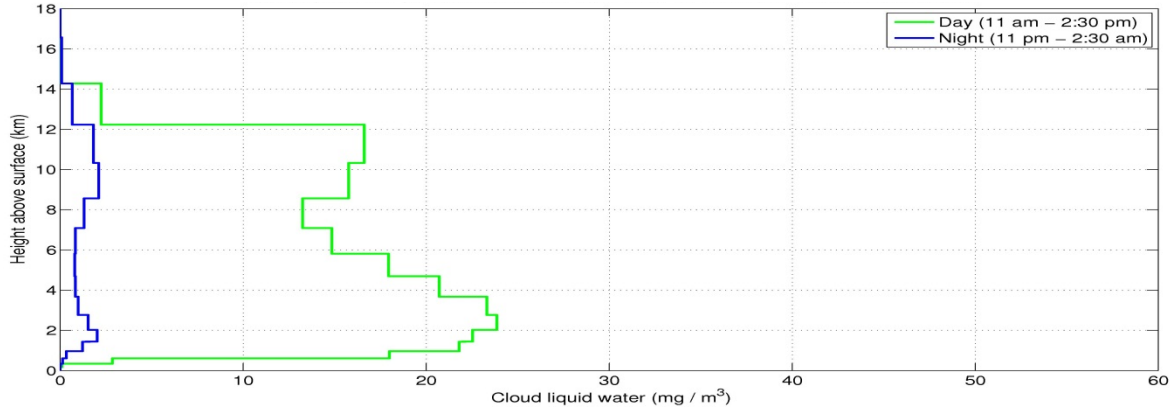
Day (11 am – 2:30 pm)
Night (11 pm – 2:30 am)
Height above surface (km)
Cloud liquid water (mg / m3)

(d)

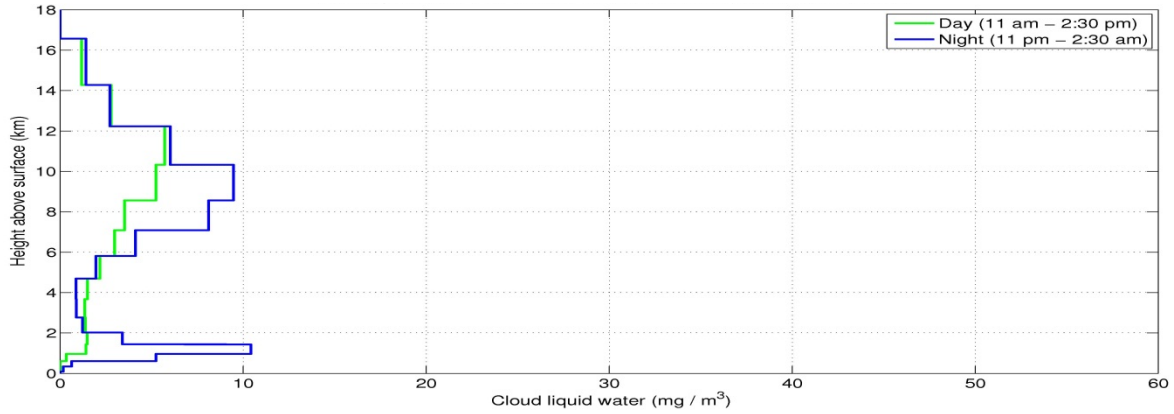

(e)

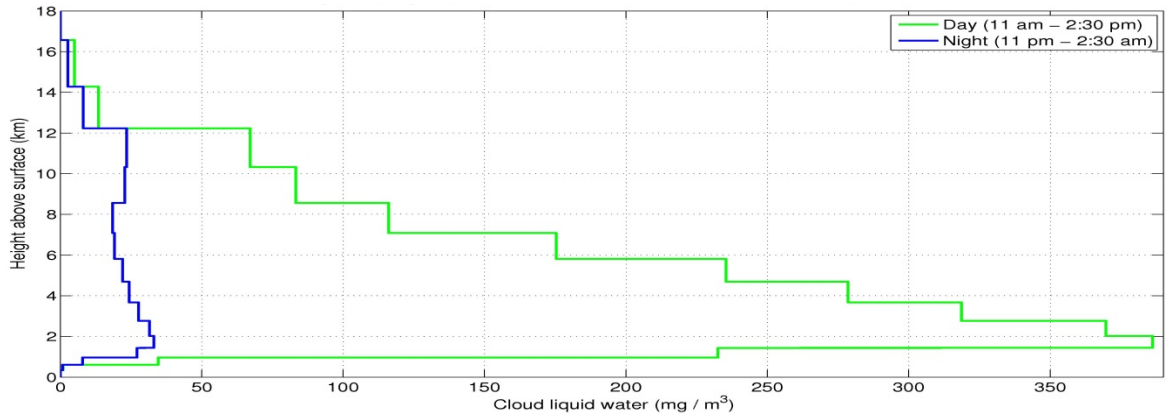

Figure 4-12. Average cloud liquid water (in mg m^{-3}) profile over central Borneo for (a) CloudSat averaged over period 2006-2011, (b) GFC-Mod, (c) GFC-New, (d) EMAN-Mod, (e) EMAN-New (note the change in x-axis). All simulations are averaged over the period 1998-2001.

(a)

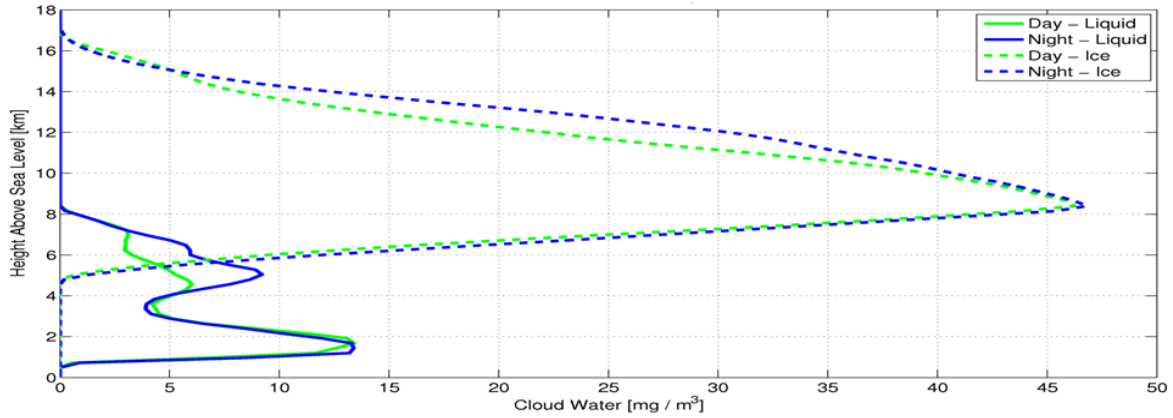
Day – Liquid
Night – Liquid
Day – Ice
Night – Ice
Height Above Sea Level [km]
Cloud Water [mg / m3]

(b)

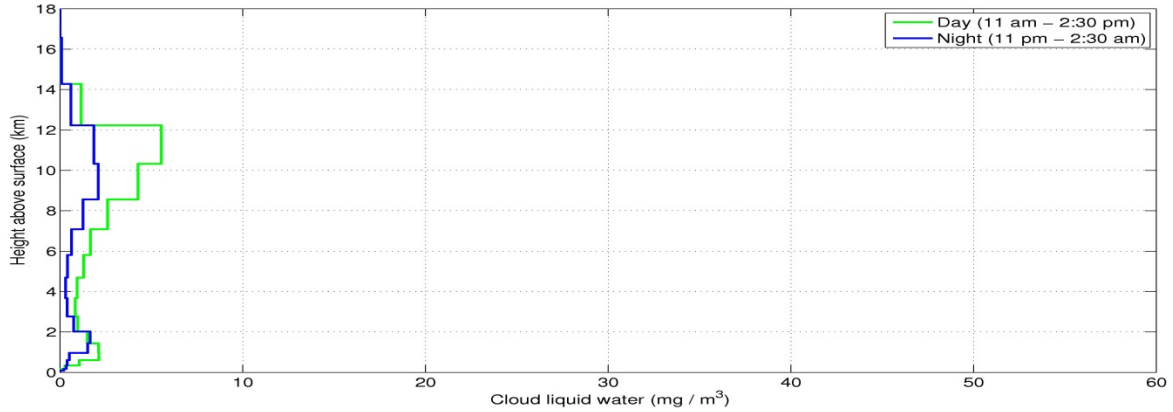
Day (11 am – 2:30 pm)
Night (11 pm – 2:30 am)
Height above surface (km)
Cloud liquid water (mg / m3)

(c)

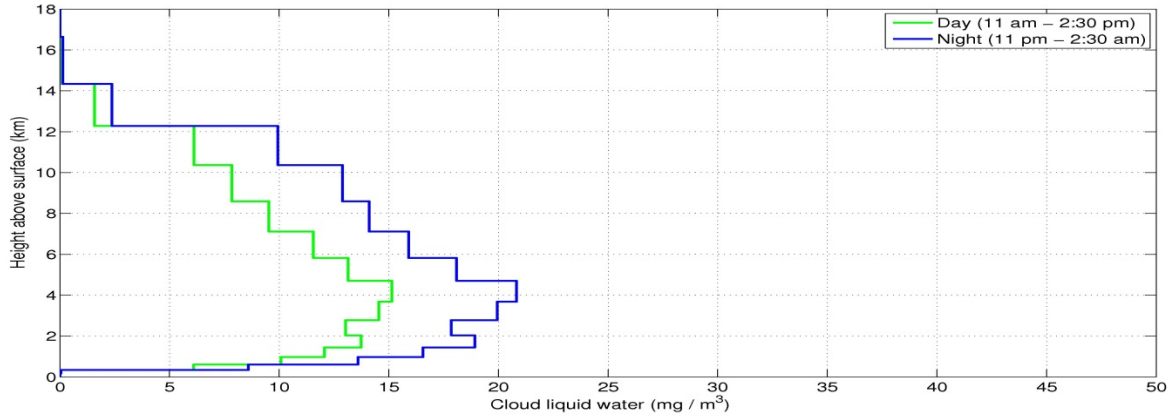
Day (11 am – 2:30 pm)
Night (11 pm – 2:30 am)
Height above surface (km)
Cloud liquid water (mg / m3)

(d)

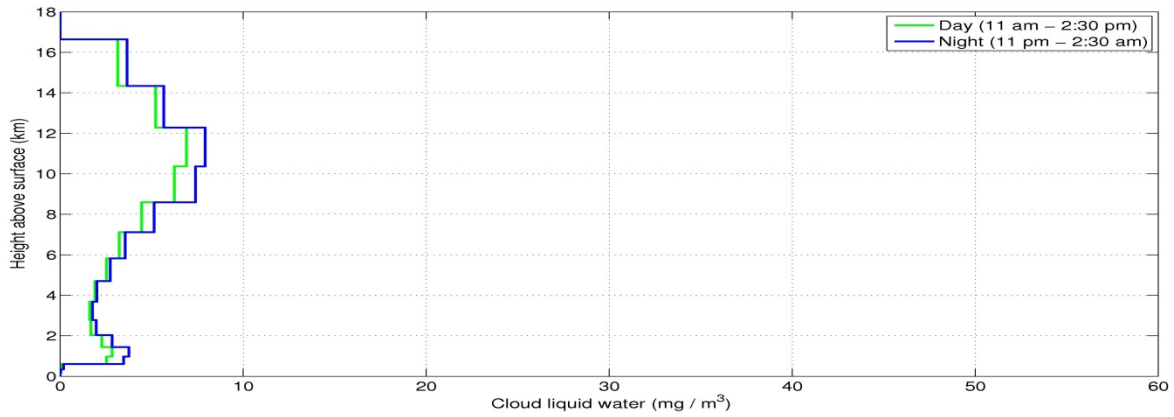

(e)

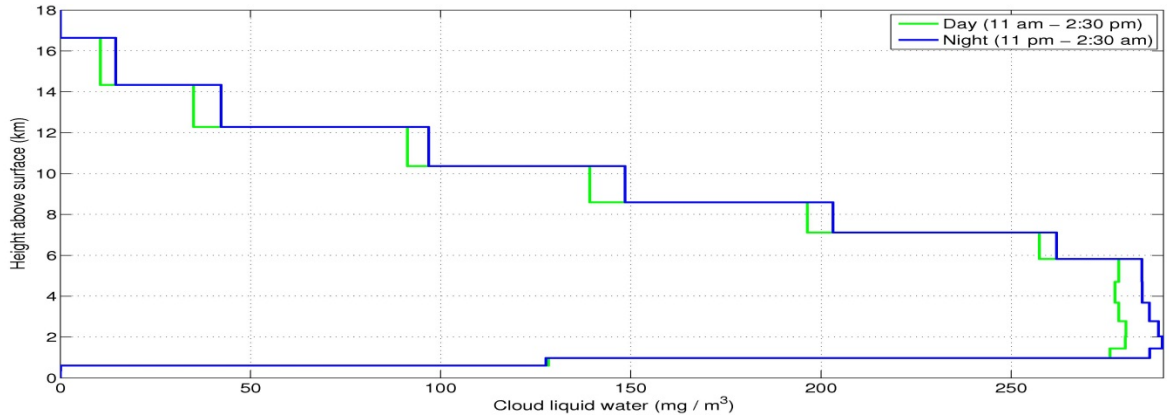

Figure 4-13. Average cloud liquid water (in mg m^{-3}) profile over western Pacific Ocean for (a) CloudSat averaged over period 2006-2011, (b) GFC-Mod, (c) GFC-New, (d) EMAN-Mod, (e) EMAN-New (note the change in x-axis). All simulations are averaged over the period 1998-2001.

The CloudSat data show distinctly different profiles of cloud water content from day to night and between land and ocean. Over central Borneo, there is a strong diurnal cycle that reflects daytime convection: midday cloud water content is heavily weighted towards the lower atmosphere, around 1-2 km, while at midnight there is more cloud water higher up around 8-12 km. On the other hand, there is virtually no diurnal cycle in cloud water content over the western Pacific Ocean: both day and night have much more cloud water in the higher atmosphere than in the lower atmosphere, and the magnitudes are comparable from day to night. This observation is consistent with the lack of a strong diurnal amplitude in rainfall observations.

There are significant model errors associated with the simulation of cloud water content in both versions of the model presented in the figures above.

Over central Borneo, both GFC-Mod and EMAN-Mod significantly underestimate the amount of CLW at both high and low elevations compared to CloudSat. During the daytime, the model error is worse in the low 1-2 km elevation range, while at night the model error is substantial at both low and high altitudes. EMAN-Mod exhibits less error at night than GFC-Mod because daytime convection with the Emanuel scheme results in more residual moisture throughout the column, which can be condensed by the SUBEX routine at night.

Over the western Pacific Ocean, GFC-Mod and EMAN-Mod simulate similar quantities of CLW for day and night, reflecting the observed lack of a strong diurnal cycle. However, the simulations significantly underestimate the magnitude of CLW, especially in the high 8-12 km range.

All of these underestimation errors are particularly worrisome given that the model output includes times of active convection and therefore would be expected to exceed the CloudSat data, in which no raining times appear.

With GFC-New and EMAN-New, daytime CLW is substantially increased over both central Borneo and the Pacific Ocean. In the main convective region 2-8 km above the surface, daytime CLW increases by a factor of 10 with GFC-New, from negligible quantities to 10-20 mg m^{-3}, while daytime CLW increases by a factor of 100 with EMAN-New, from about 3.5 mg m^{-3} to a maximum of 380 mg m^{-3} over Borneo and 280 mg m^{-3} over the Pacific Ocean. The daytime high-level CLW, above 8 km, also increases substantially with both schemes. The increased CLW improves the model performance with GFC-New but creates a significant overestimate with EMAN-New. These results illustrate the impact of changing the within-cloud value of CLW in RegCM3 from the default values to physically-realistic ones. Given the overestimation with the Emanuel scheme, it is likely that the default value of within-cloud CLW used in RegCM3 with this scheme was tuned to an unreasonably low value to reduce this simulated CLW.

There is less impact on the night-time CLW over central Borneo: it is about the same in GFC-New, while night-time CLW approximately doubles with EMAN-New. The night-time

CLW is created by the large-scale SUBEX routine, so these results suggest that there is little change to the grid-averaged moisture with GFC-New but an increase in the grid-averaged moisture with EMAN-New due to residual moisture left behind by the daytime convection.

Over the Pacific Ocean, night-time CLW increases by the about the same magnitude as daytime CLW with GFC-New and EMAN-New, such that the end result is little diurnal distinction in CLW. Again, the increase in simulated CLW improves the model performance in GFC-New but creates a significant overestimate of CLW with EMAN-New.

4.4.3 Radiative and Turbulent Heat Fluxes

Figure 4-14, Figure 4-15, Figure 4-16 and Figure 4-17 show the average diurnal cycle of incoming solar radiation (insolation) reaching the surface over land and ocean with both the Grell and Emanuel schemes, comparing the new simulations (with new convective cloud cover and CLW) to the modified simulations (from Chapter 3). The simulated radiative fluxes are compared to the SRB observations. Mean daily values are given in parentheses.

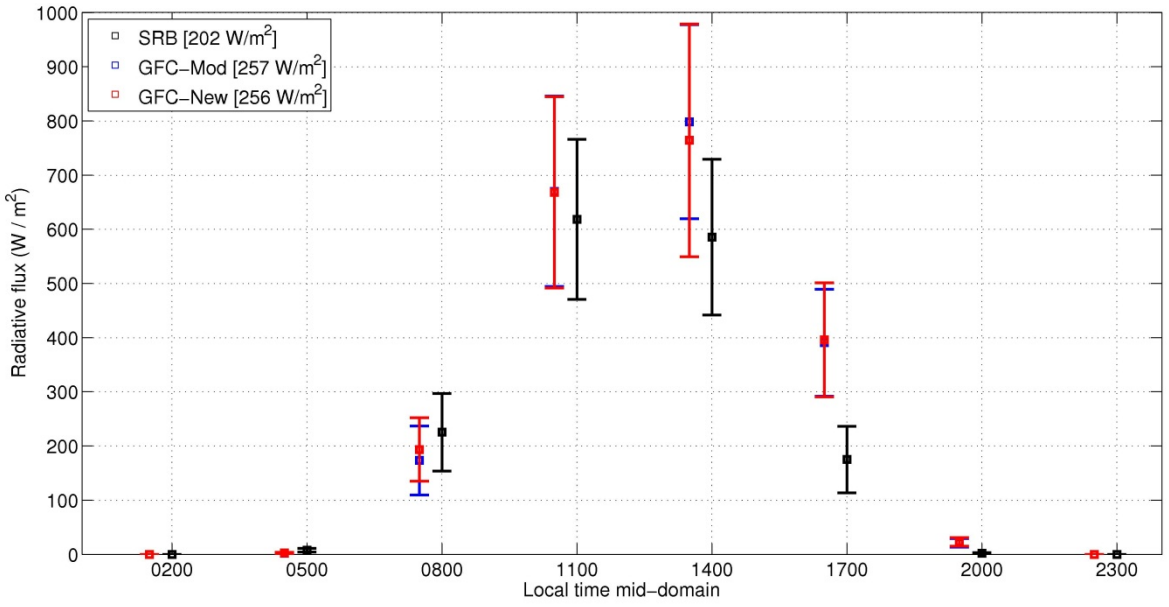

Figure 4-14. Diurnal cycle of insolation (in W m^{-2}) averaged over land for period 1998-2001, from SRB observations and simulations using Grell Fritsch-Chappell scheme with modifications from Chapter 3 (GFC-Mod), and with new convective cloud cover (GFC-New). Square symbol indicates the mean value; error bars indicate +/- 1 standard deviation.

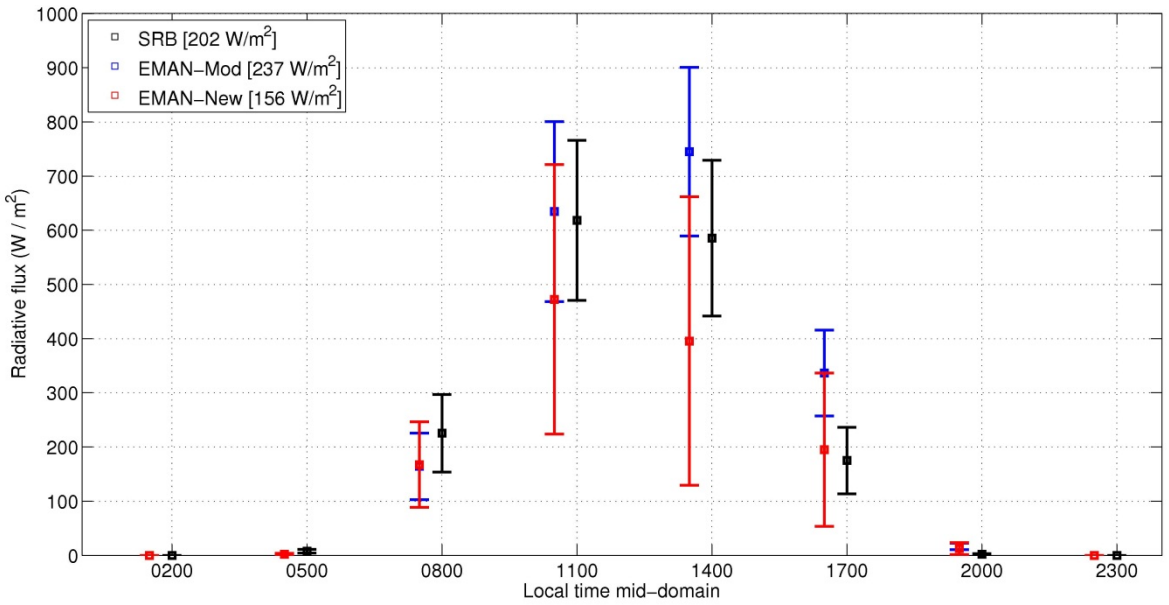

Figure 4-15. Diurnal cycle of insolation (in W m^{-2}) averaged over land for period 1998-2001, from SRB observations and simulations using Emanuel scheme with modifications from Chapter 3 (EMAN-Mod), and with new convective cloud cover (EMAN-New). Square symbol indicates the mean value; error bars indicate +/- 1 standard deviation.

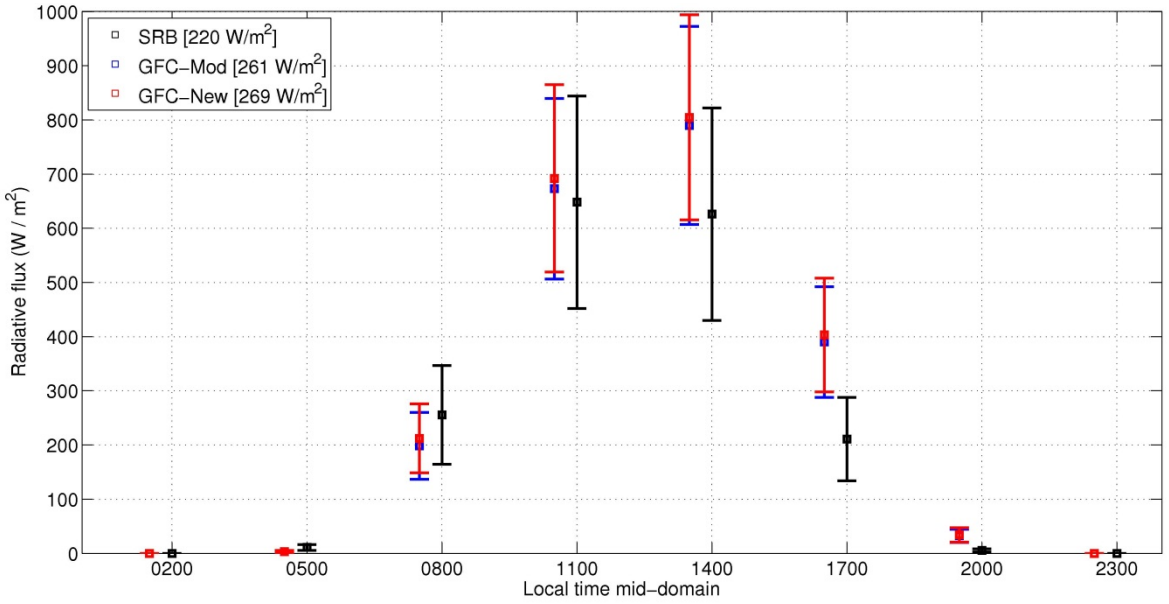

Figure 4-16. Diurnal cycle of insolation (in W m^{-2}) averaged over ocean for period 1998-2001, from SRB observations and simulations using Grell Fritsch-Chappell scheme with modifications from Chapter 3 (GFC-Mod), and with new convective cloud cover (GFC-New). Square symbol indicates the mean value; error bars indicate +/- 1 standard deviation.

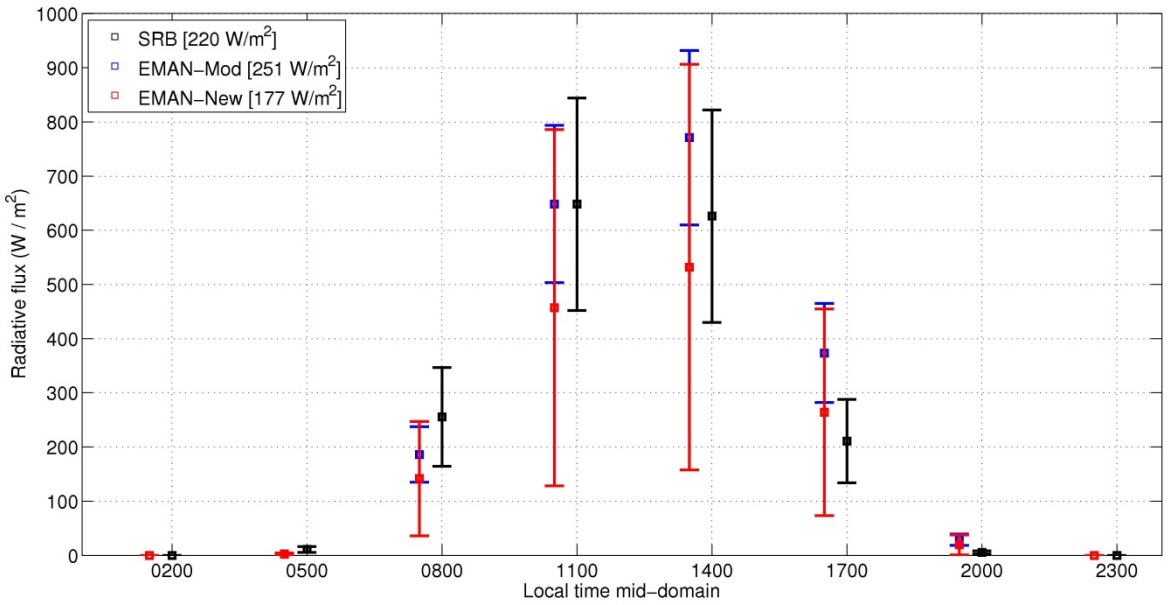

Figure 4-17. Diurnal cycle of insolation (in W m^{-2}) averaged over ocean for period 1998-2001, from SRB observations and simulations using Emanuel scheme with modifications from Chapter 3 (EMAN-Mod), and with new convective cloud cover (EMAN-New). Square symbol indicates the mean value; error bars indicate +/- 1 standard deviation.

As was shown in Chapter 3, the default cloud cover in RegCM3 results in significant overestimation of insolation over both land and ocean. Crucially, the error is primarily due to an overestimation of the early and mid-afternoon radiation. These results are consistent with the lack of cloud cover produced in the default model during daytime convection. They illustrate that the default cloud fraction does not allow the model to produce a convective-radiative feedback. In this feedback, daytime convection would be activated by radiative heating of the surface, creates cumulus clouds that reflect and absorb solar radiation, and thereby reduces the amount of radiation that reaches the surface in the afternoon.

The new parameterization for convective cloud cover allows the model to simulate a convective-radiative feedback by producing clouds in direct response to convective activity. However, the results show that the changes to cloud cover had very different impacts on the diurnal cycle of insolation using the two convection schemes.

With the Grell Fritsch-Chappell scheme, insolation changed negligibly over land and increased slightly over ocean, perpetuating a significant overestimation in insolation. This result reflects the lack of significant change to cloud cover with this scheme.

In contrast, insolation substantially decreased with the Emanuel scheme over both land and ocean, resulting in significant underestimation compared to SRB. The biggest decrease in insolation occurs in the early afternoon, due to the increased convective cloud cover. Over land, this changes the shape of the diurnal cycle of insolation, producing a late morning peak similar to the SRB observations.

Hence the results indicate that the new convective cloud fraction allows for simulation of a convective-radiative feedback. Clearly the magnitude of this feedback is over-exaggerated with the Emanuel scheme, but the changes to cloud cover and radiation with this scheme are consistent with the strength of the simulated convective motion, thereby making the model more internally consistent. That the cloud cover and radiation did not change significantly with the Grell scheme indicates that the default cloud cover had fortuitously (likely through parameter tuning) produced cloud cover that was of a comparable magnitude to the amount actually created by the scheme. Despite the lack of change with this scheme, it is considered that the new model is an improvement due to its increased internal consistency and physical realism, which should allow the model to respond more appropriately to large-scale forcings.

Changes to the surface net radiation and turbulent heat fluxes are summarized in Table 4-3.

Table 4-3 shows that changes to net radiation were consistent with the changes to insolation. Over land, net radiation decreased only slightly with the Grell scheme but decreased significantly with the Emanuel scheme. Over ocean, net radiation increases slightly with the Grell scheme but again decreases significantly with the Emanuel scheme.

The Grell scheme shows a small decrease in planetary albedo over both land and ocean due to the reduction in high cloud cover, while the Emanuel scheme shows no change in planetary albedo since the high cloud cover also showed negligible change. These results

with the planetary albedo indicate the strong influence of the high cloud cover and insignificance of the low cloud cover on simulated albedo within RegCM3.

The model simulates longwave radiation reasonably well – mean daily values of longwave radiation both down to the surface and up from the surface are within 15 W m^{-2} (4%) of observations over land and ocean.

Table 4-3. Average daily surface radiative and turbulent heat fluxes (all in W m^{-2}) over period 1998-2001 for SRB (radiative fluxes) and field studies (LH and SH) ('Observations') and simulations using the modifications from Chapter 3 ('-Mod') and new convective cloud fraction and CLW ('-New').

LAND

Simulation	SW_{dn}	SW_{up}	SW_{net}	Surface albedo	Planetary albedo	LW_{dn}	LW_{up}	R_N	LH	SH
Observations	*202*	*31*	*171*	*16%*	*48%*	*411*	*452*	*129*	*95*	*34*
GFC-Mod	257	35	222	14%	44%	401	459	164	118	48
GFC-New	256	35	221	13%	41%	396	457	160	112	50
EMAN-Mod	237	33	204	14%	49%	409	456	157	137	21
EMAN-New	156	21	135	13%	49%	414	459	90	68	23

OCEAN

Simulation	SW_{dn}	SW_{up}	SW_{net}	Surface albedo	Planetary albedo	LW_{dn}	LW_{up}	R_N	LH	SH
Observations	*220*	*14*	*206*	*6%*	*45%*	*420*	*467*	*158*	*109*	*10*
GFC-Mod	261	16	245	6%	43%	413	473	184	128	15
GFC-New	269	16	252	6%	40%	408	473	187	129	17
EMAN-Mod	251	16	235	6%	49%	420	473	182	118	7
EMAN-New	177	11	166	6%	49%	428	473	121	118	5

Notes on Table 4-3: SW_{dn} = shortwave (solar) radiation incident at the surface, SW_{abs} = net absorbed shortwave radiation at the surface, LW_{dn} = longwave radiation incident at the surface, LW_{up} = longwave radiation emitted from surface, R_N = net radiation absorbed at surface, LH = latent heat flux away from surface, SH = sensible heat flux away from surface. See Notes on Table 3-5 for explanation of albedo calculation.

Over land, the sensible heat flux (SH) and latent heat flux (LH) changed only slightly with the Grell scheme. LH decreased significantly with the Emanuel scheme, reflecting the change to net radiation at the surface. The decrease in LH was in fact so large as to cause a small increase in SH over land, despite the large reduction in net radiation. Over ocean, both

simulations show only a very small change to SH and LH, which is to be expected since the SST is fixed in these simulations.

4.4.4 Rainfall

Average total, convective and large-scale rainfall volumes over the period 1998-2001 are shown in Table 4-4.

Table 4-4. Total, convective and large-scale rainfall (all in mm day^{-1}) averaged over 1998-2001 for land and ocean from TRMM, modified simulations (from Chapter 3, 'mod') and simulations with new convective cloud cover and CLW ('new'). The relative proportions of convective and large-scale rain are shown in parentheses.

Product / Simulation	Land Average			Ocean Average		
	Total	Convective	Large-scale	Total	Convective	Large-scale
TRMM	*8.6*	*5.4 (63%)*	*3.2 (37%)*	*7.0*	*4.0 (57%)*	*3.0 (43%)*
Grell F-C mod	10.9	4.4 (40%)	6.5 (60%)	8.5	4.1 (48%)	4.4 (52%)
Grell F-C new	9.2	4.1 (45%)	5.1 (55%)	7.3	5.5 (75%)	1.8 (25%)
Emanuel mod	16.8	9.9 (59%)	6.9 (41%)	6.7	3.8 (57%)	2.9 (43%)
Emanuel new	10.2	2.6 (25%)	7.6 (75%)	10.0	3.0 (30%)	7.0 (70%)

Over land, both convection schemes show a decrease in convective rainfall with the new cloud cover. The change is small with the Grell scheme but very large with the Emanuel scheme, reflecting the respective changes to cloud cover and radiation. In both new simulations, convective rainfall is underestimated compared to the observations. Large-scale rainfall decreases with the Grell scheme but increases with the Emanuel scheme due to the changes in available moisture resulting from the new CLW. This reduces the wet bias with the Grell scheme but worsens the wet bias with the Emanuel scheme.

Over ocean, results with the Emanuel scheme are similar to over land: convective rainfall decreased and large-scale rainfall increased. But with the Grell scheme, convective rainfall over ocean increased while large-scale rainfall decreased. Again, these changes to rainfall all reflect the changes made to cloud cover and radiation.

4.4.5 Sensitivity of Cloud Cover to Rainfall Production

The rainfall results illustrate the tight coupling that exists between convection, cloud formation, radiative flux and rainfall production. It was noted in Section 2.4 that the

production of rainfall from cumulus clouds is in fact part of the convective feedback. Conversion of clouds into rainfall removes the cloud cover that blocks insolation from reaching the surface, and therefore the rate of conversion is a significant part of the convective-radiative feedback.

It was noted that the production of rainfall in the Emanuel scheme is governed by a CLW threshold that is not appropriate for use at the grid cell resolution in these simulations. In the default version of the Emanuel scheme, all CLW in excess of a threshold, CLW_T, is turned into rainfall, where the default value of the parameter is $CLW_T = 1.1$ g kg^{-1}. This represents a cloud water content similar to that observed at the point scale, as shown in Table 4-2. But in simulating rainfall production, this threshold value is compared to a grid-mean value of CLW across a 30 km grid cell. Thus the appropriate comparison needs to be a grid-mean value of CLW_T.

To test the model sensitivity to the efficiency of convective rainfall production, an experiment was run in which the threshold value was changed to $CLW_T = 0.25$ g kg^{-1}. This experiment was in all other ways identical to the simulation with new convective cloud cover presented in this chapter (named EMAN-New).

The resulting cloud cover, profiles of CLW, radiative and turbulent heat fluxes, and rainfall from this simulation are shown in the figures and tables below. All observations are as described previously.

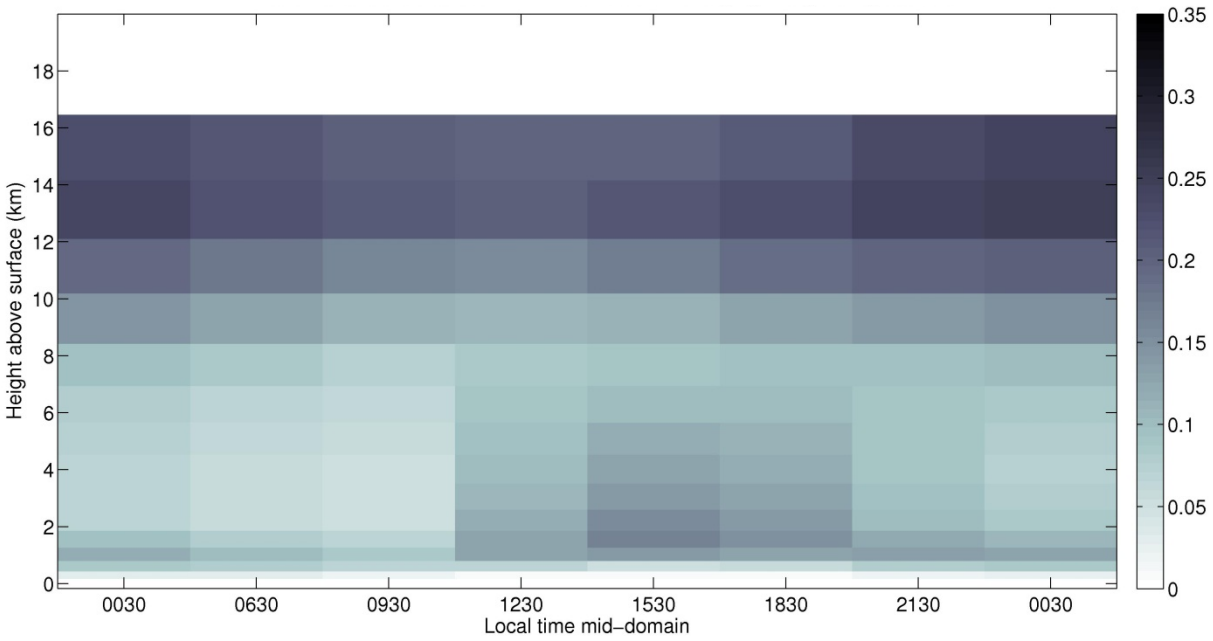

Figure 4-18. Average diurnal cycle of cloud cover over land 1998-2001 using Emanuel scheme with new convective cloud fraction, modifications from Chapter 3 and CLW_T tuned from 1.1 g kg^{-1} to 0.25 g kg^{-1}. Color bar indicates fractional coverage of grid cell.

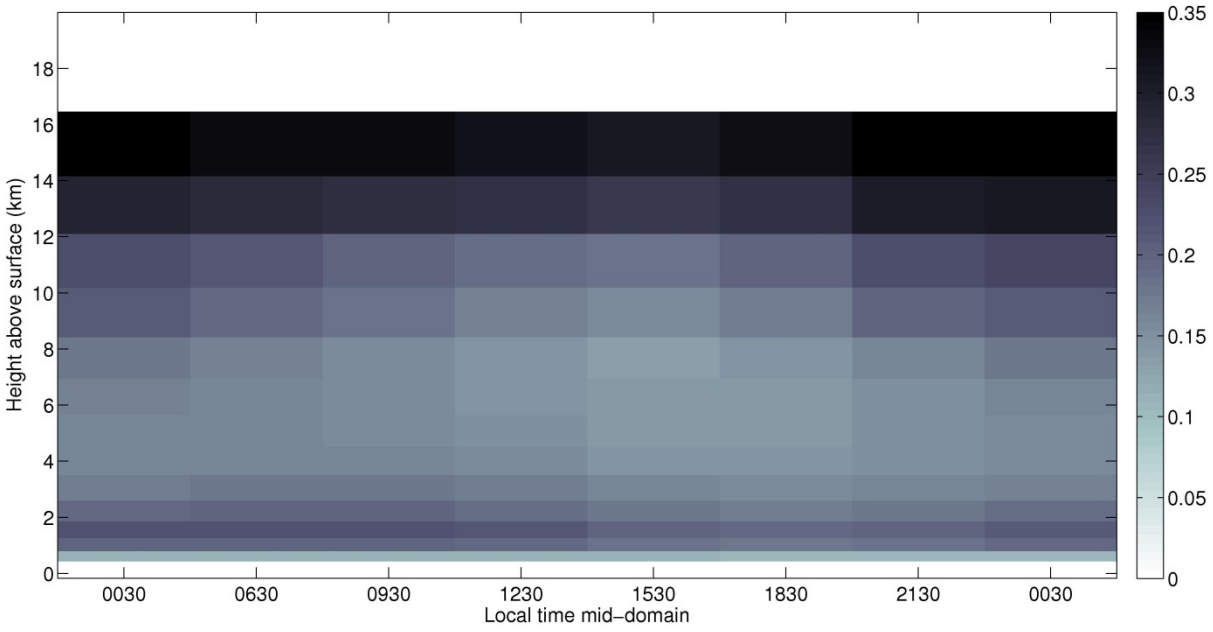

Figure 4-19. Average diurnal cycle of cloud cover over land 1998-2001 using Emanuel scheme with new convective cloud fraction, modifications from Chapter 3 and CLWT tuned from 1.1 g kg^{-1} to 0.25 g kg^{-1}. Color bar indicates fractional coverage of grid cell.

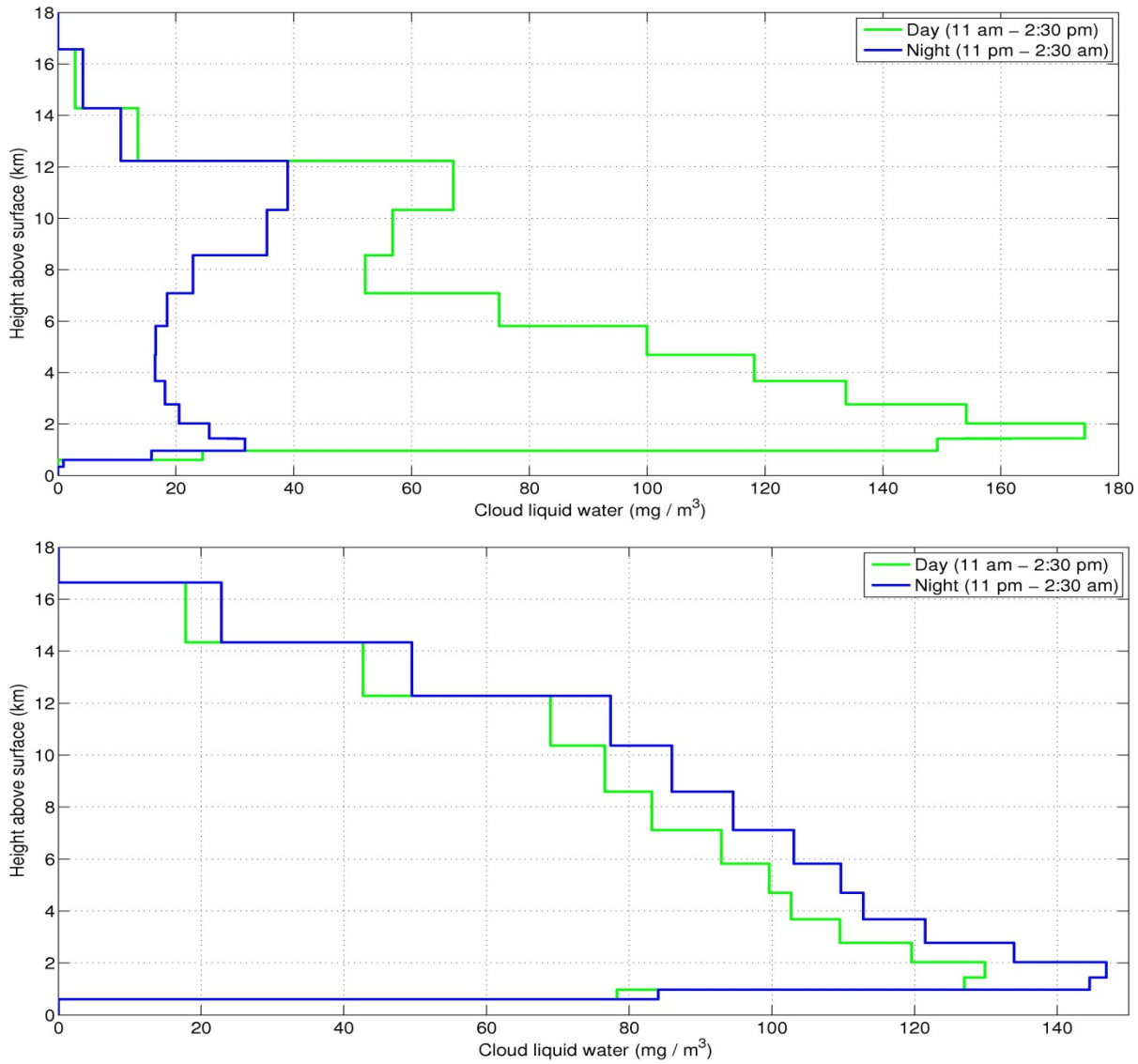

Figure 4-20. Average cloud liquid water (in mg m^{-3}) profile over (top) central Borneo and (bottom) western Pacific Ocean, simulated using the Emanuel scheme with new convective cloud fraction, modifications from Chapter 3 and CLWT tuned from 1.1 g kg^{-1} to 0.25 g kg^{-1}.

Table 4-5. Radiative and turbulent fluxes (all in W m^{-2}) averaged over 1998-2001 from SRB (radiative fluxes) and field studies (LH and SH) ('Observations') compared to simulations using the Emanuel scheme, modified (from Chapter 3, 'mod'), with new convective cloud cover and Chapter 3 modifications ('new'), and with CLW_T tuned from 1.1 g kg^{-1} to 0.25 g kg^{-1}.

LAND

Simulation	SW_{dn}	SW_{up}	SW_{net}	Surface albedo	Planetary albedo	LW_{dn}	LW_{up}	R_N	LH	SH
Observations	*202*	*31*	*171*	*16%*	*48%*	*411*	*452*	*129*	*95*	*34*
EMAN-Mod	237	33	204	14%	49%	409	456	157	137	21
EMAN-New	156	21	135	13%	49%	414	459	90	68	23
EMAN-New, tuned CLW_T	192	27	165	14%	48%	410	455	117	100	18

OCEAN

Simulation	SW_{dn}	SW_{up}	SW_{net}	Surface albedo	Planetary albedo	LW_{dn}	LW_{up}	R_N	LH	SH
Observations	*220*	*14*	*206*	*6%*	*45%*	*420*	*467*	*158*	*109*	*10*
EMAN-Mod	251	16	235	6%	49%	420	473	182	118	7
EMAN-New	177	11	166	6%	49%	428	473	121	118	5
EMAN-New, tuned CLW_T	184	12	172	7%	51%	429	473	129	117	5

Notes on Table 4-5: SW_{dn} = shortwave (solar) radiation incident at the surface, SW_{abs} = net absorbed shortwave radiation at the surface, LW_{dn} = longwave radiation incident at the surface, LW_{up} = longwave radiation emitted from surface, R_N = net radiation absorbed at surface, LH = latent heat flux away from surface, SH = sensible heat flux away from surface. See Notes on Table 3-5 for explanation of albedo calculation.

Table 4-6. Total, convective and large-scale rainfall (all in mm day^{-1}) averaged over 1998-2001 for land and ocean from TRMM ('Observations') and simulations using the Emanuel scheme, modified (from Chapter 3, 'mod'), with new convective cloud cover and Chapter 3 modifications ('new'), and with CLW_T tuned from 1.1 g kg^{-1} to 0.25 g kg^{-1}. The relative proportions of convective and large-scale rain are shown in parentheses.

Product / Simulation	Land Average			Ocean Average		
	Total	Convective	Large-scale	Total	Convective	Large-scale
TRMM	*8.6*	*5.4 (63%)*	*3.2 (37%)*	*7.0*	*4.0 (57%)*	*3.0 (43%)*
Emanuel mod	16.8	9.9 (59%)	6.9 (41%)	6.7	3.8 (57%)	2.9 (43%)
Emanuel new	10.2	2.6 (25%)	7.6 (75%)	10.0	3.0 (30%)	7.0 (70%)
Emanuel new – tuned CLW_T	10.3	5.0 (49%)	5.3 (51%)	7.9	3.5 (44%)	4.4 (56%)

The results show a significant impact from changing the efficiency of convective rainfall production. Convective cloud fraction and CLW is reduced throughout the lower and

middle atmosphere, resulting in increased insolation and net radiation absorbed at the surface. Convective rainfall increases because of the increased insolation, and large-scale rainfall decreases due to the reduction in residual moisture and large-scale cloud cover at low and middle elevations. The impact is particularly large over land surfaces, bringing the results much closer to observations. Planetary albedo changes negligibly, again showing the strong control of high cloud cover on the albedo.

This experiment suggests that the removal of convective clouds via rainfall production may play an equally significant role in the convective-radiative feedback as the formation of those clouds. However, the method used here to test this sensitivity – changing the value of the CLW_T parameter – was somewhat arbitrary. In general, the tuning of model parameters simply to achieve good simulation results without an underlying physical basis should be avoided. It is more desirable to find a physically-based method for increasing the rainfall production efficiency, one that improves model results over both land and ocean surfaces without the need for tuning. The development of such a method is described in Chapter 5.

4.5 Discussion

The new parameterization for convective cloud fraction presented in this work produces a diurnal cycle of cloud cover over land that is consistent with the convective activity, with simulated cloud in the location and timeframe that is expected due to daytime convection. The results demonstrate that the default value of within-cloud CLW in RegCM3 substantially underestimates the amount of cloud water resulting from the simulated convective activity, particularly the Emanuel scheme.

The results illustrate the influence that moist convection has on the near surface environment by mediating the incoming solar radiation and net radiation at the surface, with subsequent impacts on the turbulent heat fluxes. Changes to the near surface environment then feed back to subsequent convection, influencing the convective rainfall production. Therefore this work emphasizes the importance of explicitly linking convective motion to radiative transfer via cloud cover. This work has demonstrated that convective cloud cover is incredibly important in simulations of rainfall and radiative fluxes within RegCM3, and most

likely would be in other large-scale climate models, consistent with Arakawa's (2004) 'new objectives' for convective parameterizations.

However, the changes made in these new simulations did not bring the model results in line with observations. With both schemes, radiative fluxes, CLW profiles and the convective rainfall fraction contain significant errors. With the Emanuel scheme, cloudiness is also considerably overestimated. Therefore the results suggest that another substantial source of error related to convection exists within the model.

A sensitivity experiment indicated that the efficiency with which rainfall is produced from convective clouds could play an equally important role in the convective-radiative feedback. Increasing the rainfall efficiency with the Emanuel scheme led to reduced cloud cover and increased insolation, with subsequent improvements in surface fluxes and rainfall.

The next chapter will present a new parameterization for the conversion of convective clouds into rainfall, which is substantially more physically realistic than the existing methods within RegCM3. It will be shown that the new method can significantly improve the simulation results and bring the model very close to observations.

Chapter 5: On the Simulation of Convective Autoconversion

The rainfall that we measure at the Earth's surface is the net result of a suite of interacting microphysical processes. These include the production of supersaturation, activation of cloud condensation nuclei where supersaturation occurs, droplet growth by condensation of water vapor, stochastic coalescence and the Bergeron-Findeisen mechanism, the redistribution of condensed water mass among particles of different sizes by coalescence and drop breakup in the liquid phase, and a large variety of ice-phase and mixed-phase processes (Emanuel 1994, Geoffroy *et al*. 2008).

These processes, as well as those involved with re-evaporation of falling rain and for freezing and sublimation, operate on scales far too small to be modeled explicitly within climate models. To simulate this suite of processes would require representation of the aerosol size distribution, chemical composition and mixing state, as well as the size distribution and number concentration of each hydrometeor species (Geoffroy *et al*. 2008). The computational expense of such explicit simulation is prohibitive, so most models use one or more associated equations that parameterize the sum of these processes, which is termed *autoconversion*.

Bulk microphysics schemes are usually employed to parameterize autoconversion in GCMs and RCMs, in which the hydrometeor representation is reduced to two variables – cloud droplets and precipitating particles – that are characterized by their mixing ratios (Geoffroy *et al.* 2008). Errors associated with the representation of the microphysics involved in autoconversion are considered some of the most significant sources of error in simulations of rainfall. Emanuel (1994) proposed that semi-empirical techniques will ultimately emerge as the best way to deal with the representation of cloud microphysical processes. In a semi-empirical approach, physical principles are used to constrain the system to a more limited number of parameters; these parameters are then related to observations by statistical methods (Emanuel 1994).

Chapter 4 illustrated the critical role that convective clouds play, both in the physical world and in RegCM3, in mediating the relationship between radiation and rainfall. A sensitivity experiment suggested that the efficiency of rainfall production could be altered in a way that improved model performance, but in an unsatisfactory manner (by parameter tuning). Although explicit simulation of autoconversion processes is currently not possible within large-scale climate models, there is considerable scope for improving the way in which it is parameterized.

This chapter presents the development of a new parameterization method for convective autoconversion. This method is in the spirit of the semi-empirical approach proposed by Emanuel (1994), in which physical reasoning is used to constrain a system to a limited number of parameters that can be related to observations. A review of the existing methods for parameterizing autoconversion within GCMs and RCMs follows. A review of the theory for and observations of the conversion of cloud water into rainfall is provided in the Appendix.

5.1 Review of Existing Parameterization Methods for Autoconversion

Arguably the simplest, but most widely-used, method of representing autoconversion is the scheme developed by Kessler (1969). In this scheme, the rate of cloud autoconversion increases with the cloud content but is zero for amounts below some threshold, i.e.

$$\frac{dM}{dt} = k_1(m - a) \qquad (5\text{-}1)$$

$k_1 > 0$ when $m > a$, $k_1 = 0$ when $m < a$

where M = rainwater mixing ratio, m = cloud water mixing ratio, $k_1 = 10^{-3}$ sec^{-1} and a = cloud water threshold value below which cloud conversion does not occur. Kessler (1969) noted that cloud amounts greater than 1 g m^{-3} are usually associated with production of precipitation.

Major assumptions of the Kessler scheme are that the cloud is free of ice and that the population of water particles is bimodal, consisting of a population of small cloud droplets

whose terminal velocity is minute compared to typical vertical air velocities, and a population of raindrops that obeys the exponential Marshall-Palmer distribution (Emanuel 1994). The assumption of a bimodal distribution of water-drop sizes has considerable observational and theoretical support, and the exponential distribution is a natural starting point since it is a single-parameter distribution that describes observed distributions quite well (Emanuel 1994). Therefore the assumptions made by the Kessler scheme seem reasonable, although small departures from these distributions have been observed and may introduce error (Rosenfeld and Ulbrich 2003).

Kessler (1969) stated that "various effects of nature and cloud seeding can be represented by the choices of k_1 and a". This statement suggests that this very simple representation of the autoconversion process masks a raft of intricate, unresolved microphysical processes, so that the appropriate choice of parameter values for a given location depends on the nature of the cloud at that location.

The Kessler (1969) form of autoconversion was implemented in the Colorado State University GCM (Fowler *et al*. 1996) using a threshold value of $q_{crit} = 0.25$ g kg^{-1} and in MM5 (Grell *et al.* 1994) using a threshold value of $q_{crit} = 0.5$ g kg^{-1}. The scheme is also employed in the cloud-resolving model System for Atmospheric Modeling Version 6.3 (SAM 6.3) (described in Khairoutdinov and Randall 2003), using a threshold cloud liquid water mixing ratio of $q_{c0} = 1$ g kg^{-1} (Blossey *et al.* 2007).

Cotton (1972) proposed that, since the precipitation formation process takes a certain amount of time for the droplet population to broaden to the extent that rapid conversion takes place, one should parameterize the autoconversion rate to be a function of liquid water content and the 'age' of a parcel of droplets. Unfortunately, the need to estimate the Lagrangian timescale of a population of cloud droplets is not practical in climate models (Manton and Cotton 1977).

In developing their model of cumulus parameterization, Arakawa and Schubert (1974) used the following parameterization of the rainfall rate out of a sub-ensemble of cumulus clouds at a given elevation z:

$$r(z) = C_0 l(z) \tag{5-2}$$

where C_0 = constant parameter and l(z) = mixing ratio of cloud liquid water.

Lord (1982) proposed a similar autoconversion function, in which rainfall production is taken to be proportional to the vertical flux of cloud water in the updraft as:

$$R = C_0 M_u l \tag{5-3}$$

where C_0 = 0.002 m^{-1}, M_u = updraft mass flux, l = cloud water.

This form of autoconversion is used within CAM4.0 (Neale *et al.* 2010).

Manton and Cotton (1977) proposed an autoconversion rate that explicitly depended on the concentration and radius of cloud water droplets:

$$S_c = f_c \rho_c H(\overline{\rho_c} - \rho_{cm}) \tag{5-4}$$

where S_c = source of rainfall (initial generation of rain by the coalescence of two cloud water droplets to yield a rain drop), f_c = mean collision frequency for cloud water droplets that become rain drops after colliding, ρ_c = cloud water density, $H(x)$ = Heaviside unit step function and ρ_{cm} = minimum mean cloud water density below which there is no conversion. The overbar denotes the mean value of a random variable (i.e. the ensemble average). The threshold cloud water density, ρ_{cm}, is given by:

$$\rho_{cm} = \frac{4}{3}\pi \rho_{wt} r_{cm}^3 N_c \tag{5-5}$$

where ρ_{wt} = density of water, r_{cm} = minimum mean droplet radius required for conversion and N_c = mean cloud water droplet concentration. The mean collision frequency, f_c, is given by (Manton and Cotton 1977):

$$f_c = \alpha\left(\rho_{wt}\, {}^{g}/_{\mu_0}\, N_c^{1/3}\right)\left(\overline{\rho_c}/\rho_{wt}\right)^{4/3} \quad (5\text{-}6)$$

where α = 0.057 and μ_0 = viscosity of air.

The Manton-Cotton autoconversion parameterization is far more sophisticated than the Kessler form, but is still problematic. Its implementation within a large-scale model requires simulation of the droplet concentration and droplet radius. Many GCMs and RCMs do not include these prognostic variables. Also, this parameterization is still dependent upon grid-average values of the different variables and does not explicitly recognize the subgrid variability that exists within cloud droplet populations.

Fritsch and Chappell (1980) presented a parameterization of mid-latitude organized convection intended for mesoscale numerical models (defined as those with a grid cell size up to 20 km). Precipitation efficiency in the Fritsch and Chappell (1980) model represents the fraction of initial precipitation that reaches the ground surface after re-evaporation. This efficiency, *E*, is described as a function of vertical shear of the horizontal wind, *V*, in the layer from cloud base to cloud top:

$$\mathrm{E} = 1.591 - 0.639\frac{\Delta \mathrm{V}}{\Delta \mathrm{z}} + 0.0953\left(\frac{\Delta \mathrm{V}}{\Delta \mathrm{z}}\right)^2 - 0.00496\left(\frac{\Delta \mathrm{V}}{\Delta \mathrm{z}}\right)^3 \quad (5\text{-}7)$$

$$\mathrm{E} = 0.9 \text{ for } \Delta \mathrm{V}/\Delta \mathrm{z} < 1.35$$

The convective precipitation rate was given as:

$$P = ES \quad (5\text{-}8)$$

where *S* = rate of supply of moisture to the updraft, defined as the sum of the vertical flux of vapor and liquid at about 150 mb above the lifted condensation level (Fritsch and Chappell 1980).

Following Kuo (1974), Krishnamurti *et al*. (1983) represented the rainfall rate within their cumulus parameterization as:

$$R = I(1 - b) \tag{5-9}$$

where I = total supply of moisture and b = moistening parameter with a mean value of 0.3. By using the GATE dataset and radar estimates of rainfall rates to optimize the parameters in their parameterization through a multiple regression approach, the authors were able to get good agreement between their model and observations. However, the authors note that in general such good agreement would not be possible in the application to most sparse data networks over the tropics (Krishnamurti *et al*. 1983).

In the model described by Sundqvist *et al*. (1989)[1], the rate of release of precipitation of both convective and stratiform types is given by:

$$\mathrm{P} = \mathrm{c_0 m}\left[1 - \exp\left(-\left(\frac{\mathrm{m}}{\mathrm{bm_r}}\right)^2\right)\right] \tag{5-10}$$

where $1/c_0$ = characteristic timescale for the conversion of cloud droplets into raindrops, b = cloud cover, m_r = within-cloud threshold value for cloud water and m = grid-cell value of cloud water (hence m/b is the within-cloud value of cloud water). The parameter m_r is therefore assigned a value typical of individual cloud types, which is invariant to grid resolution. The values of c_0 and m_r are modified by temperature to account for the more rapid autoconversion processes involving ice.

This method of autoconversion was adopted by Tiedtke (1993) and is used in the NASA GISS GCM (Del Genio *et al.* 1996).

Albrecht (1989) described the results of a simple parameterized model built to represent cloudiness fraction, which included a variable for precipitation efficiency. The removal of water by precipitation processes was assumed to be:

[1] Interestingly, Sundqvist *et al.* (1989) noted that 'models that have radiation effects included, and thus need information on cloudiness, describe this with diagnostic formulations that often given little regard to consistency with the model-produced condensation fields'. This seems to be the case with RegCM3, as shown in Chapter 4.

$$dl_c/dz = -al_c \tag{5-11}$$

where z = height, l_c = cloud liquid water and a = precipitation efficiency factor in units of km^{-1}, where $0 < a < 1$. Albrecht (1989) found that the cloudiness fraction was highly sensitive to the value of the precipitation efficiency factor, since higher values removed cloud liquid water at a rate of 1/e when $a = 1$.

Some large-scale climate models that have prognostic droplet size and concentration variables include autoconversion parameterizations that suppress autoconversion unless the volume-mean cloud droplet radius in a grid box exceeds a prescribed threshold r_{crit} (Rotstayn 2000). Once r_{crit} is prescribed and the cloud droplet number concentration N_d is known at a grid point, the critical cloud liquid-water mixing ratio below which no autoconversion can occur can be estimated from (Manton and Cotton 1977):

$$\mathrm{q_{crit}} = {}^{4}/_{3}\,\pi\rho_{\mathrm{w}}\mathrm{r_{crit}^{3}}\,{}^{\mathrm{N_d}}/_{\rho_{\mathrm{air}}} \tag{5-12}$$

Beheng (1994) proposed a similar parameterization for stratiform clouds, in which precipitation formation is dependent upon the cloud droplet number concentration. In this scheme, the autoconversion rate is derived from the stochastic collection equation, which describes the time evolution of a droplet spectrum changing by collisions among droplets of different size. This scheme is used in the ECHAM5 GCM (Lohmann and Roeckner 1996).

Many bulk microphysical schemes that have been implemented in GCMs were initially developed for cloud-resolving models, in which local values of the microphysical fields are resolved, and therefore their extension to GCMs might be considered questionable (Geoffroy *et al*. 2008). The onset of precipitation is highly sensitive to the size of the biggest cloud droplets, which in turn depends upon the local values of the liquid water content and cloud droplet concentration. In a GCM, the liquid water content is distributed over the cloud fraction of the model grid, so its mean value is significantly smaller than the peak values that are simulated by a cloud-resolving model or that might be observed in reality (Geoffroy *et al*. 2008).

GCM simulations can show a marked sensitivity to parameters that control the autoconversion process. It seems to be common practice that the values of autoconversion parameters in GCMs, such as the threshold cloud droplet radius at which collection starts to be active or the critical cloud water content at which autoconversion might be initiated, have to be tuned to compensate for some other deficiency (Rotstayn 2000).

For models that use a critical cloud water mixing ratio threshold, it is common to use a value considerably smaller than the within-cloud value of about 1 g kg^{-1} suggested by Kessler (1969). For example, the United Kingdom Meteorological Office Unified Model uses a threshold value of 0.2 g kg^{-1}, the Colorado State University GCM uses 0.25 g kg^{-1}, the NASA GISS GCM uses 0.5 g m^{-3} and the Scripps Institute of Oceanography GCM uses 0.3 g kg^{-1} (Xu *et al.* 2005). The cloud resolving model SAM 6.3 employs a threshold of 1 g kg^{-1}, which is close to the average observed cloud liquid water content of convective clouds and therefore likely to be more realistic. Such a high value is able to be used in this model because it runs at a scale sufficiently small (with a horizontal resolution of about 1 km) to resolve the natural variability in convective activity that is unachievable by GCMs and RCMs. For models that have a prognostic droplet radius and concentration, observations suggest that the critical drop size radius is r_{crit} = 10-15 μm, but GCMs typically use 4.5-7.5 μm in order to get good simulated values of cloud liquid water (Rotstayn 2000, Geoffroy *et al*. 2008).

The lower, tuned model values could be interpreted as grid-mean thresholds for cloud water content, and therefore comparable to the grid-mean simulated condensate. But because these thresholds are not functions of the actual subgrid variability in condensate, they must be manually tuned to account for different model resolution, domain and choice of parameterization schemes. Their use is therefore less than ideal.

Rotstayn *et al.* (2000) added a new treatment of stratiform clouds to the CSIRO GCM that attempted to simulate the subgrid-scale variability in stratiform autoconversion. The assumed subgrid moisture distribution from the model's condensation scheme was applied in each grid box to determine the fraction of the cloudy area in which the mean within-cloud mixing ratio exceeded a prescribed threshold, and autoconversion occurred only in that fraction of the grid cell (Rotstayn *et al.* 2000). The total water mixing ratio is assumed to

follow a symmetric triangular probability density function (PDF) about its grid-box-mean value. This improved method for treating stratiform autoconversion allowed the critical value of the threshold radius to be increased from 7.5 μm in the old treatment to 9.3 μm in the new treatment, close to the observed value of 10 μm, in order to achieve the same simulated values of liquid water path (Rotstayn *et al.* 2000). This scheme represents an interesting development in the parameterization of autoconversion. However, it uses a questionable symmetric triangular PDF to represent the distribution of water vapor, and it requires that droplet number concentration be a prognostic variable, which is not the case for many climate models including RegCM3.

An approach called 'super-parameterization' has been suggested as perhaps the most realistic way for representing convection within large-scale climate models (e.g. Khairoutdinov and Randall 2001, Iorio *et al*. 2004, Khairoutdinov *et al*. 2005, Li *et al*. 2012). In this method, a high-resolution cloud-resolving model is embedded into each grid column of a large-scale model so that an explicit simulation of convective processes replaces the convective parameterization. It has been argued that super-parameterization improves the representation of subgrid-scale processes because the interactions between cloud dynamics, cloud and aerosol microphysics, radiation and turbulence can be explicitly resolved (Li *et al*. 2012).

However, it should be noted that the use of a cloud-resolving model in this way may not necessarily yield better model performance. Explicit representations of convective and turbulent processes introduce additional complexity into the simulation, necessitating further model evaluation, and may impact the simulation at the larger scale in ways unforeseen. These representations also contain their own sets of parameters requiring specification, which could introduce additional uncertainty and does not alleviate the existing need for parameter specification. Finally, super-parameterization has a significantly higher computational burden than a conventional convective parameterization: Randall *et al*. (2003) estimate that a GCM with super-parameterization will be 100-1000 times more computationally expensive than the same GCM with conventional parameterizations. Hence, at least for the time being, this method is unlikely to be feasible for most climate modelers.

A summary of the autoconversion functions currently employed in selected large-scale models is shown in Table 5-1.

Table 5-1. Autoconversion functions in selected climate models.

Model	Treatment of Convective Cloud Cover
RegCM3 – Emanuel convection scheme	$precip(z) = \overline{CLW}(z) - CLW_T$ where $\overline{CLW}(z)$ = grid-scale CLW within model layer z, CLW_T = 1.1 g/kg.
RegCM3 – Grell convection scheme	$precip(z) = \frac{c_0 dz}{1 + c_0 dz}(q_u - q_{rch})$ where c_0 = 0.002, dz = depth of model layer, q_u = water vapour mixing ratio of updraft, q_{rch} = water vapour mixing ratio of environment.
MM5 (Grell *et al.* 1994)	$P_{RC} = k_1(q_c - q_{crit})$ where $k_1 = 10^{-3}$ s^{-1}, q_c = condensate, q_{crit} = 0.5 g/kg.
Colorado State University GCM (Fowler *et al*. 1996)	dM/dt = k_1*(m – *a*) $k_1 > 0$ when m > *a*, k_1 = 0 when m < *a* where M = rainwater mixing ratio, m = cloud water mixing ratio, $k_1 = 10^{-3}$ sec^{-1} and *a* = cloud water threshold value below which cloud conversion does not occur = 0.25 g kg^{-1}
HadGEM1 (Hadley Center; Martin *et al.* 2006)	HadGEM1 uses an updated version of the Wilson and Ballard (1999) microphysics scheme. Transfers between water categories (ice, liquid water, vapor, and rain) are calculated based on physical process equations using particle size information.
CAM4 (National Center for Atmospheric Research; Neale *et al.* 2010)	$R = C_0 M_u l$ where C_0 = 0.002 m^{-1}, M_u = updraft mass flux, *l* = cloud water, as in Lord (1982).
GFDL (NOAA Geophysical Fluid Dynamics Laboratory AM2/LM2; Rotstayn *et al* 2000, Tiedtke 1993)	$\frac{dq_{l,au}}{dt} = -C_{au}\frac{0.103 g E_{au}\rho_a^{4/3}}{\mu(N_d\rho_l)^{1/3}}\left(\frac{q_{l,au}}{C_{au}}\right)^{7/3} H\left(\frac{q_{l,au}}{C_{au}} - q_{crit}\right)$ $q_{crit} = {}^4/_3\,\pi\rho_w r_{crit}^3 N_d/\rho_{air}$ where μ = dynamic viscosity of air, N_d = cloud droplet number concentration, g = gravitational acceleration, E_{au} = 0.55 is the mean collection efficiency, H() is the Heaviside step function, which suppresses autoconversion until $q_l/C > q_{crit}$, ρ = density.
ECHAM5 (Lohmann and Roeckner 1996)	Autoconversion rate, Q_{aut} (kg/kg/s) is based on Beheng (1994): $Q_{aut} = (\gamma_1 6.\,10^{28} n^{-1.7}(10^{-6}N_l)^{-3.3}(10^{-3}\varrho q_{cl})^{4.7})/\varrho$ where γ_1 = 15 (efficiency of rain formation), n = 10 (width parameter of initial cloud droplet spectrum), N_l = cloud droplet number concentration (which is empirically related to sulphate aerosol concentration rather than explicitly simulated), q_{cl} = within-cloud cloud water mixing ratio ($q_{cl} = q_c/b$), ϱ = air density. Different values of N_l are used for maritime and continental clouds.
SAM 6.3 (System for Atmospheric Modeling Version 6.3, Khairoutdinov and Randall 2003)	$rain = k_1(q_c - q_{c0})$ where $k_1 = 10^{-3}$ s^{-1}, q_c = cloud liquid water mixing ratio, q_{c0} = 1.0 g/kg.

5.2 Existing Parameterization of Convective Autoconversion in RegCM3

The Grell convection scheme in RegCM3, with either the Fritsch-Chappell or Arakawa-Schubert closure, uses an autoconversion function similar to Arakawa and Schubert (1974) to calculate the rainfall produced at a given elevation, *R(z)*:

$$R(z) = \frac{c_0 \Delta z}{1 + c_0 \Delta z}(q_u - q_{rch}) M_u \tag{5-13}$$

where c_0 = 0.002, Δz = depth of model layer, q_u = water vapor mixing ratio of updraft, q_{rch} = water vapor mixing ratio of environment and M_u = updraft mass flux.

There is no discussion of this formulation in Grell (1993) or the RegCM3 manual, and so it is assumed that the value of c_0 is taken from Lord (1982) since the same parameter value appears there. The default model layers are defined within RegCM3 to be thinner in the lower atmosphere and increase in thickness with increasing height above the surface. Therefore this form of autoconversion function results in an efficiency of around 0.5 in the region up to 3 km elevation and a maximum efficiency of around 0.8 at high altitudes within RegCM3.

The Emanuel convection scheme within RegCM3 uses a Kessler form of autoconversion to calculate the production of rainfall at a given elevation, *R(z)*:

$$R(z) = \overline{CLW}(z) - CLW_T \tag{5-14}$$

where $\overline{CLW}(z)$ = grid-scale CLW within model layer *z*, CLW_T = threshold value of CLW = 1.1 g kg^{-1}. The threshold value used in the Emanuel scheme is closer to observed values of cloud density and therefore likely to be more realistic. However, it represents a point-scale threshold value, while the cloud water mixing ratio CLW used in the model is the grid-mean CLW. Hence there is a mismatch of scales in the default formulation within RegCM3.

5.3 A New Parameterization for Autoconversion in Convective Clouds

A new method has been developed to represent autoconversion within RegCM3. This method is in the spirit of the semi-empirical approach described by Emanuel (1994), in which physical principles are used to constrain a system to a limited number of parameters, whose values are then related to observations.

As a first-order approximation, the long-term average efficiency of rainfall production can be considered constant. Empirical relationships can then be used to frame an expression for the mean autoconversion, as follows. When non-zero rainfall is simulated within a model grid cell, the fractional area of the grid cell that contains rainfall can be estimated using the relationship derived in Eltahir and Bras (1993):

$$\mu = \bar{R}/_{R_{clim}} \tag{5-15}$$

where μ = fractional coverage of rainfall, $\bar{R}$ = grid-average simulated rainfall and R_{clim} = climatological rainfall intensity, which is the average rainfall intensity that is observed when there is non-negligible rainfall and may be geographically variable. This relationship is analogous to the relationship using CLW_{clim} in Section 4.3 to derive the fractional coverage of convective cloud.

The fractional coverage of rainfall, μ, within a raining model grid cell may also be expressed as the portion of the cloudy area within the grid cell that produces rainfall, i.e.

$$\mu = f_r FC_{cnv} \tag{5-16}$$

where f_r = fraction of total cloudy area that is raining, and FC_{cnv} = fractional coverage of convective cloud. The expression (4-9) derived in Section 4.3 can be used to obtain:

$$\mu = f_r \frac{\overline{CLW}}{CLW_{clim}} \tag{5-17}$$

where CLW_{clim} = climatological cloud liquid water density, the mean observed cloud water content, as in Section 4.3. This relationship is illustrated in the schematic below.

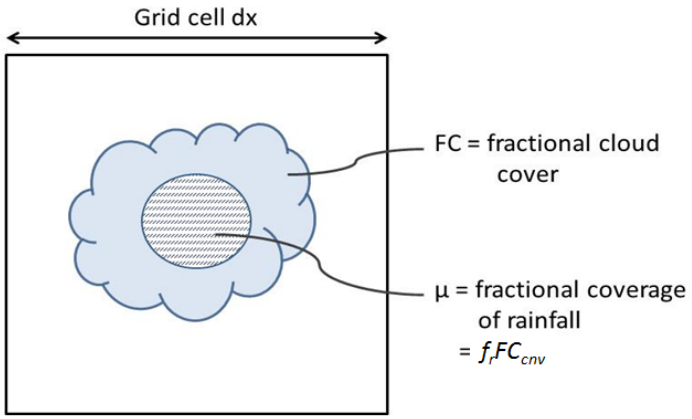

Figure 5-1. Relationship between fractional cloud cover, FC, and fractional coverage of rainfall, μ.

The climatological values of rainfall and CLW can then be used as a framework for the mean autoconversion. Combining the two expressions for the fractional coverage of rainfall yields:

$$\frac{\bar{R}}{R_{clim}} = f_r \frac{\overline{CLW}}{CLW_{clim}} \tag{5-18}$$

The simulated grid-average rainfall, $\bar{R}$, can be represented as some fraction, f_e, of the simulated CLW, i.e.

$$\bar{R} = f_e \overline{CLW} \tag{5-19}$$

where $\bar{R}$ = grid-mean rainfall, $\overline{CLW}$ = simulated grid-mean convective CLW, as in Section 4.3, and f_e = autoconversion efficiency. The autoconversion efficiency, f_e, can then be expressed as a function of the long-term average variables and the simulated grid-mean CLW:

$$\frac{f_e \overline{CLW}}{R_{clim}} = f_r \frac{\overline{CLW}}{CLW_{clim}} \tag{5-20}$$

$$\rightarrow f_e = f_r \frac{R_{clim}}{CLW_{clim}} \tag{5-21}$$

The form of f_r is now required. In the physical world, if CLW is distributed according to some unique PDF, then the fractional coverage of rainfall f_r is equivalent to the portion of that PDF that exceeds some autoconversion threshold CLW_T, i.e.

$$f_r = \int_{CLW_T}^{\infty} f_{CLW} dCLW \tag{5-22}$$

The form of f_{CLW} must now be specified. The distribution of CLW has been fitted to a lognormal distribution (Foster *et al*. 2006) and a Weibull distribution (Iassamen *et al.* 2009). Rainfall drop size distributions have been fitted to exponential (Marshall and Palmer 1948), lognormal (Rosenfeld and Ulbrich 2003) and gamma (e.g. Ulbrich 1983, Testud *et al.* 2001) distributions. For simplicity and in the absence of a well-defined PDF for CLW, an exponential distribution of CLW is used here (noting that other distributions can potentially also collapse to the exponential distribution with appropriate parameter choices). It is also noted that a lognormal distribution for CLW was attempted in this work but no significant differences from an exponential distribution were found in the results. The exponential distribution is also advantageous since it can be integrated analytically *a priori,* increasing computational efficiency.

If the observed CLW is distributed exponentially with a mean of CLW_{clim}, then:

$$f_{CLW} = \frac{1}{CLW_{clim}} exp\left(-\frac{CLW}{CLW_{clim}}\right) \tag{5-23}$$

$$\rightarrow f_r = \int_{CLW_T}^{\infty} \frac{1}{CLW_{clim}} exp\left(-\frac{CLW}{CLW_{clim}}\right) dCLW \tag{5-24}$$

$$\therefore f_r = exp\left(-\frac{CLW_T}{CLW_{clim}}\right) \tag{5-25}$$

$$\rightarrow f_e = exp\left(-\frac{CLW_T}{CLW_{clim}}\right)\frac{R_{clim}}{CLW_{clim}} \quad (5\text{-}26)$$

This relationship represents the long-term climatological rainfall production efficiency, i.e. the autoconversion rate. It could be evaluated using mean observed values of convective CLW and rainfall intensity and then used within a large-scale climate model to represent the average autoconversion rate.

However, the expression in (5-26) represents a spatial average of autoconversion efficiency, which is assumed constant in time, while at the point-scale the autoconversion rate will be dynamic and spatially variable. It is desirable to capture this temporal and spatial variability within the model to improve the physical realism of the simulation.

To achieve this, a point-scale expression for autoconversion can be used to derive the impact of small-scale variability at the scale of a grid cell. The grid-scale autoconversion can then be used to constrain the long-term mean autoconversion relationship from (5-26).

At the point-scale, i.e. the scale of a small parcel of a convective cloud, the amount of rainfall that is produced will be a function of the cloud droplets that are large enough to fall out of the cloud parcel. This volume can be represented as:

$$R = \alpha(CLW - CLW_T)^n \quad (5\text{-}27)$$

where R = point-scale rainfall, CLW = amount of cloud liquid water within the cloud parcel, CLW_T = point-scale threshold volume of CLW that must be exceeded to produce rainfall and n = parameter that represents the degree of linearity of the autoconversion process. The parameter α (it is assumed that $\alpha = 1$) ensures that the units remain dimensionally proportional for cases when $n \neq 1$.

This point-scale relationship follows the Kessler form and would duplicate the Kessler method if $n = 1$. However, the generalized form in which $n \neq 1$ accounts for the many complexities involved in converting cloud droplets to rainfall, including the effects of turbulent mixing and variability in cloud condensation nuclei size and abundance, which are currently poorly observed and quantified.

If the convective CLW within a model grid cell is distributed with a certain PDF f_{CLW}, as discussed in Section 4.3, then the simulated grid-scale convective rainfall, $\bar{R}$, can be written as:

$$\bar{R} = \alpha \int_{CLW_T}^{\infty} (CLW - CLW_T)^n f_{CLW} dCLW \tag{5-28}$$

Within a model grid cell, if the simulated convective CLW is assumed to follow an exponential distribution, then:

$$f_{CLW} = \frac{1}{\overline{CLW}} exp\left(-\frac{CLW}{\overline{CLW}}\right) \tag{5-29}$$

where $\overline{CLW}$ = mean value of simulated f_{CLW}, which can be taken as the simulated grid-scale value of convective CLW.

Then the grid-scale simulated convective rainfall can be expressed as:

$$\bar{R} = \alpha \int_{CLW_T}^{\infty} (CLW - CLW_T)^n \frac{1}{\overline{CLW}} exp\left(-\frac{CLW}{\overline{CLW}}\right) dCLW \tag{5-30}$$

$$\rightarrow \bar{R} = \alpha \overline{CLW}^n \Gamma(n+1) exp\left(-\frac{CLW_T}{\overline{CLW}}\right) \tag{5-31}$$

where Γ = gamma function, which can be evaluated via look-up tables.

This expression can be used with (5-19) to derive a dynamic, grid-scale measure of the autoconversion efficiency, f_e:

$$f_e = \alpha \overline{CLW}^{n-1} \Gamma(n+1) exp\left(-\frac{CLW_T}{\overline{CLW}}\right) \tag{5-32}$$

This function now permits calculation of the grid-mean convective rainfall using the simulated grid-scale value of convective CLW, with specification of two parameter values: CLW_T and n (remembering that the assumption $\alpha = 1$ has already been made). It is desirable to have these values constrained by observations of the autoconversion process.

Unfortunately, as discussed in Appendix A, current observations of CLW are limited to non-precipitating retrievals (also see the discussion of CloudSat data in Section 4.4) and hence there are no direct observations available of autoconversion.

But observations have been made of the radius required for a cloud droplet to be converted into a precipitating raindrop. Observations have also been made of the droplet number concentration at the time that this critical threshold radius is breached. An approximate value of CLW_T can be estimated from these observations, as follows:

$$CLW = \frac{4}{3}\pi\rho N_d r^3 \tag{5-33}$$

where *CLW* = cloud water content in g m^{-3}, ρ = liquid water density in g m^{-3}, N_d = droplet concentration in m^{-3} and *r* = radius of cloud droplets in m.

Table 5-2 lists the critical droplet radius and droplet concentration that have been observed for the onset of precipitation in continental and maritime clouds.

Table 5-2. Observations used to constrain new autoconversion function.

Cumulus Cloud Type	Quantity	Value	Reference
Continental, general	Liquid water content	0.1 – 3 g m^{-3}	Rosenfeld and Lensky 1998
	Liquid water content	1 g m^{-3}	Rogers and Yau 1989
	Critical droplet radius, r_{crit}	9-10 µm	Brenguier *et al.* 2000
	Droplet concentration, N_d	Median = 228 cm^{-3}, third quartile = 310 cm^{-3}	Squires 1958
Continental, biomass burning	Critical droplet radius, r_{crit}	3-8 µm	Reid *et al.* 1999
	Critical droplet concentration, N_d	3000 cm^{-3}	Reid *et al*. 1999
Maritime	Liquid water content	0.25 – 1.3 g m^{-3}	Rangno and Hobbs 2005
	Liquid water content	0.4 – 1.2 g m^{-3}	Warner 1955
	Critical droplet radius, r_{crit}	15 µm	Kubar *et al.* 2009
	Critical droplet radius, r_{crit}	12-15 µm	Rangno and Hobbs 2005
	Critical droplet radius, r_{crit}	13-14 µm	Brenguier *et al.* 2000
	Critical droplet concentration, N_d	60 cm^{-3}	Kubar *et al.* 2009
	Critical droplet concentration, N_d	70 cm^{-3}	Rangno and Hobbs 2005
	Droplet concentration, N_d	Median = 45 cm^{-3}	Squires 1958

Since the islands in the Maritime Continent often experience biomass burning, it is likely that cloud condensation nuclei over the islands in this region are influenced by these aerosols. Therefore it seems reasonable to adopt $r_{crit} \approx 8$ μm and $N_d \approx 700$ cm^{-3}. This leads to $CLW_T \approx 1.5$ g m^{-3}. Over ocean, it seems reasonable to adopt $r_{crit} \approx 14$ μm and $N_d \approx 60$ cm^{-3}. This leads to $CLW_T \approx 0.7$ g m^{-3}. It seems sensible to set $CLW_T > CLW_{clim}$, since the average observed cloud density is likely to be non-precipitating and higher densities than average would be required for rainfall. Given that the observed value of $CLW_{clim} \approx 0.7$ g m^{-3} (see Table 4-2), it seems reasonable to set $CLW_T = 0.75$ g m^{-3} over ocean.

Now it remains to evaluate the parameter *n*. One method to approximate this parameter is to find the value that on average allows for the dynamic autoconversion given by equation (5-32) to match the long-term mean autoconversion given by (5-26).

The expression (5-26) requires the climatological rainfall, R_{clim}, and the climatological CLW, CLW_{clim}.

Data from Singapore's Changi airport meteorological station (described in Chapter 2), TRMM's 3B42 product (described in Chapter 2) and Table 1 of Eltahir and Bras (1993) suggest that the surface rainfall rate is $R_{land} \approx 4.85$ mm hr^{-1} and $R_{ocean} \approx 3.5$ mm hr^{-1}. The climatological rainfall mass mixing ratio for falling rainfall, rather than the rainfall rate measured at the surface, is required for implementation into the model. These mass mixing ratios can be calculated using the functions from Marshall and Palmer (1948) and Rosenfeld and Ulbrich (2003), as follows.

Marshall and Palmer (1948) derived distributions of raindrop sizes based on measurements of raindrops recorded on dyed filter papers in Ottawa during the summer of 1946. The relationship between the mixing ratio of rain water M and the surface rainfall rate was determined directly from experimental records and separately calculated from the derived equations (see Table 1 of Marshall and Palmer 1948). The authors found:

$$\mathrm{M} = 0.072\mathrm{R}^{0.88} \tag{5-34}$$

where M = rain water mass (g m^{-3}) and R = rainfall rate (mm hr^{-1}).

Rosenfeld and Ulbrich (2003) used a large dataset to update the values of this M-R relationship. The authors compiled observations of the Z-R relationship and used those data to calculate values of the coefficient A and exponent b in the relationship: $Z=AR^b$. Those values were then used to deduce the behavior of integral parameters, following the method described in Ulbrich (1983). Using 23 different data sources, Rosenfeld and Ulbrich (2003) deduced values of the coefficients and parameters satisfying an M-R relationship of the form described above from measurements of the drop size distribution and the Z-R relationships. A general relationship for tropical convective rainfall was described by (Rosenfeld and Ulbrich 2003):

$$\mathrm{M} = 0.08\mathrm{R}^{0.885} \tag{5-35}$$

where M = rainfall water mass in g m^{-3} and R = rainfall rate in mm hr^{-1}. This result compares well with the Marshall-Palmer relationship.

Using the expression in (5-35) results in climatological rainfall of $R_{clim,land}$ = 0.32 g m^{-3} and $R_{clim,ocean}$ = 0.24 g m^{-3}.

The data presented in Table 4-2 suggest that $CLW_{clim} \approx 1.2$ g m^{-3} for land and $CLW_{clim} \approx 0.7$ g m^{-3} for ocean.

Substituting the observed values for R_{clim} and CLW_{clim} and the estimated values of CLW_T (CLW_T = 1.5 g m^{-3} over land and CLW_T = 0.75 g m^{-3} over ocean) into equation (5-26) yields $f_e \approx 1$ over both land and ocean. This implies that the long-term mean convective autoconversion is very efficient (note that this calculation makes no assumptions about the re-evaporation of rainfall and thus the final volume of rainfall received at the ground surface). Hence the value of the parameter *n* must result in a dynamic autoconversion function that on average leads to $f_e \approx 1$.

Mean values of the simulated grid-scale $\overline{CLW}$ are now required to evaluate the dynamic autoconversion. With both the Grell and Emanuel convection schemes, the average simulated grid-scale $\overline{CLW}$ values (i.e. the condensate simulated by each scheme prior to removal of rainfall) were determined to be approximately 2.5 g m^{-3} over land and 2 g m^{-3} over ocean. Model output is not shown here for brevity.

This leads to values of n = 0.9 over land and n = 0.94 over ocean. Therefore the following expressions can be used to calculate the grid-mean convective rainfall:

$$\rightarrow \bar{R} = \overline{CLW}^{0.9} 0.9618 exp\left(-\frac{0.0015}{\overline{CLW}}\right) \qquad \text{for land} \qquad (5\text{-}36)$$

$$\rightarrow \bar{R} = \overline{CLW}^{0.94} 0.9761 exp\left(-\frac{0.00075}{\overline{CLW}}\right) \qquad \text{for ocean} \qquad (5\text{-}37)$$

where $\overline{CLW}$ is the simulated grid-scale CLW in kg kg^{-1}.

RegCM3 uses only a single prognostic variable related to clouds – the cloud liquid water mixing ratio – but in reality the autoconversion rate is heavily dependent upon the type of hydrometeor within the cloud. In particular, the conversion of cloud ice crystals to precipitation is known to be much faster than the conversion of cloud liquid droplets (Rogers and Yau 1989). To account for this difference, the Emanuel convection scheme scales the value of CLW_T for temperatures below a certain threshold, as follows:

$$CLW_{T,actual} = CLW_T \qquad \text{for } T \geq 0^oC \qquad (5\text{-}38a)$$

$$CLW_{T,actual} = CLW_T\left(1 - {}^{T}/_{-55^oC}\right) \qquad \text{for } -55^oC \leq T \leq 0^oC \qquad (5\text{-}38b)$$

$$CLW_{T,actual} = 0 \qquad \text{for } T \leq -55^oC \qquad (5\text{-}38c)$$

This scaling allows the autoconversion rate to increase in the presence of cold clouds, where ice crystals would be expected to form and dominate the precipitation formation process. This same scaling has been used with the new formulation for autoconversion and is applied to the derived values of CLW_T given above.

It is noted that the specific values of CLW_{clim}, R_{clim}, r_{eff} and N_d that are used here are chosen from within ranges of observed values. Hence there is some flexibility in the choice of these values that could be explored by the model user.

Precipitation tends to develop more rapidly than is generally predicted from theories about diffusional growth of droplets and subsequent coalescence to precipitation-sized particles (Stephens and Haynes 2007), and the factors that determine the time scale of the

process are not well understood, especially on the global scale (Khain *et al*. 2000). Several hypotheses have been proposed to explain the difference between the theory and observed rainfall production, including the presence of giant nuclei, various effects of turbulence and localized enhancement of the collision efficiency (Emanuel 1994, Stephens and Haynes 2007). It is considered likely that these kinds of non-linear effects are responsible for the result that $n \neq 1$ in this derivation.

It is worthwhile to compare the new formulation to the original Kessler form. If a value of $n = 1$ is assumed with the new formulation, and the corresponding value of CLW_T is then derived using observed values of R_{clim} and CLW_{clim} for the Maritime Continent region, a value of $CLW_T \approx 0.3$ g m^{-3} would be obtained, similar to the 'tuned' values of CLW_T that are used in some GCMs as discussed in Section 5.1, and similar to the sensitivity experiment presented in Section 4.4.5. This tuning compensates for the lack of subgrid variability in autoconversion that exists in most large-scale climate models, and hence the need for a grid-mean conversion threshold. The generalized form developed here, where $n \neq 1$ and subgrid-variability in CLW is explicitly accounted for, removes the need for a tuned grid-mean value.

The new formulation for autoconversion presented here has some significant advantages over the default forms that exist within the Emanuel and Grell convection schemes in RegCM3:

1. It explicitly recognizes the sub-grid variability in CLW that exists in reality and how that variability would affect the grid-scale conversion process;
2. Only 2 parameters have to be specified, one dependent upon the other, which are constrained by observations of existing climate; and
3. It provides a parameterization of autoconversion that is consistent across convection schemes, bringing added realism to the model independently of model user choices.

It is noted that this method deals only with the formation of warm (i.e. liquid) rainfall and does not represent the processes that are specific to ice or mixed phases, such as ice nucleation, formation of graupel and hail, rapid growth of crystals in the presence of supercooled water, and melting of all forms of ice (Emanuel 1994). These processes may have strong effects on the evolution of tall convective clouds and large-scale and mesoscale

systems (Emanuel 1994). However, observations and understanding of the microphysical processes related to ice phases are scarce. At the present time, constructing an ice-phase parameterization similar to the one presented above would rely on gross assumptions and could hardly be expected to be physically realistic or to improve upon the existing representation of precipitation formation in RegCM3. Hence it is acknowledged that a detailed treatment of ice-phase precipitation should be a priority for future work.

5.4 Performance of New Formulation for Autoconversion in RegCM3

Simulations were run using RegCM3-IBIS with both the Grell with Fritsch-Chappell closure and Emanuel convection schemes to test the new formulation for autoconversion in place of the default formulations. These simulations are named '-Auto' in the results presented below and also contain the new formulation for FC_{cnv}, as presented in Chapter 4 using CLW_{clim} = 1.2 g m^{-3} for land and CLW_{clim} = 0.7 g m^{-3} for ocean, and the modifications presented in Chapter 3 with respect to the PBL height, surface fluxes and new simulation of large-scale cloud formation within the PBL. Domain set up, initial and boundary conditions were identical to those described in Chapters 2 and 3. Datasets used for comparison include the TRMM rainfall products, SRB radiative fluxes, turbulent LH and SH fluxes, ISCCP cloud cover and CloudSat data, described in Chapters 2, 3 and 4. Simulations named '-Mod' are from Chapter 3 and simulations named '-New' are from Chapter 4 (with new FC_{cnv}).

5.4.1 Cloud Fraction

The time-mean horizontal fractional cloud cover simulated by RegCM3-IBIS for the period 1998-2001 is compared to the ISCCP data in Figure 5-2, Figure 5-3 and Figure 5-4, for the low, mid-level and high cloud categories respectively.

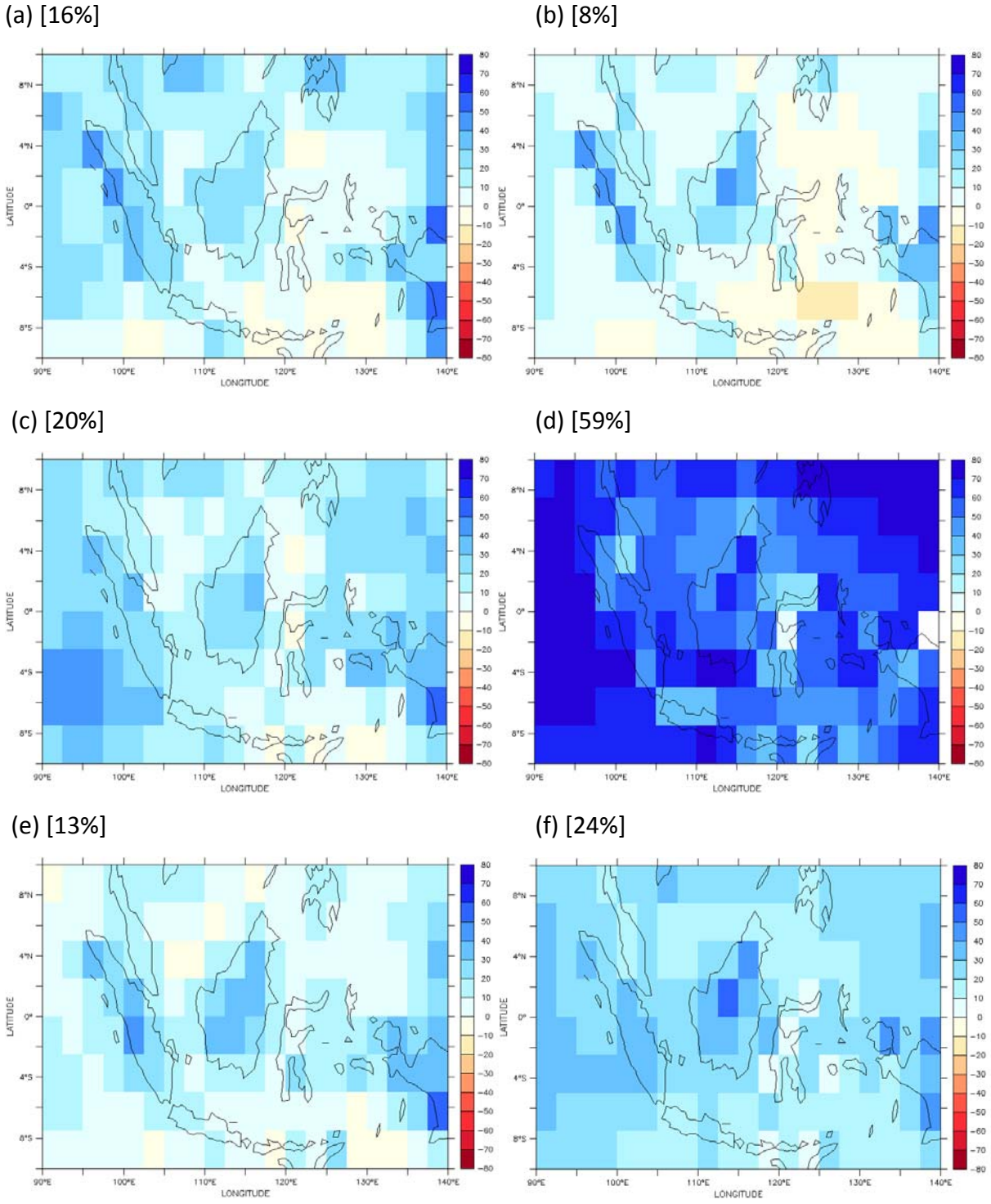

Figure 5-2. Average low cloud fraction for 1998-2001: simulation minus ISCCP data for (a) GFC-Mod, (b) EMAN-Mod, (c) GFC-New, (d) EMAN-New, (e) GFC-Auto and (f) EMAN-Auto. Domain-averaged error (model – ISCCP cloud fraction) is shown in parentheses. Color bar indicates fractional coverage of grid cell.

(a) [-10%]

(b) [-2%]

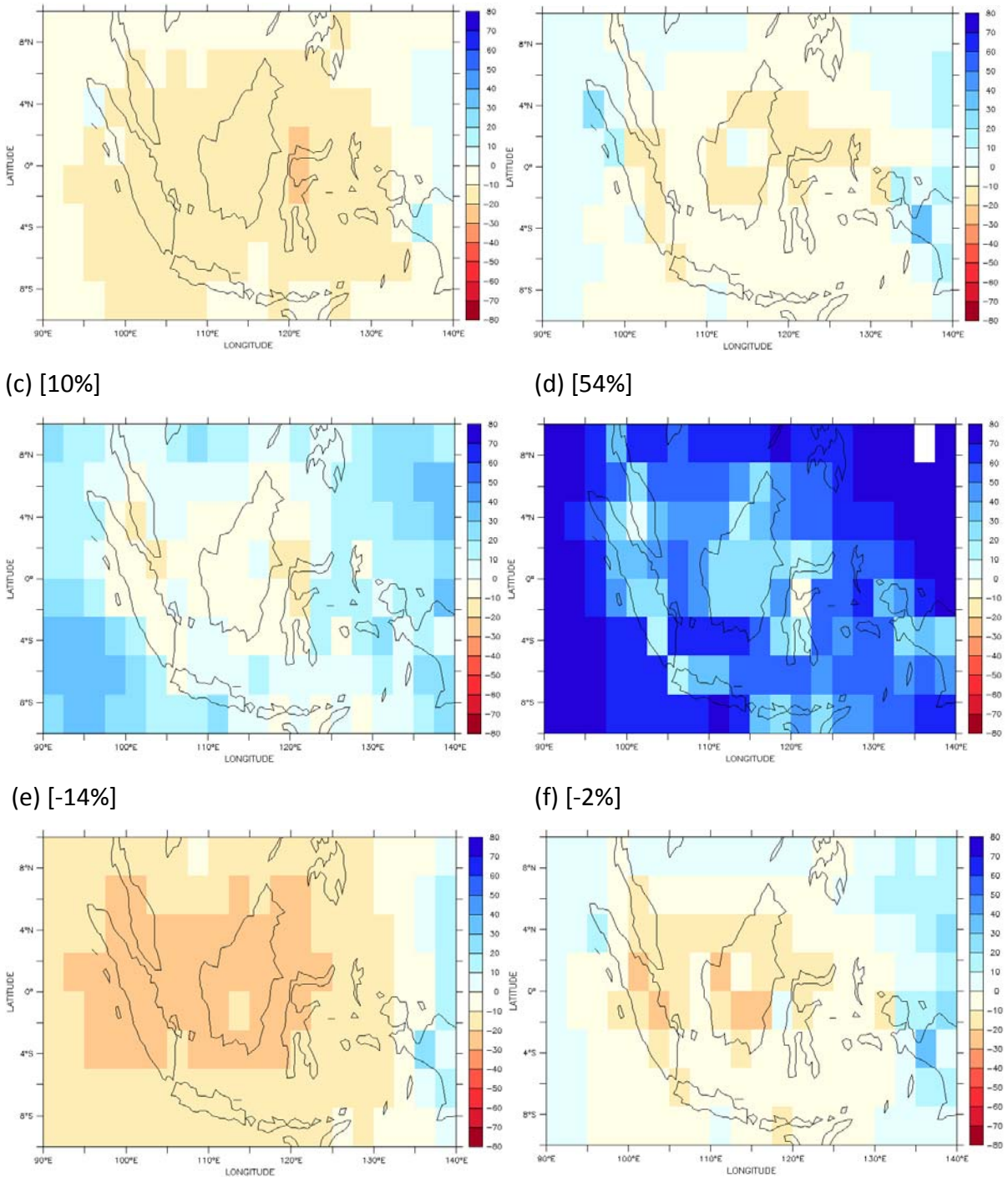

(c) [10%]

(d) [54%]

(e) [-14%]

(f) [-2%]

Figure 5-3. Average middle cloud fraction for 1998-2001: simulation minus ISCCP data for (a) GFC-Mod, (b) EMAN-Mod, (c) GFC-New, (d) EMAN-New, (e) GFC-Auto and (f) EMAN-Auto. Domain-averaged error (model – ISCCP cloud fraction) is shown in parentheses. Color bar indicates fractional coverage of grid cell.

(a) [24%]

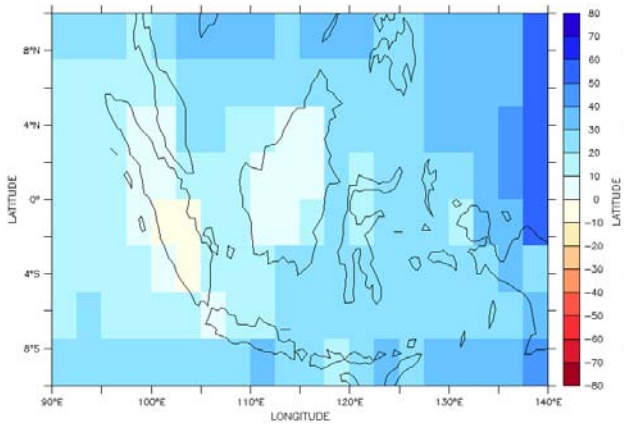

(b) [35%]

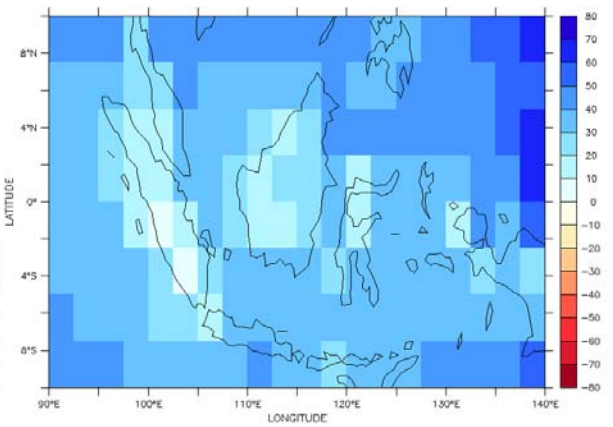

(c) [14%]

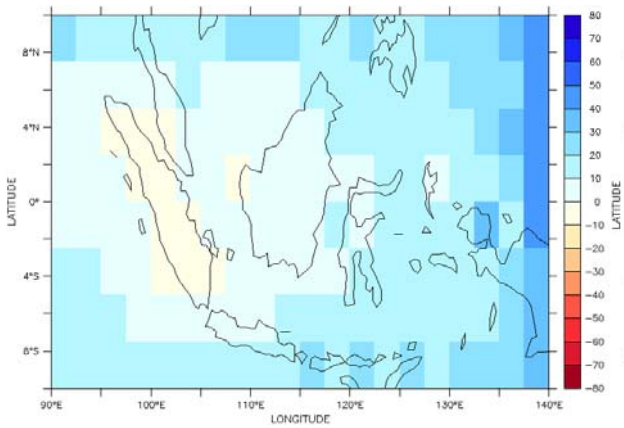

(d) [34%]

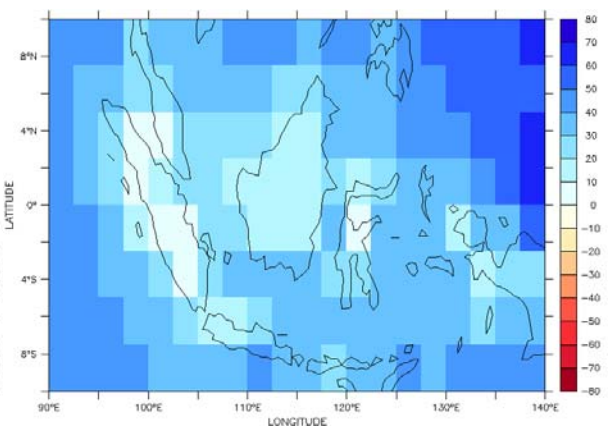

(e) [20%]

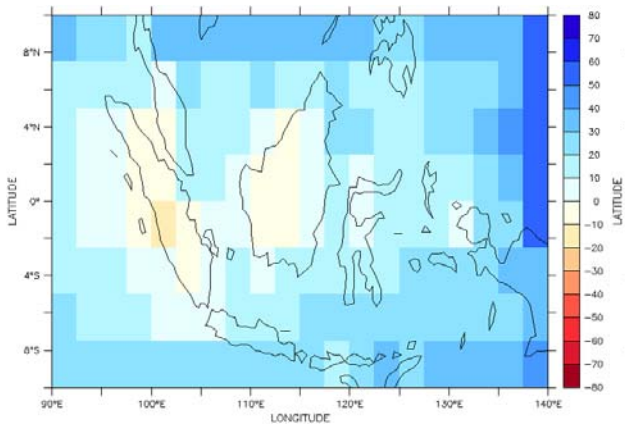

(f) [33%]

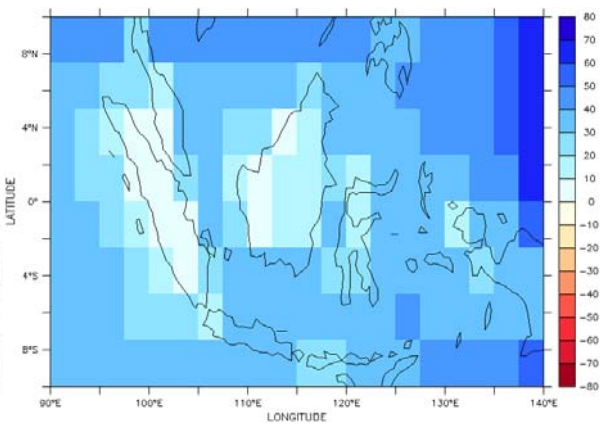

Figure 5-4. Average high cloud fraction for 1998-2001: simulation minus ISCCP data for (a) GFC-Mod, (b) EMAN-Mod, (c) GFC-New, (d) EMAN-New, (e) GFC-Auto and (f) EMAN-Auto. Domain-averaged error (model – ISCCP cloud fraction) is shown in parentheses. Color bar indicates fractional coverage of grid cell.

The figures show that the new autoconversion formulation had a significant impact on the cloud fraction in both simulations.

GFC-Auto and EMAN-Auto have significantly less low and middle cloud cover than GFC-New and EMAN-New. The difference is especially dramatic for EMAN-Auto. For both convection schemes, the previous overestimation bias in low cloud cover relative to ISCCP has been substantially reduced, and GFC-Auto produces low clouds comparable to that of GFC-Mod. However, some overestimation bias in low cloud remains with both schemes, particularly over land.

With both GFC-Auto and EMAN-Auto, the mid-level cloud is reduced to coverage comparable to that of GFC-Mod and EMAN-Mod. This has removed the overestimation bias compared to ISCCP that was created in GFC-New and EMAN-New, and EMAN-Auto in particular shows good agreement with the ISCCP data. There is an observed cloud cover minimum in the middle atmosphere, and hence it is encouraging that the RegCM3 simulations capture this minimum. Zuidema (1998) used soundings obtained over the TOGA-COARE study site and co-located satellite-derived brightness temperatures to show that there is a minimum in cloud cover in the 600-800 mb region over the tropical western Pacific warm pool under all weather conditions. It is thought that this cloud cover minimum is due to detrainment of convective clouds into layers of enhanced stability around the 600-800 mb region (Zuidema 1998).

All the simulations presented here show an overestimation of high cloud relative to ISCCP, which does not show much sensitivity to any of the changes made in this thesis with either convection scheme. High cloud cover is primarily produced by the SUBEX routine in these simulations as the result of moisture transported aloft by convective motion. Although the convective updraft did change between simulations (as evidenced by changes to convective rainfall, Table 4-6 and Table 5-4) due to the different radiative forcing produced by different low and mid-level cloud cover, it seems that the degree to which the updraft mass flux changed was not sufficient to significantly affect the calculation of high large-scale cloud. This issue will be discussed further in Section 5.5.

Figure 5-5 and Figure 5-6 show the mean diurnal cycle of the cloud cover profile over land for the period 1998-2001, respectively for the Grell Fritsch-Chappell and Emanuel schemes, and Figure 5-7 and Figure 5-8 show the same profiles for ocean.

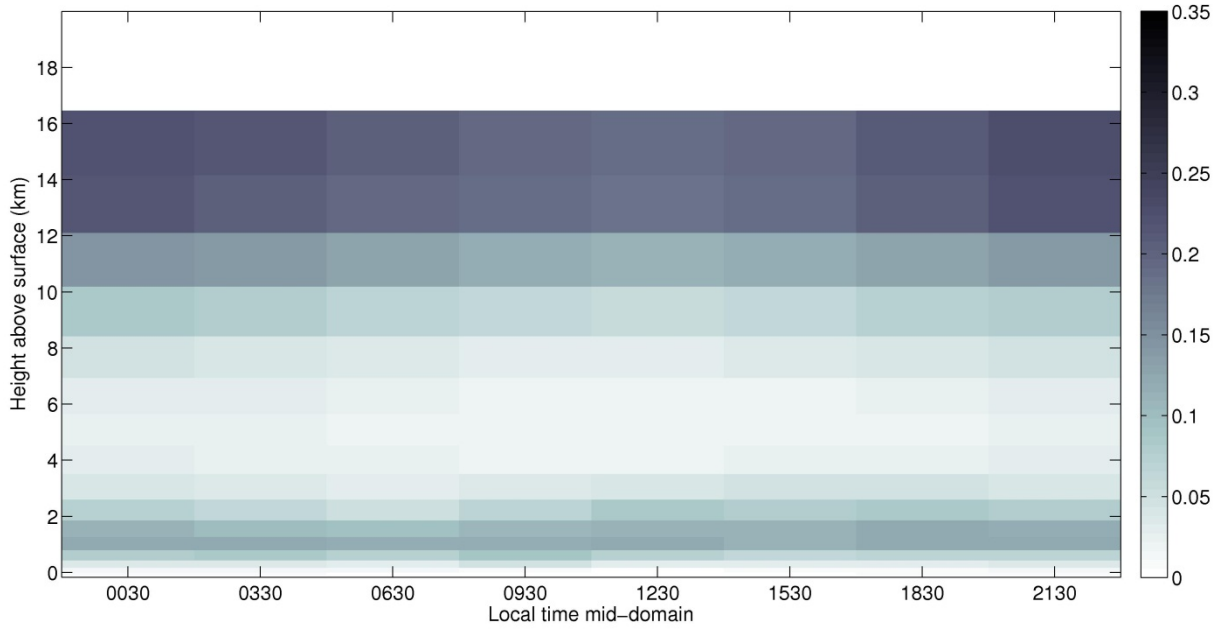

Figure 5-5. Average diurnal cycle of cloud cover over land 1998-2001 using Grell Fritsch-Chappell scheme with new autoconversion formulation. Color bar indicates fractional coverage of grid cell.

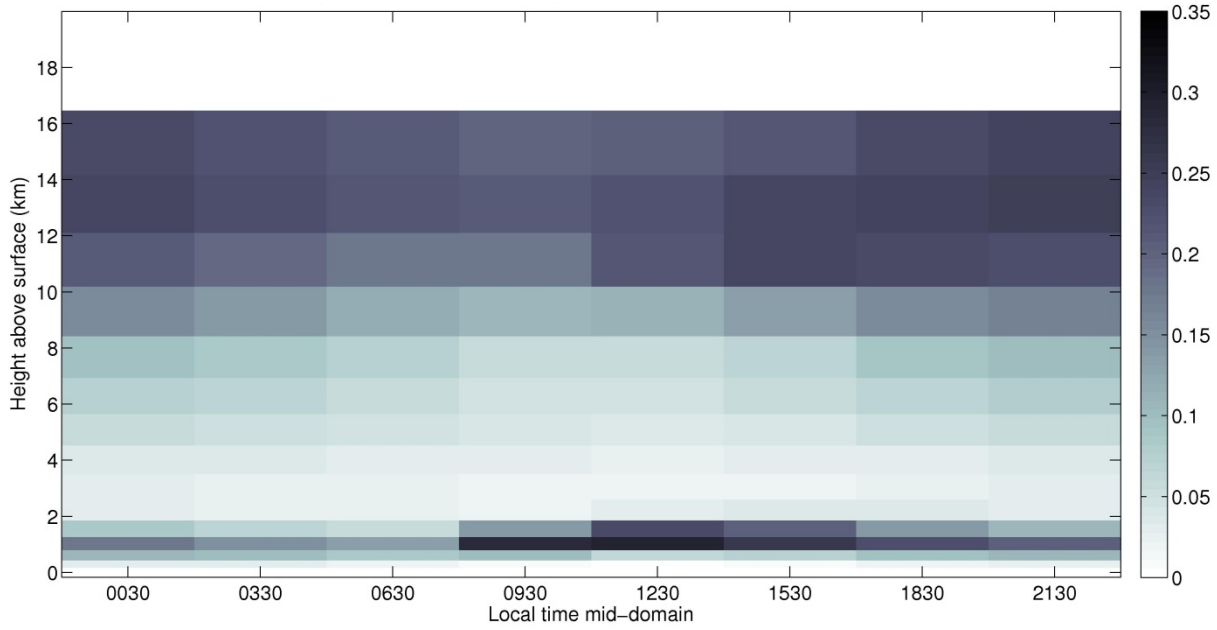

Figure 5-6. Average diurnal cycle of cloud cover over land 1998-2001 using Emanuel scheme with new autoconversion formulation. Color bar indicates fractional coverage of grid cell.

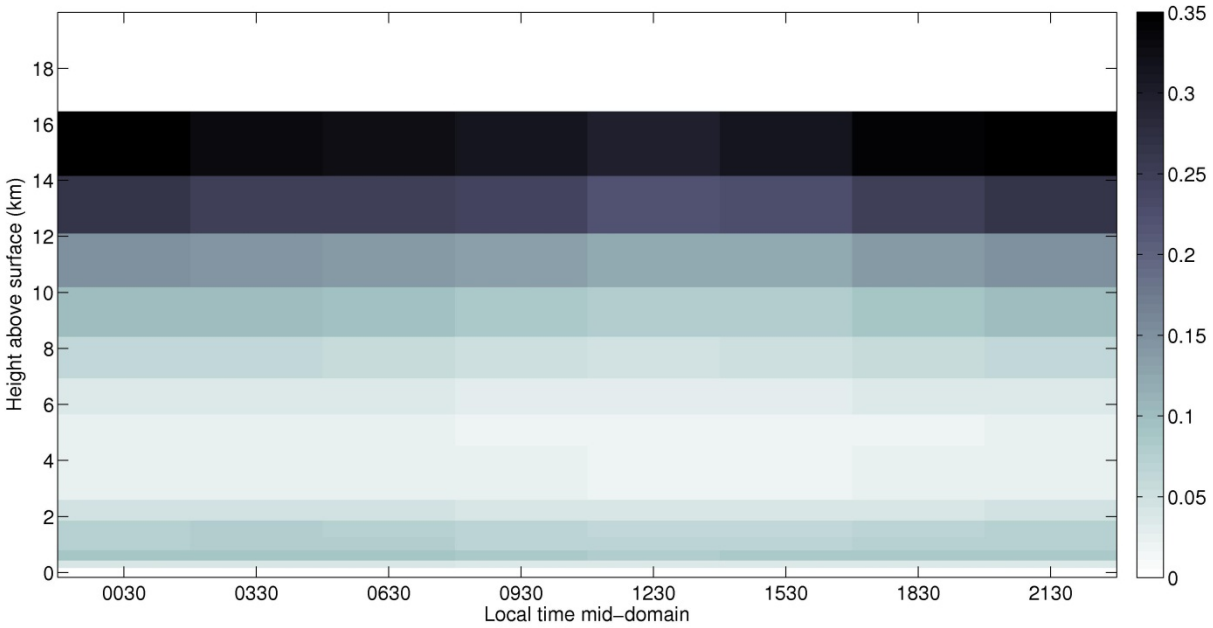

Figure 5-7. Average diurnal cycle of cloud cover over ocean 1998-2001 using Grell Fritsch-Chappell scheme with new autoconversion formulation. Color bar indicates fractional coverage of grid cell.

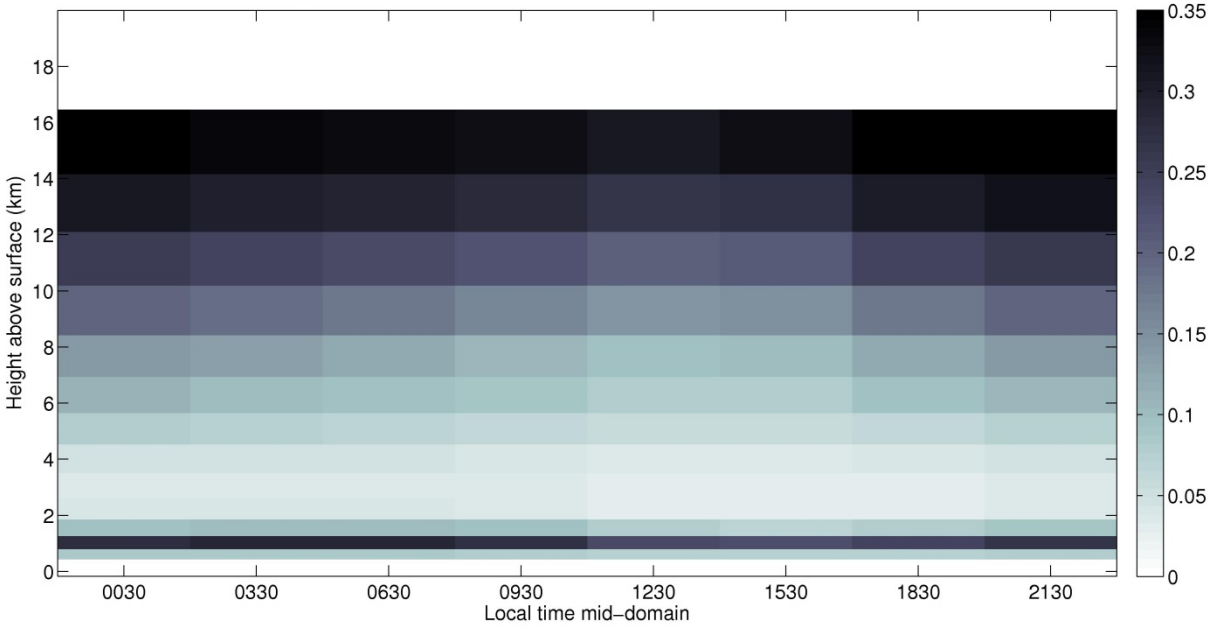

Figure 5-8. Average diurnal cycle of cloud cover over ocean 1998-2001 using Emanuel scheme with new autoconversion formulation. Color bar indicates fractional coverage of grid cell.

These figures more clearly illustrate the impact that the new autoconversion formulation had on the convective cloud cover.

Over land, the signature of daytime convective activity can still be seen from 9:30 am to about 6:30 pm, but the residual cloud is mostly confined to the lower parts of the cloudy region just above cloud base, where precipitation is not as efficient. The low cloud is denser in the new GFC-Auto simulation compared to the previous GFC-New simulation, but less high cloud is produced. Conversely, more high cloud is produced in the new EMAN-Auto simulation compared to the previous EMAN-New simulation, although the low cloud has been reduced. With both schemes, the new autoconversion formulation has almost entirely removed the column of cloud that was so prominent in the Chapter 4 results, associated with convective activity. This suggests that the rainfall efficiency has been substantially increased in the 3-8 km region with the new autoconversion formulation, such that convective cloud produced in this region is quickly converted into rainfall and dissipated.

Despite the consistent reduction in mid-level cloud, the impact of the new autoconversion formulation on high and low cloud cover suggests very different impacts to convective mass flux and vertical transport. With the Grell scheme, a reduction in high cloud cover suggests less vertical transport of moisture due to convection, and the increase in low cloud cover indicates that more condensate is remaining in cloud form at low levels rather than being rained out. But with the Emanuel scheme, a reduction in low cloud cover and increase in high cloud cover suggests that more convective rainfall is being produced and there is an increase in vertical transport of moisture to high altitudes. Therefore it is expected (and shown in Table 5-4) that the new autoconversion formulation has produced a net increase in rainfall production with the Emanuel scheme but a net decrease in rainfall production with the Grell scheme. This will discussed further in Section 5.5.

Over ocean, Figure 5-7 and Figure 5-8 show that the new formulation has also removed the cloud in the range 2-6 km above the surface where the bulk of the convective cloud was shown to exist in Chapter 4. With both simulations, the high cloud cover occupies fewer model layers but covers a greater fractional area within the layers it occupies, especially at the top of the atmospheric column. Low cloud cover is reduced to a relatively thin layer 1-2 km above the surface.

It is important to note the differences in the diurnal cycles of cloud cover between the earlier simulations and the ones with the new autoconversion. Figure 5-2 to Figure 5-4 indicate that the time-mean cloud cover compared to ISCCP is not very different between the cloud cover from the modified simulations presented in Chapter 3 and this latest work. But Figure 5-5 and Figure 5-6 clearly show that the diurnal cycles are shifted such that the maximum low cloud cover occurs in the afternoon in GFC-Auto and EMAN-Auto rather than at night, as was the case for GFC-Mod and EMAN-Mod. This phase shift has significant implications for radiative fluxes (described in Section 5.4.3).

5.4.2 Cloud Water Content

Figure 5-9 and Figure 5-10 compare the simulated CLW from the simulations with the new autoconversion formulation to the cloud water content measured by CloudSat. Note that the CLW profiles plotted for each simulation represent the radiatively-active CLW, i.e. the CLW 'seen' by the radiation scheme within RegCM3. The figures show that the new autoconversion formulation had a substantial impact on the profiles of CLW over both land and ocean.

Consistent with the reduction in afternoon mid-level cloud cover, Figure 5-9 and Figure 5-10 show substantial reductions in daytime CLW in the 2-8 km elevation range with both GFC-Auto and EMAN-Auto. These reductions result in a minimum of CLW at around 6 km elevation, comparable to the minimum observed in the CloudSat data, and remove much of the overestimation in CLW that was present in GFC-New and EMAN-New throughout the vertical column. The increase in CLW below 4 km simulated by GFC-Auto improves the performance of this scheme relative to the CloudSat data, such that the peak CLW around 2 km elevation matches closely with the CloudSat observations.

(a)

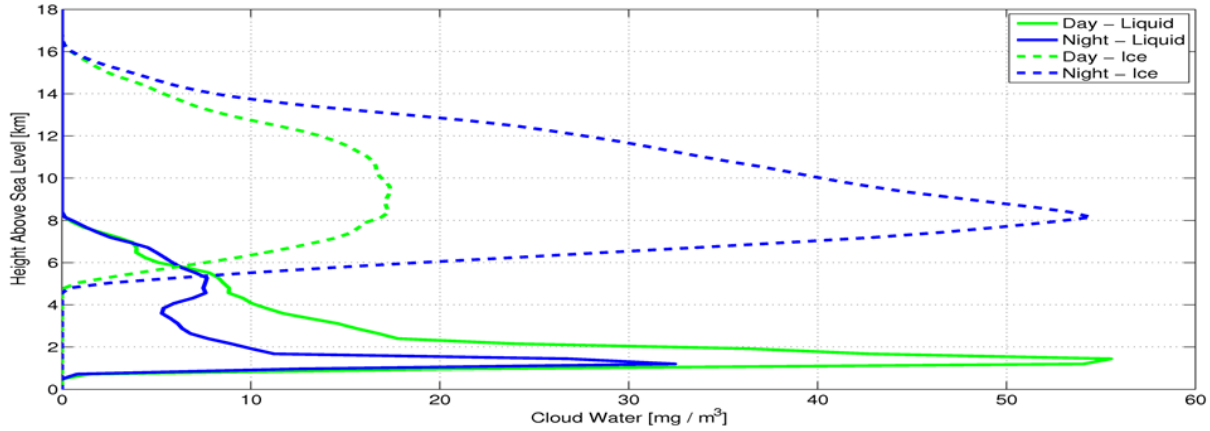

(b)

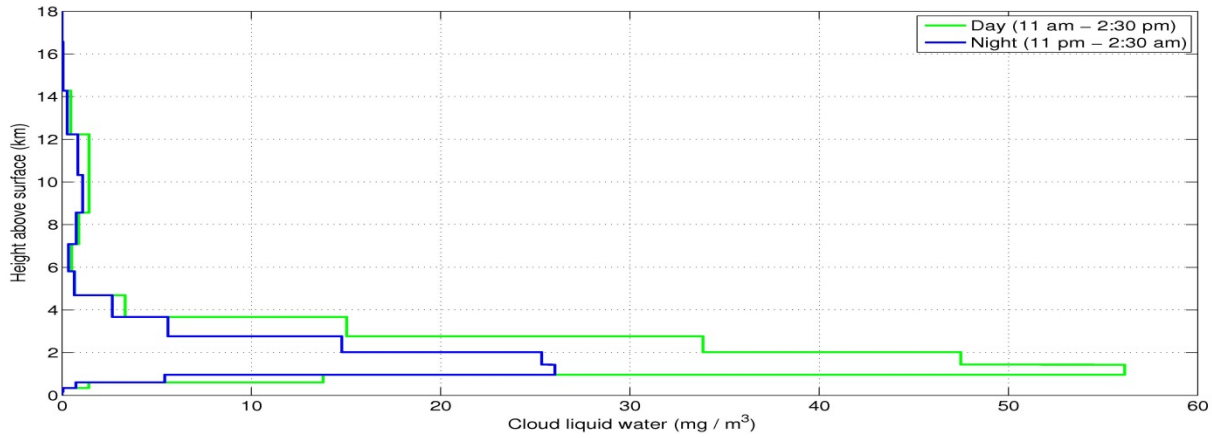

(c)

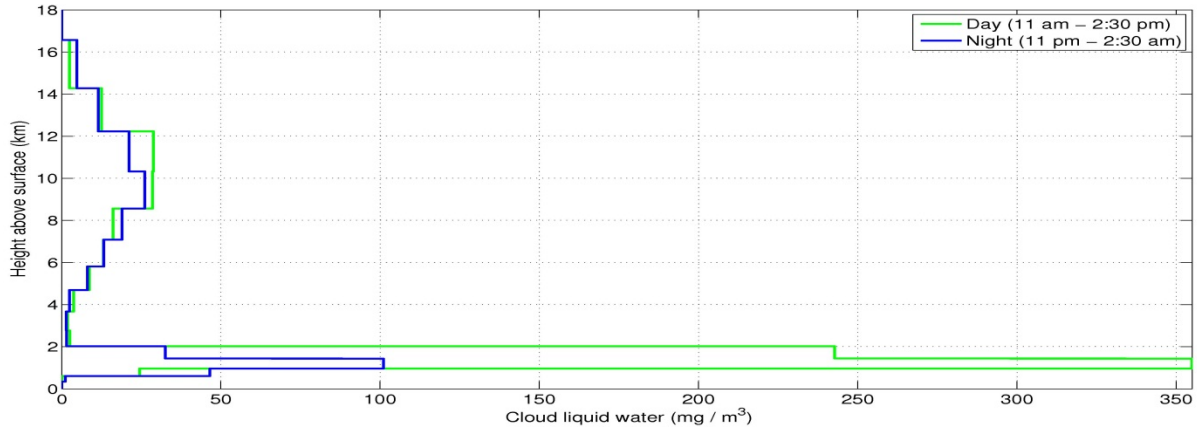

Figure 5-9. Average cloud liquid water (in mg m^{-3}) profile over central Borneo from (a) CloudSat for period 2006-2011, (b) simulation using Grell Fritsch-Chappell scheme with new convective cloud cover for period 1998-2001, (c) as for middle but using Emanuel scheme (note the change in x-axis).

(a)

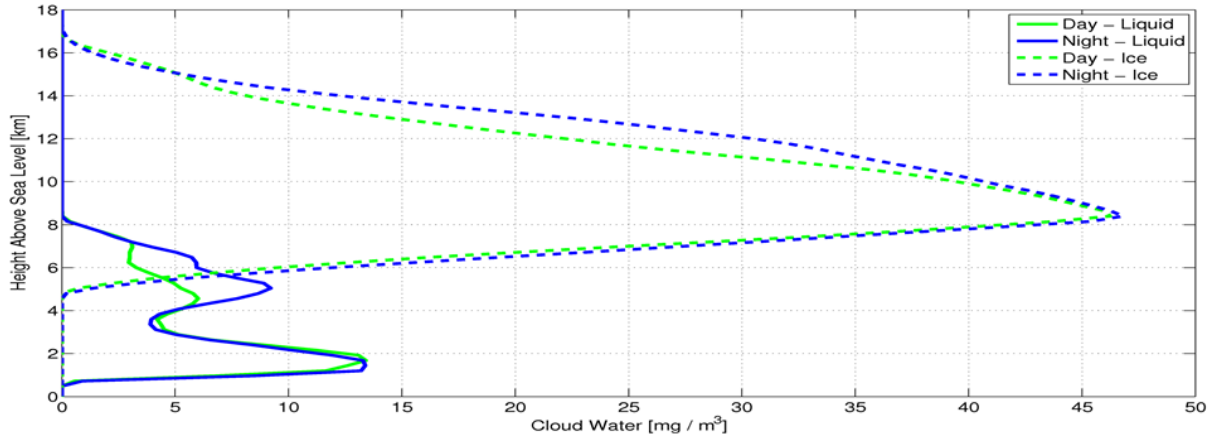

(b)

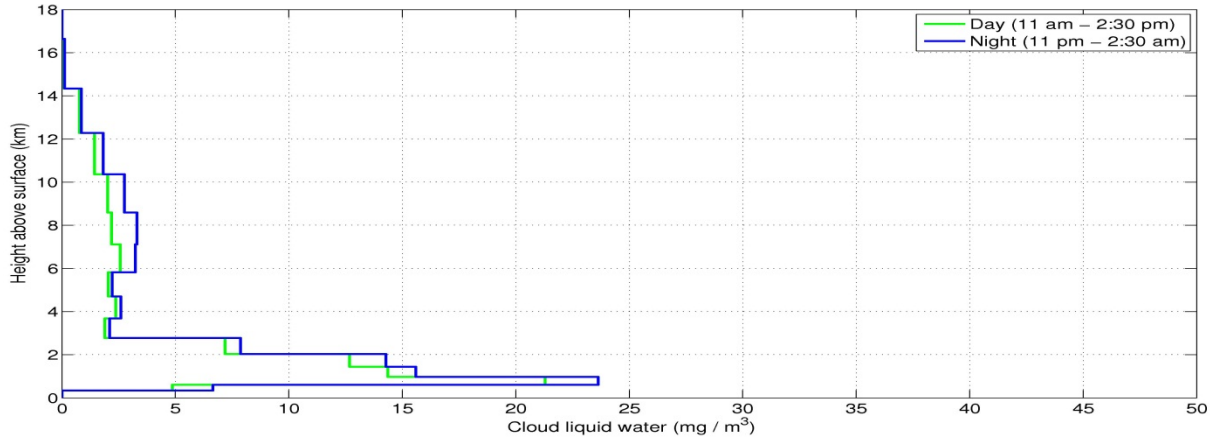

(c)

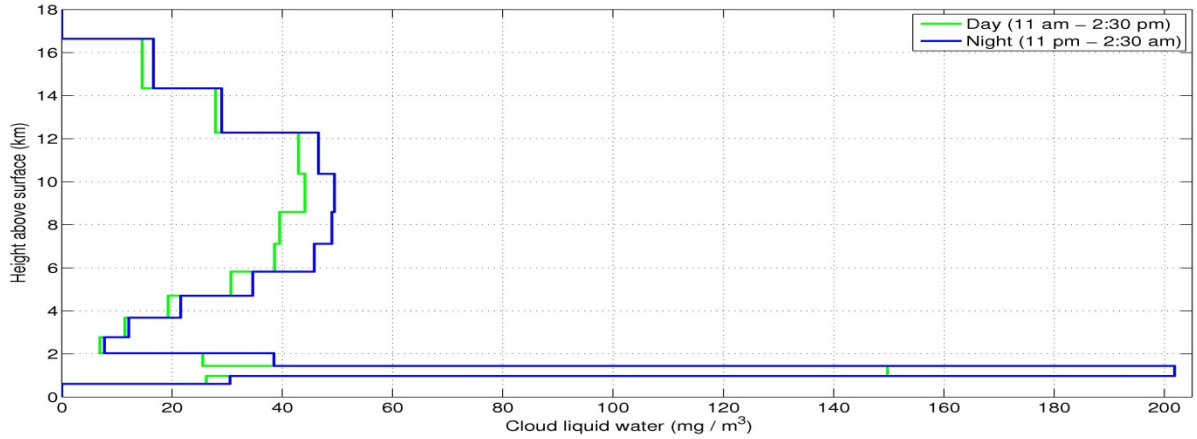

Figure 5-10. Average cloud liquid water (in mg m^{-3}) profile over western Pacific Ocean from (a) CloudSat for period 2006-2011, (b) simulation using Grell Fritsch-Chappell scheme with new convective cloud cover for period 1998-2001, (c) as for middle but using Emanuel scheme (note the change in x-axis).

However, some differences remain between the simulated CLW and CloudSat. GFC-Auto shows severe underestimation of high CLW, at 8-14 km elevation, over both central Borneo and the western Pacific Ocean. (Note that the x-axes on the plots for EMAN-Auto are different to those for CloudSat; EMAN-Auto actually compares well to CloudSat at high elevations.) The simulated high CLW did not change significantly between GFC-Mod and GFC-Auto, and even in GFC-New the increased values of CLW were not sufficient to match CloudSat. The simulated convective updraft mass flux with the Grell scheme is substantially weaker than with the Emanuel scheme. These results suggest that the weaker Grell flux is inadequate to represent the moisture transport associated with convection over the Maritime Continent region.

Low CLW, below 2 km elevation, simulated by EMAN-Auto is significantly higher than the CloudSat data. However, it is difficult to determine whether this represents an error in the model or not. The model output contains many instances when convective rainfall is present and the CloudSat data is only from non-precipitating retrievals. Also, the CLW values simulated by the Emanuel scheme fall within the range of observed CLW, as shown in Table 5-2. Therefore it is possible that the low CLW simulated by the Emanuel scheme is actually close to realistic CLW.

5.4.3 Radiative and Turbulent Heat Fluxes

Figure 5-11 to 5-14 show the average diurnal cycle of incoming solar radiation (insolation) reaching the surface over land and ocean with the SRB observations and all six simulations presented in this chapter, including modifications to the PBL region ('-Mod'), those modifications plus the new convective cloud fraction ('-New') and all changes including the new autoconversion formulation ('-Auto'). Mean daily values are given in parentheses.

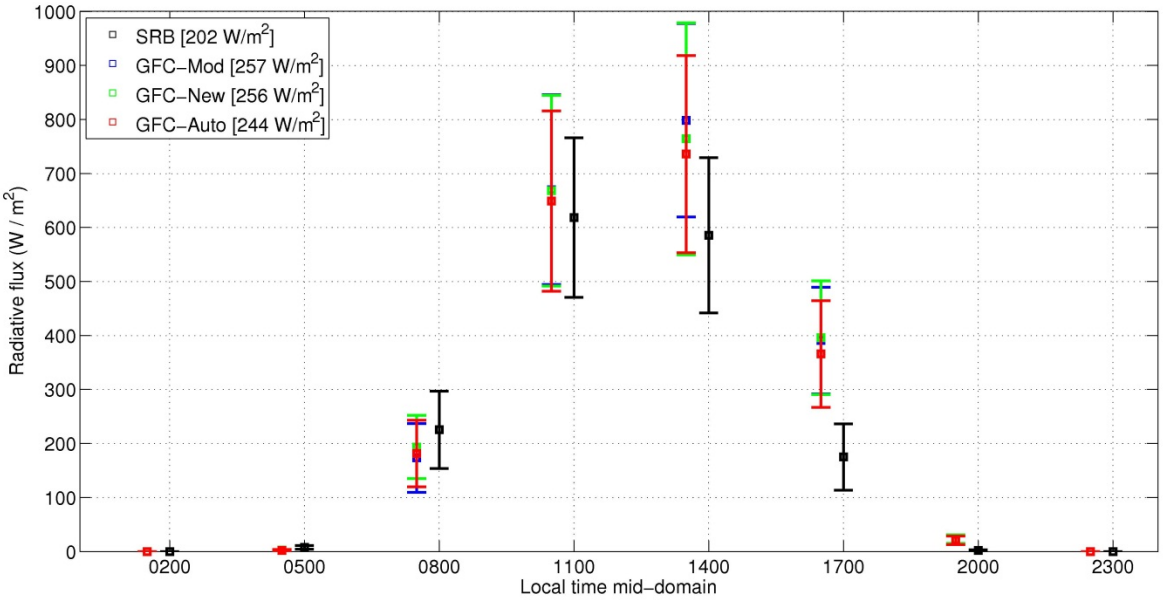

Figure 5-11. Diurnal cycle of incoming solar radiation (in W m^{-2}) averaged over land for period 1998-2001, from SRB observations and simulations using Grell Fritsch-Chappell scheme with modifications from Chapter 3 ('GFC-Mod'), those modifications plus the new convective cloud fraction and CLW from Chapter 4 ('GFC-New') and new autoconversion formulation combined with all other changes ('GFC-Auto'). Square symbol indicates mean value; error bars indicate +/- 1 standard deviation.

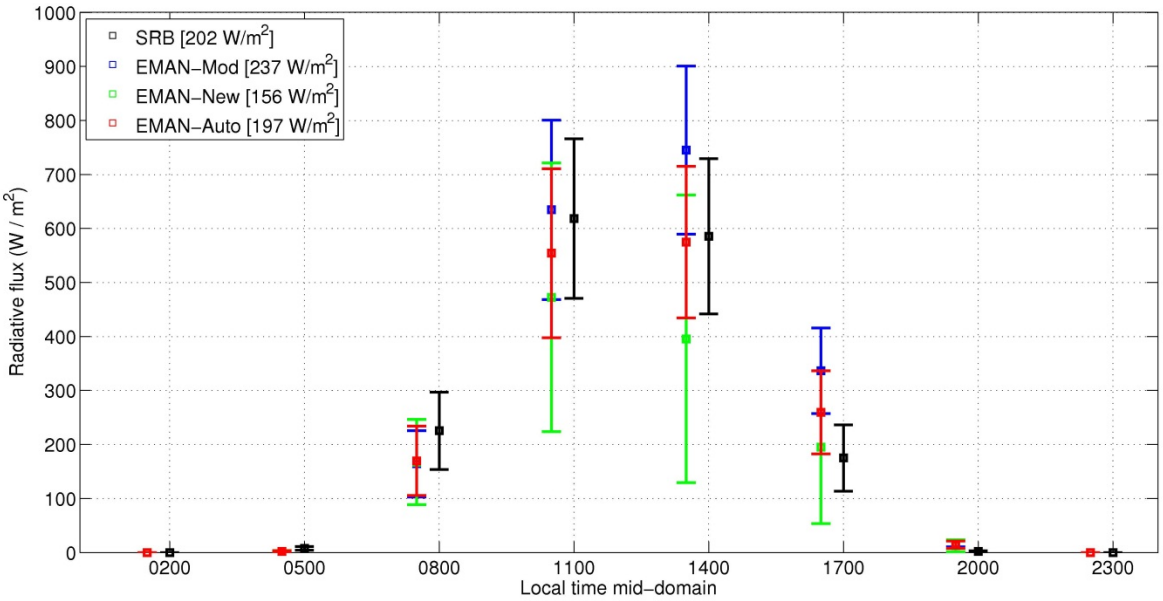

Figure 5-12. As for Figure 5-11 but with the Emanuel convection scheme. Square symbol indicates mean value; error bars indicate +/- 1 standard deviation.

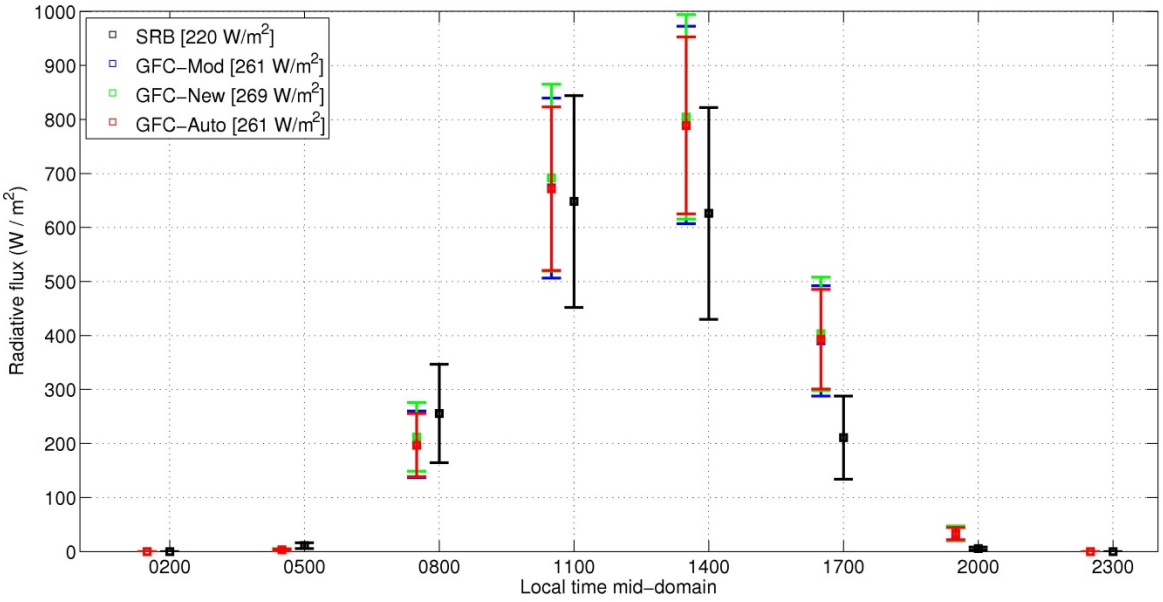

Figure 5-13. Diurnal cycle of incoming solar radiation (in W m^{-2}) averaged over ocean for period 1998-2001, from SRB observations and simulations using Grell Fritsch-Chappell scheme with modifications from Chapter 3 ('GFC-Mod'), those modifications plus the new convective cloud fraction and CLW from Chapter 4 ('GFC-New') and new autoconversion formulation combined with all other changes ('GFC-Auto'). Square symbol indicates mean value; error bars indicate +/- 1 standard deviation.

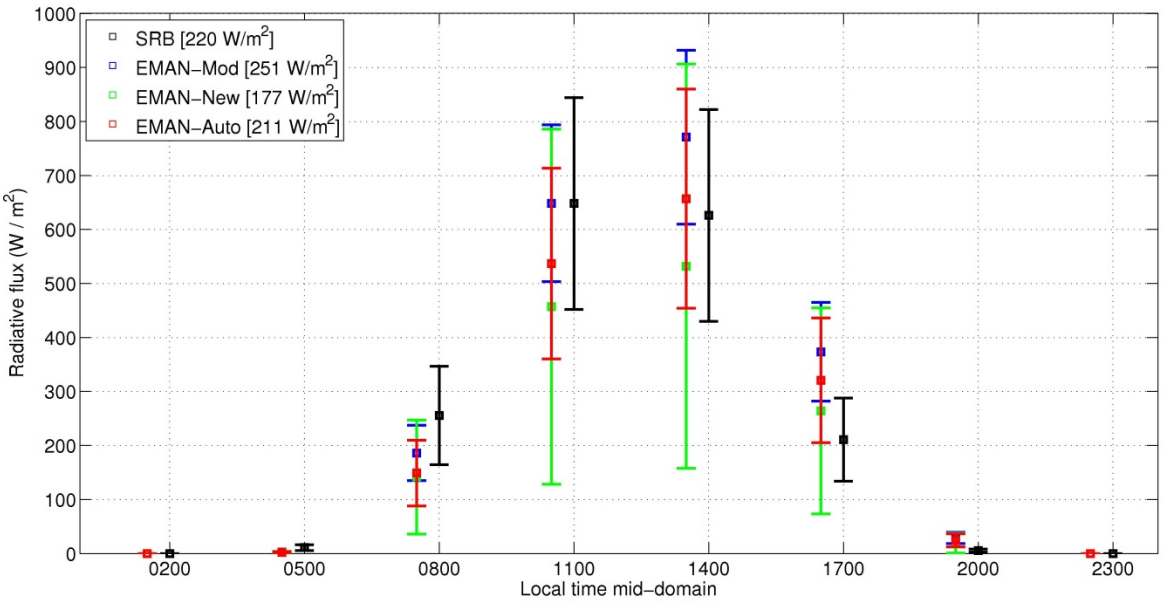

Figure 5-14. As in Figure 5-13 but using the Emanuel convection scheme. Square symbol indicates mean value; error bars indicate +/- 1 standard deviation.

The results show that the new autoconversion formulation had a small impact on solar radiation with the Grell scheme but a substantial impact with the Emanuel scheme, over both land and ocean surfaces.

Over land, incoming and net absorbed solar radiation were slightly decreased with GFC-Auto, particularly during the early afternoon when convective activity is strongest. This is consistent with the increase in low cloud cover in the early afternoon shown in the previous figures. This decrease in solar radiation brings the results closer to the SRB observations compared to GFC-Mod and GFC-New, but there is still residual overestimation of solar radiation with this scheme, particularly in the early afternoon. Over ocean, insolation with GFC-Auto was reduced slightly relative to GFC-New and brought back to the magnitude of GFC-Mod. This reflects the increase in high cloud that was produced by this simulation. However, the peak insolation is overestimated by nearly 200 W m^{-2} in the early afternoon over both land and ocean with all the Grell simulations.

It was shown that the simulated low- and mid-level cloud cover and CLW in GFC-Auto compared well to ISCCP and CloudSat, and that high cloud cover was overestimated but high CLW was underestimated. Since incoming radiation is affected by both the cloud fraction and cloud liquid water path, the overestimation of insolation shown by GFC-Auto must result from the deficiency in the cloud liquid water path at high altitudes. In turn, this is the result of weak convective updraft mass flux simulated by this scheme.

The results of EMAN-Auto show that the new autoconversion formulation led to a significant increase in insolation over both land and ocean surfaces compared to EMAN-New but less insolation than EMAN-Mod. This is consistent with the significant reduction in cloud cover and CLW in the new simulation due to the change in rainfall efficiency. Over land, the new EMAN-Auto simulation produces a small underestimation in solar radiation in the late morning, but the simulated afternoon radiation is much improved. In general, the diurnal cycle of solar radiation over land matches reasonably well to the SRB observations with this new simulation. Over ocean, the new EMAN-Auto simulation produces some underestimation of solar radiation in the morning and overestimation in the late afternoon,

but again the diurnal cycle is much improved compared to the SRB observations. It is especially encouraging that the peak insolation matches well, both in magnitude and timing.

The average daily radiative and turbulent heat fluxes are summarized in Table 5-3 for all the simulations presented in this chapter.

Table 5-3. Average daily surface radiative and turbulent heat fluxes (all in W m^{-2}) over period 1998-2001 for SRB (radiative) and field studies (LH and SH) ('Observations'), compared to simulations using the modifications from Chapter 3 ('-Mod'), those modifications plus the new convective cloud fraction and CLW ('-New'), and simulations with the new autoconversion formulation combined with all other changes ('-Auto').

LAND

Simulation	SW_{dn}	SW_{up}	SW_{net}	Surface albedo	Planetary albedo	LW_{dn}	LW_{up}	R_N	LH	SH
Observations	*202*	*31*	*171*	*16%*	*48%*	*411*	*452*	*129*	*95*	*34*
GFC-Mod	257	35	222	14%	44%	401	459	164	118	48
GFC-New	256	35	221	13%	41%	396	457	160	112	50
GFC-Auto	244	33	211	14%	39%	402	463	150	93	58
EMAN-Mod	237	33	204	14%	49%	409	456	157	137	21
EMAN-New	156	21	135	13%	49%	414	459	90	68	23
EMAN-Auto	197	29	168	15%	46%	411	455	124	105	20

OCEAN

Simulation	SW_{dn}	SW_{up}	SW_{net}	Surface albedo	Planetary albedo	LW_{dn}	LW_{up}	R_N	LH	SH
Observations	*220*	*14*	*206*	*6%*	*45%*	*420*	*467*	*158*	*109*	*10*
GFC-Mod	261	16	245	6%	43%	413	473	184	128	15
GFC-New	269	16	252	6%	40%	408	473	187	129	17
GFC-Auto	261	17	244	7%	40%	412	473	183	125	13
EMAN-Mod	251	16	235	6%	49%	420	473	182	118	7
EMAN-New	177	11	166	6%	49%	428	473	121	118	5
EMAN-Auto	211	14	197	7%	49%	426	473	150	120	5

Notes on Table 5-3: SW_{dn} = shortwave (solar) radiation incident at the surface, SW_{abs} = net absorbed shortwave radiation at the surface, LW_{dn} = longwave radiation incident at the surface, LW_{up} = longwave radiation emitted from surface, R_N = net radiation absorbed at surface, LH = latent heat flux away from surface, SH = sensible heat flux away from surface. See Notes on Table 3-5 for explanation of albedo calculation.

Over land, Table 5-3 shows that the new autoconversion formulation improved the net radiation with both convection schemes, although the Grell scheme still produces an overestimation of net radiation while the Emanuel scheme matches well to observations.

The planetary albedo is underestimated over land with the new GFC-Auto simulation due to the reduction in high cloud cover, while the planetary albedo continues to match observations well with the new EMAN-Auto simulation.

LH fluxes over land are improved with both new simulations, but with some overestimation using the Emanuel scheme. There is still substantial error with both schemes in the SH flux – SH is significantly overestimated with the Grell scheme and underestimated with the Emanuel scheme. These errors are reflective of other simulation errors: overestimation of insolation with the Grell scheme drives high SH flux, while overestimation of rainfall with the Emanuel scheme (Table 5-4) drives high LH flux. Therefore these results illustrate how sensitively the partitioning of energy at the land surface responds to the available radiation and moisture.

Over ocean surfaces, significant overestimation of insolation persists with the new GFC-Auto simulation. The planetary albedo is slightly underestimated with this scheme. Net radiation is substantially improved in the new EMAN-Auto simulation, bringing the results close to observations, while planetary albedo remains unchanged since high cloud cover did not change. As expected, given the forced SST used in these simulations, the LH and SH fluxes did not change significantly over ocean in the new simulations. Since the SSTs are fixed in this simulation, turbulent heat fluxes over the ocean show little sensitivity to the surface net radiation. However, if an ocean model were coupled to RegCM3, the results with GFC-Auto indicate that significant errors would likely propagate through the model system due to significant overestimation of net radiation. A coupled model used with EMAN-Auto should provide substantially better simulation over the ocean.

The new autoconversion function had considerable positive outcomes on EMAN-Auto: across all the radiative flux, turbulent heat flux and albedo metrics presented in Table 5-3, EMAN-Auto shows good agreement with the observations, with the exception of some underestimation of sensible heat flux. This outcome indicates that the combination of

changes made to the model leads to improved physical realism throughout the simulation, including the convective-radiative feedback, and not merely in the representation of clouds. Therefore it is considered that EMAN-Auto would show improved sensitivity and response to changes in large-scale forcings.

5.4.4 Rainfall

Average total, convective and large-scale rainfall volumes over the period 1998-2001 are shown in Table 5-4. The results show divergent behavior between the two convection schemes in response to the new autoconversion function.

Table 5-4. Total, convective and large-scale rainfall (all in mm day^{-1}) averaged over 1998-2001 for land and ocean from TRMM ('Observations'), modified simulations (from Chapter 3, '-Mod'), simulations with new convective cloud fraction and CLW ('-New') and simulations with new autoconversion formulation ('-Auto'). The relative proportions of convective and large-scale rain are shown in parentheses.

Product / Simulation	Land Average			Ocean Average		
	Total	Convective	Large-scale	Total	Convective	Large-scale
TRMM	*8.6*	*5.4 (63%)*	*3.2 (37%)*	*7.0*	*4.0 (57%)*	*3.0 (43%)*
GFC-Mod	10.9	4.4 (40%)	6.5 (60%)	8.5	4.1 (48%)	4.4 (52%)
GFC-New	9.2	4.1 (45%)	5.1 (55%)	7.3	5.5 (75%)	1.8 (25%)
GFC-Auto	5.9	3.1 (52%)	2.8 (48%)	4.8	2.9 (61%)	1.9 (39%)
EMAN-Mod	16.8	9.9 (59%)	6.9 (41%)	6.7	3.8 (57%)	2.9 (43%)
EMAN-New	10.2	2.6 (25%)	7.6 (75%)	10.0	3.0 (30%)	7.0 (70%)
EMAN-Auto	9.9	5.4 (55%)	4.5 (45%)	6.1	3.7 (61%)	2.4 (39%)

Table 5-4 shows that the new autoconversion formulation led to a reduction in convective rainfall over both land and ocean with GFC-Auto. This result seems inconsistent given that the new autoconversion function is more efficiency than the default formula used with this scheme. Also it was noted that the number of grid points undergoing convection at any given timestep was significantly increased between GFC-New and GFC-Auto. Hence these results suggest that the Grell scheme produced less rainfall at the surface as the result of more active convection and efficient rainfall production. This counter-intuitive outcome is discussed further in Section 5.5.

Table 5-4 shows an increase in convective rainfall over both land and ocean with EMAN-Auto, compared to EMAN-New. This result is consistent with the increase in rainfall efficiency and reduction in cloud cover associated with the new autoconversion function. The simulated convective and total rainfall volumes produced by EMAN-Auto are a reasonable match to the TRMM data over both land and ocean, showing considerable improvement on the previous simulations using the Emanuel scheme. Large-scale rainfall also decreased over land with both simulations and over ocean with the Emanuel scheme, reflecting the general decrease in cloud cover (and hence available condensate) in those cases.

The net effect is a reduction in total rainfall over both land and ocean with both convection schemes. Over both land and ocean, this improves the results with the Emanuel scheme but produces underestimation of total and convective rainfall with the Grell scheme. The differences in the results produced by the Grell and Emanuel schemes are the consequence of very different approaches to simulating convective updraft mass flux. Section 5.5 below presents a detailed discussion of these approaches and the implications for their use in large-scale climate models such as RegCM3.

Figure 5-15 and Figure 5-16 show the rainfall histograms for land and ocean, respectively, using both convection schemes. To compare the impact of all the changes made in Chapters 3 to 5, the default version of the model is compared to the simulations combining the modifications to the PBL, new convective cloud fraction and CLW, and new autoconversion (named '-Auto' in this chapter).

With the Grell scheme, the changes led to an increase in the frequency of rainfall production, which reduced the non-raining times. But this new rainfall was of very low intensity, which worsened the error in the low intensity rainfall histogram. This is consistent with the other results presented above – the changes with the Grell scheme have produced more convective activity but reduced the total rainfall volume. The reason for this discrepancy is discussed in Section 5.5.

Conversely, the changes made with the Emanuel scheme led to a reduction in convective activity, which improved the non-raining part of the rainfall histogram. Both

large-scale and convective rainfall were decreased with the model changes, which is reflected in changes to the rainfall histogram at all intensities. These changes are consistent with the other results to radiation and cloud cover, as presented above.

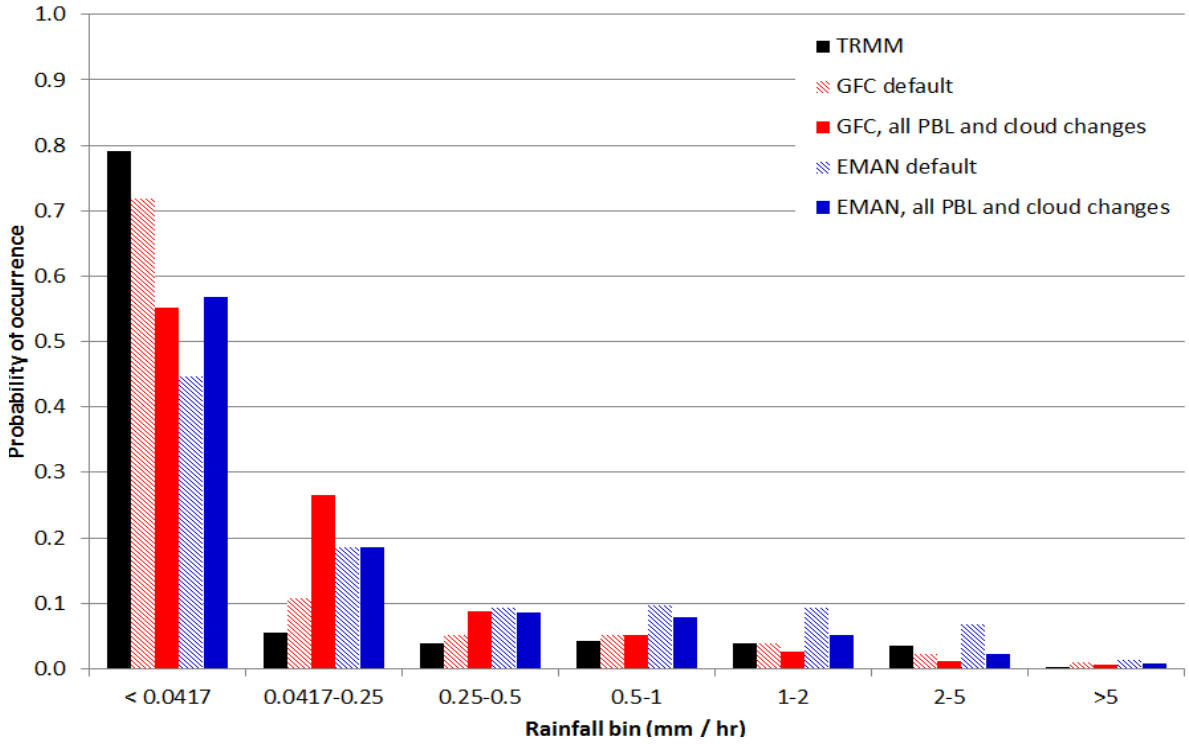

Figure 5-15. Rainfall histogram, with rainfall intensities in mm hr^{-1}, averaged over land grid cells for period 1998-2001, comparing TRMM to simulations using Grell with Fritsch-Chappell (GFC) and Emanuel (EMAN) convection schemes with the default version of the model and incorporating all changes made to the PBL, cloud cover and autoconversion in Chapters 3 to 5.

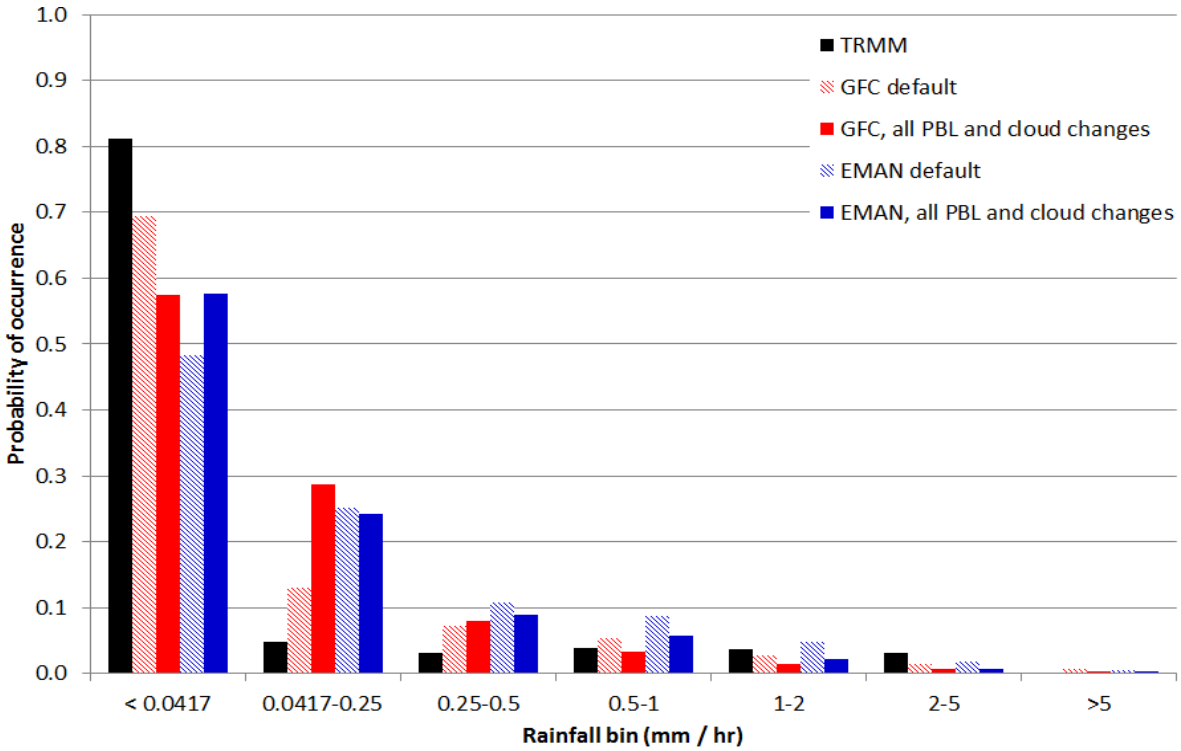

Figure 5-16. As in Figure 5-15 but for ocean grid cells.

Figure 5-17 and Figure 5-18 show the average diurnal cycles of rainfall averaged over land and ocean, respectively, for the new simulations ('-Auto'). The figures show that the considerable reduction in rainfall with GFC-Auto has almost removed the diurnal cycle of rainfall. Rainfall over land is now missing a distinct diurnal peak. With EMAN-Auto, the magnitude of rainfall over land is considerably improved, but the diurnal cycle is still phase-shifted compared to TRMM, with the average peak occurring about 6 hours too early.

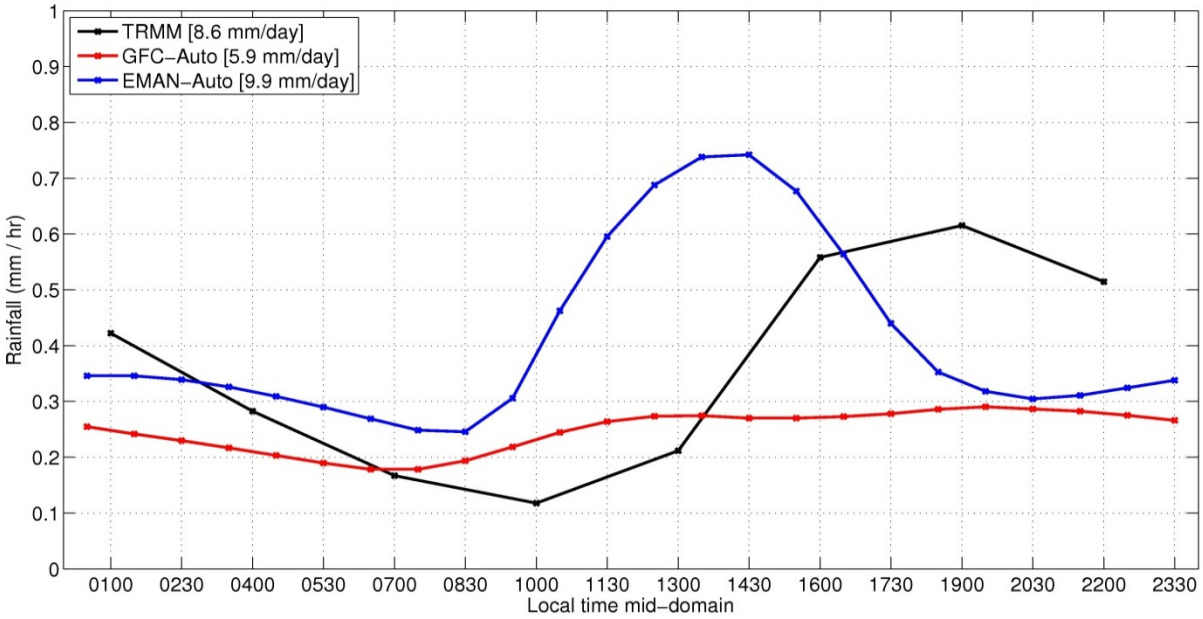

Figure 5-17. Diurnal cycle of rainfall (in mm hr^{-1}) averaged over land for period 1998-2001 for TRMM and the new simulations with all modifications (to PBL region, convective cloud fraction and autoconversion, '-Auto').

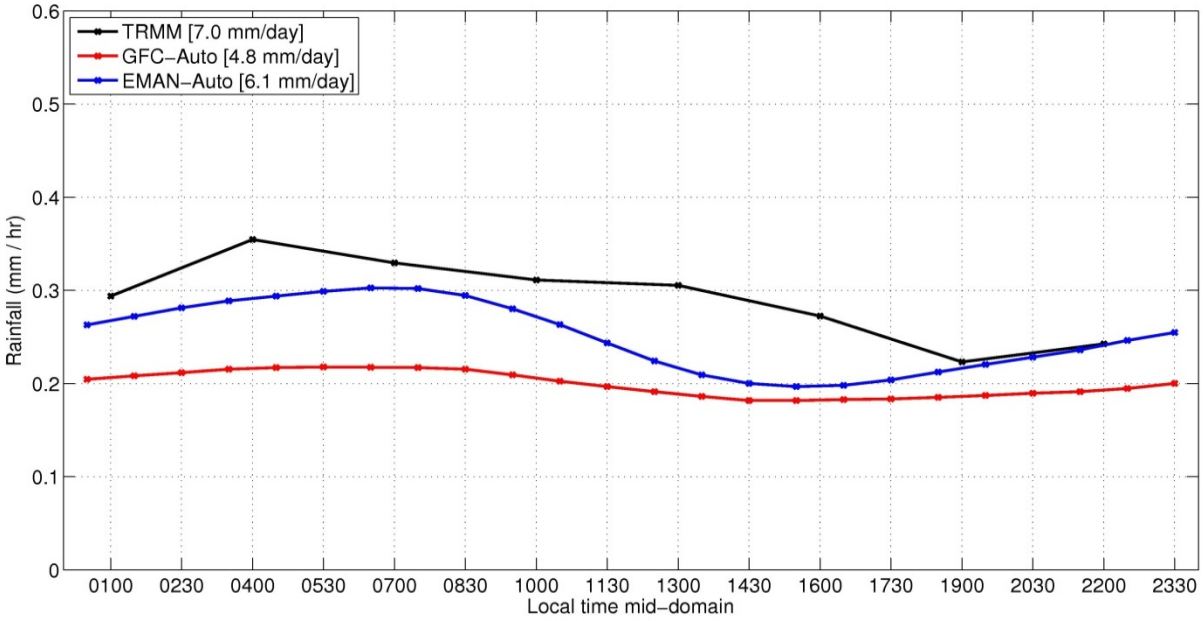

Figure 5-18. Diurnal cycle of rainfall (in mm hr^{-1}) averaged over ocean for period 1998-2001 for TRMM and the new simulations with all modifications (to PBL region, convective cloud fraction and autoconversion, '-Auto').

5.4.5 Temperature and Humidity

The simulated near-surface temperature and moisture fields were also evaluated.

Temperature, water vapor mixing ratio and relative humidity are taken from the ERA40 reanalysis product (Uppala *et al.* 2005), which was interpolated from its original 2.5^{o} resolution to the model grid when used for lateral boundary conditions. The lowest atmospheric layer values are taken from ERA40. To permit a fair comparison, variables simulated by the model were output for the free atmosphere immediately above the canopy rather than using the designated 'anemometer' values. The anemometer height in the model is 10 m above the surface, which actually lies within the vegetated canopy simulated by IBIS over land in this region (which has a height of about 20 m). Therefore the above-canopy simulated values are comparable to the lowest vertical layer from ERA40.

Temperature observations are also taken from the University of East Anglia's Climatic Research Unit (CRU) TS3.0 product (Harris *et al.* 2012), which provides monthly mean temperatures based on interpolation between meteorological stations. Data from CRU is available at 0.5^{o} resolution globally for the period 1901-2006.

Figure 5-19 shows the temperature over land averaged for the period 1998-2001, comparing the CRU TS3.0 and ERA40 values to those simulated by the Grell with Fritsch-Chappell (GFC) and Emanuel (EMAN) convection schemes using the default version of the model (as described in Chapter 2) with the version presented in this chapter incorporating all the modifications to the PBL region, convective cloud cover and CLW, and autoconversion formulation (named '-Auto'). Only land values are shown since SSTs are forced in the simulations and CRU TS3.0 only contains values for land surfaces.

(a) [26.4 °C]

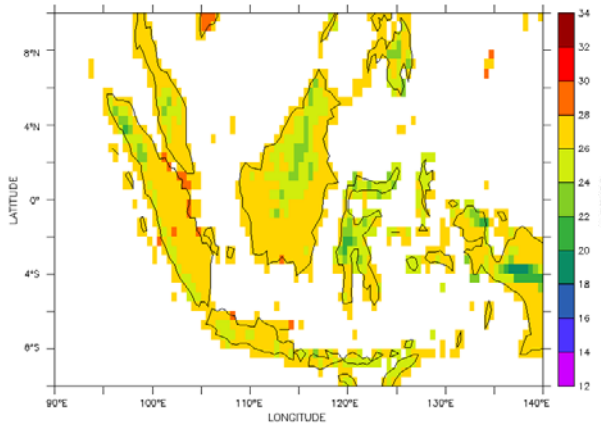

(b) [25.3 °C]

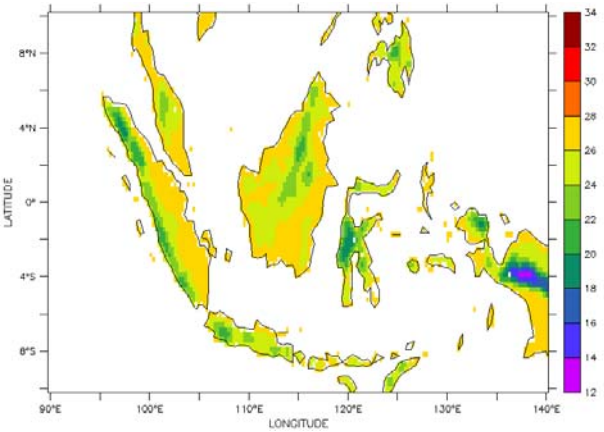

(c) [25.8 °C]

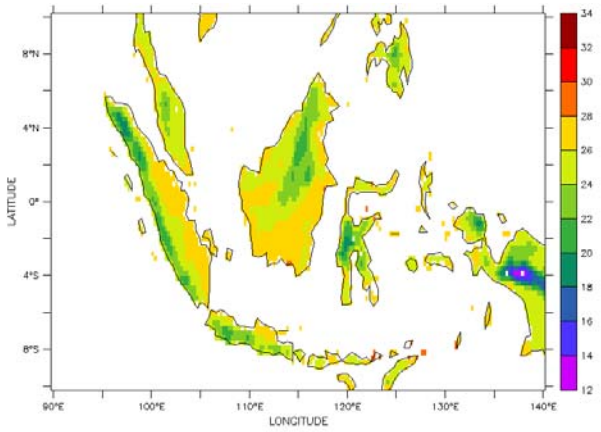

(d) [26.1°C]

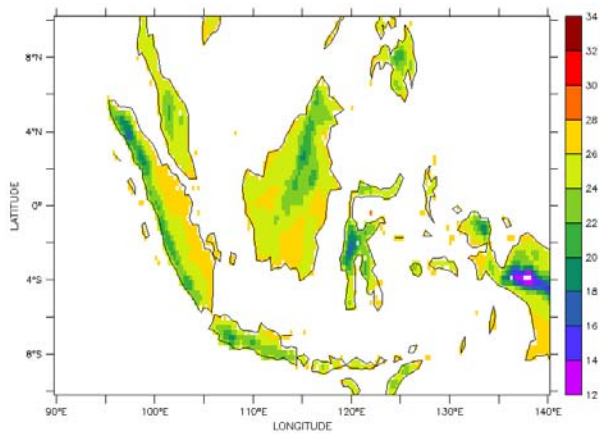

(e) [25.4 °C]

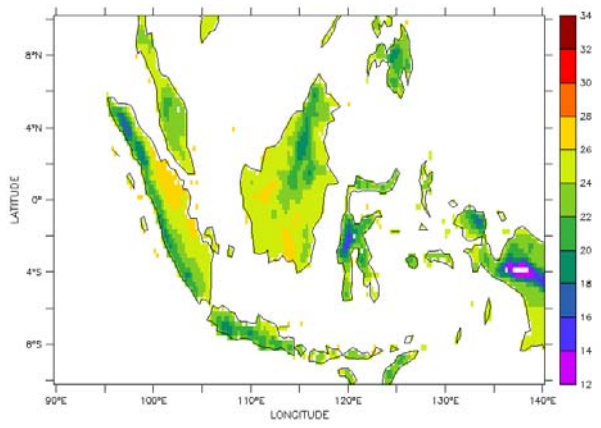

(f) [25.7 °C]

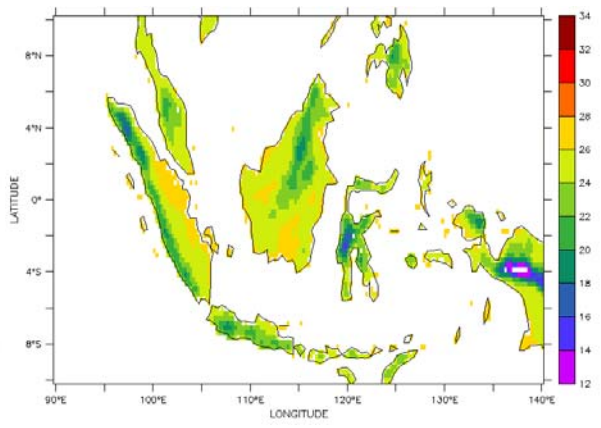

Figure 5-19. Average temperature (in °C) for period 1998-2001 over land surfaces within the model domain, from (a) CRU TS3.0, (b) lowest atmospheric layer from ERA40, (c) GFC default, (d) EMAN default, (e) GFC-Auto simulation, (f) EMAN-Auto simulation. Land-average values are given in parentheses.

There are two important considerations when comparing the model output to the observations. Firstly, the CRU TS3.0 temperature data are taken from surface measurements and therefore will be warmer than the free atmosphere (i.e. lowest model layer) values taken from ERA40 and the model output. Secondly, ERA40 lower atmosphere temperature is known to contain a cold bias over certain regions of the globe. Simmons *et al.* (2004) showed that over Australia, ERA40 has an average cold bias of 0.13 ^{o}C over the period 1979-2001. Those authors stated that a cold bias also exists in ERA40 over the tropics, but the magnitude of this bias was not given (Simmons *et al.* 2004). The near surface air temperature in ERA40 is a better match to the CRU observations in the northern hemisphere than the southern due to the greater number of surface measurements in the northern hemisphere: 75% of the radiosonde measurements used to inform ERA40 come from the northern hemisphere, while only 10% come from the southern hemisphere and 15% from the tropics (Andræ *et al*. 2004). Hence the lower atmosphere temperature in ERA40 will likely be lower than the values simulated by RegCM3.

Figure 5-19 shows that the model simulates the spatial patterns in temperature very well, in all versions. The default version of the model with both convection schemes overestimated the free atmosphere temperature with respect to ERA40 by 0.5-0.8 ^{o}C, consistent with the overestimation in insolation produced in the default model. In the new version of the model ('-Auto'), the bias is reduced to 0.1-0.4 ^{o}C. This is considered a good match to observations, especially given that 1) the ERA40 lower atmosphere temperature contains some unspecified cold bias, and 2) the coarse resolution of the ERA40 product will tend to lose detail over the islands and exhibit less extreme temperatures.

Table 5-5 shows the average lower free atmosphere temperature (T), water vapor mixing ratio (Q) and relative humidity (RH) over land and ocean, for the period 1998-2001. Simulations with both the Grell with Fritsch-Chappell (GFC) and Emanuel (EMAN) convection schemes are shown, comparing the default version of the model (as described in Chapter 2) with the version presented in this chapter incorporating all the modifications to the PBL region, convective cloud cover and CLW, and autoconversion formulation (named '-Auto').

Table 5-5 shows that the Grell scheme tends to underestimate the lower atmosphere moisture over both land and ocean compared to ERA40, which leads to underestimation of the relative humidity. This is likely to be a by-product of the weak convective mass flux exhibited by this scheme, which results in less moisture transport away from the surface and less rainfall to provide inputs of moisture to the surface. Over the ocean, the lower atmosphere temperature simulated by the Grell scheme matches well to ERA40. However, given the known cold bias in ERA40, it is likely that the Grell scheme also simulates a cold bias in the lower atmosphere temperature over the ocean.

In contrast, the Emanuel scheme shows good simulation of the lower atmosphere moisture compared to ERA40, due to its stronger convective flux. The moisture is reduced slightly in the new version of the model due to the reduced convection in this simulation (resulting from the reduced insolation).

Both simulations using the Emanuel scheme underestimate the relative humidity compared to ERA40, particularly over the ocean. This is due to the higher temperature simulated by the Emanuel scheme compared to ERA40. Simmons *et al.* (2004) do not specify the magnitude of the cold bias over the tropics in ERA40, so it is not possible to determine whether the higher temperature simulated by the Emanuel scheme is in error. But at least some of the difference in lower atmosphere temperature between the Emanuel simulations and ERA40 can be attributed to a cold bias in the reanalysis. Additionally, it was noted that the SSTs in ERA40 are on average 0.15 ^{o}C lower than the OISST dataset used to force the SSTs in the simulations, which would contribute to higher near surface temperatures over ocean in RegCM3 compared to ERA40. Therefore it is considered that a significant fraction, if not all, of the apparent underestimation in relative humidity exhibited by the Emanuel simulations is in fact the result of error in the ERA40 temperature fields.

Table 5-5. Near-surface temperature (T, in ^{o}C), water vapor mixing ratio (Q, in g kg^{-1}) and relative humidity (RH, in %) averaged for the period 1998-2001 over land and ocean surfaces within the model domain. The lowest vertical layer from ERA40 is compared to the free atmosphere (above canopy) values simulated by the Grell with Fritsch Chappell (GFC) and Emanuel (EMAN) convection schemes with the default and improved versions of the model.

Product / Simulation	Land Average			Ocean Average		
	T (^{o}C)	Q (g kg^{-1})	RH (%)	T (^{o}C)	Q (g kg^{-1})	RH (%)
ERA40	*25.3*	*17.2*	*81.9*	*26.9*	*17.9*	*78.8*
GFC-Default	25.8	15.7	72.5	26.9	17.4	76.5
GFC-Auto	25.4	15.6	75.5	26.9	17.1	75.7
EMAN-Default	26.1	17.2	79.3	27.8	17.7	73.7
EMAN-Auto	25.7	16.9	79.5	27.9	17.6	73.1

5.5 Discussion

5.5.1 Residual Model Error

Despite the substantial improvements documented here with regard to convective clouds and radiation, there are some residual model errors that need to be discussed.

The simulated rainfall histogram shows persistent error in the non-raining and low intensity rainfall categories, exhibiting more frequent low-intensity rainfall than is observed in TRMM. A variety of sensitivity experiments were tried (not shown here) to investigate the magnitude of change required to the model such that the histogram would match TRMM. It was determined that only by shutting off the convective rainfall could the non-raining and low intensity rainfall bins of the histogram match the observations. Obviously this is not a physically-meaningful or desirable option. But it does suggest that the use of a convective parameterization scheme will likely lead to a mismatch between the simulated and observed rainfall histograms.

Although the TRMM data used here is of a similar resolution to the model – 25 km in the data, 30 km in the simulation – very different physical approximations are made between the model and the observations. Rainfall for a grid cell in TRMM represents real, point-scale rainfall data averaged to the scale of 25 km. Rainfall for a grid cell in the model represents the application to 30 km of a parameterization intended to represent the mean behavior of an ensemble of rainfall events (cumulus cells). Hence it is questionable whether

it is even reasonable to expect a large-scale climate model to reproduce the observed rainfall statistics. At the very least, it is encouraging that the results presented here with the Emanuel scheme, which shows improvement across a suite of performance metrics, also shows a tendency in the histogram towards matching the TRMM data.

The average diurnal cycle of rainfall across the land grid cells in the model also shows persistent error with respect to the TRMM data, with an average diurnal peak that is several hours ahead of the observations. This issue will be investigated in detail in Chapter 6.
Two significant errors remain in the new simulations with both convection schemes with respect to cloud cover and CLW: overestimation of high cloud fraction and overestimation of low-level cloud cover and CLW. While these errors should be further explored in future work, there are two factors that must be considered.

The first is that the CLW data from CloudSat is only retrieved at non-precipitating times due to problems with using the retrieval algorithm when rainfall droplets are present. But as discussed in Chapter 4, convective CLW is produced by the model predominately during times when rainfall occurs. This mismatch could result in the CloudSat observations missing some high values of CLW that are produced immediately prior to rainfall events. It should also be noted that the high values of low-level CLW simulated by the Emanuel scheme are actually within the range of values observed in cumulus clouds, as shown in Table 5-2. Therefore the apparent overestimation of CLW in the lower atmosphere produced by the model may not in fact be an error, but rather an illustration of the discrepancy between observations and model output. Improved observations of CLW during rainfall events would clarify this issue and help to further improve the model. The overestimation of low cloud fraction, however, still remains to be addressed.

The second factor that should be considered is the manner in which high-level (above about 8 km altitude) cloud cover is simulated. It was shown that the high-level CLW simulated by the Emanuel scheme was a good match to CloudSat and the planetary albedo was close to SRB observations with some small overestimation over the ocean, even though the high cloud fraction was considerably overestimated compared to ISCCP. It was also shown that the high-level CLW simulated by the Grell scheme is underestimated compared

to CloudSat and the planetary albedo is underestimated compared to SRB, even though the high cloud fraction is overestimated compared to ISCCP. This suggests that the way in which cloud fraction is calculated is not entirely consistent with the simulated water content at high altitudes.

High cloud cover simulated by the model is primarily non-convective, produced by the SUBEX scheme within RegCM3. SUBEX calculates cloud cover as a function only of the mean value of relative humidity within a grid box, without accounting for subgrid variability of that humidity or other factors that may impact the formation of non-convective cloud, such as varying rates of condensation and coalescence that might occur with different types of hydrometeors and subgrid variability in ice nuclei. In addition, the work presented in this thesis has explicitly dealt only with warm (i.e. above freezing) clouds, so any convective cloud that is tall enough to penetrate into freezing altitudes will also be missing these ice-phase hydrometeors. There are many processes affecting the formation of ice-phase precipitation (Emanuel 1994), and the issue of non-linear effects of aerosol abundance and type has already been mentioned in this chapter. It was noted previously by Pal *et al.* (2000) that the lack of an ice-phase representation in SUBEX is a serious deficiency, and perhaps the overestimation of high cloud fraction documented here is the result of this deficiency. Therefore it is considered that the representation large-scale cloud cover within RegCM3 should be revisited, and the role of ice phase hydrometeors should be made a priority for future work.

5.5.2 Implications of Choice of Convective Parameterization

As was the case in Chapter 4, the new autoconversion formulation led to very different results with the two convection schemes. With the Emanuel scheme, cloud cover is reduced when rainfall efficiency is increased using the new autoconversion formulation. This allows more solar radiation to penetrate to the land surface, which provides more energy in the lower atmosphere and increases the low-level instability. This in turn triggers stronger convection, producing more convective rainfall. But with the Grell scheme, the new autoconversion formulation led to a reduction in high cloud cover, increase in low cloud cover and reduction in convective rainfall over land, suggesting that convective activity was

reduced in the new simulation even though model diagnostics showed a general increase in the amount of convective activity.

The reasons for these differences require further discussion because they have implications for how these convection schemes are used within large-scale climate models.

In both schemes, the volume of convective rainfall received at the surface is the product of the updraft mass flux and the amount of precipitable water produced in each layer through the vertical column, less any re-evaporation of rainfall that occurs between the cloud and the ground. Model testing showed that the amount of condensate produced within each grid cell is very similar between the two schemes. Hence the major cause of the difference in convective rainfall between the Grell and Emanuel schemes is the simulation of updraft mass flux and any re-evaporation of rainfall.

In the Emanuel scheme (Emanuel and Živković-Rothman 1999), the time rate of change of the cloud-base updraft mass flux, M_b, is calculated by:

$$\frac{\partial M_b}{\partial t} = \frac{\alpha}{\Delta t}\left(T_{\rho P} - T_\rho + \Delta T_k\right)_{LCL} - \frac{D}{\Delta t} M_b \qquad (5\text{-}39)$$

where α = 0.2 (fixed parameter), $T_{\rho P}$ = density temperature of a parcel lifted adiabatically from the sub-cloud layer, T_ρ = environmental density temperature, ΔT_k = specified temperature deficit at the LCL that allows convection to proceed in the presence of negative buoyancy, D = 0.1 (fixed parameter that represents a small damping effect), Δt = time step, which is used to normalize α and D, and the right-hand side of the equation is evaluated at the lifted condensation level (LCL).

Density temperature, T_ρ, is the temperature of a saturated air parcel that has the same density and virtual temperature, T_v, at the same pressure level as an unsaturated air parcel with temperature T and mixing ratio q (Betts and Bartlo 1991), i.e.,

$$T_v = T(1 + 0.61q) = T_\rho\left[1 + 0.61 q_s\left(T_\rho\right)\right] \qquad (5\text{-}40)$$

In all the simulations presented here, the value of ΔT_k was set equal to zero so that no negative buoyancy would be permitted in the presence of convection. This decision was made on the basis that setting $\Delta T_k = 0$ would require the LCL and LFC (level of free convection) to coincide for convection to proceed, which seems more reasonable than allowing free convection in the presence of negative available potential energy (also known as negative CAPE, or convective inhibition).

Hence the cloud-base updraft mass flux in the Emanuel convection scheme is solely dependent on the degree of instability at the LCL. This makes convection with the Emanuel scheme very sensitive to changes in the near surface environment, such that convective rainfall directly reflects the lower atmosphere instability related to incoming radiation. This sensitivity was clear in the results presented in Chapters 4 and 5.

The basis for the Grell scheme is the work of Arakawa and Schubert (1974), who developed a method to parameterize the interaction between a cumulus cloud ensemble and the large-scale environment based on the theory of moist convective quasi-equilibrium. The crux of this work is the cloud work function, which is an integral measure of the buoyancy energy available for convection and provides the necessary closure for the scheme. The updraft mass flux is derived based on the assumption that the cloud work function is in quasi-equilibrium such that the time rate of change of the total cloud work, A_t, is approximately zero, i.e.,

$$dA_t/dt = \left(dA_t/dt\right)_{LS} + \left(dA_t/dt\right)_{CU} = F(\lambda) + \int_\lambda K(\lambda,\lambda')\, m_b(\lambda') d\lambda \approx 0 \qquad (5\text{-}41)$$

where $F(\lambda)$ = change in the cloud work function due to the change in the large-scale variables, $K(\lambda,\lambda)$ = modification of the environment due to the cumulus cloud ensemble, $m_b(\lambda)$ = updraft base mass flux, λ characterizes the cloud type, and the subscripts *LS* and *CU* refer to the large-scale and cumulus effects respectively (Grell 1993). The updraft base mass flux, $m_b(\lambda)$, can therefore be found as the ratio of the effects from the large-scale to the modifications due to the cumulus cloud ensemble:

$$m_b = -F/K \tag{5-42}$$

The two closures available with the Grell scheme in RegCM3, i.e. the Arakawa-Schubert and Fritsch-Chappell, provide different ways to calculate the large-scale effect *F*:

$$F = {(A_t" - A_t)}/{\Delta t} \quad for\ Arakawa - Schubert \tag{5-43a}$$

$$F = {A_t}/{\Delta \tau} \quad for\ Fritsch - Chappell \tag{5-43b}$$

where A_t = buoyant energy available for convection, $A_t"$ = amount of buoyant energy available for convection in addition to the buoyant energy generated by the large-scale (i.e. non-convective) processes over the period Δt, Δt = time step between calls to convection routine, and $\Delta \tau$ = timescale for convective adjustment (the default value is 30 minutes within RegCM3).

The modification due to the cumulus cloud ensemble is:

$$K = {(A_t' - A_t)}/{0.005\Delta t} \tag{5-44}$$

Therefore the updraft mass flux is calculated as follows, using the Fritsch-Chappell closure:

$$m_b = \frac{-A_t}{A_t' - A_t} \frac{0.005\Delta t}{\Delta \tau} \tag{5-45}$$

The total cloud work, A_t, within the cloud ensemble and in the environment is calculated from:

$$A_t = A_u + \epsilon A_d \tag{5-46}$$

where A_u = measure of the efficiency of kinetic energy generation inside the cloud, A_d = measure of the efficiency of the kinetic energy dissipation by the cloud, and ϵ = ratio of

downdraft mass flux to updraft mass flux. The efficiency of kinetic energy generation, A_u, and kinetic energy dissipation, A_d, are calculated from the following, respectively:

$$A_u(\lambda) = \int_{z_B}^{z_T} \frac{g}{C_P T(z)} \frac{\eta_u(\lambda,z)}{1+\gamma} \left[h_u(\lambda,z) - \tilde{h}^*(z)\right] dz \quad (5\text{-}47)$$

$$A_d(\lambda) = \int_{z_0}^{z_{sur}} \frac{g}{C_P T(z)} \frac{\eta_d(\lambda,z)}{1+\gamma} \left[\tilde{h}^*(z) - h_d(\lambda,z)\right] dz \quad (5\text{-}48)$$

where z_T = cloud top, z_B = cloud base, z_{sur} = height of model layer next to surface, z_0 = originating level of downdraft (level of minimum moist static energy), g = gravitational acceleration, C_P = heat capacity of air, $T(z)$ = temperature at height z, $\eta(\lambda)$ = normalized mass-flux profile of ensemble of cloud elements λ, h_u = moist static energy of updraft (i.e. moist static energy of lifted parcel's originating level), h_d = moist static energy of downdraft (i.e. at originating level of downdraft, which is at the level of minimum moist static energy) and $\tilde{h}^*$ = saturation moist static energy of the environment.

Therefore the updraft mass flux in the Grell scheme is primarily a function of the difference in moist static energy between the updraft and the downdraft, and how that difference is affected by convective activity.

The results from the Grell simulations can therefore be understood in this context: if the moist static energy in the updraft (coming from the lifted parcel's originating level) is increased while the moist static energy higher in the atmosphere remains the same, the convective mass flux will increase and so will convective rainfall. But if the moist static energy at the originating level of the downdraft in the middle atmosphere decreases, i.e. the strength of the downdraft increases, this will serve to reduce the convective mass flux and therefore reduce the convective rainfall.

The results documented in this work illustrate how these different approaches to convective mass flux impact the simulation results. When rainfall efficiency is increased using the Emanuel scheme, cloud cover decreases and insolation increases, leading to higher instability in the lower atmosphere and consequently stronger updraft mass flux. This in turn increases the convective rainfall. So increasing the rainfall efficiency creates a positive

feedback loop with the Emanuel scheme that results in increased rainfall. However, when rainfall efficiency is increased using the Grell scheme, this dries out the atmosphere, reducing the mid-level moist static energy and increasing the downdraft strength. This results in a decrease to the convective mass flux. Hence an increase in rainfall efficiency actually produces less total rainfall at the surface with the Grell scheme.

In developing their cumulus parameterization, Arakawa and Schubert (1974) used a time-integrated updraft mass flux that represented the mean cloud mass flux over the life time of a cumulus cloud, taken to be the timescale for moist convective adjustment. This timescale was said to be of order 10^3-10^4 seconds (30 minutes to 3 hours) (Arakawa and Schubert 1974). Stephens and Haynes (2007) used MODIS and CloudSat observations to find the rate of coalescence over the global oceans, and confirmed that the time scale for coalescence over the oceans between 60^{o}S and 60^{o}N is between 6 minutes and 3 hours, with the majority (73%) of observations in the range 26 minutes to 3 hours. The basis for the quasi-equilibrium theory is that the convective adjustment timescale is significantly smaller than the timescale of the large-scale processes that create the instability driving convection, which is of order 10^5 seconds (about 1 day) (Arakawa and Schubert 1974).

The convective adjustment time scale was intended to be virtually instantaneous in the sense that it is basically the same as the computational timestep for implementing the physics (Arakawa 2004). It is noted that the GCMs, into which the Arakawa and Schubert (1974) scheme was originally implemented, were of resolution order 100-200 km, with a computational timestep on the order of hours, suitable for assuming an almost instantaneous adjustment of the atmospheric stability due to convection.

However, an RCM running at the scale of tens of kilometers typically has a timestep of a few minutes. In the simulations presented in this study, the grid cell size of 30 km necessitated a timestep of 1 minute for computational stability. Hence a single computational timestep only represents a fraction of the lifetime of a cumulus cloud, and could take place during either the development or decay phase of a cloud. The timestep used here is substantially less than that required to assume that convective adjustment is 'instantaneous'. Therefore the time-averaged mass flux used in the scheme developed by

Arakawa and Schubert (1974), which forms the basis for the Grell scheme within RegCM3, is not considered appropriate for simulations that require a description of the time evolution of the convective event.

The Emanuel scheme, on the other hand, achieves adjustment towards quasi-equilibrium during the time integration of explicitly formulated transient processes (Arakawa 2004). Arakawa (2004) stated that approaches like the Emanuel scheme, which prognostically determine the cumulus mass flux, should be developed further, for two reasons: 1) they have computational and physical advantages in practical applications, and 2) without a theory on the transient behavior of cumulus activity, the existence or nonexistence of quasi-equilibrium cannot be rigorously discussed.

Therefore this thesis argues that the Emanuel scheme is much better suited for use in an RCM than the Grell scheme (or others based on Arakawa and Schubert, 1974) for studies of processes with timescales significantly less than that required for the classical assumption of quasi-equilibrium. This is particularly relevant for simulations of tropical convection, such as over the Maritime Continent. The work presented in this chapter shows that the Emanuel scheme can produce good simulation performance across a range of performance metrics – cloud cover, CLW, radiation, turbulent surface heat fluxes and rainfall – when combined with improvements to simulation of the PBL region, convective cloud cover and convective autoconversion.

5.6 Summary

The results presented above demonstrate that the model performance is significantly impacted by incorporating subgrid variability in CLW content and autoconversion efficiency into the simulation of convection. Combined with the new convective cloud fraction presented in Chapter 4 and the modifications presented in Chapter 3, the new autoconversion formulation results in simulated cloud cover that is closer to the ISCCP data and CLW profiles that are much improved compared to the CloudSat data relative to the previous simulations. Crucially, the diurnal cycle of cloud cover now exhibits an afternoon signature of the low- to mid-level convective activity, while maintaining a reasonable vertical profile of the CLW and reproducing the observed minimum at about 4-6 km elevation. The

new autoconversion formulation also improved the simulation of solar radiation, providing a good match to the SRB data particularly with the Emanuel scheme.

With both convection schemes, the model modifications improved simulation of the convective rainfall fraction: decreasing the fraction with the Emanuel scheme and increasing the convective fraction with the Grell scheme. It should also be noted that the modifications dramatically reduced the wet bias simulated by the Emanuel scheme over land, but without creating a substantial dry bias over the ocean. Hence the ratio of land-to-ocean rainfall simulated by this scheme was improved compared to the observations. This improvement was not intentional, in the sense that the modifications did not attempt to change rainfall over land in a different manner to ocean. Hence these results indicate that the modifications made to the model have resulted in increased physical realism rather than model tuning.

The results with the new autoconversion simulations suggest two things: 1) the new autoconversion function is significantly more efficient at producing rainfall than the default formulation in both the Grell and Emanuel schemes, and 2) the original cloud cover produced by RegCM3 was the result of two compensating deficiencies – firstly in creating the cloud (which was addressed in GFC-New and EMAN-New), and secondly in removing the cloud via rainfall (which is addressed in GFC-Auto and EMAN-Auto). Hence the original cloud cover was reasonably close to ISCCP at low and middle levels due to what could be considered an effective combination of tuning. With the new formulations for cloud cover and autoconversion, similar cloud cover is produced but with much more physical realism. This added realism has important ramifications for other aspects of the simulation, including net radiation and rainfall, and allows the model to respond with appropriate sensitivity to changes in insolation and large-scale forcing.

Once again, the results illustrate the influence that moist convection has on the near surface environment by mediating the incoming solar radiation and net radiation at the surface, with subsequent impacts on the turbulent heat fluxes over land. The dissipation of convective cloud due to rainfall can produce an effect similar in magnitude to the formation of the cloud, as shown by the results using the Emanuel scheme, highlighting the importance of correctly representing the convective-radiative feedback in large-scale climate models.

There are likely to be other important feedbacks of these new formulations for cloud cover and autoconversion, such as different sensitivity to changing global climate variability. It is also likely that the new formulations used in other locations will produce different results to the default version of the model. When coupled to an ocean model, instead of being forced with SSTs as in this study, it is also likely that the new formulations for cloud cover and autoconversion will produce very different results than the default version of the model, since the radiative forcing of the ocean surface is so different.

The work presented so far in this thesis has looked at the average diurnal cycle of processes related to convection over the period 1998-2001, and has focused on the mean behavior of land and ocean cells within the model domain. However, the average diurnal rainfall cycle (as shown in Figure 5-17) masks considerable spatial variability across the model domain. Chapter 6 will address the issue of spatial variability in the diurnal cycle over the Maritime Continent. Behavior over the larger islands, shown to have persistent simulation error, is explored in more detail with a view to isolating the specific processes that cannot be captured with a large-scale climate model like RegCM3. Chapter 7 will then explore the influence of temporal variability on the diurnal cycle.

Chapter 6: Spatial Variability in the Diurnal Cycle

This thesis was introduced with a description of the incredible geographic variability that exists over the Maritime Continent region. Given this physical variability, it should not be surprising that the diurnal cycle of rainfall also varies considerably across the region in response to different mechanisms influencing cloud formation, initiation of convection and the relative importance of large-scale (resolvable) to small-scale (subgrid-scale) processes.

The work presented in Chapter 5 showed that there was substantial improvement made to the average model performance over land cells within the model domain, but that the model contained residual error in the timing of the average diurnal rainfall peak. This chapter investigates the spatial variability associated with this diurnal peak, identifying locations where the model performs well compared to observations and locations where the model performs poorly. A review of the processes known to affect diurnal rainfall across the Maritime Continent region is presented, with discussion of the potential difficulties in representing some of these processes in large-scale climate models. It is outside the scope of this analysis to address the residual model error; rather the intention here is to elucidate the reasons why it exists.

6.1 Spatial Analysis of Diurnal Rainfall Cycle

Figure 5-17 showed that the average diurnal rainfall cycle over land exhibits a peak around 7 pm in the TRMM observations. The TRMM data were used to determine how much spread exists in the timing of the rainfall peak across the Maritime Continent region. For each grid cell within the model domain, the average local time of day of peak rainfall over the period 1998-2001 was identified and is shown in Figure 6-1. Land surfaces are of particular interest in this analysis, since they exhibit the largest error in the simulations, so ocean cells are masked out in the figure.

Figure 6-1 shows that the diurnal peak shown for TRMM in Figure 5-17 is the result of averaging very different diurnal cycles. Mid-afternoon peaks are noticeable along coastal

areas and smaller, flatter islands, such as the southern Malay Peninsula, much of Java, coastal parts of Borneo and the southern Philippine island of Mindanao. Evening peaks are observed further north on the Malay Peninsula, along the west coast of Sumatra and in inland parts of Borneo and western New Guinea. A night-time peak is observed along the center of Sumatra and parts of inland Borneo, while a late night to early morning peak dominates much of central Borneo.

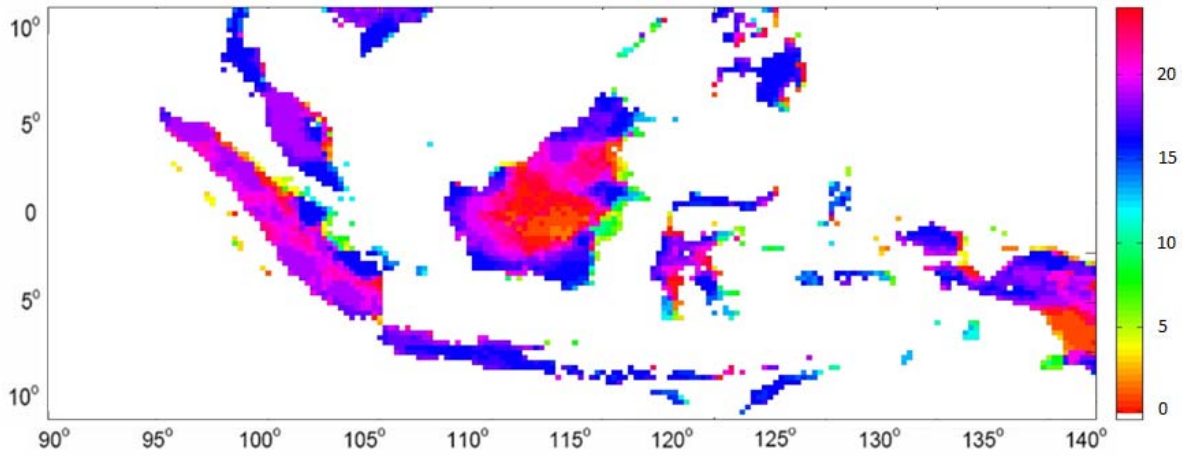

Figure 6-1. Local time (see color bar) of diurnal rainfall peak from TRMM, averaged over 1998-2001. Ocean cells have been masked out for clearer visualization of land cells.

To evaluate the spatial variability in the diurnal rainfall peak within RegCM3-IBIS, similar maps of the peak rainfall time were made using the Emanuel scheme with both the default version of the model (Figure 6-2) and the new version, which incorporates all the modifications contained in Chapters 3 to 5 (Figure 6-4). The differences in peak rainfall time between TRMM and the simulations are shown in Figures 6-3 and 6-5.

To make it easier to visually distinguish locations of least and greatest error, the color bar in Figures 6-3 and 6-5 has been set such that errors of the same magnitude are the same color, regardless of sign.

Figures 6-2 and 6-4 show that the different versions of the model exhibit nearly identical diurnal timing of the rainfall peak. Rainfall begins in the late morning over the inland parts of Sumatra and Borneo on relatively flat land (i.e. not over the mountains), on the northern and southern coasts of western New Guinea, and on the smaller islands. By

mid-afternoon, the peak rainfall is over the Borneo coastline, the eastern coast of Sumatra and much of the Malay Peninsula. Night-time peaks are simulated over the mountainous regions of western Sumatra, Borneo, Sulawesi, New Guinea and the Malay Peninsula. The latest rainfall peak occurs in the early hours of the morning over the mountains in north-central Borneo.

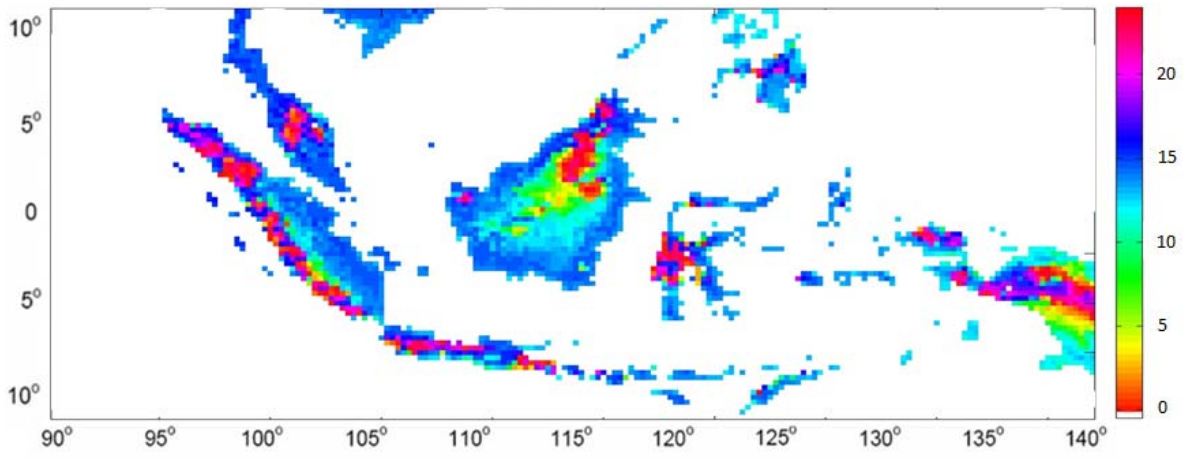

Figure 6-2. Local time (see color bar) of diurnal rainfall peak averaged over 1998-2001, using Emanuel scheme with the default version of RegCM3. Ocean cells have been masked out for clearer visualization of land cells.

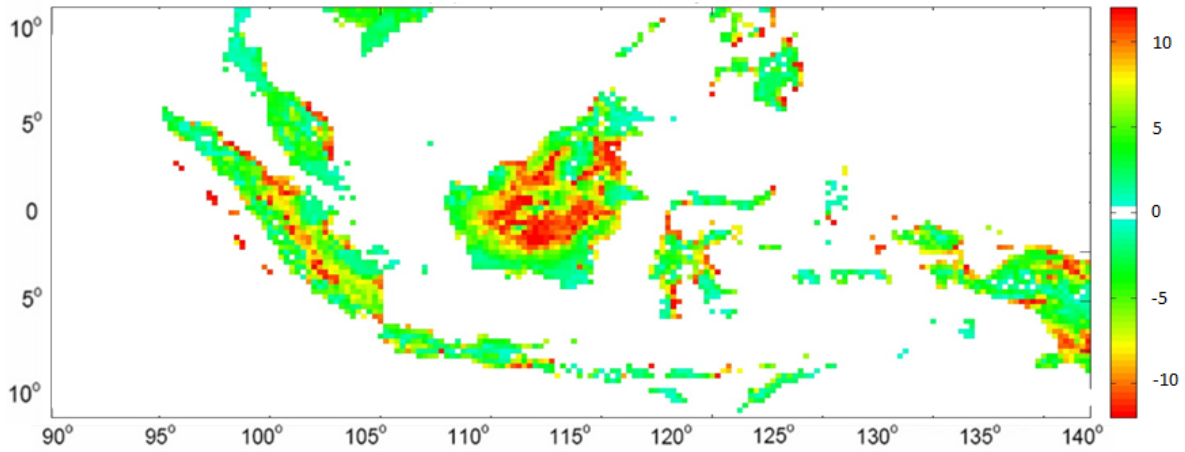

Figure 6-3. Difference in timing (hours) of diurnal rainfall peak averaged over 1998-2001, TRMM minus RegCM3-IBIS using Emanuel scheme with the default model. Ocean cells have been masked out for clearer visualization of land cells.

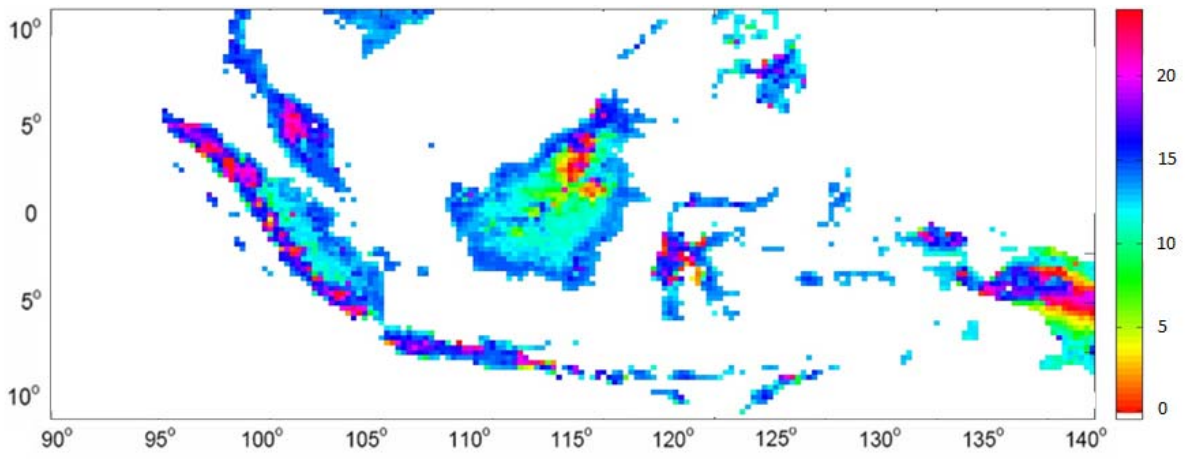

Figure 6-4. Local time (see color bar) of diurnal rainfall peak averaged over 1998-2001, using Emanuel scheme with the new version of RegCM3-IBIS incorporating all modifications presented in Chapters 3 to 5. Ocean cells have been masked out for clearer visualization of land cells.

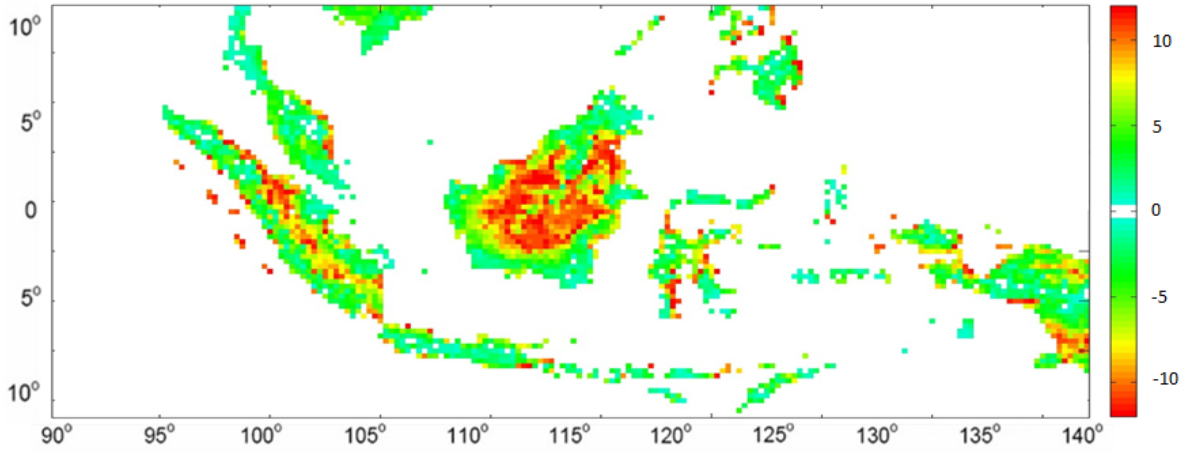

Figure 6-5. Difference in timing (hours) of diurnal rainfall peak averaged over 1998-2001, TRMM minus RegCM3-IBIS using Emanuel scheme with the new version of the model incorporating all modifications presented in Chapters 3 to 5. Ocean cells have been masked out for clearer visualization of land cells.

Figures 6-3 and 6-5 indicate that there are some locations within the model domain where the simulated rainfall peak matches well to the TRMM peak – over much of the Malay Peninsula and Java, the coastal regions of Borneo, the mountains of western New Guinea and many of the smaller islands. Given that the temporal resolution of TRMM is 3 hours, it is considered that simulated error up to 3 hours is not unreasonable, and so these aforementioned locations are considered to exhibit good model performance. There is some

moderate error of up to 5 hours difference associated with the mountains on the west coast of Sumatra and the mountains in northern Borneo, as well as parts of the Malay Peninsula.

However, Figures 6-3 and 6-5 indicate that there are some locations within the model domain that experience tremendous error in the timing of the diurnal peak in comparison to TRMM, on the order of 8-12 hours difference. The largest error is concentrated along the central part of Sumatra and the inland areas of Borneo adjacent to the high mountain peaks.

A phase error in the diurnal cycle of nearly half a day is certainly alarming, but it is not unique to RegCM3. Similar phase errors in the diurnal rainfall peak over the Maritime Continent have been shown by: Wang *et al.* (2007), using the Regional Climate Model from the International Pacific Research Center at a resolution of 0.5^{o}; Hara *et al.* (2009), using the Japan Meteorological Research Institute's General Circulation Model (MRI-GCM) at 20 km resolution; Ploshay and Lau (2010), using the GFDL GCM run at a resolution of 0.5^{o} x 0.625^{o}; and by Love *et al.* (2011), using the UK Met Office's Unified Model in simulations run at 40 km and 12 km resolutions. Hara *et al.* (2009) also showed that the MRI-GCM significantly overestimated rainfall along the mountain ranges of western Sumatra and northern Borneo, while underestimating the rainfall over the ocean off the west coast of Sumatra and over southern Borneo.

To determine if there are particular characteristics associated with locations exhibiting a certain magnitude of error, three pieces of data were compared to the phase errors simulated by RegCM3-IBIS shown above. Figure 6-6 shows the proximity of every land grid cell to the ocean, i.e. it indicates how far inland from the coast each grid point is located. Figure 6-7 shows the topography used in the simulations presented above, from the GTOPO30 dataset (United States Geological Survey 1996). Figure 6-8 shows the standard deviation of the topography contained within each 30 km grid cell with respect to the input dataset that was interpolated over each cell, i.e. it indicates how much topographic detail was lost in the process of interpolating from a 10 arc-minute dataset to a 30 km grid cell.

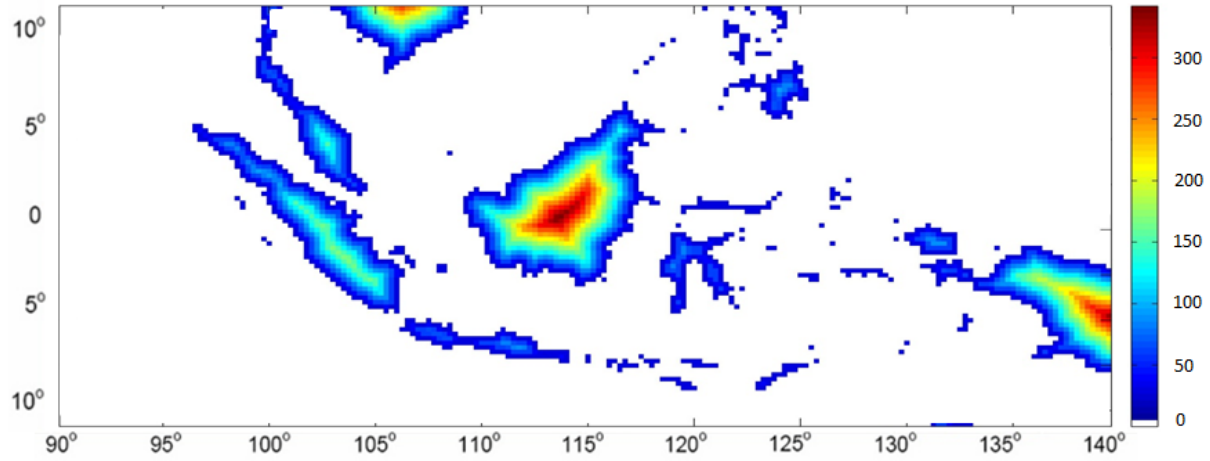

Figure 6-6. Distance to coastline (meters) for each land grid cell within domain.

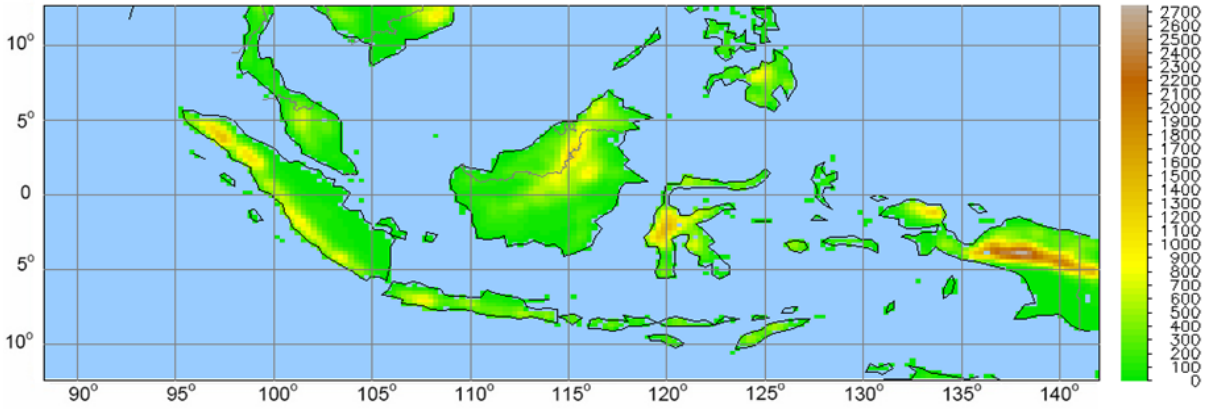

Figure 6-7. Topography (meters) used in simulations: the Geological Survey's Global 30 arc second elevation dataset (GTOPO30), aggregated to 10 arc minutes (United States Geological Survey 1996) and interpolated to the 30 km grid used in simulations.

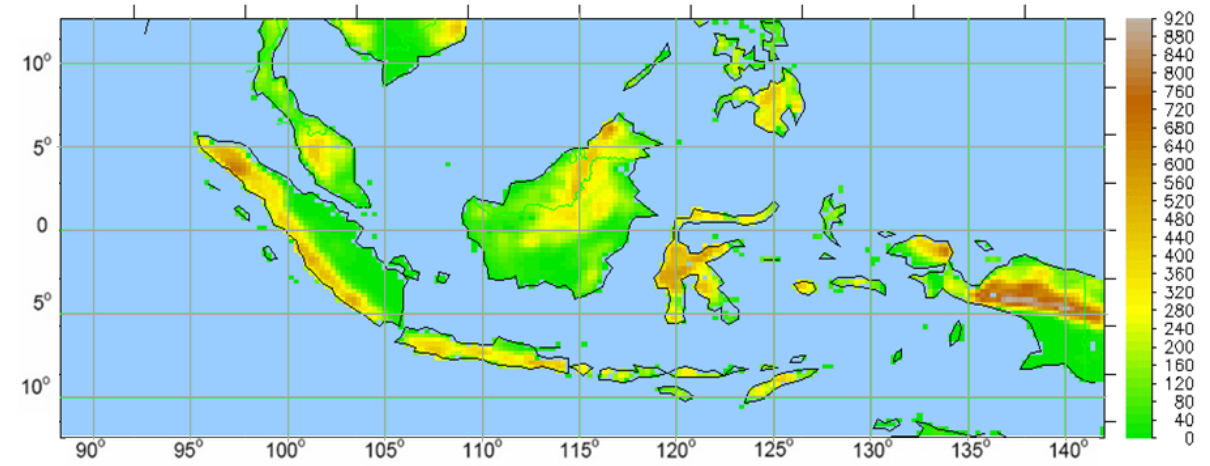

Figure 6-8. Standard deviation of topography (meters) contained within each 30 km grid cell compared to the GTOPO30 input data interpolated within each grid cell.

Each land grid cell within the domain was assigned a matrix containing these three pieces of information – distance to coastline, elevation and standard deviation of within-cell topography – as well as the error in the timing of the diurnal rainfall peak at that grid cell. The land grid cells were then grouped into three brackets based on the magnitude of the timing error: 0–3 hours difference between the model and TRMM, 3–6 hours difference, and more than 6 hours difference. Within each bracket, the mean distance to coastline, elevation and topographic standard deviation were calculated. The analysis was conducted for the simulations using the default version of the model and the new version incorporating all modifications, both with the Emanuel scheme.

The results are shown in Table 6-1. The results confirm that the locations with the smallest error in the timing of the diurnal rainfall peak are located near the coastlines. Error increases with distance away from the coast, but interestingly the error is larger over locations with lower elevation than with higher elevation. This confirms that the locations with the greatest error are over the inland parts of the large islands that are next to the mountains, but not over the mountains themselves. The results in Table 6-1 also show that the timing error is not simply associated with grid cells that are unable to resolve topographic gradients, since the locations with the worst error also have the smallest variability in elevation.

Table 6-1. Mean characteristics of locations within model domain exhibiting similar error in timing of diurnal rainfall peak with respect to TRMM, comparing the Emanuel scheme with the default version of RegCM3-IBIS to the new version incorporating all modifications presented in Chapters 3 to 5. All values are in meters.

Diurnal Peak Timing Error	0 - 3 hours	3 - 6 hours	> 6 hours
EMAN default			
Mean distance to coastline	76	83	113
Mean elevation	552	416	220
Standard deviation of within-cell topography	227	200	139
EMAN new			
Mean distance to coastline	67	75	119
Mean elevation	542	394	248
Standard deviation of within-cell topography	234	182	142

Hence there is specific clustering of locations with error in the simulated diurnal cycle of rainfall. To illustrate the observed variability in the diurnal rainfall cycles across the domain, five sub-regions were chosen for further analysis, as shown in Figure 6-9. These regions were chosen as representative of the varying characteristics shown in Table 6-1.

Region A ('Malay Peninsula') is coastal and flat, and Figures 6-3 and 6-5 suggest that the diurnal timing was simulated well at this location. Region B ('highland Borneo') is inland and at comparatively high elevation. It appears that the simulated diurnal timing is also reasonably good at this location. By contrast, Region C ('lowland Borneo') is inland but flat, and Figures 6-3 and 6-5 suggest that this location contains large error in the diurnal timing. This location is therefore representative of the right-hand column of Table 6-1. Region D ('northern Sumatra') is coastal but at high elevation. This location therefore provides a comparison to the coastal Malay Peninsula and elevated highland Borneo. Finally, Region E ('southern Sumatra') is also coastal and flat, similarly to the Malay Peninsula, but Figures 6-3 and 6-5 suggest that the diurnal timing contains considerable error at this location.

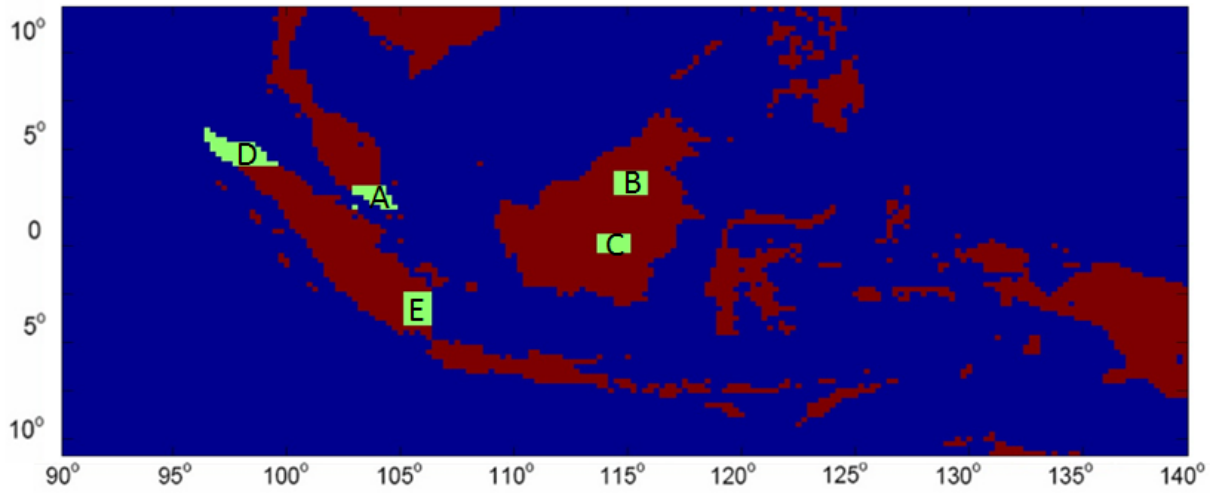

Figure 6-9. Location of sub-regions used in spatial analysis: (A) Malay Peninsula, (B) Highland Borneo, (C) Lowland Borneo, (D) Northern Sumatra, (E) Southern Sumatra.

Figures 6-10 to 6-14 below present the average diurnal rainfall cycle over these five sub-regions for the period 1998-2001, compared to TRMM, for the default and new versions of the model.

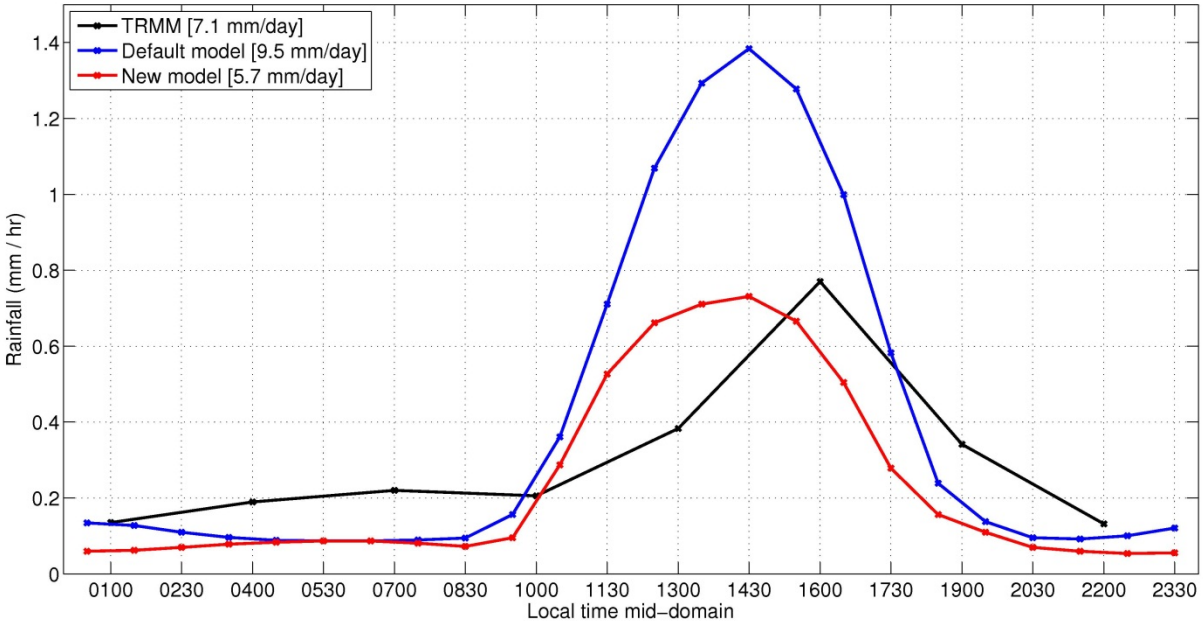

Figure 6-10. Diurnal cycle of rainfall (in mm hr^{-1}) averaged over Malay Peninsula sub-region for period 1998-2001 for TRMM and simulations using Emanuel scheme with default version of the model and version with all modifications (to PBL region, convective cloud fraction and autoconversion). Mean values are given in parentheses.

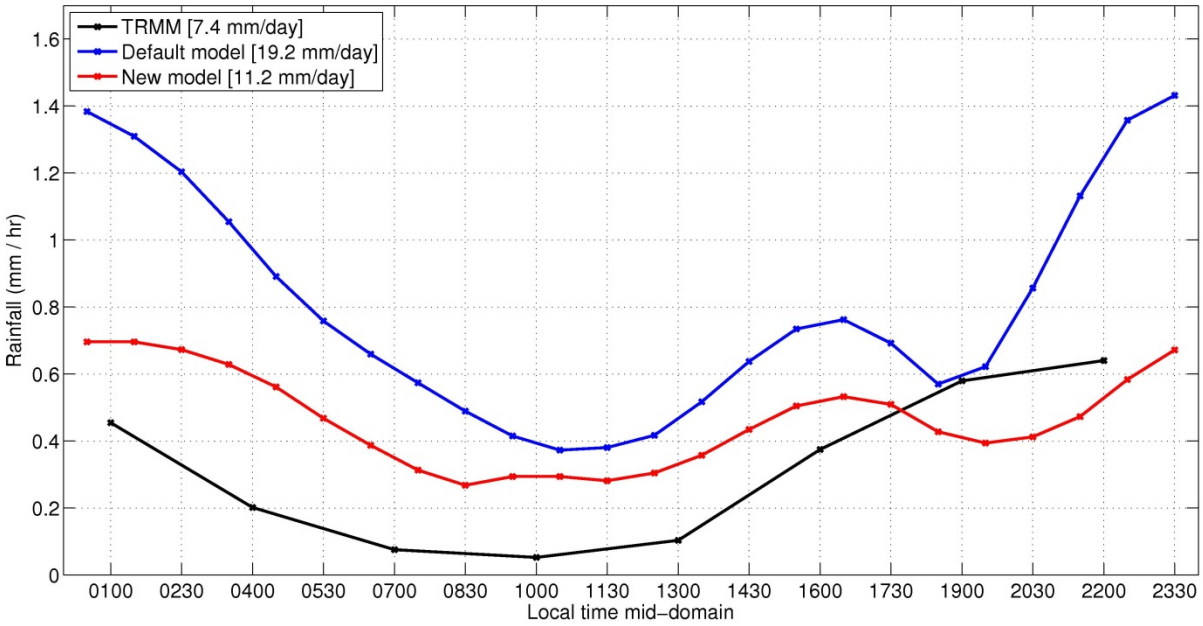

Figure 6-11. Diurnal cycle of rainfall (in mm hr^{-1}) averaged over highland Borneo sub-region for period 1998-2001 for TRMM and simulations using Emanuel scheme with default version of the model and version with all modifications (to PBL region, convective cloud fraction and autoconversion). Mean values are given in parentheses.

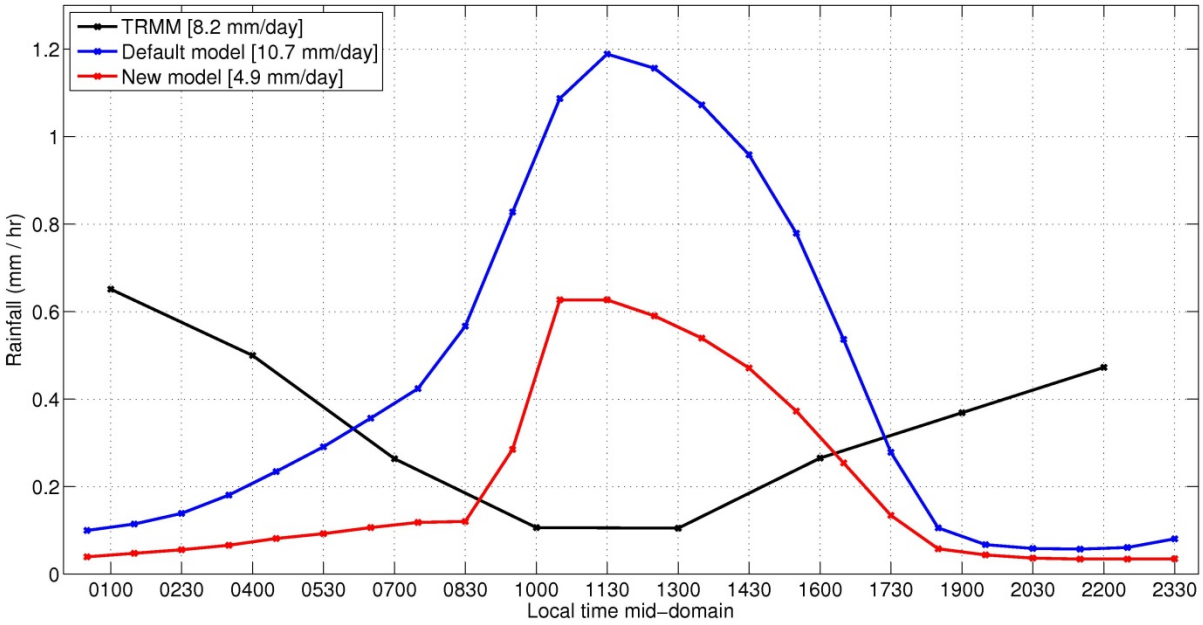

Figure 6-12. Diurnal cycle of rainfall (in mm hr^{-1}) averaged over lowland Borneo sub-region for period 1998-2001 for TRMM and simulations using Emanuel scheme with default version of the model and version with all modifications (to PBL region, convective cloud fraction and autoconversion). Mean values are given in parentheses.

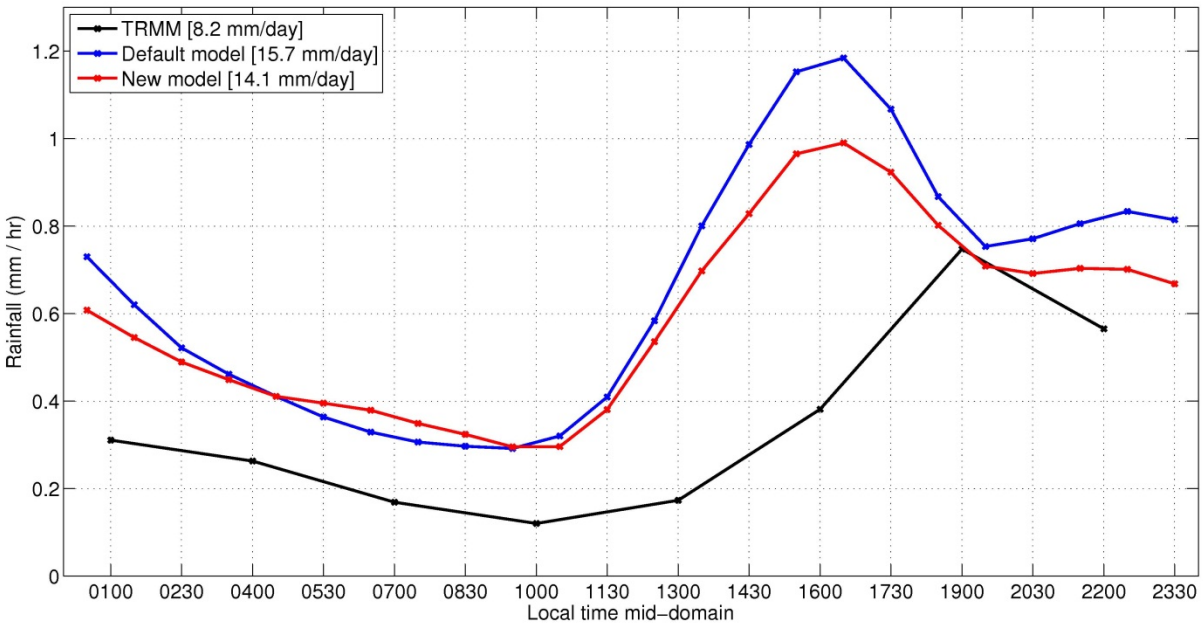

Figure 6-13. Diurnal cycle of rainfall (in mm hr^{-1}) averaged over northern Sumatra sub-region for period 1998-2001 for TRMM and simulations using Emanuel scheme with default version of the model and version with all modifications (to PBL region, convective cloud fraction and autoconversion). Mean values are given in parentheses.

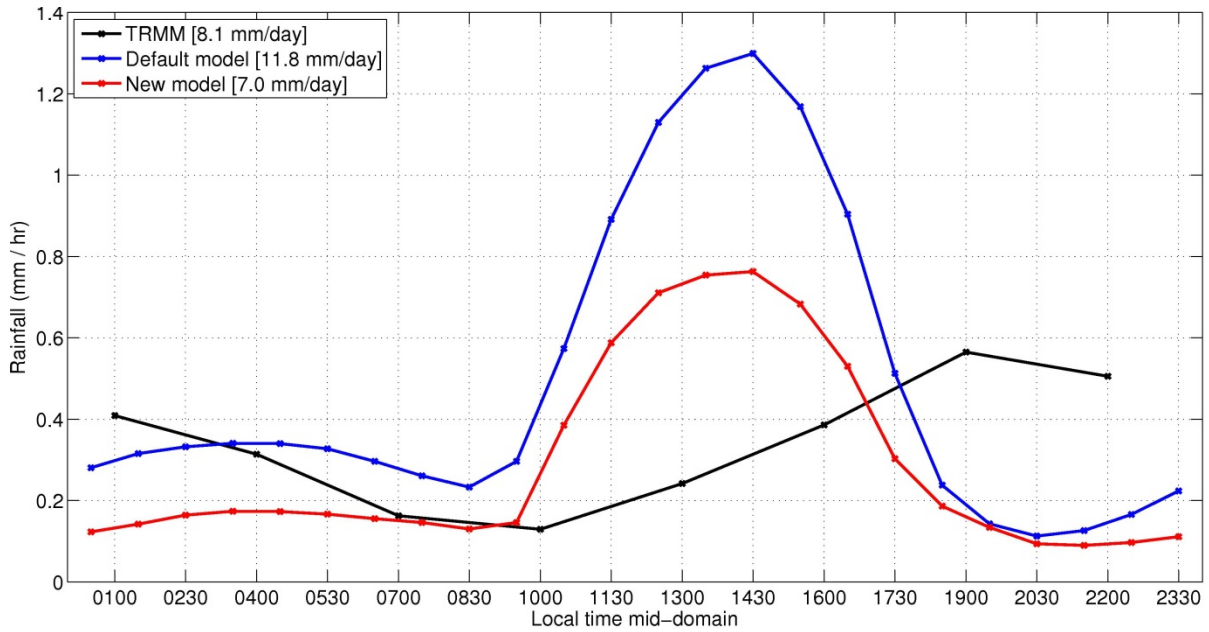

Figure 6-14. Diurnal cycle of rainfall (in mm hr^{-1}) averaged over southern Sumatra sub-region for period 1998-2001 for TRMM and simulations using Emanuel scheme with default version of the model and version with all modifications (to PBL region, convective cloud fraction and autoconversion). Mean values are given in parentheses.

Figures 6-10 to 6-14 illustrate the spatial variability in the diurnal rainfall cycle across this region and the relative performance of the model in attempting to capture this variability.

Over the Malay Peninsula sub-region, the new version of the model shows considerable improvement in the simulated rainfall volume compared to the default model and provides a reasonably good match to TRMM. It appears from Figure 6-10 that the model simulates the diurnal rainfall peak occurring about an hour earlier than observations, but it must be remembered that the TRMM data only has a 3-hourly temporal resolution. It is therefore considered that the model performs well over this location.

Over the highland Borneo sub-region, the new version of the model again provides improvement over the default version, substantially reducing the overestimation bias. The model also captures the observed midnight rainfall peak at this location, although it is noted that both versions of the model contain an unusual dip in rainfall at around 7pm that is not present in the TRMM data.

Figure 6-12 illustrates the 12-hour phase shift in the diurnal rainfall cycle that is simulated by the model over much of inland Borneo. At this location, the new model improves on the overestimation bias that was exhibited by the default version of the model, but there appears to be some systemic problem in the model that leads it to completely mis-time the diurnal peak at this location. This issue is discussed further in Section 6.3.

Figure 6-13 shows that the simulated rainfall over northern Sumatra did not change appreciably between the two versions of the model. The new model contains considerable overestimation bias compared to TRMM, and the diurnal peak appears about 3 hours too early in the model.

Over southern Sumatra, the volume of rainfall simulated by the new model is improved significantly compared to the default version. However, the rainfall peak is simulated about 6 hours earlier than in TRMM over this location.

The total, convective and large-scale rainfall volumes simulated by both versions of the model over the five sub-regions are summarized in Table 6-2. The proportion of convective and large-scale rainfall listed as observations come from the TRMM 3A12 product (which is the gridded version of the 2A12 product) and the work of Mori *et al.* (2004).

The observations show that there is spatial variability not only in the total rainfall volume but also in the relative convective and large-scale rainfall fractions. The highest fraction of convective rainfall occurs over the Malay Peninsula. The southern Sumatra and both Borneo sub-regions exhibit convective rainfall fractions close to the land average (of 63%), while the northern Sumatra sub-region shows the lowest convective fraction out of the five.

The simulations reproduce most of this variability, but with some differences compared to TRMM. In both of the simulations, the large majority of rainfall is from convection over the Malay Peninsula, lowland Borneo and southern Sumatra. The simulated fraction is higher than in the observations, but the table shows that the volume of convective rainfall is a reasonable match to TRMM in the new simulation. Therefore the error in the simulated convective fraction actually comes from an underestimation of large-scale rainfall over these locations, rather than an overestimation of convective rainfall.

Table 6-2 indicates that the model simulates the convective fraction reasonably well over highland Borneo and northern Sumatra, where large-scale rainfall contributes 36% and 42% respectively of the total rainfall volume in the observations. This indicates that the model simulates a higher fraction of large-scale rainfall over areas of higher elevation than over lower elevation. This result is consistent with observations of prolonged night-time rainfall over mountainous areas within the Maritime Continent due to mesoscale systems, and is discussed further in Section 6.3 below.

Table 6-2. Total, convective and large-scale rainfall (all in mm day^{-1}) averaged over 1998-2001 for each sub-region shown in Figure 6-9, comparing the Emanuel scheme with the default version of RegCM3-IBIS to the new version incorporating all modifications presented in Chapters 3 to 5. The relative proportions of convective and large-scale rain are shown in parentheses.

Observations / Simulation	Total	Convective	Large-scale
Malay Peninsula - TRMM	*7.1*	*4.9 (69%)*	*2.2 (31%)*
EMAN default	9.5	8.1 (85%)	1.4 (15%)
EMAN new	5.7	4.5 (79%)	1.2 (21%)
Highland Borneo - TRMM	*7.4*	*4.7 (64%)*	*2.7 (36%)*
EMAN default	19.2	10.3 (54%)	8.9 (46%)
EMAN new	11.2	6.9 (62%)	4.3 (38%)
Lowland Borneo - TRMM	*8.2*	*5.2 (64%)*	*3.0 (36%)*
EMAN default	10.7	7.5 (70%)	3.2 (30%)
EMAN new	4.9	4.1 (85%)	0.8 (15%)
Northern Sumatra - TRMM	*8.2*	*4.8 (58%)*	*3.4 (42%)*
EMAN default	15.7	8.8 (56%)	6.9 (44%)
EMAN new	14.1	7.3 (52%)	6.8 (48%)
Southern Sumatra - TRMM	*8.1*	*5.3 (66%)*	*2.8 (34%)*
EMAN default	11.8	8.3 (70%)	3.5 (30%)
EMAN new	7.0	5.0 (72%)	2.0 (28%)

The average surface radiative fluxes for the period 1998-2001 are summarized in Table 6-3 for each of the five sub-regions. The results show that the new model shows improvement to the simulation of radiative fluxes across all sub-regions, consistent with the improvement to the land averages presented in Chapter 5. Some sub-regions exhibit more error than others. For example, the incoming and surface absorbed shortwave radiation over the Malay Peninsula is still overestimated in the new model compared to observations, while land albedo and the surface reflected shortwave radiation are underestimated over both the

Borneo locations. This suggests that the albedo-related parameters attributed to evergreen broadleaf forest within the IBIS land cover (see Figure 2-1) underrepresent the observed albedo of the tropical forest over this island.

However, the difference between the default and new versions of the model is far greater than the difference between the observations and the new model version. Therefore it is considered that the remaining radiative flux errors shown in Table 6-3 for the new model are not the cause of the errors in the timing of the diurnal rainfall cycle. In general, it is considered that the new model performs reasonably well at representing the observed radiative fluxes across the different sub-regions.

Table 6-3. Average daily surface radiative fluxes (all in W m^{-2}) over period 1998-2001 for SRB ('Observations') and for each sub-region shown in Figure 6-9, comparing the Emanuel scheme with the default version of RegCM3-IBIS to the new version incorporating all modifications presented in Chapters 3 to 5.

Observations / Simulation	SW_{dn}	SW_{up}	SW_{net}	Surface albedo	Planetary albedo	LW_{dn}	LW_{up}	R_N
Malay Peninsula	*190*	*31*	*159*	*16%*	*48%*	*417*	*457*	*119*
EMAN default	242	42	201	17%	48%	422	469	154
EMAN new	207	38	170	18%	44%	416	461	125
Highland Borneo	*204*	*39*	*165*	*19%*	*50%*	*400*	*439*	*126*
EMAN default	222	28	194	13%	54%	400	442	152
EMAN new	202	26	176	13%	47%	392	440	128
Lowland Borneo	*195*	*38*	*157*	*19%*	*50%*	*408*	*443*	*122*
EMAN default	213	27	186	13%	53%	422	460	148
EMAN new	189	25	164	13%	48%	416	460	120
Northern Sumatra	*196*	*24*	*172*	*12%*	*50%*	*410*	*452*	*130*
EMAN default	213	31	182	15%	52%	407	451	138
EMAN new	208	31	176	15%	46%	398	445	129
Southern Sumatra	*197*	*37*	*160*	*19%*	*50%*	*414*	*457*	*116*
EMAN default	233	39	194	17%	49%	424	468	150
EMAN new	199	35	164	18%	45%	419	461	122

6.2 Higher Resolution Simulations

Having determined that the largest simulation errors with respect to the diurnal rainfall peak occur over locations adjacent to mountains, it is questionable whether the errors result simply from the grid cell resolution; perhaps the size of these islands and the topographic gradients involved require higher resolution than was previously used.

To test this possibility, two further simulations were run. One contained higher horizontal resolution and used 10 km grid spacing (instead of 30 km); the other contained higher vertical resolution and used 29 vertical model layers (instead of 18). A third simulation comprising increased resolution in both the horizontal and vertical was attempted, but the timestep required to ensure numerical stability was so small that it made the computational expense prohibitive. Both high resolution simulations used the new version of the model, incorporating all modifications made in Chapters 3 to 5.

The average surface radiative fluxes and rainfall results from these two high resolution simulations are shown in Table 6-4 and Table 6-5 below, compared to the version shown previously with 30 km horizontal resolution and 18 vertical levels.

Table 6-4. Average daily surface radiative fluxes (all in W m^{-2}) over period 1998-2001 for SRB ('Observations') and for simulations using the Emanuel scheme with the new version of RegCM3-IBIS incorporating all modifications presented in Chapters 3 to 5, for different vertical and horizontal resolutions.

LAND

Observations / Simulation	SW_{dn}	SW_{up}	SW_{net}	Surface albedo	Planetary albedo	LW_{dn}	LW_{up}	R_N
Observations	*202*	*31*	*171*	*16%*	*48%*	*411*	*452*	*129*
30 km, 18 levels	197	29	168	15%	46%	411	455	124
10 km, 18 levels	217	31	186	14%	44%	405	454	138
30 km, 29 levels	191	27	164	14%	46%	412	458	119

OCEAN

Observations / Simulation	SW_{dn}	SW_{up}	SW_{net}	Surface albedo	Planetary albedo	LW_{dn}	LW_{up}	R_N
Observations	*220*	*14*	*206*	*6%*	*45%*	*420*	*467*	*158*
30 km, 18 levels	211	14	197	7%	49%	426	473	150
10 km, 18 levels	236	16	221	7%	47%	421	473	169
30 km, 29 levels	226	15	211	7%	49%	424	473	162

Table 6-5. Total, convective and large-scale rainfall (all in mm day^{-1}) averaged over 1998-2001 for land and ocean from TRMM ('Observations') and for simulations using the Emanuel scheme with the new version of RegCM3-IBIS incorporating all modifications presented in Chapters 3 to 5, for different vertical and horizontal resolutions. The relative proportions of convective and large-scale rain are shown in parentheses.

Product / Simulation	Land Average			Ocean Average		
	Total	Convective	Large-scale	Total	Convective	Large-scale
Observations	*8.6*	*5.4 (63%)*	*3.2 (37%)*	*7.0*	*4.0 (57%)*	*3.0 (43%)*
30 km, 18 levels	9.9	5.4 (55%)	4.5 (45%)	6.1	3.7 (61%)	2.4 (39%)
10 km, 18 levels	10.4	6.9 (66%)	3.5 (34%)	6.0	3.5 (58%)	2.5 (42%)
30 km, 29 levels	12.3	3.4 (28%)	8.9 (72%)	8.1	1.6 (20%)	6.5 (80%)

Interestingly, the results show that the higher resolution simulations did not improve upon the results using the lower resolution. Increasing the horizontal resolution tended to increase the convective rainfall, resulting in increased incoming shortwave radiation and decreased downward longwave radiation. Increasing the vertical resolution had the opposite effect, reducing the convective rainfall and increasing cloud cover, leading to a reduction in the incoming shortwave radiation. It was shown in Chapter 3 that the large-scale rainfall (produced by the SUBEX routine) is very sensitive to the number of vertical layers containing cloud cover. It is considered likely that the simulation results using 29 vertical layers reflect this sensitivity.

Maps of the local time of the diurnal rainfall peak were made for the two higher resolution simulations and are shown in Figure 6-15 and Figure 6-16. The figures show that these simulations contain very similar timing to the former resolution simulations. Hence it does not appear that the diurnal cycle timing errors are simply the result of an issue with model resolution, at least not to the scales used here. It is noted that 10 km is the smallest grid cell size that is usually considered acceptable to use with a convective parameterization scheme, and therefore represents the highest resolution possible with RegCM3.

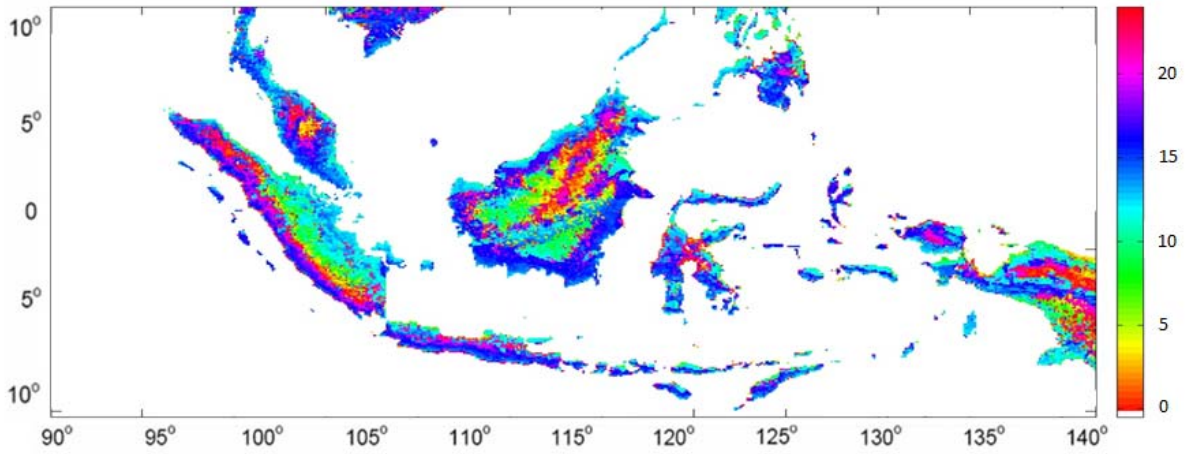

Figure 6-15. Local time (see color bar) of diurnal rainfall peak averaged over 1998-2001, using Emanuel scheme with the new version of RegCM3-IBIS incorporating all modifications presented in Chapters 3 to 5, using 10 km resolution (18 vertical layers). Ocean cells have been masked out for clearer visualization of land cells.

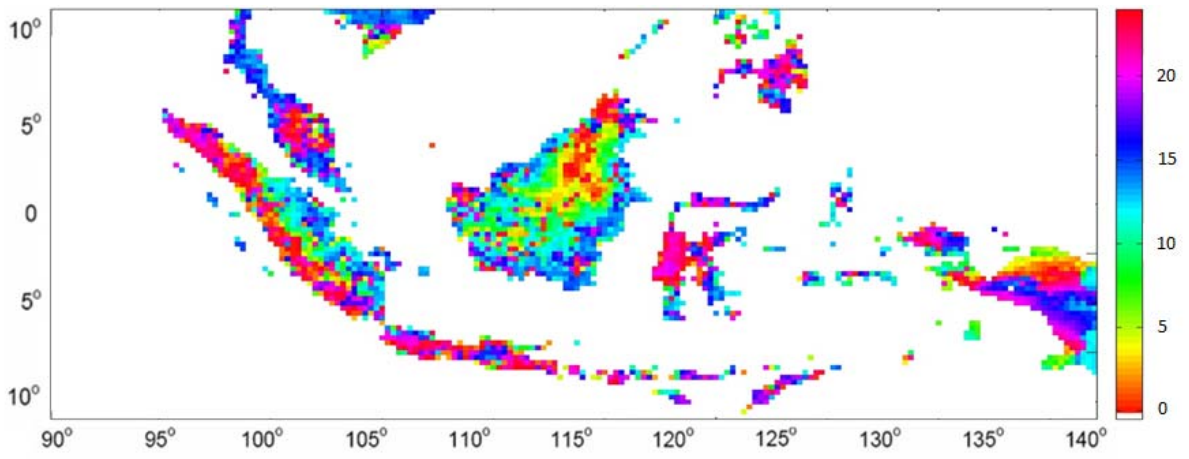

Figure 6-16. Local time (see color bar) of diurnal rainfall peak averaged over 1998-2001, using Emanuel scheme with the new version of RegCM3-IBIS incorporating all modifications presented in Chapters 3-5, using 29 vertical layers (30 km resolution). Ocean cells have been masked out for clearer visualization of land cells.

There is a long history of experiments addressing the effects of changing the horizontal resolution of GCMs. Boyle and Klein (2010) noted the following studies that pertain to the simulation of tropical processes – Neale and Slingo (2003) using HadAM3 (resolutions from 2.5° x 3.75° to 0.83° x 1.25°), Hack *et al.* (2006) using CAM3 (resolutions 2.8° and 1.4°), Lau and Ploshay (2009) using GFDL AM2 (resolutions from 2° to 0.25°), Shaffrey *et al*. (2009) using HiGEM (0.83° x 1.25°) and HadGEM (1.25° x 1.875°), Gent *et al*. (2009) using CAM (resolutions of 2° and 0.5°), and Zhao *et al*. (2009) using the GFDL GCM (at 0.5° resolution). Boyle and Klein (2010) themselves used CAM4 (at resolutions 2° to 0.25°). A common result in these resolution studies is that the gains in model performance from the higher resolution were fairly moderate. The tendency is for higher resolutions to produce a better spatial distribution of rainfall at the expense of increased overestimation errors.

Boyle and Klein (2010) argue that this is not surprising since convection remains unresolved in the finest resolution (0.25°) used. The implication then is that the major sources of error in these GCMs are small-scale processes related to convection, and that only by explicitly resolving these processes can models adequately reproduce observations.

The analysis presented thus far in this chapter has shown that there is systemic error in the simulation of the diurnal rainfall cycle within RegCM3-IBIS that is not resolved by

changing model resolution, similar to the GCM studies listed above. This error is concentrated over specific locations within the domain and appears to be most significant over inland, lowland areas. The next section will review the diurnally-varying processes observed over the Maritime Continent region and identify the specific processes that create the simulation error.

6.3 Review of Diurnal Processes over the Maritime Continent

6.3.1 Local Instability and Thermally-Driven Circulations

Kikuchi and Wang (2008) showed that the diurnal cycle over the tropics exhibits two strong modes of variability. The first mode represents the general temporal differences between the stationary rain peaks over land and ocean. This mode is associated with the convective response of the lower atmosphere to daytime shortwave radiative heating and nocturnal longwave radiative cooling (Teo *et al.* 2011). The diurnal cycle of radiative heating has two major effects: 1) it causes local destabilization of the atmosphere, and 2) spatial variations in radiative heating create mesoscale thermally-driven circulations (Yang and Smith 2006).

The most widely-studied of these circulations is the land-sea breeze circulation. Diurnal land-sea temperature variations occur as a result of the low heat capacity of land compared to that of water. When the water temperature is near the diurnal mean of the land temperature (as is the case over the Maritime Continent region), the land will tend to be warmer than water in daytime and cooler during night-time. This will produce a solenoidal circulation between the land and water that will drive a frontogenesis process, concentrating the upward lifting along a “sea breeze front” or a “land breeze front” depending on whether it is day or night (Yang and Smith 2006). Over the water during the afternoon or over the land during the evening, sinking motion predominates in compensation for the lifting, suppressing rain. These regions of lifting tend to be too shallow to initiate deep convection except in the tropics, where high humidity creates low cloud bases and relatively low levels of free convection (Yang and Smith 2006). Land breezes tend to be much shallower and weaker than sea breezes, because night-time radiative cooling

produces temperature changes only in a shallow layer near the land surface, especially in humid and cloudy tropical conditions, and the cooling land surface creates a stable boundary layer that inhibits vertical motion (Wu *et al.* 2009).

A similar circulation is created between mountains and valleys (areas of lower elevation). The air directly above a mountaintop is warmed more rapidly, due to proximity to the land surface, than air at a similar altitude over an adjacent valley. The effect may be enhanced if the lower-lying grounded is shaded by the mountain. Convection will therefore tend to begin at higher elevation, creating a region of lower pressure into which air flows upwards from the bottom of the slope. The circulation is reversed at night due to radiative cooling.

Observational studies carried out over specific islands within the Maritime Continent region have illustrated the strong influence that local instability and thermally-driven circulations have on rainfall over this region.

Ichikawa and Yasunari (2006) and Zhou and Wang (2006) described the diurnal rainfall cycle over Borneo and New Guinea, respectively, using TRMM data. Over these islands, rainfall begins along the coasts and over the central mountains by late morning. As the sea breeze front moves inland during the afternoon, rainfall increases over locations inland from the coast. Rainfall also strengthens over the central mountains during the afternoon, as the onshore and upslope circulations converge and strengthen. Over Borneo, this convergence results in the formation of mesoscale convective systems, which lead to persistent rainfall until midnight over the central part of the island. These systems gradually migrate away from the mountains overnight. Over New Guinea, rainfall also weakens over the mountains at night as downslope winds develop and split the rainband into two, propagating away from the mountain in both north and south directions. Offshore rainfall develops near both islands in the early morning as rainfall over land dissipates. Convective rainfall peaks in the afternoon over these islands, while stratiform rainfall peaks at night and in the early morning.

Wu *et al.* (2009b) showed that similar local circulations are created over the island of Sumatra. Upslope winds driven by diurnal heating at the surface of the mountains reinforce

the daytime sea breezes, with the result that a notable thermally-induced local circulation develops on the western coast of the island on a daily basis (Wu *et al.* 2009b).

To evaluate the ability of RegCM3-IBIS to reproduce these thermally-driven circulations, the diurnal variations in wind fields, temperature anomalies and radiative cooling are shown in the following figures. The results come from the improved version of the model (as described in Chapter 5) and are averaged over the 1998-2001 simulation period.

Figure 6-17 shows the simulated diurnal cycle of the meridional winds along the longitude 114^{o}E, which cuts through the center of Borneo. The vertical axis shows the terrain-following sigma coordinate, from the surface up to approximately 750 mb. The figure shows that simulation of a sea breeze circulation begins in the late morning and strengthens into the afternoon, with convergence over the mountains in the center of the island at about 1^{o}N. The circulation weakens at night and in the early morning, though it never completely reverses. This is consistent with the note from Wu *et al.* (2009) above, that the night-time land breeze is much weaker than the daytime sea breeze.

Figure 6-18 shows the simulated diurnal temperature anomaly (hourly temperature minus the daily mean) and vectorized zonal and vertical winds (with the vertical component amplified 10 times for easier visualization) along latitude 2^{o}S, cutting through the islands of Sumatra, Borneo and Sulawesi. The vertical axis is again in sigma coordinates, up to an elevation of about 350 mb. The figure clearly shows the diurnal heating and cooling of the islands, with daytime convergence and strong lifting over the islands against the background mean easterly flow.

Daytime shortwave radiative heating of the surface simulated by the model has already been evaluated in prior chapters. To evaluate the simulated night-time radiative cooling of the land surface, Figure 6-19 shows the diurnal cycle of longwave radiative flux upwards from the surface from the SRB data, averaged over the period 1998-2001, and Figure 6-20 shows the simulated longwave radiative flux upward from the surface from the new version of the model using the Emanuel scheme.

The figures show that the model simulates the diurnal amplitude of the radiative cooling reasonably well compared to the SRB data. The model appears to overestimate the longwave flux during the middle of the day over some land surfaces, likely associated with the small overestimation of surface temperature shown in Table 5-5. But the daytime spatial patterns and the night-time radiative cooling match well to the observations.

It is therefore considered that the diurnally-varying thermal circulations are simulated well by the improved version of the model. This assertion is bolstered by the results of the spatial analysis presented in Section 6.1. As mentioned above, the coastal areas of the islands are observed to experience convective rainfall first, as a result of local instability and the onset of sea breeze circulations. It was shown in Figure 6-5 that the coastal areas generally exhibited small errors in the timing of the diurnal rainfall peak compared to TRMM, and Figure 6-10 showed that the new version of the model simulates the diurnal cycle of rainfall very well over the southern Malay Peninsula. Therefore the first mode of variability in the diurnal cycle, as described by Kikuchi and Wang (2008), is simulated well within the improved version of RegCM3-IBIS.

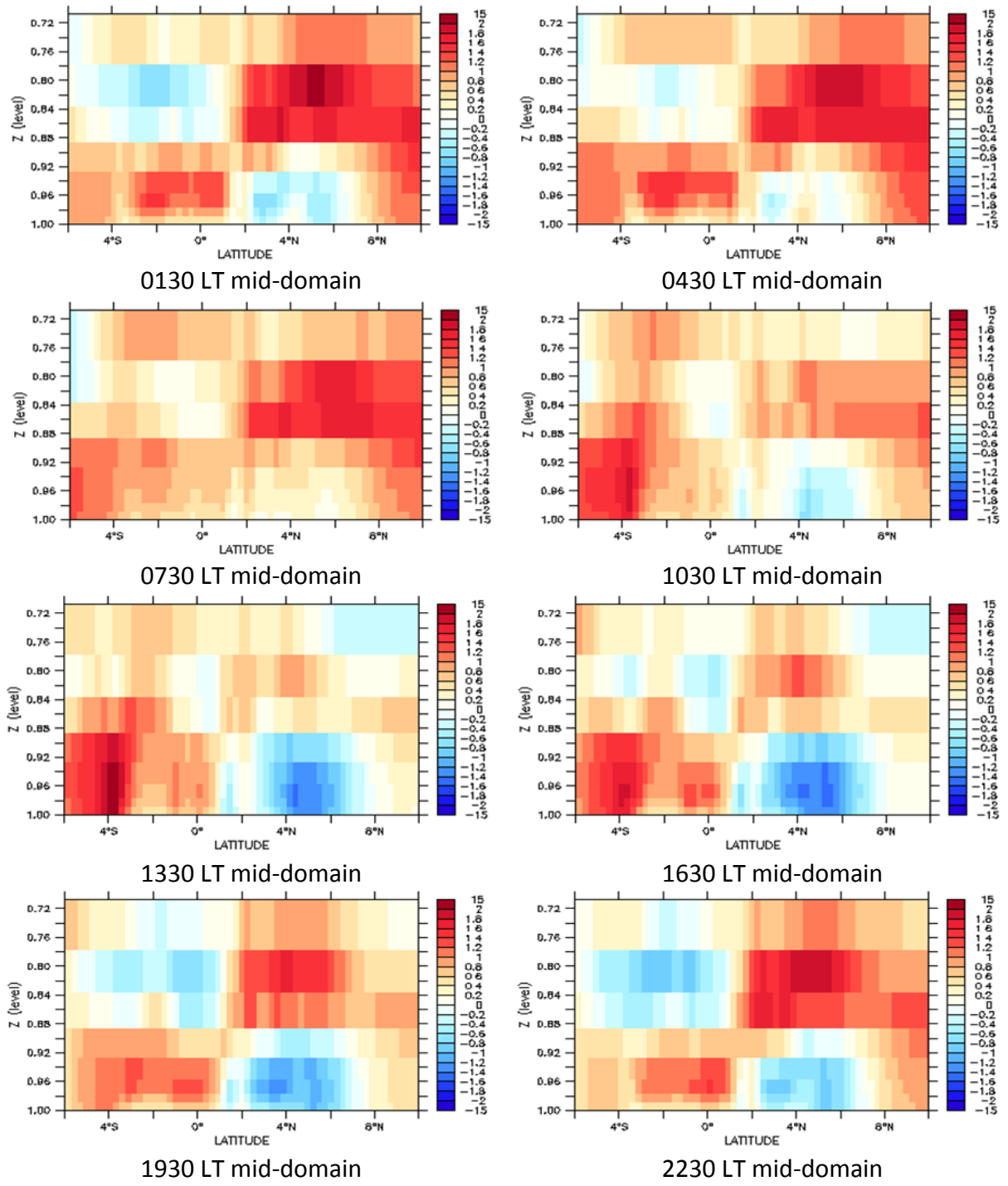

Figure 6-17. Diurnal cycle averaged over the period 1998-2001 of meridional wind (m s^{-1}) along 114°E through Borneo from simulation using Emanuel scheme with new version of the model. Vertical axis shows sigma levels up to about 750 mb. Local time for the center of the domain is given at the bottom of each panel.

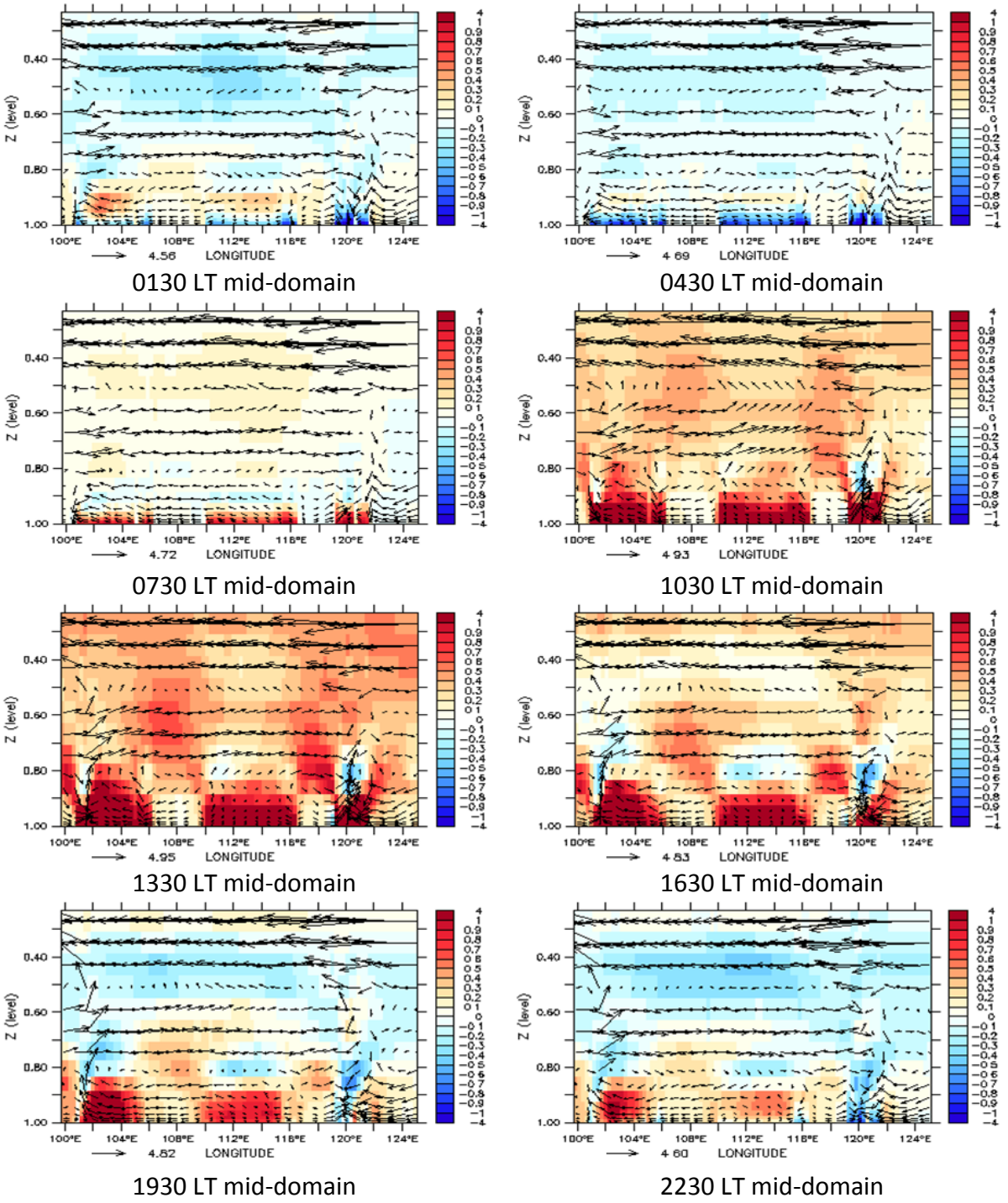

Figure 6-18. Diurnal cycle averaged over the period 1998-2001 of temperature anomaly (^{o}C, see color bar) with zonal and vertical winds (m s^{-1}, with vertical wind component amplified 10 times) along 2^{o}S from simulation using Emanuel scheme with new version of the model. Vertical axis shows sigma levels up to about 350 mb. Local time for the center of the domain is given at the bottom of each panel. Arrows underneath each panel indicate the maximum wind strength.

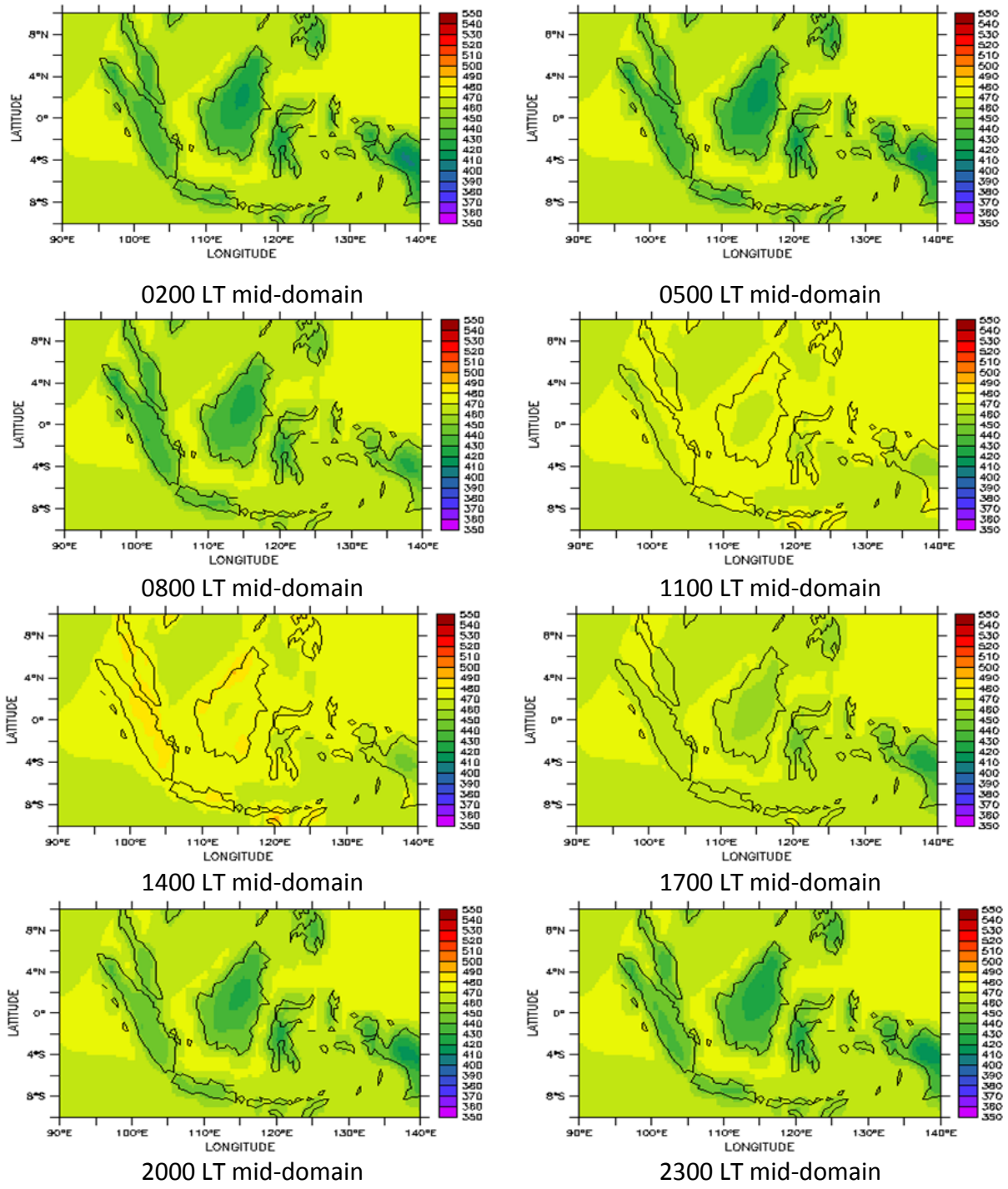

Figure 6-19. Diurnal cycle averaged over the period 1998-2001 of longwave radiation (in W m^{-2}) away from surface (i.e. radiative cooling) from SRB observations. Local time for the center of the domain is given at the bottom of each panel.

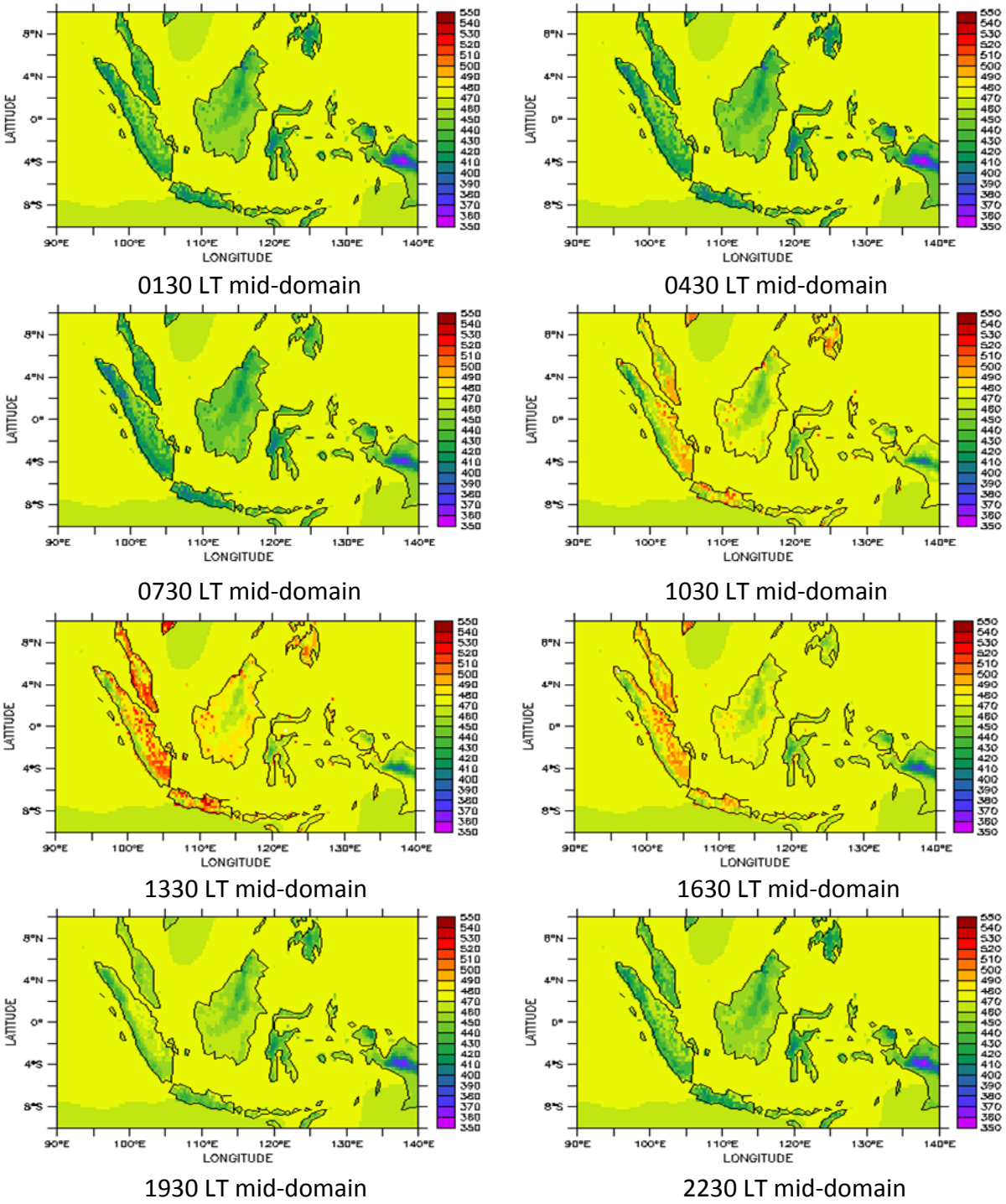

Figure 6-20. Diurnal cycle averaged over the period 1998-2001 of longwave radiation (in W m^{-2}) away from surface (i.e. radiative cooling) from simulation using Emanuel scheme with new version of the model. Local time for the center of the domain is given at the bottom of each panel.

6.3.2 Propagation of Convective Rainfall

Kikuchi and Wang (2008) described a second mode of variability in the diurnal cycle over the Maritime Continent that represents the propagation of rainfall peaks. Several specific mechanisms for rainfall propagation across the islands and offshore regions of the Maritime Continent have been identified. These include the land-sea breeze circulations described above, as well as up- and downslope winds on elevated terrain, gravity waves, gravity currents generated from deep convection (Teo *et al.* 2011), the movement of mesoscale convective systems with the background flow, and self-generating convective fronts ahead of cold outflows from convective downdrafts. The propagation of convective rainfall via self-generating mechanisms (squall lines) appears to be a particularly dominant feature of the region.

Over Sumatra, convection over the mountains frequently creates a zone of cold surface outflow, which leads to convection at the leading edge (Wu *et al.* 2009b). In the late afternoon and evening, rainfall has been observed to migrate both westward and eastward away from the mountain peaks (Mori *et al.* 2004, Love *et al.* 2011, Teo *et al.* 2011) with a speed and direction roughly corresponding to the horizontal wind below 4 km (Sakurai *et al*. 2009). The migrating systems are structured with convective precipitation in the forward and stratiform precipitation in the rearward regions of the migratory direction (Sakurai *et al*. 2009). These observations suggest that the migration of the precipitation systems arises from the generation of new convective cells over the leeward side by self-replication of convective cells and background advection (Sakurai *et al*. 2009).

Similar propagation of rainfall has been observed over: the leeward side of the Borneo mountains, with a propagation phase speed close to the 700 hPa wind speed (Ichikawa and Yasunari 2006); over New Guinea, both inland from the coast with penetration of the sea breeze front (Zhou and Wang 2006) and away from the mountains as downslope winds develop (Ichikawa and Yasunari 2008); along the northeastern coast of the Malay Peninsula and the eastern coast of Sulawesi (Teo *et al.* 2011); around the Khorat Plateau of Indochina, associated with migration of a cold air mass resulting from daytime convection (Takahashi *et al.* 2010); and over the Indochina Peninsula, propagating at the speed of the

gravity current under the interaction between the cold pool from the convection and an ambient wind near the surface (Satomura 2000).

Gravity waves have also been implicated in the propagation of cloud systems and temperature anomalies over the tropics, including the Maritime Continent region (Yang and Slingo 2001, Joseph *et al.* 2008, Kikuchi and Wang 2008). Love *et al*. (2011) argued that propagation of a gravity wave forced by the stratiform convection (i.e. the heating profile present later in the day comprising upper tropospheric heating and mid-tropospheric cooling) is the crucial element in controlling the offshore propagation of convection over Sumatra. Mapes *et al.* (2003) and Warner *et al.* (2003) have also described rainfall migration to offshore regions from northwestern South America, thought to be caused by gravity waves emanating off the land topography.

Despite the observed importance of these propagation mechanisms for convective rainfall production, simulation of rainfall propagation has proven problematic for large-scale climate models.

Hara *et al.* (2009) showed that the MRI-GCM, run at a 20 km resolution, could accurately simulate the manner in which convection is generated over a mountain range or near the coast from the afternoon to the evening, but could not simulate propagation of the convective system. Ploshay and Lau (2010) showed that the GFDL GCM, run at a resolution of 0.25^{o} x 0.3125^{o}, could not reproduce the observed night-time precipitation peaks at the equator over Borneo or the seaward migration of diurnal signals off the western Sumatra and northern Borneo coasts. Love *et al.* (2011), using the UK Met Office Unified Model, found that propagation of rainfall across Sumatra was distinctly absent at both 12 km and 40 km resolutions – precipitation was dominated by a strong diurnal cycle anchored to the land area of Sumatra. Teo *et al.* (2011) showed that WRF, run at 25 km resolution with a convective parameterization scheme, could produce most of the local diurnal rain features, but the nocturnal rain propagation speed was much slower in the model than in observations and there was no effective propagation of the evening rain features from land into the coastal seas off the Borneo.

To determine if the improved version of RegCM3-IBIS is capable of reproducing the observed propagation of convective signals, time-longitude plots were constructed of the diurnal anomalies in rainfall (shown in Figure 6-21) and temperature (shown in Figure 6-22) over the year 1998. The plots were made along 2°S latitude and cut through the islands of Sumatra, Borneo and Sulawesi.

Figure 6-21 shows that the majority of the diurnal rainfall over Sumatra and Borneo occurs during the afternoon, during 1200-1800 LT. There is little indication of rainfall propagation with time, with the exception of some rainfall propagation across land-sea boundaries on the western coasts of Sumatra and Sulawesi in the early morning. Rainfall over Borneo in particular shows a distinct lack of any land-based propagation.

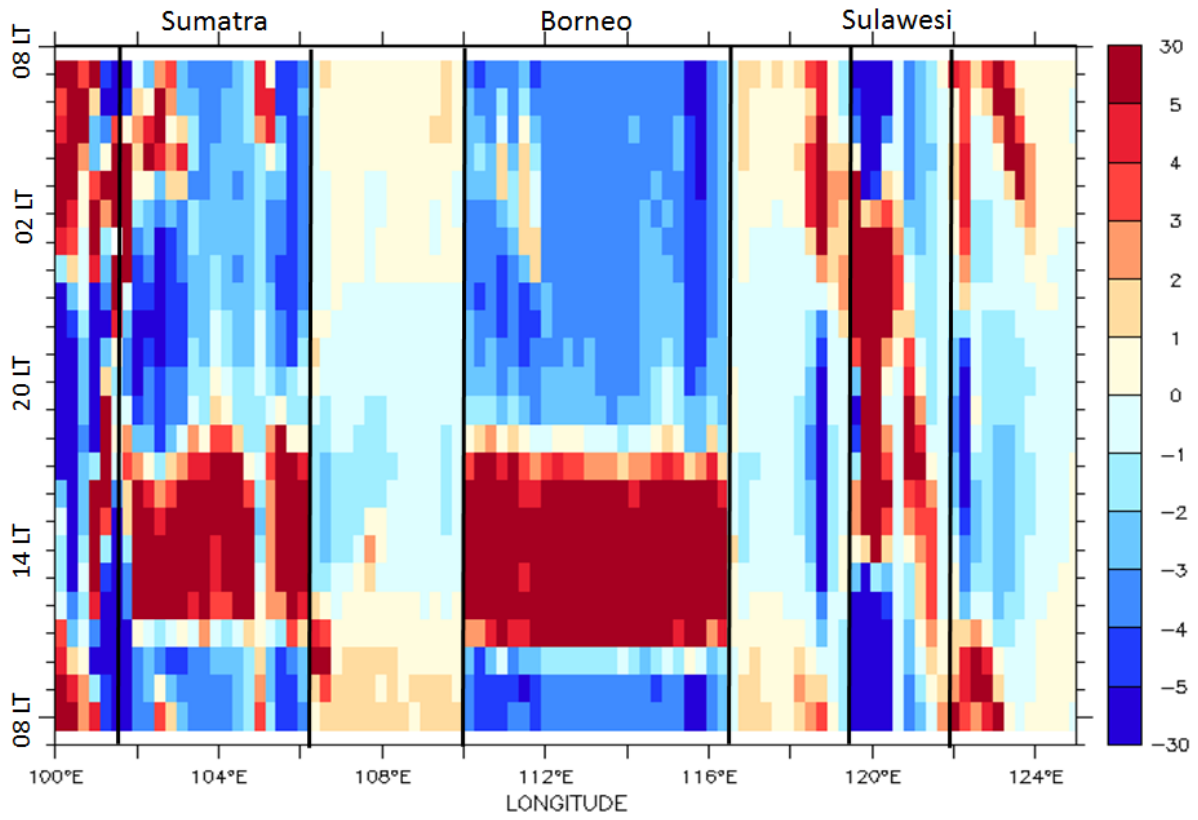

Figure 6-21. Time-longitude plot along latitude 2°S of diurnal rainfall anomaly (in mm day^{-1}), calculated as the rainfall at each time of day minus the daily mean rainfall, averaged over 1998 for the simulation using the new version of the model with the Emanuel scheme. Local time is shown on the vertical axis. The boundaries of the larger islands are marked with black lines.

Consistent with the rainfall anomaly, Figure 6-22 shows that there is no discernible signal of temperature anomaly propagation in the simulation. A warm anomaly is generated in the lower atmosphere over the islands during the day, but this anomaly seems to be stationary and diminish in place by night-time. There is no indication of a warm anomaly propagating from Sulawesi towards Borneo, as suggested by other observational and modeling studies.

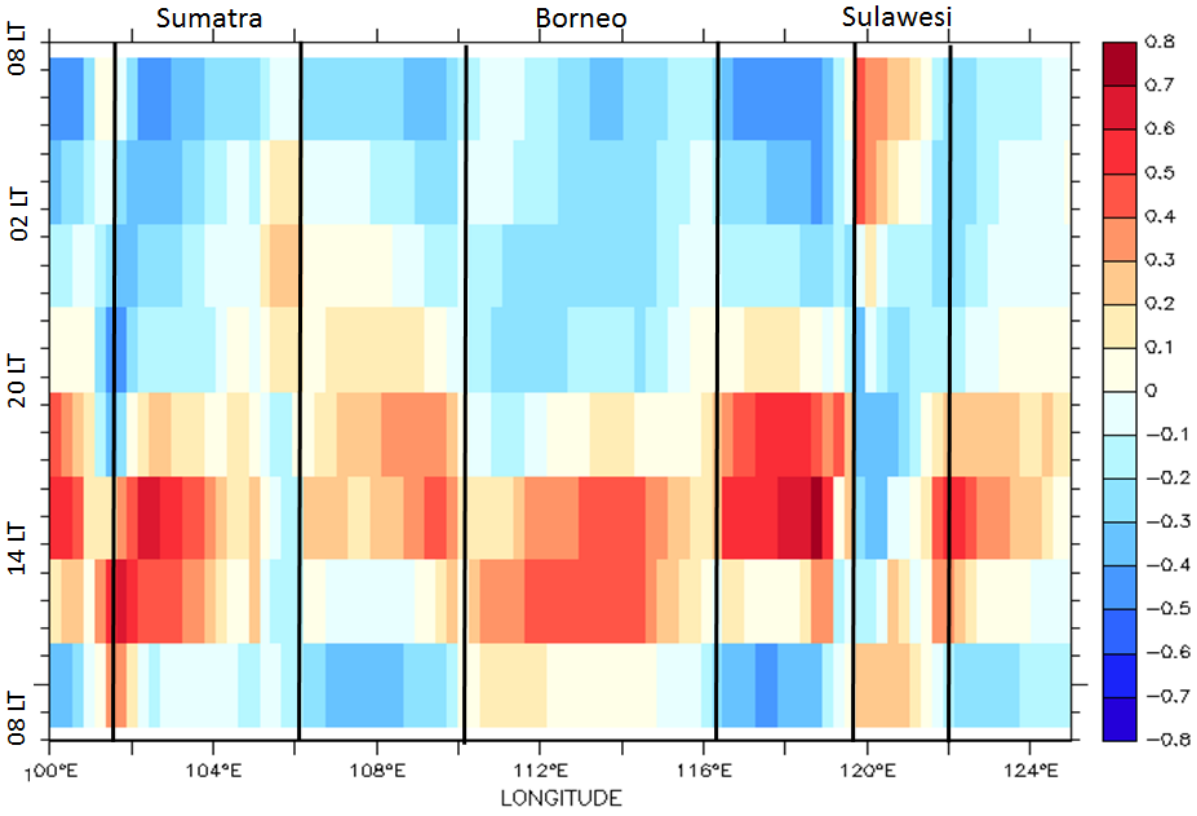

Figure 6-22. Time-longitude plot along latitude 2°S of diurnal temperature anomaly (in °C), calculated as the temperature at each time of day minus the daily mean temperature, averaged over 1998 for the simulation using the new version of the model with the Emanuel scheme. Local time is shown on the vertical axis. The boundaries of the larger islands are marked with black lines.

These results are consistent with all the other results presented thus far in this thesis, and indicate that RegCM3 suffers similar deficiencies to other large-scale climate models with regard to the migration of convective rainfall.

In contrast, studies have shown that high resolution, cloud-resolving models are capable of reproducing the observed rainfall propagation signals. Hara *et al*. (2009) showed

that WRF, run with a 3.5 km grid and no cumulus parameterization, could simulate the diurnal cycle of rainfall over Borneo and Sulawesi very well compared to TRMM. Wu *et al*. (2009a) showed that MM5, run with an inner nested grid of 6 km resolution and explicit convection, could simulate propagation of precipitable water and temperature anomalies between Sulawesi and eastern Borneo. Simulations with the UK Met Office Unified Model, run at a resolution of 4 km with explicit convection, exhibited similar maximum amplitudes to TRMM and matched the timing well, with distinct propagation signals both eastward and westward (Love *et al.* 2011).

As noted in Section 6.2, Boyle and Klein (2010) suggest that only by explicitly resolving the processes associated with convection will it be possible to accurately simulate the diurnal rainfall cycle. The scales at which the propagation mechanisms operate suggest that this is the case.

Tompkins (2001) used a high-resolution, cloud-resolving model to simulate the cold outflows produced by deep convection, which become triggers for the next generation of convective cells. In these simulations, the diameter of cold outflow patches varied from 3 km to 18 km, with a mean of 8.6 km and a downdraft vertical velocity on the order of 0.5 m s^{-1} (Tompkins 2001). May and Rajopadhyaya (1999) measured the vertical velocities of convective downdrafts over Darwin and reported velocities of 1-2 m s^{-1}. In both of these studies, the vertical velocity associated with convective downdrafts is substantially greater than the average environmental vertical velocity, which is on the order of 1 cm s^{-1}. Lane *et al*. (2001) argued that a model resolution of 4 km was required for simulation of squall lines, and even finer resolution is needed for simulation of convective downdrafts and gravity waves.

Therefore it seems that a GCM or RCM, using a typical convective parameterization scheme and running at a resolution of tens of kilometers, is not capable of reproducing these mechanisms that lead to propagation of convective rainfall.

6.4 Summary of Diurnal Processes and Simulation in RegCM3

This chapter has presented a more detailed analysis of the diurnal rainfall cycle, highlighting spatial variability in the simulated diurnal rainfall peak and discussing the mechanisms that create this variability.

The dominant mode of diurnal variability in the Maritime Continent is attributable to the convective response of the lower atmosphere to local instability, primarily driven by shortwave (SW) radiative heating and longwave (LW) radiative cooling. These processes create convective rainfall locally and drive land-sea breeze and mountain-valley breeze circulations. The simulated wind patterns, LW cooling and SW heating indicate that the improved version of RegCM3 is adequately reproducing the observed local breeze circulations over the Maritime Continent. Over locations where these local breeze circulations dominate, such as Java and the southern Malay Peninsula, the improved model reproduces the diurnal cycle very well.

The model also reproduces the diurnal cycle reasonably well over the mountain peaks. Over these locations, convection begins in the afternoon due to local instability. Cumulus mergers produce mesoscale convective systems (MCSs) that result in persistent rain throughout the night. In the model, the daytime moisture convergence results in large quantities of residual condensate after the daytime convective adjustment is finished. This residual moisture in the model is then re-evaporated and converted into stratiform clouds and rainfall by the SUBEX routine, producing a night-time rainfall peak in accordance with observations. These results indicate that the model's method of converting residual convective condensate into vapor for SUBEX to re-convert into large-scale condensate is adequate for approximating the creation of an MCS.

There are three locations within the domain where the model produces egregious error in timing of the diurnal cycle – inland Sumatra, inland west Borneo and inland east Borneo. In these locations, rainfall is attributable mainly to propagation of convective rainfall that originates over nearby mountain peaks and coastlines.

Over these large islands, observations show that daytime convection produces cold outflows that spread down the mountain slopes (in the case of mountaintop convection) and

away from the coastlines (in the case of the sea breeze front). These outflows trigger localized convection at the leading edge, which leads to further production of cold outflows and perpetuates the migration. The propagation is enhanced when it is in the same direction as the mean low-level winds. The MCSs produced over central Borneo by daytime cumulus mergers also propagate with the mean background flow, maintaining considerable spatial coherency. Convection is strengthened if the migrating convective front collides with a night-time mountain breeze or remnant sea breeze, causing forced lifting. There are also suggestions that gravity waves propagate temperature anomalies created by the daytime convection, although the role of these anomalies in enhancing or suppressing convection requires further investigation. The simulation results presented in this thesis indicate that RegCM3 does not reproduce these propagation mechanisms.

It is proposed that a major deficiency in RegCM3, and most likely in all other large-scale climate models, is an inability to represent the convective downdrafts that drive cold outflows from regions of strong convection. This deficiency results from the coarse resolution used in large-scale climate models compared to the scale of convective processes, which necessitates using a convective parameterization scheme and prohibits explicit simulation of the different elements of a convective cell, including the cold outflow. A secondary deficiency within RegCM3 is a lack of spatial and temporal coherency in cloud cover, especially over land-sea boundaries and topographic gradients. This is likely due to the distinct separation in simulated cloud types within the model and the use of different parameter sets over different surfaces for each cloud type. It is also likely that the lack of any freezing hydrometeors (e.g. cloud ice) within RegCM3 contributes to the observed cloud deficiencies, since the deep convection that produces MCSs would contain a large fraction of below-freezing particles.

The dominant diurnal processes observed over the island of Borneo are summarized in the schematics shown in Figure 6-23, Figure 6-24, Figure 6-25 and Figure 6-26 (note that these figures are for illustrative purposes only and are not drawn to scale). These schematics also include the processes observed over Sumatra and New Guinea, although these figures were not made to represent those islands explicitly. Processes that are represented poorly

or not at all within the model are shown in red. It is considered that these processes are responsible for the simulated errors in the timing of diurnal rainfall and therefore represent targets for future work.

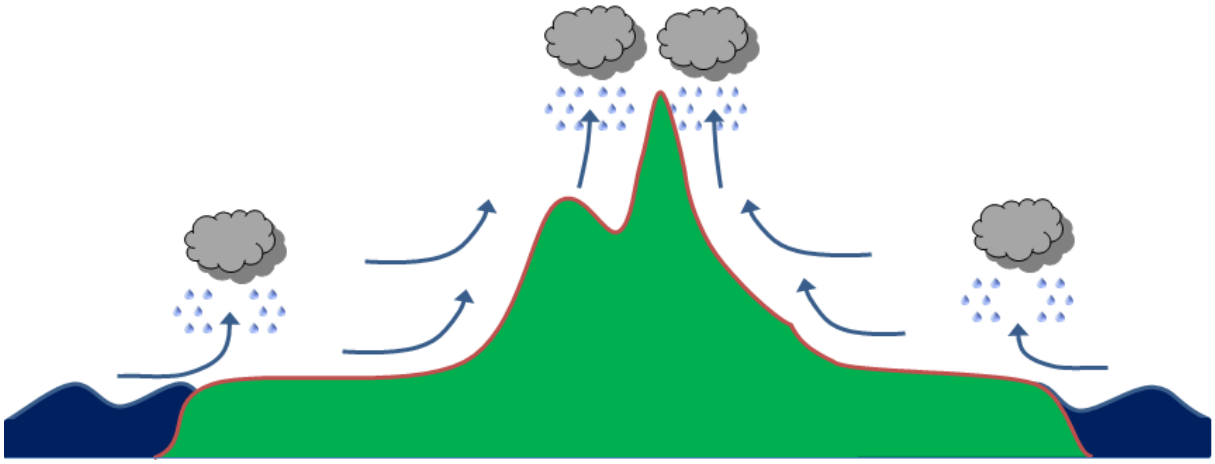

Figure 6-23. Schematic of rainfall processes over Borneo at approximately 1000-1200 LT. Sea breezes and local instability initiate convective rainfall over the coastlines, while valley breezes and local instability initiate convective rainfall over the mountains.

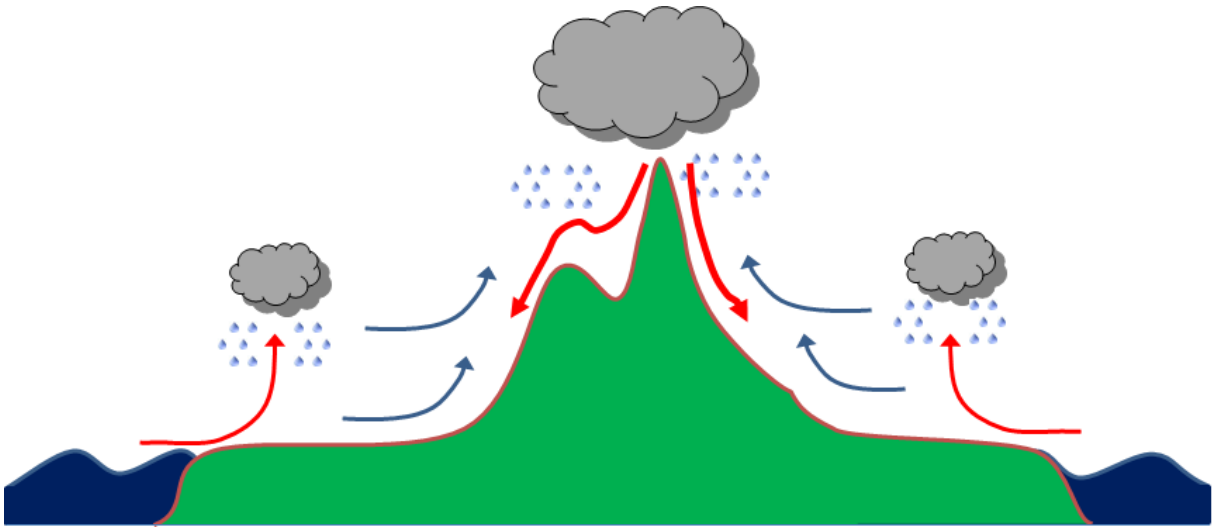

Figure 6-24. Schematic of rainfall processes over Borneo at approximately 1600 LT. Convective rainfall propagates inland from the coast with the sea breeze. Local circulations and instability continue to drive convective rainfall over the mountains. Cumulus mergers begin over the mountains, creating large cloud structures. Cold outflows, created by convective downdrafts over the mountains, begin to flow down towards the flat inland areas, triggering localized convection.

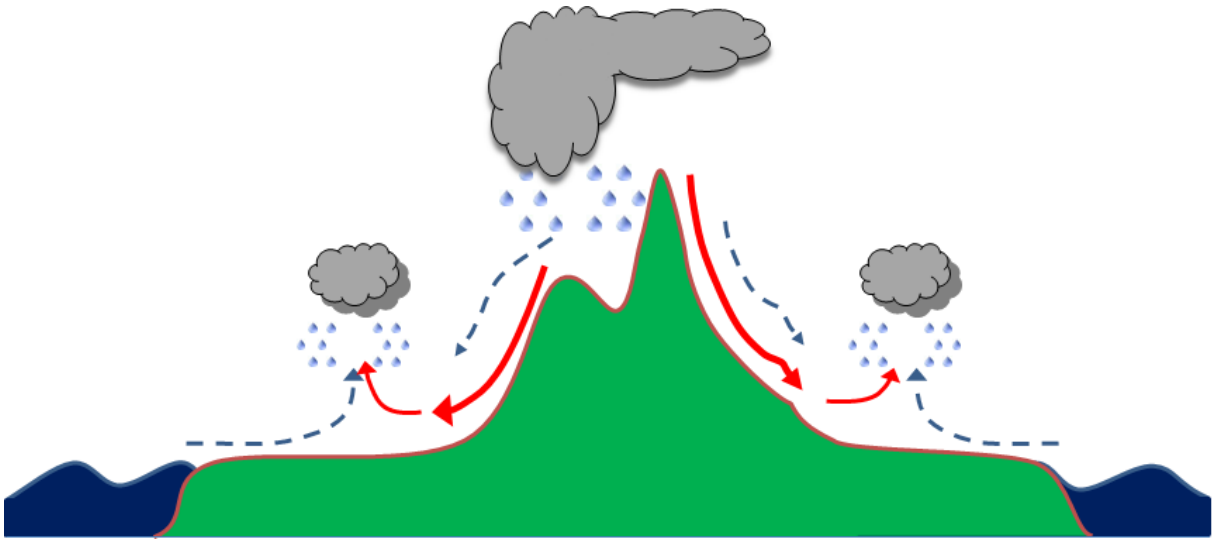

Figure 6-25. Schematic of rainfall processes over Borneo at approximately 2000-2200 LT. Remnant sea breezes (shown by blue dashed lines near coasts) collide with the cold outflows created by convective downdrafts, triggering rainfall over the inland areas of the island. Mountain breezes (shown by blue dashed lines over mountains) begin to form in response to radiative cooling, although these are very weak. A fully-developed mesoscale convective system (MCS) is present over the mountains and begins to move with the mean flow.

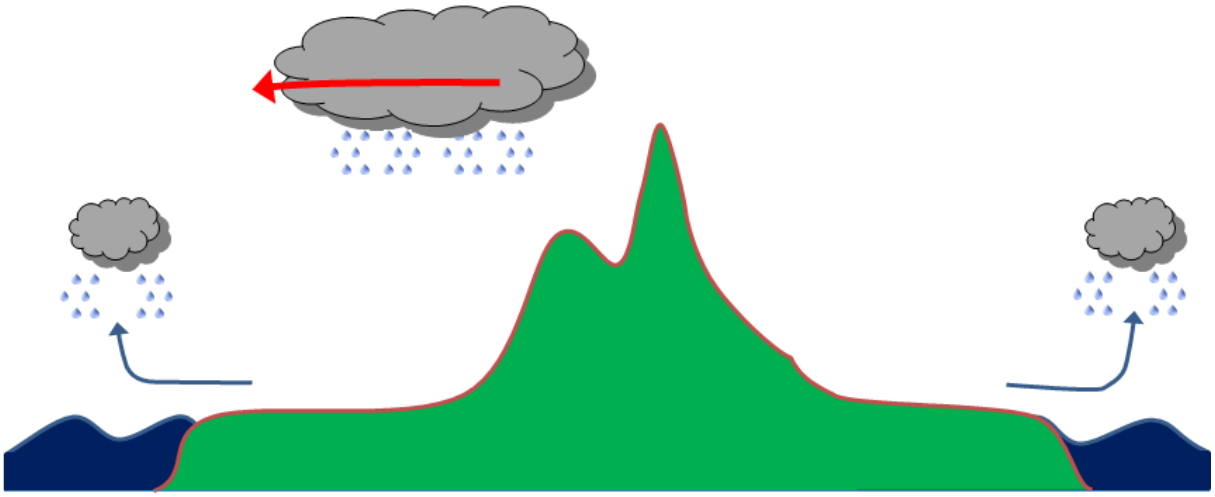

Figure 6-26. Schematic of rainfall processes over Borneo at approximately 0000-0200 LT. The MCS propagates away from the mountains with the mean flow, producing rainfall over the inland areas of the island. It will continue moving leeward throughout the night, arriving offshore by the early morning. A combination of land breezes, remnant cold outflows and weak mountain breezes triggers convective rainfall offshore.

Chapter 7: Temporal Variability in the Diurnal Cycle

The work presented in this thesis thus far has only investigated the diurnal cycle averaged over a 4-year period, 1998-2001. It is of considerable interest whether the newly improved version of the model will perform as well over longer simulation periods as it does over this relatively short period. Therefore this chapter will evaluate the model performance over a 19-year simulation period, and demonstrate that the improvements achieved by the modifications described in this work are consistent over this longer time period.

The longer-term simulation will then be used to explore temporal variability in the diurnal cycle. While the diurnal cycle of rainfall is one of the strongest modes of variability in the climate of the Maritime Continent (Yang and Slingo 2001, Kitoh and Arakawa 2005), it can be enhanced or suppressed due to the presence of large-scale flows, such as those associated with effects of the El Niño-Southern Oscillation (ENSO), monsoonal circulations and intraseasonal disturbances (Slingo *et al.* 2003).

El Niño episodes reflect periods of unusually warm SSTs across the eastern tropical Pacific Ocean, while La Niña episodes represent periods of unusually cool SSTs in the same region. As the warmest SSTs move eastward toward the central Pacific Ocean during an El Niño event, with accompanying weakening of the zonal easterly winds associated with the Pacific Walker circulation, the strongest convection follows and suppresses convection over the Maritime Continent (see Figure 7-1). The effect is particularly pronounced since El Niño maxima tend to occur during the northern winter, when convective rainfall is usually at a maximum over the Maritime Continent (Neale and Slingo 2003).

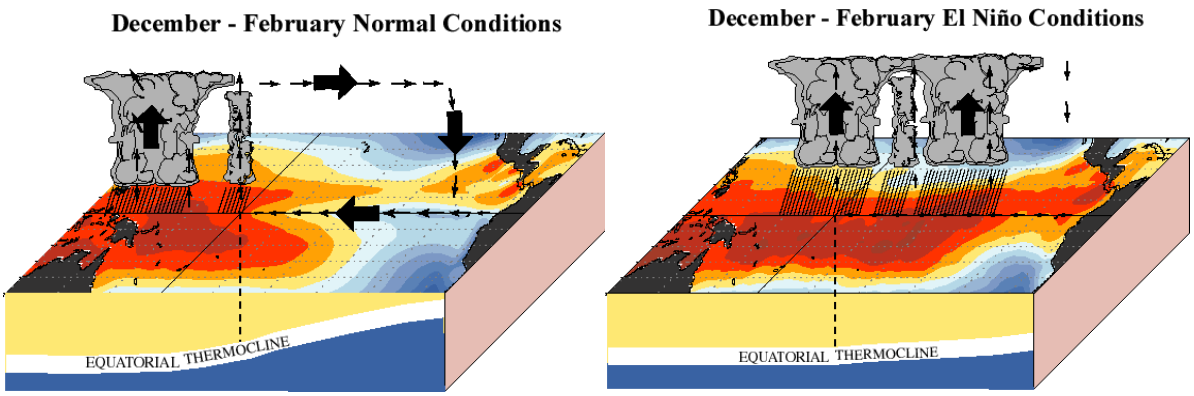

Figure 7-1. Schematic showing the typical circulation and temperature patterns over the Pacific Ocean under (left) average and (right) El Niño conditions during the northern winter. El Niño episodes feature reduced easterly winds across the Pacific in the lower atmosphere and reduced westerly winds in the upper atmosphere. These conditions reflect a reduced strength of the equatorial Walker Circulation. (From NOAA Climate Prediction Center, Accessed 22 October 2012. <http://www.cpc.ncep.noaa.gov/products/analysis_monitoring/ensocycle/enso_schem.shtml>)

The northern winter (December-February) monsoon circulation transports significant quantities of warm moist air from north of the equator that converges with the trade wind flow south of the equator to create conditions strongly conducive to convection during this season (Neale and Slingo 2003). The magnitude of the diurnal cycle is generally largest during the December-February wet season and smallest during the June-August dry season. The action of cold surges, which strengthen the Asian winter monsoon flow from north of the equator towards the Maritime Continent, also enhances convective activity during the monsoon season by converging with land breezes, as described by Houze *et al.* (1981), Johnson and Priegnitz (1981) and Johnson and Kriete (1982) offshore from the northwest of Borneo.

The timing and duration of convection also vary in association with the passage of intraseasonal disturbances, especially the Madden-Julian Oscillation (MJO). The MJO is characterized by an eastward propagation around the tropics of alternating regions of enhanced and suppressed convection. Previous studies using satellite cloud imagery have shown that the amplitude of the diurnal cycle is strongest during the convectively inactive phase of the MJO, and that it decreases during the active phase (Sui and Lau 1992, Chen and

Takahashi 1995). Ichikawa and Yasunari (2006) showed that convection around the island of Borneo is enhanced when the mean zonal winds are westerly and suppressed when the mean zonal winds are easterly, associated with intraseasonal disturbances such as the MJO. Ichikawa and Yasunari (2008) also showed that convective processes and monsoonal rainfall over the island of New Guinea differ between the easterly and westerly wind regimes of the MJO. The authors noted that the influence of topography, while observed under both wind regimes, was stronger under the easterly regime when conditions were generally drier (Ichikawa and Yasunari 2008). Modulation in the diurnal propagation signal also occurs over Sumatra: eastward propagation of convection accompanies only low-level westerlies related to the passage of MJO disturbances, whereas westward propagation of convection occurs year-round (Sakurai *et al*. 2005).

It is outside the scope of this work to conduct a detailed investigation of the different influences of all these various large-scale forcings on the diurnal cycle across the Maritime Continent; each mode of variability merits a separate investigation. However, since the work presented thus far has only analyzed the mean diurnal cycle, it is of some interest to explore how the improved version of the model performs under different conditions.

The interannual variability associated with ENSO has been chosen for closer investigation. This chapter will examine the influence of specific El Niño and La Niña events on the simulation of diurnal convective processes, and in particular whether the newly improved version of the model can capture the observed variability over the Maritime Continent. Some evaluation of the interseasonal variability is also conducted.

7.1 Model Performance Over a 19-year Simulation Period

Two simulations were set up in a similar manner – i.e. same model domain and resolution – to the default version of RegCM3-IBIS and the newly improved version (incorporating the modifications to the PBL from Chapter 3, the new convective cloud fraction and new convective autoconversion formulation) that have previously been described. These simulations both used the Emanuel scheme, since the improved version of the model with the Emanuel scheme better performance than the Grell scheme (see Chapter

5). The default and improved model versions are referred to as EMAN-Def and EMAN-New, respectively, in the simulations presented below.

Simulations were begun at 1 July 1982 and ended 31 December 2001. The first 6 months of output were ignored to allow for spin-up. The remaining 19 simulation years (1983-2001) were used for model evaluation. These years were chosen so that the same datasets could be used for lateral boundary conditions and the same observational datasets could be used for comparison, to maintain consistency with the previous 4-year simulations. The NOAA OISST weekly-mean 1^{o} x 1^{o} dataset begins in 1982; SRB and ISCCP observations begin in July 1983. All initial and boundary conditions are as described in previous chapters.

For comparison to the model, the following datasets were used: SRB for radiative fluxes, ISCCP for fractional cloud cover, and CRU TS3.0 and ERA40 datasets for temperature. The WHOI dataset for latent heat (LH) and sensible heat (SH) fluxes over ocean is also used. Over land, it is assumed that the LH and SH measured by various field studies over the islands, as shown in Table 2-4, also apply over the 19-year period.

TRMM data is only available from 1998 and hence a different satellite-based dataset was used for rainfall evaluation over the 19-year period. The Global Precipitation Climatology Project (GPCP) Version 2.2 Combined Precipitation dataset is available at monthly resolution from 1979 to the present. This product combines surface-based rainfall measurements and satellite precipitation data into 2.5^{o} x 2.5^{o} global grids (Adler *et al*. 2003). GPCP data is provided by the NOAA/OAR/ESRL PSD, located at Boulder, Colorado, from their website at [http://www.esrl.noaa.gov/psd/]. Unfortunately, the monthly resolution of this dataset prohibits analysis of the diurnal rainfall cycle as was conducted for the 4-year simulation. But an equivalently high resolution dataset as TRMM is not available for the years prior to the launch of that satellite, so the analysis presented here only evaluates the simulation of the temporal mean rainfall volume. For comparison to the GPCP data, the land-only CRU TS3.0 rainfall is also shown.

Since CloudSat was only launched in 2006, and the 5 available years of CLW data have already been used for comparison to the 4-year simulations in other chapters, it was considered inappropriate to use this dataset for the 19-year evaluation.

7.1.1 Cloud Fraction

The average diurnal cycle of the vertical cloud cover profile was very similar between the two simulation periods of 1983-2001 and 1998-2001. Therefore a brief summary is presented here and figures are not shown for brevity.

Over land with EMAN-Def, there is a maximum in low cloud cover at night and a minimum during the daytime, due to the default formulation of convective cloud fraction within RegCM3. The high level clouds are limited by the restriction to have the second-highest model layer cloud-free, and very dense cloud is formed at 12-14 km altitude in the evening. In contrast, cloud cover over land with EMAN-New shows a signature of daytime convection in the lower atmosphere, with a minimum in low cloud cover occurring at night. High clouds in EMAN-New extend up to 16 km but have a smaller fractional coverage.

Over ocean, there is very little cloud in the lower atmosphere with EMAN-Def, and again the high cloud is limited to 14 km because of the restriction in the second-highest model layer. EMAN-New shows significantly more high cloud cover, especially at 14-16 km altitude, and a dense bank of low cloud around 1 km above the surface.

The time-mean horizontal fractional cloud cover over the period 1983-2001 is compared to the ISCCP data in Figure 7-2. The results show that the simulated cloud cover over the period 1983-2001 is very similar to that simulated over the period 1998-2001. There is some overestimation of low cloud cover, which is stronger over land in the default case, EMAN-Def, and stronger over ocean in the improved model, EMAN-New. There is some underestimation of mid-level cloud cover in the center of the domain with both simulations. High cloud cover is overestimated with both simulations, and the error is worsened with EMAN-New. These simulations show that the improved version of the model produces very similar time-mean fractional cloud cover as the default version of the model, even though the diurnal cycle of cloud cover is very different.

Hence the simulated cloud cover in these 19-year simulations is consistent with that produced over the 4-year simulation.

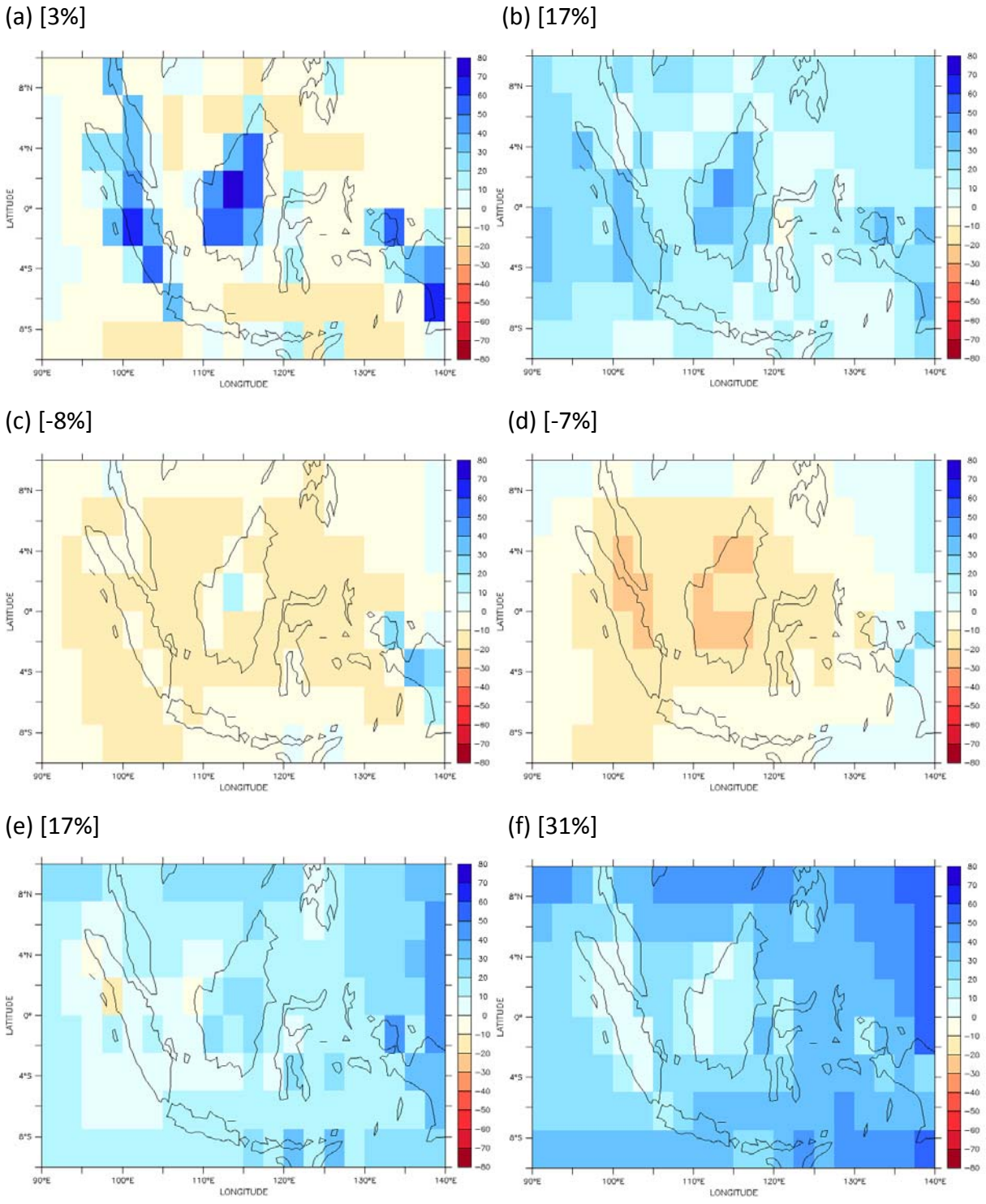

Figure 7-2. Average cloud fraction over 1983-2001: EMAN-Def simulation minus ISCCP data for (a) low, (c) middle and (e) high clouds, and EMAN-New simulation minus ISCCP data for (b) low, (d) middle and (f) high clouds. Domain-averaged error (model – ISCCP cloud fraction) is shown in parentheses. Color bar indicates fractional coverage of grid cell.

7.1.2 Radiative and Turbulent Heat Fluxes

Average daily radiative and turbulent heat fluxes for the period 1983-2001 are shown in Table 7-1, compared to the SRB observations for the same time period and the LH and SH values measured by the field studies described earlier. The results from the 4-year simulation are also shown for comparison. As with the cloud fraction, the results from the 19-year simulations are similar to the 4-year simulations.

Over land, EMAN-Def significantly overestimates the insolation at the earth's surface, particularly over ocean surfaces. This overestimation occurs despite good simulation of the planetary albedo, especially with the Emanuel scheme. The overestimation of insolation propagates into error in the simulated net radiation, LH and SH over land with EMAN-Def. With EMAN-New, simulated insolation matches very well to the SRB. There is a small underestimation of planetary albedo. EMAN-New has a small underestimation of net radiation over the 19-year simulation, primarily due to a combination of small errors in the simulated longwave radiation. Both EMAN-Def and EMAN-New show underestimation error in SH, as was the case with the 4-year simulation, although the bias is reduced in EMAN-New.

Over ocean, the results from EMAN-New also show considerable improvement in the simulation of insolation, with a very good match to observations and removal of the significant overestimation bias that was present in EMAN-Def. There is a small underestimation of net radiation with EMAN-New, again primarily due to small errors in the longwave radiation. Both EMAN-Def and EMAN-New show some overestimation of LH and underestimation of SH over the ocean, as was the case in the 4-year simulation. These biases were not appreciably changed by the model modifications. It is considered that this is due to the fixed SSTs used in these simulations.

Therefore the results from the 19-year simulations support the results from the 4-year simulations: improvements to the diurnal cycle of cloud cover and insolation propagate into improvements in the mean radiative and turbulent heat fluxes over longer time periods.

Table 7-1. Average daily surface radiative and turbulent heat fluxes (all in W m^{-2}) over 19-year period 1983-2001 and 4-year period 1998-2001, comparing SRB (radiative fluxes) and field studies (LH and SH) ('Obs.') to the Emanuel scheme with the default version of RegCM3-IBIS (EMAN-Def) and the new version incorporating all modifications presented in Chapters 3 to 5 (EMAN-New).

LAND

Product / Simulation	SW_{dn}	SW_{up}	SW_{net}	Surface albedo	Planetary albedo	LW_{dn}	LW_{up}	R_N	LH	SH
Obs. – 19 years	*207*	*28*	*180*	*13%*	*47%*	*410*	*452*	*138*	*95*	*43*
EMAN-Def	226	32	195	14%	48%	412	460	147	126	22
EMAN-New	208	30	179	14%	44%	406	457	128	100	29
Obs. – 4 years	*202*	*32*	*170*	*16%*	*48%*	*411*	*452*	*129*	*95*	*34*
EMAN-Def	213	30	183	14%	50%	416	457	141	134	6
EMAN-New	197	29	169	14%	46%	411	455	124	105	20

OCEAN

Product / Simulation	SW_{dn}	SW_{up}	SW_{net}	Surface albedo	Planetary albedo	LW_{dn}	LW_{up}	R_N	LH	SH
Obs. – 19 years	*225*	*14*	*211*	*6%*	*44%*	*419*	*466*	*164*	*102*	*8*
EMAN-Def	271	17	254	6%	43%	412	471	194	118	5
EMAN-New	226	15	211	7%	46%	419	471	159	119	5
Obs. – 4 years	*220*	*14*	*206*	*6%*	*45%*	*420*	*467*	*158*	*109*	*10*
EMAN-Def	257	16	241	6%	45%	418	473	186	126	4
EMAN-New	211	14	197	7%	49%	426	473	150	120	5

Notes on Table 7-1: SW_{dn} = shortwave (solar) radiation incident at the surface, SW_{abs} = net absorbed shortwave radiation at the surface, LW_{dn} = longwave radiation incident at the surface, LW_{up} = longwave radiation emitted from surface, R_N = net radiation absorbed at surface, LH = latent heat flux away from surface, SH = sensible heat flux away from surface. See Notes on Table 3-5 for explanation of albedo calculation.

7.1.3 Rainfall

Average rainfall over the period 1983-2001 is shown in Figure 7-3 for both EMAN-Def and EMAN-New compared to GPCP (for land and ocean) and CRU TS3.0 (for land only). The domain-averaged rainfall for land and ocean is shown in parentheses. CRU and GPCP show very similar spatial patterns and volumes of rainfall.

The results show that EMAN-Def overestimates rainfall over land areas compared to both CRU and GPCP, with rainfall particularly concentrated along areas of high elevation, consistent with the 4-year simulation results. EMAN-New significantly decreases these high rainfall peaks, resulting in domain-averaged rainfall over land that matches to the

observations. Over the ocean, both EMAN-Def and EMAN-New simulate very similar total rainfall volumes, both underestimated compared to GPCP. As was shown in Chapter 6, the modifications made in the improved version of the model did not change the spatial variability in rainfall, only the magnitudes. Given the relatively coarse resolution of the observations compared to the model grid, it is considered that the model simulates the spatial patterns of rainfall reasonably well.

(a) [land only: 7.3 mm day^{-1}] (b) [land: 7.2 mm day^{-1}, ocean: 5.7 mm day^{-1}]

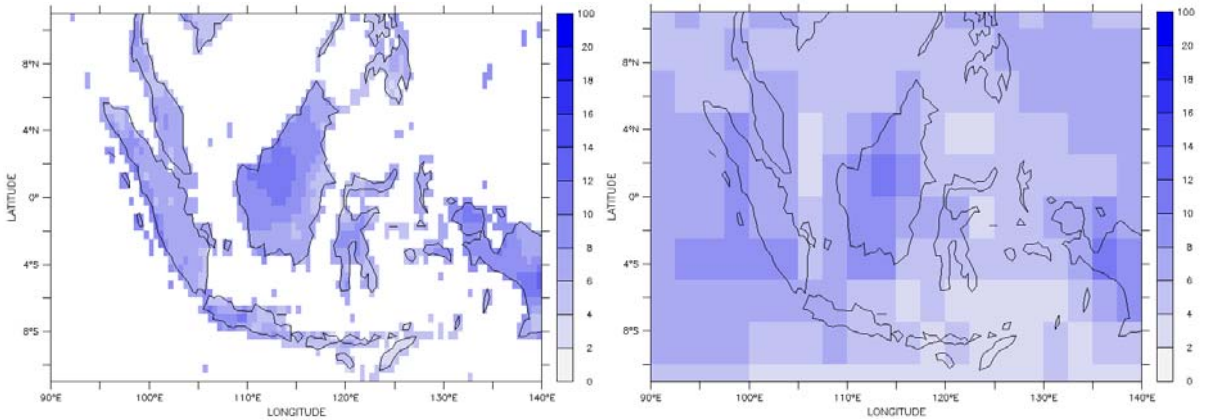

(c) [land: 10.3 mm day^{-1}, ocean: 3.9 mm day^{-1}] (d) [land: 7.3 mm day^{-1}, ocean: 4.0 mm day^{-1}]

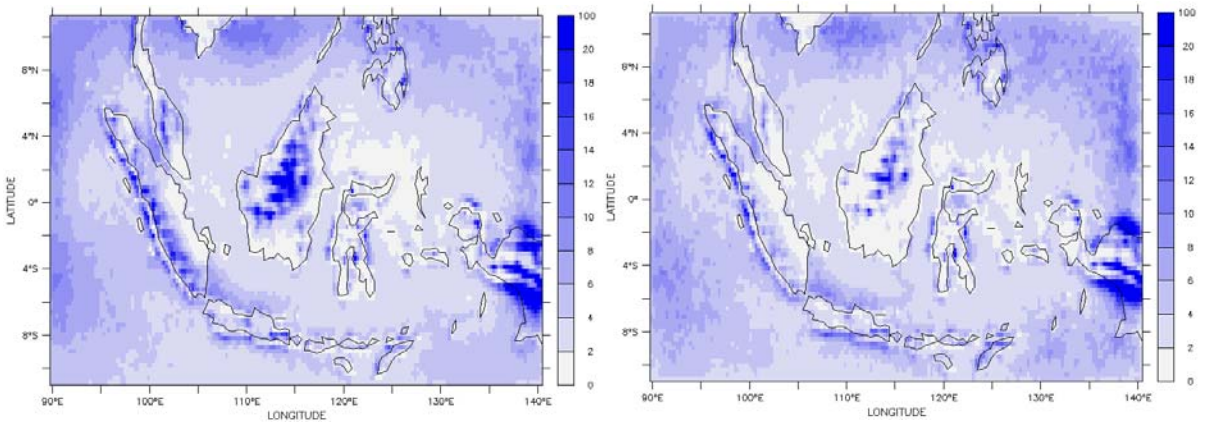

Figure 7-3. Average rainfall (in mm day^{-1}) for period 1983-2001, from (a) CRU TS3.0, (b) GPCP V2.2, (c) EMAN-Def (default) simulation, (d) EMAN-New simulation (incorporating all modifications presented in Chapters 3 to 5). Domain-average values are given in parentheses.

The total, convective and large-scale rainfall volumes averaged over land and ocean for 1983-2001 are shown in Table 7-2 for the EMAN-Def and EMAN-New simulations. The

total rainfall volume is from the GPCP observations. Since the TRMM product is not available for the entire simulation period, the convective fraction that was observed in 1998-2001 (shown previously) was applied to the GPCP rainfall volume to obtain an estimate of the convective and large-scale rainfall volumes over the longer time period.

The results show that EMAN-New removes the wet bias over land that was present in EMAN-Def through reductions in both the convective and large-scale rainfall components, keeping the relative fractions of convective and large-scale rainfall the same in both simulations. Over ocean, the total rainfall volume is the same between the simulations but the relative fractions of convective and large-scale rainfall are changed. EMAN-New produces less convective and more large-scale rainfall than EMAN-Def over the ocean, bringing the convective-to-large-scale ratio closer to observations. The dry bias over the ocean exhibited by both versions of the model will be discussed further in Section 7.3.

Table 7-2. Total, convective and large-scale rainfall (all in mm day^{-1}) averaged over 1983-2001 for land and ocean for the EMAN-Def and EMAN-New simulations. The relative proportions of convective and large-scale rain are shown in parentheses. For comparison to observations, the total rainfall volume is from GPCP data for the period 1983-2001. The convective and stratiform fractions have been taken from TRMM (1998-2001) and applied to the total GPCP volume.

Product / Simulation	Land Average			Ocean Average		
	Total	Convective	Large-scale	Total	Convective	Large-scale
Observations	*7.2*	*4.5 (63%)*	*2.7 (37%)*	*5.7*	*3.2 (57%)*	*2.5 (43%)*
EMAN-Def	10.3	6.6 (64%)	3.7 (36%)	3.9	3.2 (82%)	0.7 (18%)
EMAN-New	7.3	4.5 (62%)	2.8 (38%)	4.0	2.6 (65%)	1.4 (35%)

7.1.4 Temperature

Average temperature for the period 1983-2001 is shown in Figure 7-4 for land cells only (since SSTs are fixed in the simulation). As described in Chapter 5, the simulated values represent the temperature of the lower free atmosphere directly above the canopy. The ERA40 values have been interpolated to the model domain as part of pre-processing the boundary conditions for the model.

The figure shows that the model simulates the spatial patterns in temperature very well, in both versions. EMAN-Def overestimates the free atmosphere temperature with

respect to ERA40 by 1.0 ^{o}C, consistent with the overestimation in insolation produced in the default model. In EMAN-New, the bias is reduced to 0.8 ^{o}C. This is a smaller change than was shown in Chapter 5 over the 4-year period. However, it is considered that the model simulates temperature reasonably well over land in this domain, given that the coarser resolution of the original ERA40 product would lose detail over the islands and exhibit less extreme temperatures.

(a) [26.0 ^{o}C] (b) [25.0 ^{o}C]

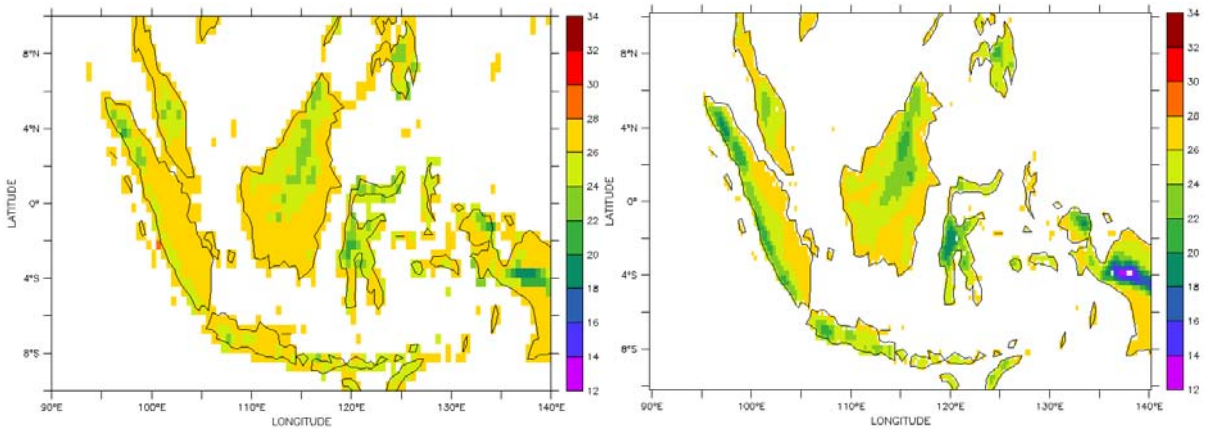

(c) [26.0 ^{o}C] (d) [25.8 ^{o}C]

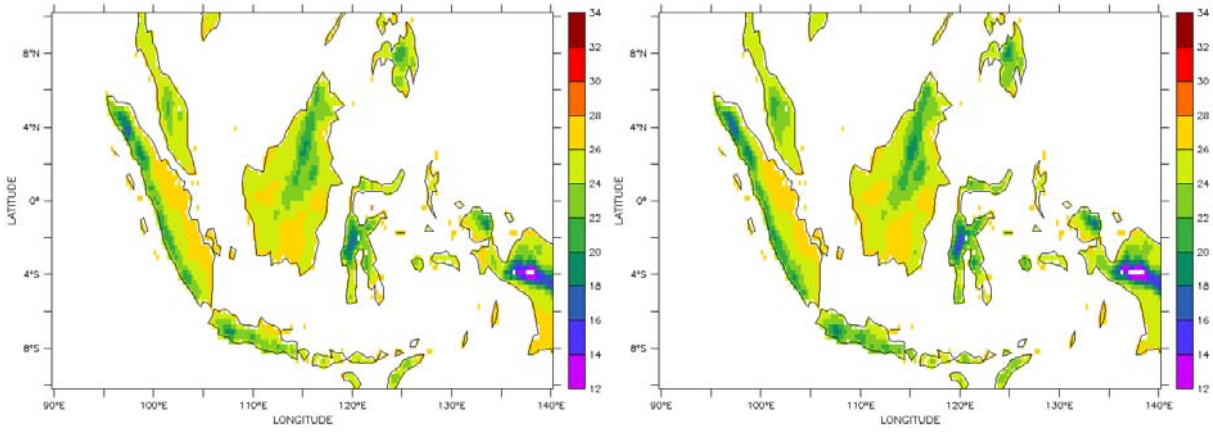

Figure 7-4. Average temperature (in ^{o}C) for period 1983-2001 over land surfaces within the model domain, from (a) CRU TS3.0, (b) lowest atmospheric layer from ERA40, (c) EMAN-Def (default) simulation, (d) EMAN-New simulation (incorporating all modifications presented in Chapters 3 to 5). Land-average values are given in parentheses.

7.1.5 Discussion

The analysis presented above indicates that the 19-year simulations perform similarly to the 4-year simulations presented earlier in this thesis. In particular, it is encouraging that the 19-year simulation using the improved version of the model shows consistently improved performance relative to the observations compared to the default version of the model.

It is considered that this longer simulation is akin to validation for the improved version of the model. The modifications made to the model in Chapters 3 to 5 were tested against observations only over a 4-year period; this period represents calibration of the model. The remaining 15 years of the longer-term simulation were previously untested against observations and therefore provide an independent set of results with which to assess the model performance. If the changes made to the RegCM3-IBIS model system were the result of merely parameter tuning or fitting to a specific set of observational data over the initial 4-year period, then it would not necessarily be expected that simulations over a longer time period should continue to exhibit reasonable performance. The fact that the 19-year simulation performs well against observations indicates that the modifications made to the model were made in a physically-realistic and consistent manner.

Additionally, the results presented here support the assertion made in Chapter 1: poor representation of the diurnal cycle is a major source of error in climate simulations over the Maritime Continent. The work in this thesis has focused entirely on improving the representation of diurnal-scale processes, which are driven by localized convective instability. But the results presented in this section indicate that the improved version of the model also shows better performance over much longer timescales. Therefore this work demonstrates that future efforts to improve climate simulations over the Maritime Continent should include consideration of these relatively small-scale diurnal processes.

7.2 Influence of Specific El Niño and La Niña Events

To examine the influence of specific El Niño and La Niña events on the simulation of diurnal convective processes, 24 months of each type of episode were chosen for further

analysis. Table 7-3 shows the temperature anomaly in the eastern Pacific Ocean for each month over the 19-year simulation period 1983-2001. Months that are considered to constitute an El Niño event (warmer-than-average) are colored in red; months considered to be part of a La Niña event (colder-than-average) are colored in blue. This information comes from NOAA's Climate Prediction Center [accessed 1 October 2012].

Table 7-3. Warm (red) and cold (blue) episodes over the eastern Pacific Ocean based on a threshold of +/- 0.5 °C for the Oceanic Niño Index (ONI), based on centered 30-year base periods updated every 5 years. For historical purposes, warm and cold episodes are defined when the threshold is met for a minimum of 5 consecutive over-lapping seasons. (From NOAA's Climate Prediction Center, Available at: <http://www.cpc.ncep.noaa.gov/products/analysis_monitoring/ensostuff/ensoyears.shtm>)

1983	**2.2**	**1.9**	**1.5**	**1.2**	**0.9**	**0.6**	0.2	-0.2	**-0.5**	**-0.8**	**-0.9**	**-0.8**
1984	**-0.5**	-0.3	-0.2	-0.4	-0.5	-0.5	-0.3	-0.2	-0.3	**-0.6**	**-0.9**	**-1.1**
1985	**-1.0**	**-0.9**	**-0.7**	**-0.7**	**-0.7**	**-0.6**	**-0.5**	**-0.5**	**-0.5**	-0.4	-0.4	-0.4
1986	-0.5	-0.4	-0.2	-0.2	-0.1	0.0	0.3	**0.5**	**0.7**	**0.9**	**1.1**	**1.2**
1987	**1.2**	**1.3**	**1.2**	**1.1**	**1.0**	**1.2**	**1.4**	**1.6**	**1.6**	**1.5**	**1.3**	**1.1**
1988	**0.7**	**0.5**	0.1	-0.2	**-0.7**	**-1.2**	**-1.3**	**-1.2**	**-1.3**	**-1.6**	**-1.9**	**-1.9**
1989	**-1.7**	**-1.5**	**-1.1**	**-0.8**	**-0.6**	-0.4	-0.3	-0.3	-0.3	-0.3	-0.2	-0.1
1990	0.1	0.2	0.2	0.2	0.2	0.2	0.3	0.3	0.3	0.3	0.3	0.4
1991	0.3	0.2	0.2	0.3	**0.5**	**0.7**	**0.8**	**0.7**	**0.7**	**0.8**	**1.1**	**1.4**
1992	**1.6**	**1.5**	**1.4**	**1.2**	**1.0**	**0.7**	0.3	0.0	-0.2	-0.3	-0.2	0.0
1993	0.2	0.3	0.5	0.6	0.6	0.5	0.3	0.2	0.2	0.2	0.1	0.1
1994	0.1	0.1	0.2	0.3	0.4	0.4	0.4	0.4	**0.5**	**0.7**	**1.0**	**1.2**
1995	**1.0**	**0.8**	**0.6**	0.3	0.2	0.0	-0.1	-0.4	**-0.7**	**-0.8**	**-0.9**	**-0.9**
1996	**-0.9**	**-0.8**	**-0.6**	-0.4	-0.3	-0.2	-0.2	-0.3	-0.3	-0.3	-0.4	-0.5
1997	-0.5	-0.4	-0.1	0.2	**0.7**	**1.2**	**1.5**	**1.8**	**2.1**	**2.3**	**2.4**	**2.3**
1998	**2.2**	**1.8**	**1.4**	**0.9**	0.4	-0.2	**-0.7**	**-1.0**	**-1.2**	**-1.2**	**-1.4**	**-1.5**
1999	**-1.5**	**-1.3**	**-1.0**	**-0.9**	**-0.9**	**-1.0**	**-1.0**	**-1.1**	**-1.1**	**-1.3**	**-1.5**	**-1.7**
2000	**-1.7**	**-1.5**	**-1.1**	**-0.9**	**-0.8**	**-0.7**	**-0.6**	**-0.5**	**-0.5**	**-0.6**	**-0.8**	**-0.8**
2001	**-0.7**	**-0.6**	**-0.5**	-0.3	-0.2	-0.1	0.0	0.0	-0.1	-0.2	-0.2	-0.3

Periods of strong anomalies lasting for more than 12 months at a time were desired for this analysis. Therefore the El Niño events of 1987 and June 1991 – May 1992 and the La Niña events of 1999-2000 were chosen. The following sections show analysis of model output and observational data averaged over the months constituting each of these specific time periods (i.e. analysis labeled El Niño represents the average of the year 1987 and June 1991 – May 1992; analysis labeled La Niña represents the average of the years 1999-2000). It is noted that each ENSO event can produce different conditions, and the specific time periods chosen for analysis represent only a small sample of ENSO conditions. However, since these periods were chosen specifically to be representative of strong SST anomalies, it is considered that a comparison between them will illustrate the behavior of the model under different types of large-scale forcing.

7.2.1 Cloud Fraction

The simulated cloud cover did not change significantly between the selected El Niño and La Niña periods. Therefore the results are summarized briefly here and figures are not shown for brevity.

The diurnal cycle of the vertical cloud structure was qualitatively similar between the different events. With EMAN-Def, cloud cover over land exhibited the now familiar low cloud maximum in the early morning, low cloud minimum in the afternoon and dense high cloud cover in the evening. With EMAN-New, cloud cover over land showed the familiar low cloud mid-afternoon maximum, with the early morning exhibiting a minimum in low clouds and maximum in high clouds. Over ocean, both simulations showed the maximum cloud cover occurring at high altitudes. EMAN-Def exhibited little low-level cloud cover, while EMAN-New produced a denser band of cloud cover at 1 km elevation. Hence the results showed that the vertical cloud structure and its diurnal variability are strongly controlled by the dynamics of daytime convection in each of the specific ENSO events chosen for analysis.

Although the cloud structure did not change between the ENSO periods, the cloud fraction did change due to the large-scale conditions. With both EMAN-Def and EMAN-New, cloud fraction is higher by about 5-10% during La Niña periods than during El Niño periods.

This increase occurs at both low and high elevations at all times of day, indicating that the impact is on clouds formed both from daytime convection and from large-scale humidity.

7.2.2 Radiative Fluxes

Average radiative fluxes at the surface are shown in Table 7-4 for the selected El Niño and La Niña periods over both land and ocean.

The SRB data show differences between the two ENSO conditions: La Niña conditions lead to a higher planetary albedo (difference of 8%), less insolation (difference of 6-7%) and less net radiation (difference of 10%) at the surface. These differences reflect the more humid and cloudy conditions of La Niña.

The model, in both the default and improved versions, captures this interannual variability very well. The results are qualitatively similar to the observations, with less insolation and net radiation and higher planetary albedo during La Niña conditions than El Niño conditions. EMAN-Def shows similar sensitivity to the type of ENSO episode as the SRB observations. However, the improved model (EMAN-New) shows stronger sensitivity to changes in large-scale conditions than is observed: the planetary albedo differs by about 11% and insolation differs by about 12% between the two ENSO conditions, such that insolation is slightly overestimated during El Niño and underestimated during La Niña. These results reflect the convective-radiative feedback that is present in EMAN-New but absent in EMAN-Def. In EMAN-Def, changes to convective strength that might occur due to differences in large-scale moisture or instability only impact the simulated cloud cover through the large-scale scheme. This results in less sensitivity in the default model.

Over land, planetary albedo is decreased in EMAN-New compared to EMAN-Def due to the increase in daytime low-level cloud cover and reduction in daytime high cloud cover (note that the time-mean high cloud cover increased in EMAN-New, as shown in Figure 7-2, due to the increased night-time high cloud cover in the second-highest model layer). Despite the reduction in albedo, insolation and net radiation also decrease in EMAN-New compared to EMAN-Def. This result indicates that the reduction in surface radiation with the new model is due to increased absorption of insolation through the atmosphere resulting from

the new convective cloud cover. This effect has approximately the same impact in both types of ENSO episode, but is slightly stronger during La Niña.

Over ocean, planetary albedo is increased in EMAN-New due to the increase in high cloud cover (during the daytime). But the reduction in insolation and net radiation from EMAN-Def to EMAN-New is much larger than the change in albedo would suggest. This is again reflective of the increase in low-level cloud cover in EMAN-New, which acts to absorb some of the insolation and reduce radiation at the surface. Over the ocean, this effect is noticeably stronger during La Niña events than El Niño events.

It is interesting to note that the difference in radiative fluxes between the two simulations is of at least the same magnitude or higher than the difference within either simulation between ENSO conditions. This demonstrates the important role of the convective-radiative feedback on mediating surface radiation over this region. It also demonstrates that accurate simulation of convective processes is essential to make accurate projections of the influence of large-scale conditions over this region.

Table 7-4. Average daily surface radiative fluxes (all in W m^{-2}) for El Niño and La Niña episodes from SRB ('Obs.') and the EMAN-Def and EMAN-New simulations.

LAND

Observations / Simulation	SW_{dn}	SW_{up}	SW_{net}	Surface albedo	Planetary albedo	LW_{dn}	LW_{up}	R_N
Obs. – El Niño	*214*	*28*	*186*	*13%*	*45%*	*410*	*453*	*143*
EMAN-Def	233	32	201	14%	47%	411	463	148
EMAN-New	217	31	186	14%	42%	405	460	131
New – Def (%)	-7%	-3%	-7%	0%	-11%	-1%	-1%	-12%
Obs. – La Niña	*201*	*31*	*170*	*16%*	*49%*	*409*	*451*	*128*
EMAN-Def	211	30	181	14%	51%	417	458	141
EMAN-New	193	28	165	15%	47%	410	454	123
New – Def (%)	-9%	-5%	-9%	4%	-8%	-2%	-1%	-13%

OCEAN

Observations / Simulation	SW_{dn}	SW_{up}	SW_{net}	Surface albedo	Planetary albedo	LW_{dn}	LW_{up}	R_N
Obs. – El Niño	*234*	*15*	*219*	*6%*	*41%*	*418*	*466*	*171*
EMAN-Def	276	17	259	6%	42%	408	471	197
EMAN-New	237	16	221	7%	43%	416	471	166
New – Def (%)	-15%	-9%	-15%	7%	3%	2%	0%	-16%
Obs. – La Niña	*218*	*14*	*204*	*6%*	*46%*	*419*	*466*	*157*
EMAN-Def	262	17	245	7%	46%	417	472	190
EMAN-New	208	14	194	7%	50%	426	472	148
New – Def (%)	-21%	-18%	-21%	4%	8%	2%	0%	-22%

Notes on Table 7-4: SW_{dn} = shortwave (solar) radiation incident at the surface, SW_{abs} = net absorbed shortwave radiation at the surface, LW_{dn} = longwave radiation incident at the surface, LW_{up} = longwave radiation emitted from surface, R_N = net radiation absorbed at surface. See Notes on Table 3 to 5 for explanation of albedo calculation.

The diurnal cycle of insolation was found to be very similar between the selected El Niño and La Niña periods, with a small difference in magnitude that reflects the results shown in Table 7-4. The timing and amplitude of the diurnal cycle were similar to the results presented in Figures 5-12 and 5-14, and therefore figures are not shown here for brevity.

7.2.3 Rainfall

The spatial distribution of rainfall for the selected El Niño and La Niña periods was qualitatively very similar to the results shown in Figure 7-3, and therefore figures are not shown here for brevity.

The total, convective and large-scale rainfall volumes averaged over land and ocean for the selected El Niño and La Niña episodes are shown in Table 7-5 for the EMAN-Def and EMAN-New simulations. The total rainfall volume is from the GPCP observations. To obtain an estimate of the relative convective and large-scale rainfall fractions during each ENSO episode, the convective fraction observed by TRMM for similar episodes during the TRMM data record (1998-2011) was applied to the total rainfall from GPCP.

The GPCP data indicates that about 21% more rainfall occurs over land and about 26% more rainfall occurs over ocean during the La Niña conditions compared to the El Niño conditions. Interestingly, the observational data suggests that over land the volume of convective rainfall is similar under both conditions, but large-scale rainfall increases under the more humid La Niña conditions. Over ocean, the observations suggest that La Niña conditions produce more of both types of rainfall.

The results indicate that both EMAN-Def and EMAN-New reproduce this interannual variability with higher rainfall during the selected La Niña episodes than the El Niño episodes over both land and ocean.

Over land, EMAN-Def overestimates rainfall during both types of conditions, with worse error during La Niña conditions. EMAN-New simulates rainfall very well compared to GPCP during El Niño and overestimates during La Niña, though with much less error than EMAN-Def. During all of the selected episodes analyzed here, EMAN-New reduces the wet bias in EMAN-Def through the reduction of both convective and large-scale rainfall, as was shown for the long-term mean rainfall in Table 7-2.

Over ocean, EMAN-Def and EMAN-New produce similar rainfall under the El Niño conditions, with underestimation of the large-scale rainfall. During La Niña conditions, EMAN-Def simulates too much convective rainfall and too little large-scale rainfall. This error in the convective rainfall fraction is corrected in EMAN-New, such that EMAN-New shows good performance compared to the observations.

The results in Table 7-5 again show the impact that the model modifications have on the simulated climate. Over land, the difference between the two simulations is of the same magnitude as the difference within each simulation between the two ENSO conditions. The table also shows that the model modifications have equal impact on the convective and large-scale rainfall during El Niño conditions, but that they have less impact on the large-scale rainfall under La Niña conditions. This is due to the generally more humid atmosphere during La Niña, which provides more moisture for the large-scale scheme.

Table 7-5. Total, convective and large-scale rainfall (all in mm day^{-1}) for El Niño and La Niña periods over land and ocean for the EMAN-Def and EMAN-New simulations. The relative proportions of convective and large-scale rain are shown in parentheses. For comparison to observations, the total rainfall volume is from GPCP data. The convective and stratiform fractions have been taken from TRMM and applied to the total GPCP volume.

Product / Simulation	Land Average			Ocean Average		
	Total	Convective	Large-scale	Total	Convective	Large-scale
Obs. – El Niño	*6.3*	*4.1 (65%)*	*2.2 (35%)*	*4.8*	*2.7 (56%)*	*2.1 (44%)*
EMAN-Def	8.9	5.9 (66%)	3.0 (34%)	2.9	2.5 (87%)	0.4 (13%)
EMAN-New	6.2	4.1 (66%)	2.1 (34%)	2.9	2.1 (72%)	0.8 (28%)
New – Def (%)	-30%	-30%	-30%	0%	-16%	100%
Obs. – La Niña	*8.0*	*4.2 (53%)*	*3.8 (47%)*	*6.5*	*3.6 (55%)*	*2.9 (45%)*
EMAN-Def	14.1	8.2 (58%)	5.9 (42%)	6.0	4.7 (79%)	1.3 (21%)
EMAN-New	10.5	5.7 (55%)	4.8 (45%)	6.5	3.9 (61%)	2.6 (39%)
New – Def (%)	-25%	-30%	-19%	9%	-17%	100%

The timing of the simulated diurnal rainfall cycle was unchanged under the selected ENSO episodes, and therefore figures are not shown here for brevity. Over land under both El Niño and La Niña conditions, the daytime rainfall peak is primarily composed of convective rain, while rainfall at night-time is contributed mostly from the large-scale scheme. Over ocean, the contribution of convective rainfall to the total volume is more consistent throughout the day. The only difference in the diurnal rainfall cycle between the selected ENSO episodes was in the magnitude of the rainfall, which is reflected in Table 7-5.

In general, the timing and shape of the diurnal cycle at each of the five sub-regions (shown in Figure 6-9) is unaffected by the different ENSO conditions (or by the model modifications, as discussed in Chapter 6). Therefore, for brevity, the results are not shown here.

7.3 Interannual and Interseasonal Variability

The analysis presented in Section 7.2 focused on specific periods of different ENSO conditions, which were chosen to represent strong SST anomalies and thus different large-scale forcing. More generally, it is of interest whether the observed interannual and interseasonal variability is captured within the model. Although a complete investigation of these different large-scale forcing timescales is beyond the scope of this work, a brief analysis of the observed and simulated variability in rainfall is presented here.

Figures 7-5 and 7-6 present the total rainfall respectively for land and ocean grid cells within the model domain. The figures compare the simulated values from the default and improved versions of the model using the Emanuel scheme to the observed rainfall from GPCP over the period 1983-2001. The observed rainfall from TRMM for the period 1998-2001 is also shown for comparison. To enable the long-term variability to be seen more clearly, monthly rainfall values have been plotted using a 3-month moving average window.

When comparing the simulated rainfall to the observations, it was noted that the simulated values exhibit a trend for increasing rainfall over time. This trend is more noticeable over ocean (Figure 7-6) than land (Figure 7-5) and most likely arises from the lateral boundary conditions.

When evaluating the hydrologic cycle represented in the ERA40 reanalysis product, Hagemann *et al.* (2005) noted that precipitation in ERA40 exhibited an increasing trend over time. This trend was noticeably worse over the tropics than other regions, and was worse over ocean than over land (Hagemann *et al.* 2005). The trend was partially attributed to an erroneous bias correction that appeared during assimilation of new satellite datasets during the 1980s and 1990s. The trend remained within ERA40 even after implementing some bias correction (Hagemann *et al.* 2005). Therefore it is considered that the increasing trend shown in the simulated rainfall in Figures 7-5 and 7-6 is most likely due to propagation of error originating at the boundaries, due to the use of ERA40 for boundary conditions.

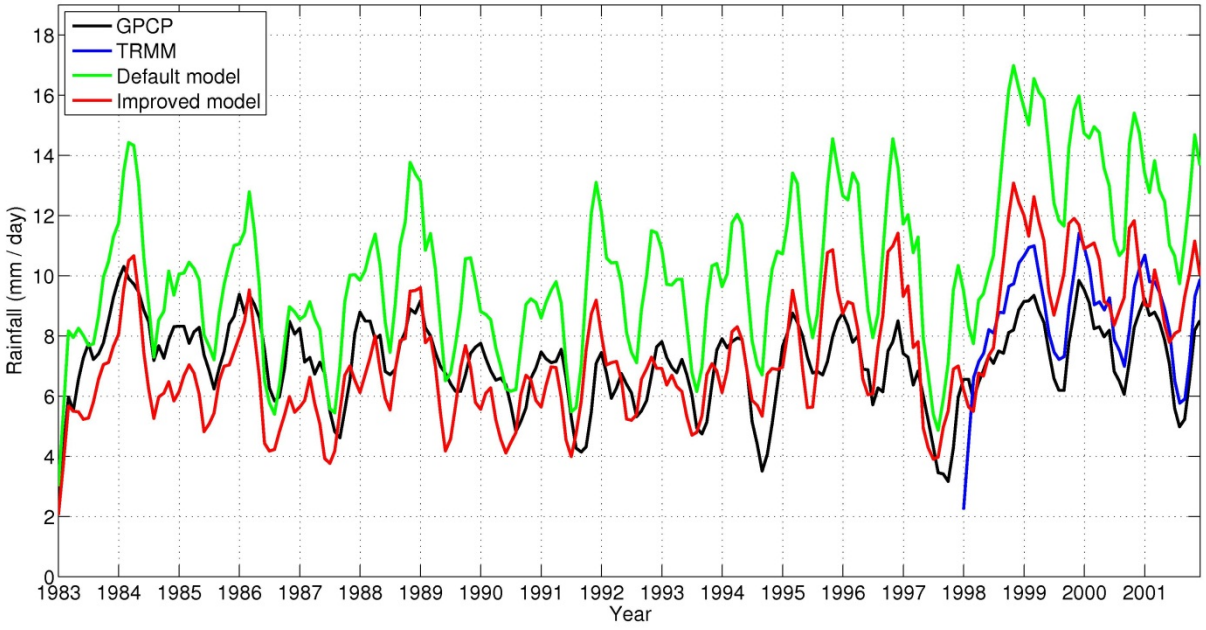

Figure 7-5. 3-month moving average of rainfall (mm day^{-1}) over land for period 1983-2001, comparing GPCP (black), TRMM (blue; for period 1998-2001), default version of RegCM3-IBIS using Emanuel scheme (green) and improved version of the model (red).

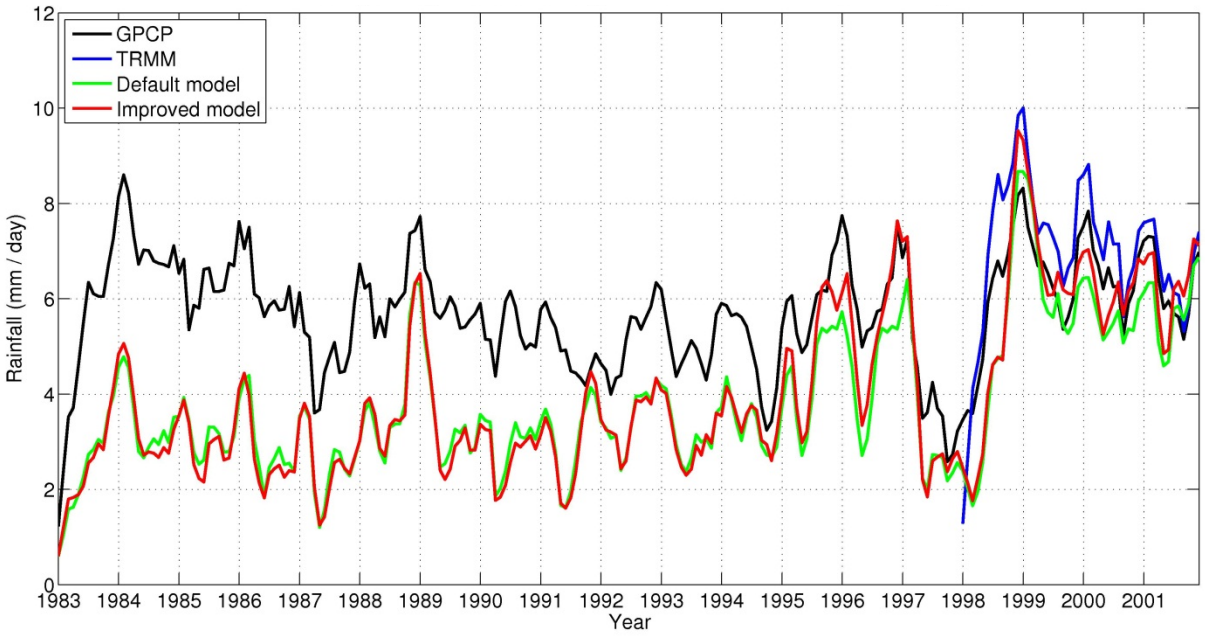

Figure 7-6. 3-month moving average of rainfall (mm day^{-1}) over ocean for period 1983-2001, comparing GPCP (black), TRMM (blue; for period 1998-2001), default version of RegCM3-IBIS using Emanuel scheme (green) and improved version of the model (red).

To allow for a better comparison of the model performance inside the domain, without the influence of error from the boundary conditions, the simulated monthly rainfall was de-trended. A linear fit to the simulated rainfall was calculated and the positive trend in rainfall was removed from the monthly values. The de-trended 3-monthly moving average of rainfall is shown in Figure 7-7 for land cells within the model domain. Figure 7-8 shows the difference between the de-trended monthly rainfall and the mean rainfall for the two versions of the model. The 3-monthly moving average of rainfall for GPCP is shown for the period 1983-2001 and the TRMM rainfall for the period 1998-2001 is also shown for comparison.

Figure 7-7 shows that the improved version of the model simulates the rainfall time series over land very well compared to the observations. Figure 7-8 also shows a very good match between the simulated interannual variability in the improved version of the model compared to the observations. By contrast, the default version of the model considerably overestimates the mean rainfall as well as the amplitude of the interannual variability.

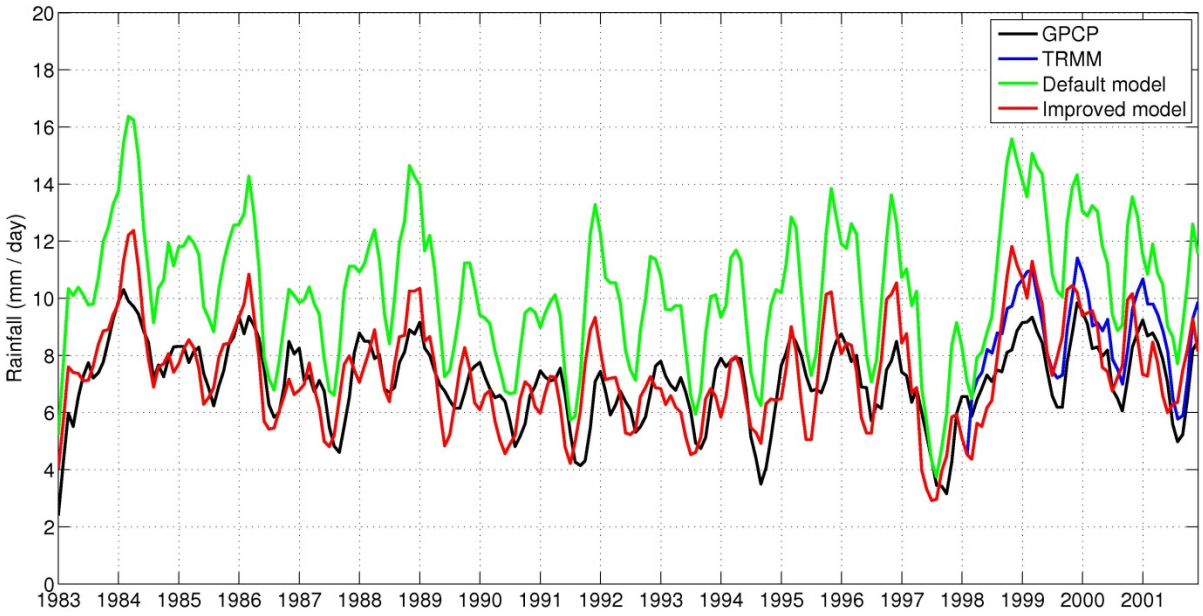

Figure 7-7. 3-month moving average of rainfall (mm day^{-1}) over land for period 1983-2001, comparing GPCP (black), TRMM (blue; for period 1998-2001), default version of RegCM3-IBIS using Emanuel scheme (green) and improved version of the model (red). A positive trend in the simulated rainfall has been removed.

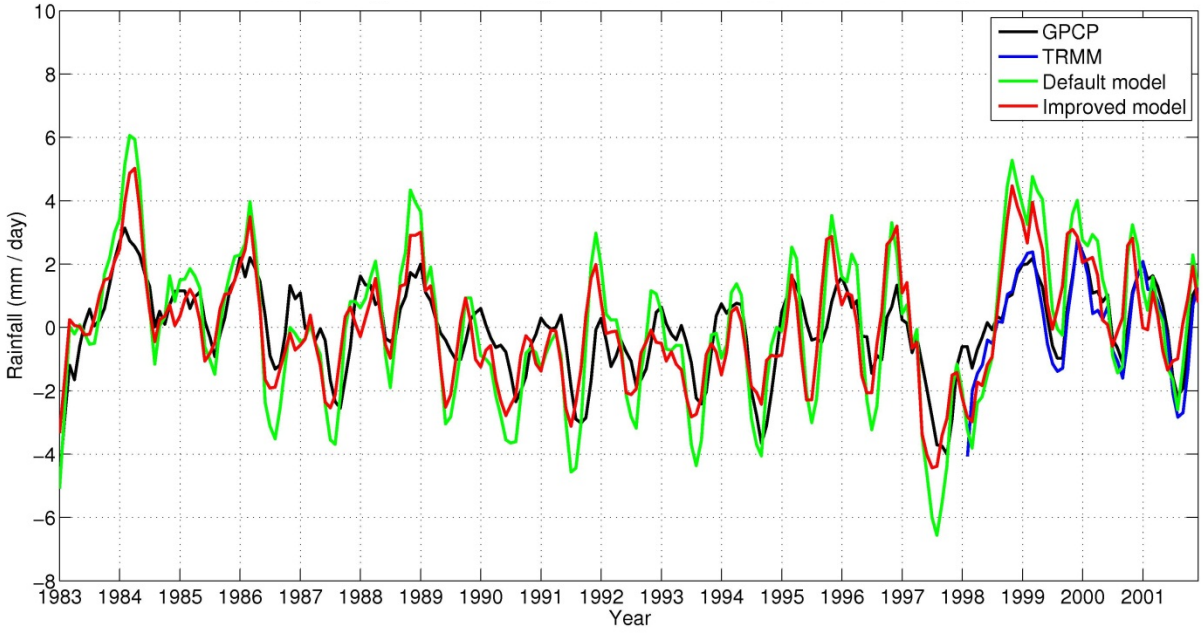

Figure 7-8. Rainfall (mm day^{-1}) over land for period 1983-2001, showing the difference between the 3-month moving average and the mean rainfall for GPCP (black), TRMM (blue; for period 1998-2001), default version of RegCM3-IBIS using Emanuel scheme (green) and improved version of the model (red). A positive trend in the simulated rainfall has been removed.

The de-trended rainfall over ocean grid cells is shown in Figure 7-9, plotted using a 3-monthly moving average window. GPCP is shown for the period 1983-2001 and the TRMM rainfall for the period 1998-2001 is also shown for comparison.

Figure 7-9 shows that both versions of the model underestimate the rainfall over the ocean compared to the observations and there is little difference between the default and improved versions, consistent with the results presented in Table 7-2. It is considered that this underestimation bias is due to the use of the ERA40 reanalysis.

When the ERA40 product was first constructed, it was noted that precipitation was considerably overestimated, particularly over the tropical oceans. This error was found to be due to error in the analysis of humidity over tropical oceans in areas of high density observations (Troccoli and Kållberg 2004). To address this error, a bias correction was implemented in ERA40 over the latitudinal range 30^{o}S to 30^{o}N, only over ocean locations. The correction was applied uniformly in the longitudinal direction. The correction improved the representation of precipitation within ERA40 over most locations, but resulted in dry biases over the western tropical Pacific Ocean and eastern tropical Indian Ocean, i.e. directly impacting the Maritime Continent (Troccoli and Kållberg 2004). The bias was noted to be on the order of 1.5-2 mm day^{-1}, the same magnitude of dry bias exhibited by the model as shown in Table 7-2. Therefore it is considered that this underestimation bias is the result of error propagating from the boundary conditions due to the ERA40 reanalysis.

To compare the interannual variability in rainfall simulated by the model to observations, Figure 7-10 shows the difference between the de-trended monthly rainfall and the mean rainfall over the period 1983-2001 for GPCP and the two versions of the model, plotted using a 3-monthly moving average window. TRMM is also shown for comparison. This figure shows that both versions of the model reproduce the observed interannual variability over the ocean very well. Therefore it is considered the model reproduces the sensitivity of rainfall to interannual large-scale forcing very well over this domain, even though the magnitude of the rainfall volume contains a dry bias.

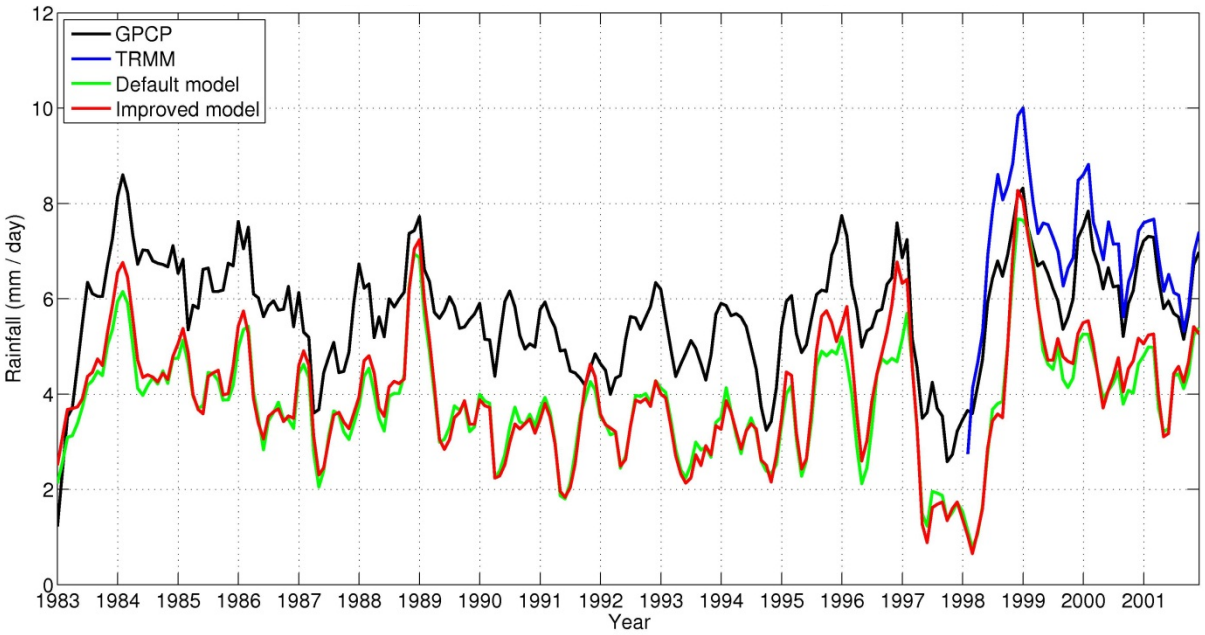

Figure 7-9. 3-month moving average of rainfall (mm day^{-1}) over ocean for period 1983-2001, comparing GPCP (black), TRMM (blue; for period 1998-2001), default version of RegCM3-IBIS using Emanuel scheme (green) and improved version of the model (red). A positive trend in the simulated rainfall has been removed.

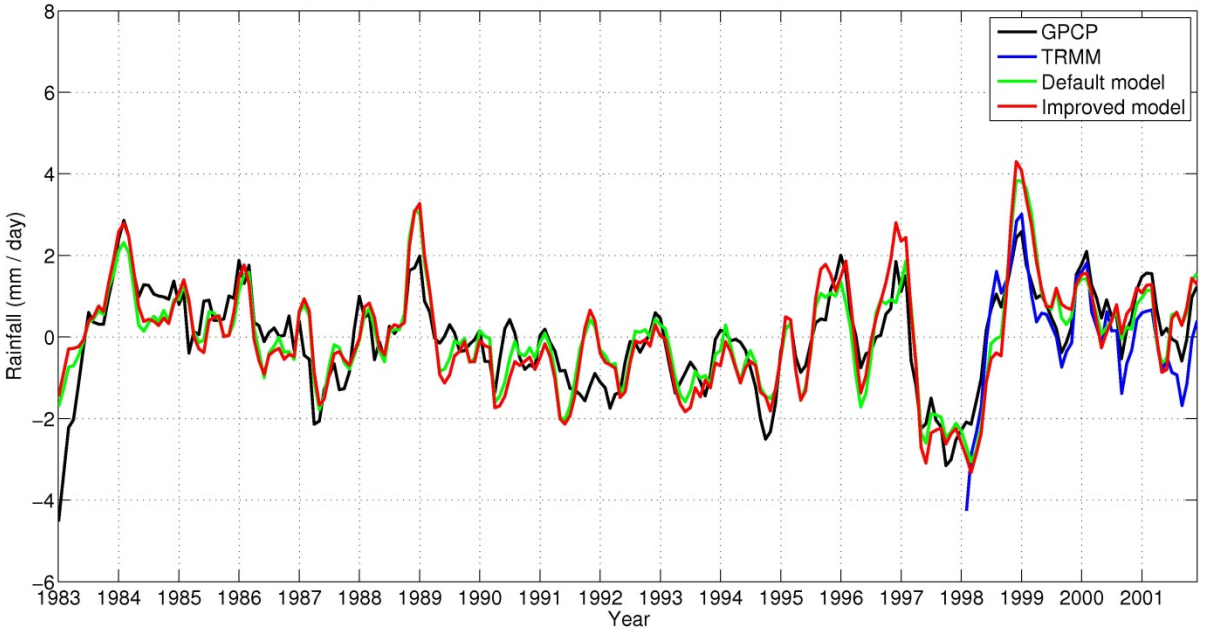

Figure 7-10. Rainfall (mm day^{-1}) over ocean for period 1983-2001, showing the difference between the 3-month moving average and the mean rainfall for GPCP (black), TRMM (blue; for period 1998-2001), default version of RegCM3-IBIS using Emanuel scheme (green) and improved version of the model (red). A positive trend in the simulated rainfall has been removed.

To compare the seasonal variability in the simulated and observed rainfall, Figures 7-11 and 7-12 show the average monthly rainfall for the period 1983-2001 from GPCP and the two versions of the model. The average monthly rainfall from TRMM for the period 1998-2001 is also shown for comparison.

Figure 7-11 shows that the improved version of the model reproduces the magnitude of the seasonal cycle over land very well compared to observations, and removes the wet bias that was present in the default version of the model. Both versions of the model present some error in simulating the time of year when the maximum and minimum rainfall is observed. The observations show the maximum rainfall occurring in December-January, while the model simulates two rainfall peaks in March and October. Similar timing errors are not apparent over ocean grid cells (Figure 7-12) and therefore the source of the error is unlikely to be the ERA40 boundary conditions. The origin of this error should be investigated further in future work.

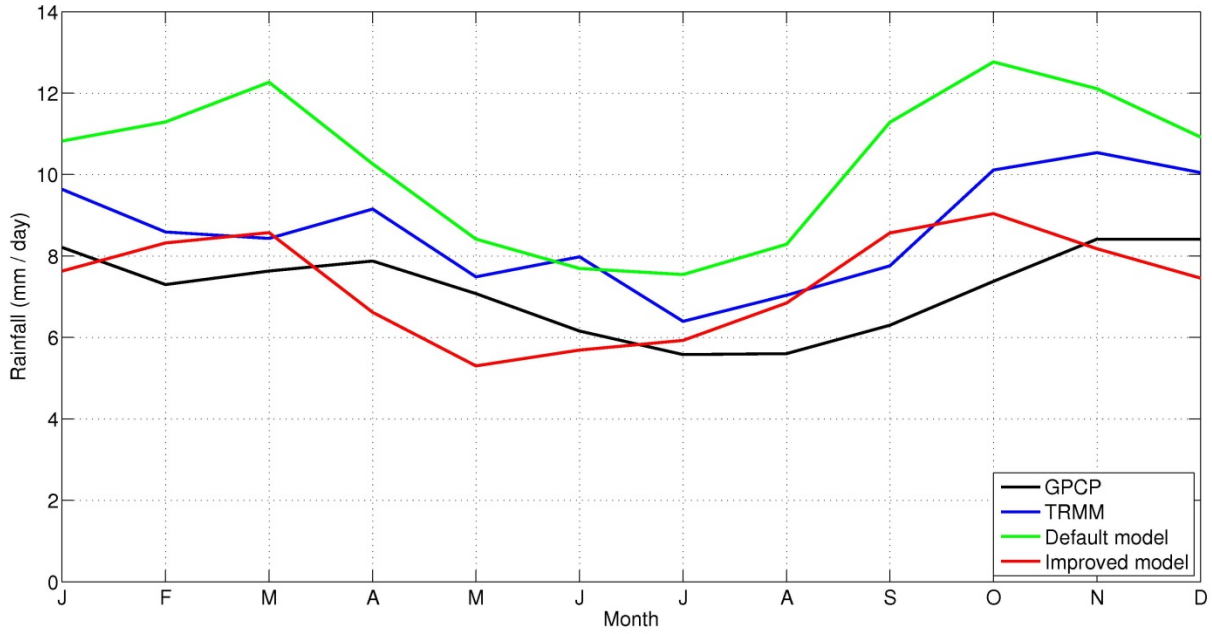

Figure 7-11. Average seasonal rainfall (mm day^{-1}) over land, comparing GPCP (black), default (green) and improved (red) versions of the model averaged for the period 1983-2001, and TRMM (black) averaged over the period 1998-2001.

Figure 7-12 shows that the model reproduces the timing of the seasonal cycle over ocean reasonably well compared to the observations, with a rainfall maximum in December-

January and a minimum in the spring. The amplitude of the seasonal cycle is exaggerated compared to the observations and there is a general dry bias in rainfall. As has already been discussed, this bias is likely due to errors propagating from the ERA40 boundary conditions.

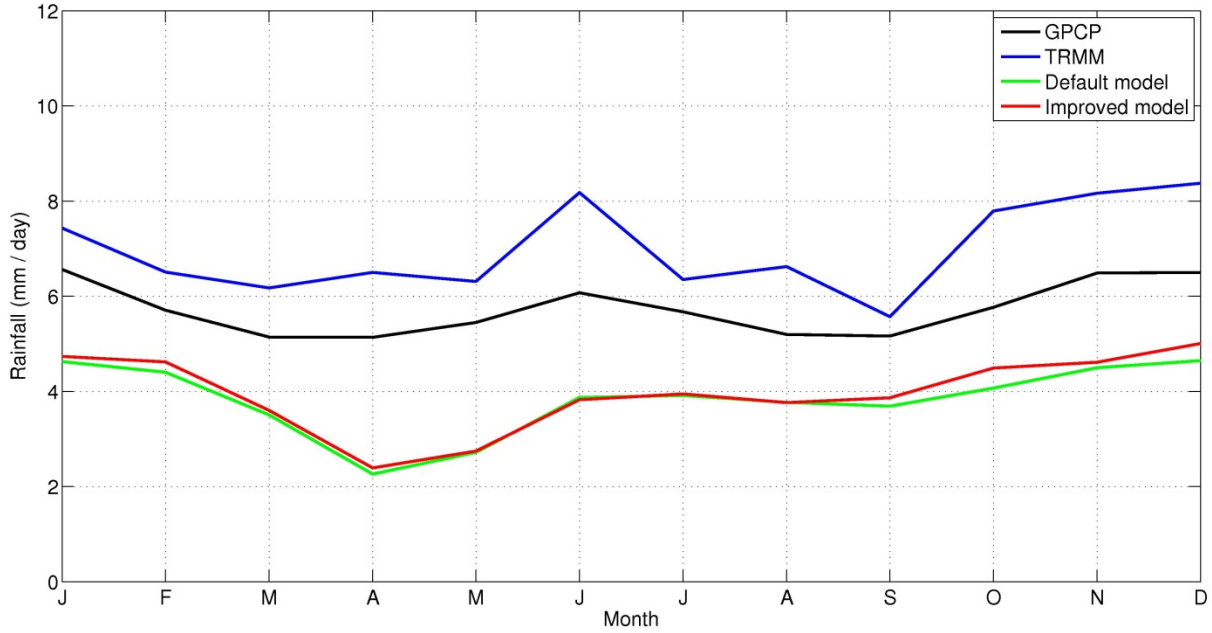

Figure 7-12. Average seasonal rainfall (mm day^{-1}) over ocean, comparing GPCP (black), default (green) and improved (red) versions of the model averaged for the period 1983-2001, and TRMM (black) averaged over the period 1998-2001.

7.4 Discussion

The analysis presented here has demonstrated the influence that different large-scale conditions, represented by specific El Niño and La Niña episodes, can have on the diurnal cycle. A corollary to these results is that a lack of sensitivity to ENSO conditions, but strong sensitivity to modifications made to the model, illustrates the influence of convection and the convective-radiative feedback.

The vertical cloud structure and diurnal timing of cloud cover were relatively unchanged by the specific ENSO events analyzed here. The timing and shape of the diurnal rainfall cycle were also unchanged by the ENSO conditions. But the modifications made in this thesis to the simulation of convective clouds changed the diurnal cycle considerably. The result was especially evident over land surfaces. Hence the diurnal cycle is shown to be dominated by the localized, diurnally-varying processes related to convection rather than by

large-scale conditions, at least at the mode of ENSO as presented here. Changing large-scale conditions affected the magnitude of the diurnal cycle, including the extent of cloud cover and the volumes of both convective and large-scale rainfall.

It is encouraging that the improved version of the model exhibited the appropriate interannual and interseasonal variability, and showed consistent improvements over the default version of the model. The improved version showed especially good performance in reproducing the observed radiative fluxes and rainfall during El Niño conditions, and in reproducing the interannual rainfall variability over land. Analysis of the interannual rainfall variability showed that the model improvements did not simply dry out the wet bias that is produced by the Emanuel scheme. Rather, the modifications improved the dry bias simulated by the default model during El Niño conditions while also improving the wet bias simulated by the default model during La Niña conditions. As mentioned in Section 5.6, these results indicate that the modifications have improved the physical realism of the simulations and have not simply 'tuned' the model to remove the wet bias simulated by the default Emanuel scheme.

However, it is noted that rainfall over the ocean within this domain showed a significant dry bias that was unchanged between the different versions of the model. Since it is known that ERA40 contains a dry bias over the ocean near the Maritime Continent, it is likely that the model bias is propagated from errors in the boundary conditions. It would be a useful exercise to evaluate the model performance over this domain with the ERA-Interim reanalysis product used to force the lateral boundary conditions instead of ERA40.

The simulation results illustrate interesting model behavior with respect to the connection between large-scale and convective rainfall. It was mentioned in Section 7.1.3 that large-scale rainfall over land is to some extent dependent upon convective activity. The vertical transport of moisture to the upper troposphere via strong convection is responsible for the formation of the high-level cloud in the model, which generates a significant portion of the large-scale rainfall. Therefore when convective motion is reduced, the large-scale rainfall is also reduced in the same manner due to the reduction in available moisture. This behavior is amplified during El Niño conditions since there is less ambient moisture,

rendering the large-scale rainfall even more dependent on the convective mass flux to transport moisture aloft.

In summary, it is considered that the analysis presented in this chapter strengthens the argument of this thesis: accurate simulation of convective processes is essential for both good simulations of the mean climate of the Maritime Continent region and for good representation of the sensitivity to changing large-scale climate variability.

Chapter 8: Conclusions and Perspectives for Further Studies

8.1 Research Summary

The work presented in this thesis aims to improve simulations of existing climate and predictions of future climate variability over the Maritime Continent by focusing on the diurnal cycle of processes related to convection. The regional climate model RegCM3, coupled to the land surface scheme IBIS, was used as a tool for (i) exploring the simulation of convective processes within large-scale climate models, (ii) investigating ways in which these processes can be represented with greater physical realism, and (iii) identifying weaknesses within these models that require further consideration.

Chapter 2 evaluated the performance of RegCM3 over the Maritime Continent, with particular attention paid to the simulation of rainfall. The work identified major errors in the simulated rainfall histogram that were not previously documented in the RegCM3 model system, particularly an underestimation of the frequency of dry periods and an overestimation of the frequency of low intensity rainfall. Additionally, this work presented errors in the simulated phase of the diurnal rainfall cycle over the Maritime Continent, with early occurrence of the daily rainfall peak over land. It was concluded that these errors originated from poor representation of convective triggering within the model.

Chapter 3 explored the role of the planetary boundary layer (PBL) region on convection via the pre-conditions for convective triggering. A novel dataset was acquired from Singapore's Changi airport that allowed calculation of the local PBL height at several times throughout the day. It was shown that the default simulation of the PBL height within RegCM3 results in an erroneously high daytime and night-time PBL. It was also shown that RegCM3 overestimates the production of large-scale clouds within the PBL, particularly at night over land. A new method for simulating this cloud cover was introduced, and an inappropriate constraint on the minimum PBL height was lifted. The work showed that

changes to the near surface environment can significantly affect the simulation of both convective and large-scale rainfall.

Chapter 4 explored the role of convective cloud fraction in simulation of the diurnal cycle. It was shown that the default formulations within RegCM3 significantly underestimate the observed cloud liquid water (CLW) over the Maritime Continent region. The default version of the model also renders the simulated near-surface environment unresponsive to convective activity by failing to represent a convective-radiative feedback. Therefore a new formulation for simulating the production of convective cloud was introduced. This new method improves the internal consistency of the model, allowing the near surface to respond to daytime convection with an appropriate convective-radiative feedback. However, it was shown that consideration is also needed of the dissipation of convective cloud cover via rainfall in order to appropriately represent the formation and decay of convective clouds.

Chapter 5 presented the development of a new method for simulating the conversion of convective cloud water into rainfall. This method contains only one independent and one dependent parameter and is fully constrained by observations. It explicitly accounts for subgrid-variability in CLW and for the many non-linearities involved in converting cloud droplets to rainfall. The generalized form of this function removes the need for a tuned grid-mean conversion threshold value, which is commonplace among large-scale climate models. This method can therefore be implemented consistently between different convective parameterizations regardless of model domain or resolution choices. It was shown that the model performance improves across a wide array of metrics, indicating that the combination of changes made to the model leads to improved physical realism throughout the entire simulation.

Chapter 6 explored the spatial variability across the Maritime Continent region with respect to the diurnal cycle of rainfall. Over locations where local breeze circulations dominate, such as Java and the southern Malay Peninsula, the improved model reproduces the diurnal cycle very well. The model also reproduces the diurnal cycle reasonably well over the mountain peaks, where convection is triggered by both local instability and the convergence of breeze circulations. However, the model exhibits considerable error in the

timing of the diurnal cycle over inland portions of the larger islands in the region. A review of the known observed diurnal processes over the region elucidated the cause for the simulation error, in the form of subgrid-scale convective processes that are not resolved within RegCM3 or other models using convective parameterization schemes.

Lastly, Chapter 7 explored the influence of specific ENSO events on the simulation of diurnal convective processes. This chapter also evaluated the ability of the model to reproduce the observed interannual and interseasonal variability in rainfall. It was shown that drier El Niño conditions contribute to lower rainfall across the Maritime Continent region by decreasing both convective and large-scale components. Large-scale rainfall is impacted more strongly due to decreases in ambient moisture, such that the influence of convection is stronger under El Niño conditions. It was shown that the model modifications made in this thesis result in improved simulation of the observed variability due to specific ENSO events with respect to cloud cover, incoming solar radiation and rainfall. The improved version of the model also leads to better simulation of the interannual and interseasonal rainfall variability. Therefore it is expected that the improved model will exhibit appropriate sensitivity to future projections of climate variability.

8.2 Major Contributions

The primary objectives of this thesis were to better understand why large-scale climate models fail to capture diurnal processes related to convection and how more physically-realistic simulations might be achieved. To that end, the work in this thesis has contributed significantly to the development of the RegCM3-IBIS model system with three key improvements:

- A method for simulating the formation of large-scale cloud cover within the PBL was developed using a bulk relative humidity threshold. This method was shown to substantially improve the simulation of night-time clouds close to the surface over land.
- A new formulation for representing the formation of convective cloud fraction was developed. This formulation was shown to improve the internal consistency and physical realism of the model by allowing representation of a convective-radiative feedback.

- A new method for parameterizing convective autoconversion was developed using observations of convective cloud water and physically-based empirical relationships. This method was shown to improve the efficiency of convective rainfall production, contributing significantly to the convective-radiative feedback in a manner that recognized realistic subgrid variability in convective clouds without the need for parameter tuning.

It is considered that these developments could be applied to other RCMs and GCMs to similarly improve model performance with respect to convection.

This thesis has also contributed to understanding of the limitations and weaknesses of this class of climate models with respect to simulations of tropical convection:

- Some parameterizations developed for mid-latitude regions are not appropriate for global application. For example, this thesis identified a problem with the minimal value used to represent the nocturnal stable PBL. There could be other similar issues within RegCM3 that are not identified in this work.
- The use of the total cloud work function within quasi-equilibrium theory (Arakawa and Schubert 1974) is not appropriate for simulating regions of strong convection in an RCM, where the computational timestep is less than what the 'instantaneous adjustment' assumption requires. This will have application to the use of the Grell scheme in other tropical locations, and for other schemes based on Arakawa and Schubert (1974).
- Certain processes that contribute to diurnal convection are not represented by RegCM3 and other GCMs/RCMs at the present time. Lack of representation of these processes contributes to substantial error in simulation of the diurnal cycle and mean rainfall. Most significantly for the Maritime Continent region, the absence of cold outflows from convective downdrafts appears critical, since it prohibits simulation of self-generation of convection and the diurnal propagation of squall lines across this region.

The model development work has led to improved understanding of the importance of convective processes in the mean climate of the Maritime Continent region, especially through demonstration of the following:

- Moist convection strongly influences the near surface environment by mediating the incoming solar radiation and net radiation at the surface, with subsequent impacts to surface turbulent heat fluxes and local hydrology.
- The dissipation of convective cloud via rainfall plays an equally important role in the convective-radiative feedback as the formation of that cloud.
- Over portions of the Maritime Continent region, the mean rainfall is a product of diurnally-varying processes related to convection that operate at very small scales.

8.3 Recommendations for Future Work

It is considered that the work documented in this thesis could springboard further research in two categories: addressing residual model errors, and application of the model to other locations and types of investigation. Suggested avenues of research along these lines are described below.

8.3.1 Addressing Residual Model Error

High and Large-scale Cloud Cover

It was shown that the high cloud fraction simulated by the Emanuel scheme was considerably overestimated compared to ISCCP, even though the high-level CLW was a good match to CloudSat and the planetary albedo had only a small overestimation compared to SRB observations with the new version of the model. It was also shown that the high cloud fraction simulated by the Grell scheme is overestimated in the new version of the model, even though the high-level CLW and the planetary albedo are both underestimated. These results suggest that the way in which cloud fraction is calculated is not entirely consistent with the simulated water content at high altitudes. Additionally, work in Chapter 6 identified that the model does not adequately represent the propagation of mesoscale convective systems (MCSs). The formation of these systems is simulated at high altitude over the mountainous regions, but they remain stationary over time.

High cloud cover simulated by the model is primarily produced by the SUBEX scheme within RegCM3. SUBEX calculates cloud cover as a function only of the mean value of relative humidity within a grid box, without accounting for subgrid variability of that

humidity or other factors that may impact the formation of non-convective cloud. It may be worth applying a similar method to large-scale cloud fraction as was developed here for convective clouds, or applying additional criteria to the calculation of large-scale cloud fraction other than relative humidity.

In addition, the work presented in this thesis related to convective clouds has explicitly dealt only with warm (i.e. above freezing) clouds, so any convective cloud that is tall enough to penetrate into freezing altitudes will be missing ice-phase hydrometeors. It was shown that cloud cover can be equally as sensitive to removal via rainfall as it is to production mechanisms; perhaps the errors in high cloud cover are due to inadequate representation of ice- and mixed-phase precipitation. It was previously noted by Pal *et al.* (2000) that the lack of an ice-phase representation in SUBEX is a serious deficiency. The role of ice phase hydrometeors should therefore be a priority for future work.

There is also a notable lack of spatial and temporal coherency in cloud cover, especially over land-sea boundaries and topographic gradients. This is likely due to the distinct separation in simulated cloud types within the model and the use of different parameter sets over different surfaces for each cloud type. In cases where residual convective condensate is re-evaporated and the SUBEX routine is required to use the residual moisture to create a stratiform cloud in place of a convective cloud, there could be some model deficiency in the timing or density of the new stratiform cloud compared to observations. It is also likely that the lack of any freezing hydrometeors (e.g. cloud ice) within RegCM3 contributes to the observed cloud deficiencies, since the deep convection that produces MCSs would contain a large fraction of below-freezing particles. Therefore it is considered that the general representation large-scale cloud cover within RegCM3 should be revisited.

Low-level Cloud Cover

Low-level cloud cover and CLW were overestimated in the new version of the model. It was suggested that the apparent overestimation of CLW in the lower atmosphere produced by the model may not be an error, but rather an illustration of the discrepancy between observations and model output. Improved observations of CLW during rainfall

events would clarify this issue and help to further improve the model. However, the overestimation of low cloud fraction still remains to be addressed. As suggested above for high cloud cover, some of the error with low cloud cover may be due to the nature of the large-scale cloud formulation. It is possible that improvements to this large-scale cloud will also improve the average low-level cloud fraction.

Subgrid-scale Convective Processes

It was shown that some of the processes responsible for creating the observed diurnal rainfall cycle over the Maritime Continent region operate on scales too small to be resolved by a large-scale climate model using a convective parameterization scheme. In particular, the model lacks representation of cold outflows driven by convective downdrafts, which lead to self-generating convection and propagation of squall lines, and of temperature anomalies propagated by gravity waves, excited by strong convection over mountainous areas. Considerable effort is required in this direction to determine a better method for parameterizing these subgrid-scale processes.

Nocturnal Stable Layer

It is likely that the nocturnal stable layer over the Maritime Continent will be shallower than other tropical regions due to the presence of significant cloud cover and a substantial vegetated canopy, both of which limit night-time radiative cooling. Therefore the lowest model layer, used as a minimum constraint on the PBL height in Chapter 3, may not be an appropriate constraint on the nocturnal stable PBL height over other tropical regions. Future work in this field may elucidate a more definitive scaling relationship (i.e. a diagnostic expression) for the tropics or another method of calculation that is more appropriate, for example derived from the rate of radiative cooling or one of the methods noted by Stull (1988).

Convection Triggering Criteria

It was noted in Chapter 2 that an alternate avenue of investigation with regard to simulation error is in the nature of the threshold criteria for triggering convection. Presently, the convection schemes in RegCM3 (and many other RCMs) contain threshold criteria that are essentially uniform in time and space and are meant to represent the mean behavior of

an ensemble of convective cells. These schemes were originally made for use in a model with a coarse resolution, such that a single grid cell could be expected to contain an ensemble of individual convective cells. However, a single grid cell in an RCM simulation might only hold one or a few convective cells, especially at the resolutions that are required to resolve the islands of the Maritime Continent region. Therefore it seems likely that both spatial and temporal variability in convective triggering will need to be incorporated into the RegCM3 model system.

8.3.2 Potential Applications of Improved Model

Simulation over Other Tropical Regions

It would be instructive to apply the improved version of the model to other tropical locations to confirm that improvements documented over the Maritime Continent are generally applicable across the tropics. It would be especially interesting to investigate if the changes made to convection hold over places with different geography. The Maritime Continent has very complex geography with thousands of islands, lots of land-sea boundaries and steep topographic gradients. Potential topics for exploration include how the changes made to convection manifest over a more continental area like South America, and how these changes affect simulation of the West African Monsoon.

Influence of Other Temporally-varying Large-scale Conditions

This thesis has focused mainly on the mean diurnal cycle over the Maritime Continent, with exploration of how the diurnal cycle is affected by interannual variability due to specific El Niño and La Niña events. An exploration of other large-scale forcings, along the lines of the analysis presented in Chapter 7, would be informative. Of particular interest are interseasonal variability, associated with movement of the Intertropical Convergence Zone and the South Asian and East Asian monsoons, and intraseasonal variability, associated with the equatorially-trapped Madden-Julian Oscillation. Both of these phenomena are known to strongly influence the diurnal cycle over the Maritime Continent.

Role of Aerosols

This work has not included the explicit simulation of aerosols, such as those formed from biomass burning across Malaysia and Indonesia. It seems unlikely that cloud condensation nuclei abundance poses a constraint to cloud formation in this region, given the large surface area occupied by ocean (which produces a large quantity of aerosols for cloud condensation nuclei) and the relatively high frequency of observed cloud cover. However, the presence of biomass burning may change the nature and concentration of condensation nuclei, resulting in different temporal and/or spatial cloud dynamics. The new parameterization for autoconversion in Chapter 5 implicitly included the effects of biomass burning, by incorporating observations of cloud droplet concentration and radius taken from locations in South America experiencing biomass burning. But there may be other ways that the nature of these aerosols impacts the regional climate, such as attenuation of incoming radiation via scattering and absorption. The impact of aerosols on the Maritime Continent could be explored in future work by utilizing the aerosol package available with RegCM3.

Coupling With an Ocean Model

The model used here did not show great sensitivity in oceanic rainfall to changes in the incoming radiation because the SSTs were forced with weekly mean values. But this region has some very shallow seas that have shown remarkable diurnal variability and sensitive responses to rainfall (e.g. Webster *et al.* 1996). Hence it is likely that forcing SSTs with a mean value, even on a weekly timescale, is not the most appropriate way to represent this region and a coupled atmosphere-ocean-land surface model is required for better simulation. In that case, the ocean model would be sensitive to the incoming radiation determined by the atmospheric model, and the egregious errors present in the default version of RegCM3 would likely lead to large feedback errors from the ocean. It would be instructive to use the RegCM3 improvements documented here in such a coupled model to verify that the ocean exhibits more realistic behavior with these improvements.

Impact On / From Different Boundary Conditions

It is expected that the newly improved version of RegCM3 would enhance simulations of global climate if used in a two-way nested domain with a GCM. It is also

expected that the newly improved model would exhibit the appropriate sensitivity to experiments in which the boundary conditions were changed, for example to mimic the IPCC's future climate change scenarios. This thesis was initially motivated by the desire for improved certainty in future climate projections, so a test of the improved model in that context would be enlightening.

Appendix A: Theory and Observations of Rainfall Production

The processes responsible for the formation of precipitation include: production of supersaturation, activation of cloud condensation nuclei where supersaturation occurs, droplet growth by condensation of water vapour, stochastic coalescence and the Bergeron-Findeisen mechanism, the redistribution of condensed water mass among particles of different sizes by coalescence and drop breakup in the liquid phase, and by a large variety of ice-phase and mixed-phase processes (Emanuel 1994; Geoffroy *et al*. 2008). In-situ and radar observations reveal strong sensitivity of many of these processes to cloud-base temperature, updraft velocity, the degree of turbulence in the cloud, the number and size distribution of condensation nuclei, and the number and distribution of freezing nuclei (Emanuel 1994).

The conversion process of cloud water into rainwater is characterized by the time scale of the sum of these processes (Suzuki *et al.* 2011). Stephens and Haynes (2007) used MODIS and CloudSat observations to find the rate of coalescence over the global oceans as a function of the droplet concentration of different size distribution modes, the mean radius of the sixth moment, the liquid water content associated with different size distribution modes and a critical mean radius threshold. Stephens and Haynes (2007) also showed that this rate could be calculated as a function of cloud-layer reflectivity measured by CloudSat and cloud optical depth and effective radius as measured by MODIS. Using these methods, Stephens and Haynes (2007) showed that the time scale for coalescence over the oceans between 60^{o}S and 60^{o}N is between 6 minutes and 3 hours, with the majority (73%) of observations in the range 26 minutes to 3 hours.

Unfortunately such a wide range of values is not particularly helpful for models in which a convective parameterization scheme may be called every few minutes. Additionally, factors that determine the time scale of the process are not well understood (e.g. Khain *et al*. 2000), especially on the global scale. Precipitation tends to develop more rapidly than is generally predicted from elementary theories about diffusional growth of droplets and subsequent coalescence to precipitation-sized particles (Stephens and Haynes 2007).

Diffusional growth theory does not account for the observed broadened size distributions that in turn support a more active coalescence process and the subsequent development of warm rain (Stephens and Haynes 2007). Several hypotheses have been forwarded to explain the observed droplet size broadening, including the presence of giant nuclei, various effects of turbulence and localized enhancement of the collision efficiency (Emanuel 1994; Stephens and Haynes 2007).

The conversion of cloud droplets to precipitation at a given height is marked by a sharp decrease in the cloud droplet concentration and water content (Rosenfeld and Lensky 1998). Some recent analyses (Lebsock *et al*. 2008; L'Ecuyer *et al.* 2009) found that the probability of precipitation, defined as the fractional occurrence of precipitation events with precipitation rate greater than a threshold value, tends to increase monotonically with cloud liquid water path (LWP) and is significantly modified by aerosol abundance (Suzuki *et al*. 2011). Droplet concentration may also be important in helping to determine the processes that form drizzle, such as collision and coalescence (Albrecht 1989). Collision efficiencies are reduced for smaller cloud drops (Rogers and Yau 1989). Albrecht (1989) proposed that an increase in droplet concentration with a consequent decrease in droplet size would decrease drizzle frequency and thus increase fractional cloudiness, enhancing cloud albedo. Albrecht (1989) also discussed observations made over southern California that showed that the clouds with the lowest droplet concentrations have the highest propensity to drizzle significantly.

Kubar *et al*. (2009) used MODIS and CloudSat data to look at cloud properties over the tropical and subtropical Pacific and Gulf of Mexico. The majority of the area analyzed was described as a pristine maritime environment, expected to have quite low cloud condensation nuclei and droplet concentrations. The authors focused on warm clouds with cloud-top temperatures above freezing. Over the Inter Tropical Convergence Zone and South Pacific Convergence Zone, 80% of the pixels were drizzling when liquid water path (LWP) exceeded about 160 g m^{-2}, effective radius exceeded 15 μm and effective droplet concentration dropped below about 60 cm^{-3} (Kubar *et al*. 2009). These drizzling clouds had cloud tops at least 2.2 km high. The results presented in Kubar *et al*. (2009) are consistent

with Albrecht (1989) in showing that (i) drizzle frequency steadily increases with LWP as effective droplet concentration is held constant, and (ii) the likelihood of drizzle tends to decrease with increasing droplet concentration if LWP is held constant. Also in agreement with Albrecht (1989), maps of effective radius and effective droplet concentration demonstrate that these two variables are strongly negatively correlated (Kubar *et al*. 2009).

Rosenfeld and Lensky (1998) presented observations of cumulus and cumulonimbus clouds growing in pristine maritime air over the central Indian Ocean. These clouds contained large cloud particles at all heights, with large droplets already in existence at warm temperatures or at small depth above cloud bases. Hence the effective radius quickly grows with height and exceeds the precipitation threshold of 14 μm at the lowest observed levels, suggesting warm rain (i.e. rain formed by water drop coalescence) formation processes starting a short distance above the cloud base (Rosenfeld and Lensky 1998).

Observations made over Sumatra, Indonesia, show clouds growing in an air mass that is highly polluted by smoke emitted from rain forest fires (Rosenfeld and Lensky 1998). Clouds formed in this air showed small water droplets at low levels, supercooled small drops higher up and glaciated anvils (Rosenfeld and Lensky 1998). These clouds are considered microphysically highly continental. The curve of T versus effective radius showed small re, well below the precipitation threshold of 14 μm up to a temperature of about -10^{o}C, indicating cloud droplet growth mainly by diffusional processes without much coalescence (Rosenfeld and Lensky 1998). Effective radius reached a maximum near -22^{o}C, implying full development of the ice phase at that temperature; hence the clouds formed precipitation mainly in the ice phase as hail, graupel and snow particles (Rosenfeld and Lensky 1998).

Once precipitation particles have formed, their fall speed carries them through the population of cloud particles and facilitates the growth of precipitation by collection within the cloud. Kessler (1969) showed that the shape of the precipitation distribution (vertically through the atmosphere) and the precipitation density are generally closely related to the ratio V/w_{max}, where V is the fall speed of the precipitation and w_{max} is the maximum (through the vertical profile) value of the vertical wind speed, i.e. the precipitation content is more closely related to the ratio of V/w_{max} than to the updraft speed alone. When the terminal fall

speed is less than the maximum updraft, the motion of precipitation is upward in some parts of the updraft column and downward where the updraft is weak, at least near the upper and lower boundaries (Kessler 1969). When the ratio V/w_{max} is large, the largest precipitation density in a vertical column tends to be near the base of the column, and the magnitude of precipitation content tends to increase with the increasing updraft. On the other hand, when the ratio is small (i.e. updrafts very strong), the steady-state precipitation density tends to be independent of the updraft speed; in an atmosphere unsaturated at the ground, the maximum precipitation density can be found near the top of the updraft column (Kessler 1969). The updraft velocities in maritime clouds are characteristically limited to below the terminal fall velocity of the raindrops, whereas no such maximum for the updraft was noted in continental convection (Zipser and LeMone 1980, Jorgensen and LeMone 1989, Zipser and Lutz 1994; as reported in Rosenfeld and Ulbrich 2003).

The majority of climate models have cloud water content as a prognostic variable, so the ability to relate the simulated cloud water to rainfall is highly desirable. Ideally, we would like to have observations of the fraction of cloud water that is converted to precipitation from different types of clouds, in order to better parameterize the conversion process in climate models. Unfortunately, our current observational abilities are limited in this respect.

Direct estimates of cloud liquid water content are only available from aircraft *in situ* measurements, confining their availability to short periods and specific locations (Saavedra *et al*. 2012). Remote sensing by ground-based microwave radiometers is increasingly used to probe the cloudy atmosphere, often in synergy with other observations, to retrieve the vertically integrated cloud liquid water path (LWP). Numerous passive and active remote sensing methods have been developed for the quantification of rainfall, typically derived from backscattered signals emitted by ground and spaceborne radars (Saavedra *et al*. 2012). However, simultaneous retrieval of cloud liquid water content and rainfall are problematic because the algorithm for retrieving cloud water is predicated on the absence of raindrop-sized particles. Simple, empirical LWP thresholds used in both cloud and rainfall retrievals are most commonly used to classify those scenes that are most likely to contain precipitation

(Stephens and Kummerow 2007). But in reality, drizzle and light precipitation are ubiquitous features of warm layered clouds and shallow convection, so the separation between precipitation and cloud is not simple nor entirely understood (Stephens and Kummerow 2007).

Few studies have been performed in order to estimate cloud and rain water path simultaneously, i.e. the partitioning of total water path into its cloud and rain components (Saavedra *et al*. 2012). This partitioning plays an important role in cloud modeling and in space-based retrieval algorithms where empirical assumptions are employed to resolve the unknown cloud-rain partition (Wentz and Spencer 1998, Hilburn and Wentz 2008).

O'Dell *et al*. (2008) used a combination of Special Sensor Microwave Imager (SSM/I), Tropical Rainfall Measuring Mission (TRMM) Microwave Imager (TMI), and the Advanced Microwave Scanning Radiometer (AMSR) for Earth Observing System (EOS) (AMSR-E) instruments to construct a climatology of cloud liquid water path for the period 1988-2005. The work by O'Dell *et al*. (2008) shows that assumptions related to the partitioning of cloud water and rainwater are a major source of systematic errors in retrievals based on spaceborne instruments, which can severely hamper the usefulness of microwave-based retrievals of cloud water and rainwater (Saavedra *et al*. 2012). Different algorithms attribute different weights to the cloud and rain component and this is the cause of large discrepancies in the different precipitation products (Saavedra *et al*. 2012).

Hilburn and Wentz (2008) reported satellite-derived relationships between columnar cloud water and rainwater over oceans for tropical observations, using the UMORA algorithm. The authors made the following conclusions by using assumptions from the work by Wentz and Spencer (1998): 1) rain is initiated at a cloud liquid water path exceeding 0.18 kg m^{-2}; 2) cloud liquid water path increases with rain liquid water path; 3) the cloud versus rain relationship levels off at high rain liquid water path, with cloud liquid water path reaching a maximum value at 1-2 kg m^{-2} (Hilburn and Wentz 2008). The resulting relationship between cloud water content and precipitation is shown in the left-hand panel of Figure A-1 (Figure 11 from Hilburn and Wentz 2008).

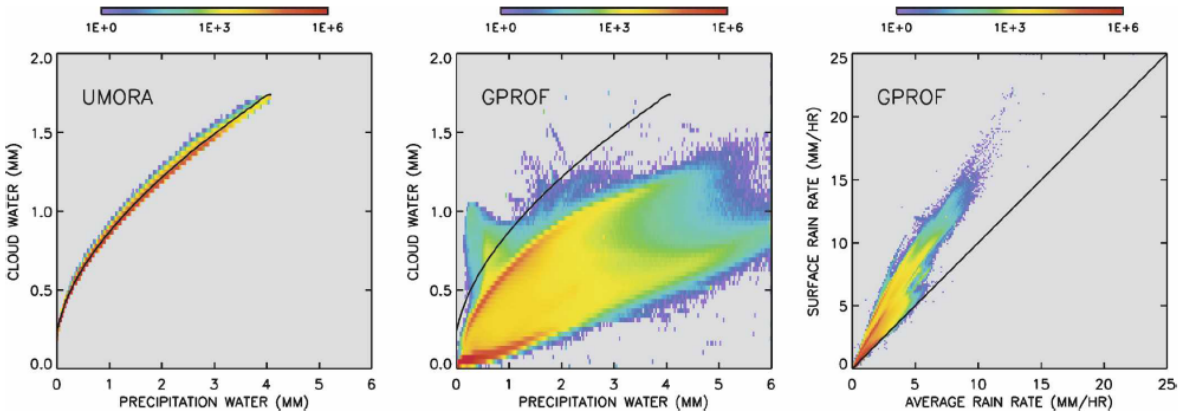

Figure A-1. Left: The relationship between cloud water (in mm) and precipitation water (in mm) in UMORA. Middle: The same relationship for GPROF, where the black line indicates the UMORA relationship. Right: The relationship between surface rain rate (in mm hr^{-1}) and columnar average rain rate (in mm hr^{-1}) in GPROF. The black line is the relationship in UMORA where the surface rain rate is identical to the columnar average rain rate. In each plot, the colours represent the number of observations in year 2003 (Figure 11 from Hilburn and Wentz 2008).

Saavedra *et al*. (2012) also reported relationships between cloud and rain liquid water paths, obtained using an improved algorithm over the Cabauw site in the Netherlands. In their work, clouds were found to support a cloud liquid water path larger than 0.55 kg m^{-2} before rain developed, which is comparable to other ground-based microwave observations (Saavedra *et al*. 2012), although rain was observed in some cases even at cloud liquid water paths below this threshold. The results by Saavedra *et al*. (2012) did not seem to favor a well-defined functional relationship between cloud and rain liquid water paths as found by Hilburn and Wentz (2008). The maximum cloud liquid water path for a given rain liquid water path tended to level off at about 1.4 kg m^{-2} while the rain liquid water path continued to increase past this value (Saavedra *et al*. 2012). Figure A-2 (Figure 10 from Saavedra *et al.* 2012) shows the partitioning between cloud water and rain water based on the authors' retrieval method.

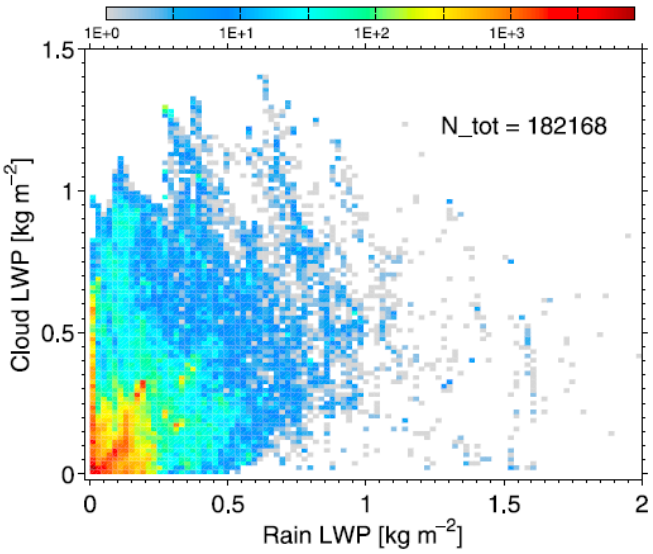

Figure A-2. Retrieved partition for cloud and rain liquid water path (LWP) (in kg m^{-2}) during the whole observation period (Class 2). The color bar indicates the number of observations in logarithmic scale (Figure 10 from Saavedra *et al*. 2012).

Comstock *et al*. (2004) analyzed 30 samples of stratocumulus data from the Eastern Pacific Investigation of Climate Processes in the Coupled Ocean-Atmosphere System (EPIC) to derive the liquid water path, the drizzle precipitation rate, and the mean cloud droplet number concentration from ship-based radar measurements and shipboard raindrop-size distribution measurements obtained using filter papers. The authors established a relationship between these three variables:

$$\mathrm{R} = 0.0156\left(\frac{\mathrm{LWP}}{\mathrm{N}}\right)^{1.75} \qquad \text{(A-1)}$$

where R = drizzle precipitation rate in mm hr^{-1}, LWP = liquid water path in g m^{-2}, N = mean cloud droplet number concentration in cm^{-3}.

Geoffroy *et al*. (2008) showed that a similar relationship could be shown using a large eddy simulation model. Those authors argued that the similarity between the Comstock *et al*. (2004) and other observations and the model results suggests that such a relationship is not fortuitous but likely physically-based (Geoffroy *et al*. 2008).

The work by Hilburn and Wentz (2008) and Saavedra *et al*. (2012) produced quite different results and therefore cannot be used to create a generalized relationship between cloud water and rainfall. These two data sets are quite different – Hilburn and Wentz (2008) reported findings over the tropical oceans, while Saavedra *et al*.'s (2012) findings are limited to a specific location over a short observational period – so we should not expect them to agree. Generally the results show that increasing rain liquid water path can be expected with increasing cloud liquid water path, but more concrete details than that will require more long-term and widespread measurements.

Stephens and Kummerow (2007) stress that cloud and precipitation observing systems developed around simple methods of retrievals are actually very complex, and that simplifying assumptions about the microphysical properties of clouds and precipitation lead to error in the retrievals of these quantities. These authors called for a more unified approach to observing clouds and precipitation properties jointly to improve retrieval problems and also to advance our understanding of important cloud and precipitation processes (Stephens and Kummerow 2007).

Appendix B: Model Code

All the model files used to set up and run the simulations presented in this thesis have been uploaded to the locker located at:

\afs\athena.mit.edu\user\e\l\eltahir\gianotti_code.

These files have also been burned to a DVD, which is in the care of Professor Eltahir at MIT.

Bibliography

Adler, R. F., G. J. Huffman, A. Chang, R. Ferraro, P. Xie, J. Janowiak, B. Rudolf, U. Schneider, S. Curtis, D. Bolvin, A. Gruber, J. Susskind and P. Arkin. 2003, 'The Version 2 Global Precipitation Climatology Project (GPCP) Monthly Precipitation Analysis (1979-Present)', *Journal of Hydrometeorology*, **4**, pp. 1147-1167.

Albrecht, B. A., C. S. Bretherton, D. W. Johnson, W. H. Schubert and A. S. Frisch. 1995, 'The Atlantic Stratocumulus Transition Experiment – ASTEX', *Bulletin of the American Meteorological Society*, **76**, pp. 889-904.

Albrecht, B. A., D. A. Randall and S. Nicholls. 1988, 'Observations of marine stratocumulus during FIRE', *Bulletin of the American Meteorological Society*, **69**, pp. 618-626.

Albrecht, B. A. 1989, 'Aerosols, cloud microphysics, and fractional cloudiness', *Science*, **245**, pp. 1227-1230.

Andræ, U., N. Sokka and K. Onogi. 2004, *ERA-40 Project Report Series No. 15: The radiosonde temperature bias corrections used in ERA-40*, European Centre for Medium Range Weather Forecasts, Reading, England.

Anthes, R. A. 1977, 'A cumulus parameterization scheme utilizing a one-dimensional cloud model', *Monthly Weather Review*, **105**, pp. 270-286.

Arakawa, A. 2004, 'The cumulus parameterization problem: past, present, and future', *Journal of Climate*, **17**(13), pp. 2493-2525.

Arakawa, A. and W. H. Schubert. 1974, 'Interaction of a cumulus cloud ensemble with the large-scale environment, Part I', *Journal of the Atmospheric Sciences*, **31**, pp. 674-701.

Asdak, C., P. G. Jarvis, P. van Gardingen and A. Fraser. 1998, 'Rainfall interception loss in unlogged and logged forest areas of Central Kalimantan, Indonesia', *Journal of Hydrology*, **206**, pp. 237-244.

Austin, R. 2007, *Level 2B Radar-only Cloud Water Content (2B-CWC-RO) Process Description Document*, Version 5.1, CloudSat Project, available from: <http://www.cloudsat.cira.colostate.edu/ICD/2B-CWC-RO/2B-CWC-RO_PD_5.1.pdf> [12 April 2012].

Bachiochi, D. R., and T. N. Krishnamurti. 2000, 'Enhanced low-level stratus in the FSU coupled ocean-atmosphere model', *Monthly Weather Review*, **128**, pp. 3083-3103.

Baker, R. D., B. H. Lynn, A. Boone, W.-K. Tao and J. Simpson. 2001, 'The influence of soil moisture, coastline curvature, and land-breeze circulations on sea-breeze initiated precipitation', *Journal of Hydrometeorology*, **2**, pp. 193-211.

Bartlein, P., 2000: *Absolute minimum temperature minus average of the coldest monthly mean temperature Worldwide Airfield Summaries* [Available online at: http://www.sage.wisc.edu/download/IBIS].

Beheng, K. D. 1994, 'A parameterization of warm cloud microphysical conversion processes', *Atmospheric Research*, **33**, pp. 193-206.

Benkley, C. W., and L. L. Schulman. 1979, 'Estimating hourly mixing depths from historical meteorological data', *Journal of Applied Meteorology*, **18**, pp. 772-780.

Bergman, J. W. and M. L. Salby. 1996, 'Diurnal variations of cloud cover and their relationship to climatological conditions', *Journal of Climate*, **9**, pp. 2802-2820.

Betts, A. K. and J. Bartlo. 1991, 'The density temperature and the dry and wet virtual adiabats', *Monthly Weather Review*, **119**, pp. 169-175.

Blossey, P. N., C. S. Bretherton, J. Cetrone and M. Kharoutdinov. 2007, 'Cloud-resolving model simulations of KWAJEX: Model sensitivities and comparisons with satellite and radar observations', *Journal of the Atmospheric Sciences*, **64**, pp. 1488-1508.

Bony, S., and J.-L. Dufresne. 2005, 'Marine boundary layer clouds at the heart of tropical cloud feedback uncertainties in climate models', *Geophysical Research Letters*, **32**, L20806, doi:10.1029/2005GL023851.

Bony, S., and K. A. Emanuel. 2001, 'A parameterization of the cloudiness associated with cumulus convection: Evaluation using TOGA COARE data', *Journal of the Atmospheric Sciences*, **58**, pp. 3158-3183.

Boyle, J., and S. A. Klein. 2010, 'Impact of horizontal resolution on climate model forecasts of tropical precipitation and diabatic heating for the TWP-ICE period', *Journal of Geophysical Research*, **115**, D23113, doi:10.1029/2010JD014262.

Brenguier, J.-L., H. Pawlowska, L. Schuller, R. Preusker, J. Fischer and Y. Fouquart. 2000, 'Radiative properties of boundary layer clouds: droplet effective radius versus number concentration', *Journal of the Atmospheric Sciences*, **57**, pp. 803-821.

Bretherton, C. S., and Coauthors. 2004, 'The EPIC 2001 stratocumulus study', *Bulletin of the American Meteorological Society*, **85**, pp. 967-977.

Bretherton, C. S., and Coauthors. 1999, 'A GCSS boundary-layer cloud model intercomparison study of the first ASTEX Lagrangian experiment', *Boundary-Layer Meteorology*, **93**, pp. 341–380.

Bruijnzeel, L. A., M. J. Waterloo, J. Proctor, A. T. Kuiters and B. Kotterink. 1993, 'Hydrological observations in montane rain forests on Gunung Silam, Sabah, Malaysia, with special reference to the '*Massenerhebung*' effect', *Journal of Ecology*, **81**(1), pp. 145-167.

Calder, I. R., I. R. Wright and D. Murdiyarso. 1986, 'A study of evaporation from tropical rain forest – West Java', *Journal of Hydrology*, **89**, pp. 13-31.

Cha, D.-H., D.-K. Lee and S.-Y. Hong. 2008, 'Impact of boundary layer processes on seasonal simulation of the East Asian summer monsoon using a Regional Climate Model', *Meteorology and Atmospheric Physics*, **100**, pp. 53-72.

Chan, S. C., and S. Nigam. 2009, 'Residual diagnosis of diabatic heating from ERA-40 and NCEP reanalyses: Intercomparisons with TRMM', *Journal of Climate*, **22**, pp. 414-428.

Chen, T.-C., and K. Takahashi. 1995, 'Diurnal variation of outgoing longwave radiation in the vicinity of the South China Sea: Effect of intraseasonal oscillation', *Monthly Weather Review,* **123**, pp. 566-577.

Chow, K. C., J. C. L. Chan, J. S. Pal and F. Giorgi. 2006, 'Convection suppression criteria applied to the MIT cumulus parameterization scheme for simulating the Asian summer monsoon', *Geophysical Research Letters*, **33**, L24709, doi:10.1029/2006GL028026.

Christensen, J. H., and Coauthors. 2007, 'Regional Climate Projections', In *Climate Change 2007: The Physical Science Basis. Contribution of Working Group I to the Fourth Assessment Report of the Intergovernmental Panel on Climate Change* [Solomon, S., D. Qin, M. Manning, Z. Chen, M. Marquis, K. B. Averyt, M. Tignor, and H. L. Miller (eds.)]. Cambridge University Press, Cambridge, United Kingdom, and New York, NY, USA.

Collier, J. C., and K. P. Bowman. 2004, 'Diurnal cycle of tropical precipitation in a general circulation model', *Journal of Geophysical Research*, **109**, doi:10.1029/2004JD004818.

Comstock, K. K., R. Wood, S. E. Yuter and C. S. Bretherton. 2004, 'Reflectivity and rain rate in and below drizzling stratocumulus', *Quarterly Journal of the Meteorological Society*, **130**, pp. 2891-2918.

Contini, D., D. Cava, P. Martano, A. Donateo and F. M. Grasso. 2008, 'Boundary layer height estimation by sodar and sonic anemometer measurements', *IOP Conference Series: Earth and Environmental Science*, **1**, doi:10.1088/1755-1307/1/1/012034.

Cotton, W. R. 1972, 'Numerical simulation of precipitation of development in supercooled cumuli', *Monthly Weather Review*, **100**, pp. 757-784.

Cruz, R.V., H. Harasawa, M. Lal, S. Wu, Y. Anokhin, B. Punsalmaa, Y. Honda, M. Jafari, C. Li and N. Huu Ninh. 2007, 'Chapter 10: Asia', *Climate Change 2007: Impacts, Adaptation and Vulnerability. Contribution of Working Group II to the Fourth Assessment Report of the Intergovernmental Panel on Climate Change*, M.L. Parry, O.F. Canziani, J.P. Palutikof, P.J. van der Linden and C.E. Hanson, Eds., Cambridge University Press, Cambridge, UK, pp. 469-506.

Dai, A. 2001, 'Global precipitation and thunderstorm frequencies. Part I: Seasonal and interannual variations', *Journal of Climate*, **14**, pp. 1092-1111.

Dai, A., and K. E. Trenberth. 2004, 'The diurnal cycle and its depiction in the Community Climate System Model', *Journal of Climate*, **17**, pp. 930-951.

Davies, H., and R. Turner. 1977, 'Updating prediction models by dynamical relaxation: An examination of the technique', *Quarterly Journal of the Royal Meteorological Society*, **103**, pp. 225-245.

Davis, N., J. Bowden, F. Semazzi, L. Xie and B. Onol. 2009, 'Customization of RegCM3 regional climate model for eastern Africa and a tropical Indian Ocean domain', *Journal of Climate*, **22**, pp. 3595-3616.

de Vries, D. A. 1963, 'Chapter 7: Thermal properties of soils', in *Physics of Plant Environment*, W. R. van Wijk (Ed.), North-Holland Publishing Company, pp. 210-235.

Dickinson, R., A. Henderson-Sellers and P. Kennedy. 1993, 'Biosphere Atmosphere Transfer Scheme (BATS) version 1e as coupled to the NCAR Community Climate Model', *NCAR Technical Note NCAR/TN-387+STR*, National Center for Atmospheric Research, Boulder, Colorado.

Dickinson, R. E., A. Henderson-Sellers, P. J. Kennedy and M. F. Wilson. 1986, 'Biosphere-Atmosphere Transfer Scheme (BATS) for the NCAR Community Climate Model', *NCAR Technical Note NCAR/TN-275+STR*, National Center for Atmospheric Research, Boulder, Colorado.

Donner, L. J., and Coauthors. 2011, 'The dynamical core, physical parameterizations, and basic simulation characteristics of the atmospheric component AM3 of the GFDL global coupled model CM3', *Journal of Climate*, **24**, pp. 3484-3519.

Dykes, A. P. 1997, 'Rainfall interception from a lowland tropical rainforest in Brunei', *Journal of Hydrology*, **200**, pp. 260-279.

Eltahir, E. A. B., and R. L. Bras. 1993, 'Estimation of the fractional coverage of rainfall in climate models', *Journal of Climate*, **6**, pp. 639-644.

Emanuel, K. A., 1994: *Atmospheric Convection*, Oxford University Press, New York, 580 p.

Emanuel, K. A. 1991, 'A scheme for representing cumulus convection in large-scale models', *Journal of the Atmospheric Sciences*, **48**(21), pp. 2313-2335.

Emanuel, K. A., and M. Živković-Rothman. 1999, 'Development and evaluation of a convection scheme for use in climate models', *Journal of the Atmospheric Sciences*, **56**, pp. 1766-1782.

Fairall, C. W., E. F. Bradley, J. E. Hare, A. A. Grachev and J. B. Edson. 2003, 'Bulk parameterization of air-sea fluxes: updates and verification for the COARE algorithm', *Journal of Climate*, **16**, pp. 571-591.

Fairall, C. W., E. F. Bradley, D. P. Rogers, J. B. Edson and G. S. Young. 1996, 'Bulk parameterization of air-sea fluxes for Tropical Ocean-Global Atmosphere Coupled-Ocean Atmosphere Response Experiment', *Journal of Geophysical Research*, **101**(C2), pp. 3747-3764.

Farouki, O. T. 1981, 'The thermal properties of soils in cold regions', *Cold Regions Science and Technology*, **5**, pp. 67-75.

Findell, K. L. 2001, *Atmospheric controls on soil moisture-boundary layer interactions*, PhD Dissertation, Massachusetts Institute of Technology, 172 p.

Foley, J. A., I. C. Prentice, N. Ramankutty, S. Levis, D. Pollard, S. Sitch and A. Haxeltine. 1996, 'An integrated biosphere model of land surface processes, terrestrial carbon balance, and vegetation dynamics', *Global Biogeochemical Cycles*, **10**(4), pp. 603-628.

Foster, J., M. Bevis and W. Raymond. 2006, 'Precipitable water and the lognormal distribution', *Journal of Geophysical Research*, **111**, D15102, doi:10.1029/2005JD006731.

Fowler, L. D., D. A. Randall and S. A. Rutledge. 1996, 'Liquid and ice cloud microphysics in the CSU general circulation model. Part I: Model description and simulated microphysical processes', *Journal of Climate*, **9**, pp. 489-529.

Francisco, R. V., J. Argete, F. Giorgi, J. Pal, X. Bi and W. J. Gutowski. 2006, 'Regional model simulation of summer rainfall over the Philippines: Effect of choice of driving fields and ocean flux schemes', *Theoretical and Applied Climatology*, **86**, pp. 215-227.

Frey, H., M. Latif and T. Stockdale. 1997, 'The coupled GCM ECHO-2. Part I: The Tropical Pacific', *Monthly Weather Review*, **125**, pp. 703-720.

Fritsch, J. M., and C. F. Chappell. 1980, 'Numerical prediction of convectively driven mesoscale pressure systems. Part 1: Convective parameterization', *Journal of the Atmospheric Sciences*, **37**, pp. 1722-1733.

Gao, X., Y. Xu, Z. Zhao, J. S. Pal and F. Giorgi. 2006, 'On the role of resolution and topography in the simulation of East Asia precipitation', *Theoretical and Applied Climatology*, **86**, pp. 173-185.

Gent, P. R., S. G. Yeager, R. B. Neale, S. Levis and D. A. Bailey. 2009, 'Improvements in a half degree atmosphere/land version of the CCSM', *Climate Dynamics*, **34**(6), pp. 819–833, doi:10.1007/s00382-009-0614-8.

Geoffroy, O., J.-L. Brenguier and I. Sandu. 2008, 'Relationship between drizzle rate, liquid water path and droplet concentration at the scale of a stratocumulus cloud system', *Atmospheric Physics and Chemistry Discussions*, **8**, pp. 3921-3959.

Giorgi, F., R. Francisco and J. S. Pal. 2003, 'Effects of a sub-grid scale topography and land use scheme on the simulation of surface climate and hydrology. Part I: Effects of temperature and water vapour disaggregation', *Journal of Hydrometeorology*, **4**, pp. 317-333.

Giorgi, F., M. R. Marinucci and G. T. Bates. 1993, 'Development of a second-generation regional climate model (RegCM2). Part II: Convective processes and assimilation of lateral boundary conditions', *Monthly Weather Review*, **121**, pp. 2814-2832.

Global Soil Data Task, International Geosphere-Biosphere Programme, Data and Information System. 2000, *Global soil data products CD-ROM*, International Geosphere-Biosphere Programme, Data and Information System (IGDP-DIS), Potsdam, Germany.

Goh, K. C. 2003, 'Hydrological studies and water resource concerns in Southeast Asia', *Singapore Journal of Tropical Geography*, **24**(1), pp. 86-110.

Grell, G. A. 1993, 'Prognostic evaluation of assumptions used by cumulus parameterizations', *Monthly Weather Review*, **121**, pp. 764-787.

Grell, G. A., J. Dudhia and D. R. Stauffer. 1994, 'Description of the fifth generation Penn State/NCAR Mesoscale Model (MM5)', *Technical Report TN-398+STR*, National Center for Atmospheric Research, Boulder, Colorado.

Gultepe, I., and G. A. Isaac. 1997, 'Liquid water content and temperature relationship from aircraft observations and its applicability to GCMs', *Journal of Climate*, **10**, pp. 446-452.

Hack, J., J. M. Caron, G. Danabasoglu, K. W. Oleson, C. Bitz and J. Truesdale. 2006, 'CCSM-CAM3 climate simulation sensitivity to changes in horizontal resolution', *Journal of Climate*, **19**(11), pp. 2267–2289.

Hagemann, S., K. Arpe and L. Bengtsson. 2005, *ERA-40 Project Report Series No. 24: Validation of the hydrological cycle of ERA-40*, European Centre for Medium Range Weather Forecasts, Reading, England.

Hahmann, A. N., and R. E. Dickinson. 2001, 'A fine-mesh land approach for general circulation models and its impact on regional climate', *Journal of Climate*, **14**, pp. 1634-1646.

Hall, T. J., and T. H. Vonder Haar. 1999, 'The diurnal cycle of west Pacific deep convection and its relation to the spatial and temporal variation of tropical MCSs', *Journal of the Atmospheric Sciences*, **56**, pp. 3401-3415.

Hara, M., T. Yoshikane, H. G. Takahashi, F. Kimura, A. Noda and T. Tokioka. 2009, 'Assessment of the diurnal cycle of precipitation over the Maritime Continent simulated by a 20 km mesh GCM using TRMM PR data', *Journal of the Meteorological Society of Japan*, **87A**, pp. 413-424.

Harris, I., P. D. Jones, T. J. Osborn, D. H. and Lister. 2012, 'Updated high-resolution grids of monthly climatic observations - the CRU TS3.10 dataset', Submitted to *International Journal of Climatology*.

Heffter, J. L. 1980, 'Transport layer depth calculations', *Second Joint Conference on Applications of Air Pollution Meteorology*, New Orleans, LA.

Hilburn, K. A., and F. J. Wentz. 2008, 'Intercalibrated passive microwave rain products from the Unified Microwave Ocean Retrieval Algorithm (UMORA)', *Journal of Applied Meteorology and Climatology*, **47**, pp. 778-794.

Holtslag, A. A. M., and B. A. Boville. 1993, 'Local versus nonlocal boundary-layer diffusion in a global climate model', *Journal of Climate*, **6**, pp. 1825-1842.

Holtslag, A. A. M., E. I. F. de Bruijn and H.-L. Pan. 1990, 'A high-resolution air mass transformation model for short-range weather forecasting', *Monthly Weather Review*, **118**, pp. 1561-1575.

Houze Jr, R. A., S. G. Geotis, F. D. Marks Jr and A. K. West. 1981, 'Winter monsoon convection in the vicinity of North Borneo. Part 1: Structure and time variation of the clouds and precipitation', *Monthly Weather Review*, **109**(8), pp. 1595-1614.

Huffman, G. J., R. F. Adler, D. T. Bolvin, G. Gu, E. J. Nelkin, K. P. Bowman, Y. Hong, E. F. Stocker and D. B. Wolff. 2007, 'The TRMM Multisatellite Precipitation Analysis (TMPA): Quasi-Global, Multiyear, Combined-Sensor Precipitation Estimates at Fine Scales', *Journal of Hydrometeorology*, **8**, pp. 38-55.

Iassamen, A., H. Sauvageot, N. Jeannin and S. Ameur. 2009, 'Distribution of tropospheric water vapor in clear and cloudy conditions from microwave radiometric profiling', *Journal of Applied Meteorology and Climatology*, **48**, pp. 600-615.

Ichikawa, H., and T. Yasunari. 2008, 'Intraseasonal variability in diurnal rainfall over New Guinea and the surrounding oceans during Austral summer', *Journal of Climate*, **21**, pp. 2852-2868.

Ichikawa, H., and T. Yasunari. 2006, 'Time-space characteristics of diurnal rainfall over Borneo and surrounding oceans as observed by TRMM-PR', *Journal of Climate*, **19**, pp. 1238-1260.

Im, E.-S., J.-B. Ahn, A. R. Remedio and W.-T. Kwon. 2008, 'Sensitivity of the regional climate of East/Southeast Asia to convective parameterizations in the RegCM3 modelling system. Part 1: Focus on the Korean Peninsula', *International Journal of Climatology*, doi:10.1002/joc.1664.

Iorio, J. P., P. B. Duffy, B. Govindasamy, S. L. Thompson, M. Khairoutdinov and D. Randall. 2004, 'Effects of model resolution and subgrid-scale physics on the simulation of precipitation in the continental United States', *Climate Dynamics*, **23**, pp. 243–258, doi:10.1007/s00382-004-0440-y.

Jakob, C., and S. A. Klein. 1999, 'The role of vertically varying cloud fraction in the parameterization of microphysical processes in the ECMWF model', *Quarterly Journal of the Meteorological Society*, **125**, pp. 941-965.

Janowiak, J. E., A. Gruber, C. R. Kondragunta, R. E. Livezey and G. J. Huffman. 1998, 'A comparison of the NCEP-NCAR reanalysis precipitation and the GPCP rain gauge-satellite combined dataset with observational error considerations', *Journal of Climate*, **11**, pp. 2960-2979.

Jenkins, G. S. 1997, 'The 1988 and 1990 summer season simulations for West Africa using a regional climate model', *Journal of Climate*, **10**, pp. 1255-1272.

Johnson, R. H., and D. C. Kriete. 1982, 'Thermodynamic and circulation characteristics of winter monsoon tropical mesoscale convection', *Monthly Weather Review*, **110**, pp. 1898-1911.

Johnson, R. H., and D. L. Priegnitz. 1981, 'Winter monsoon convection in the vicinity of north Borneo. Part 2: Effects on large-scale fields', *Monthly Weather Review*, **109**, pp. 1615-1628.

Jorgensen, D. P., and M. A. LeMone. 1989, 'Vertical velocity characteristics of oceanic convection', *Journal of the Atmospheric Sciences*, **46**, pp. 621-640.

Joseph, B., B. C. Bhatt, T. Y. Koh and S. Chen. 2008, 'Sea breeze simulation over the Malay Peninsula in an intermonsoon period', *Journal of Geophysical Research*, **113**, doi:10.1029/2008JD010319.

Kanamitsu, M., W. Ebisuzaki, J. Woollen, S.-K. Yang, J. J. Hnilo, M. Fiorino and G. L. Potter. 2002, 'NCEP-DOE AMIP-II Reanalysis (R-2)', *Bulletin of the American Meteorological Society*, **83**, pp. 1631-1643. [Dataset available online at: http://www.cpc.ncep.noaa.gov/products/wesley/reanalysis2/index.html]

Karlsson, J., G. Svensson, S. Cardoso, J. Teixeira and S. Paradise. 2010, 'Subtropical cloud-regime transitions: Boundary layer depth and cloud-top height evolution in models and observations', *Journal of Applied Meteorology and Climatology*, **49**, pp. 1845-1858.

Keenan, T. D., B. R. Morton, M. J. Manton and G. J. Holland. 1989, 'The island thunderstorm experiment (ITEX) – a study of tropical thunderstorms in the maritime continent', *Bulletin of the American Meteorological Society*, **70**, pp. 152-159.

Keenan, T. D. and Coauthors. 2000, 'The Maritime Continent Thunderstorm Experiment (MCTEX): Overview and some results', *Bulletin of the American Meteorological Society*, **81**, pp. 2433-2455.

Kessler, E. 1969, 'On the distribution and continuity of water substance in atmospheric circulations', *Meteorological Monographs*, **10**(32), American Meteorological Society, 84 p.

Khain, A., M. Ovtchinnikov, M. Pinsky, A. Pokrovsky and H. Krugliak. 2000, 'Notes on the state-of-the-art numerical modeling of cloud microphysics', *Atmospheric Research*, **55**(3-4), pp. 159-224.

Khairoutdinov, M. F., D. A. Randall and C. DeMott. 2005, 'Simulations of the atmospheric general circulation using a cloud resolving model as a super-parameterization of physical processes', *Journal of the Atmospheric Sciences*, **62**, pp. 2136–2154, doi:10.1175/JAS3453.1.

Khairoutdinov, M. F., and D. A. Randall. 2003, 'Cloud resolving modeling of the ARM summer 1997 IOP: Model formulation, results, uncertainties, and sensitivities', *Journal of the Atmospheric Sciences*, **60**, pp. 607-625.

Khairoutdinov, M. F., and D. A. Randall. 2001, 'A cloud resolving model as a cloud parameterization in the NCAR Community Climate System Model: Preliminary results', *Geophysical Research Letters*, **28**, pp. 3617–3620, doi:10.1029/2001GL013552.

Kiehl, J. T., J. J. Hack, G. B. Bonan, B. A. Boville, B. P. Breigleb, D. L. Williamson and P. J. Rasch. 1996, 'Description of the NCAR Community Climate Model (CCM3)', *NCAR Technical Note TN-420+STR*, [Available online at: http://www.cgd.ucar.edu/cms/ccm3/TN-420/].

Kikuchi, K., and B. Wang. 2008, 'Diurnal precipitation regimes in the global tropics', *Journal of Climate*, **21**, pp. 2680-2696.

Kitoh, A., and O. Arakawa. 2005, 'Reduction in tropical rainfall diurnal variation by global warming simulated by a 20-km mesh climate model', *Geophysical Research Letters*, **32**, doi:10.1029/2005GL023350.

Koracin, D., and R. Berkowicz. 1988, 'Nocturnal boundary-layer height: Observations by acoustic sounders and predictions in terms of surface-layer parameters', *Boundary-Layer Meteorology*, **43**, pp. 65-83.

Kothe, S., and B. Ahrens. 2010, 'On the radiation budget in regional climate simulations for West Africa', *Journal of Geophysical Research*, **115**, D23120, doi:10.1029/2010JD014331.

Krishnamurti, T. N., S. Low-Nam and R. Pasch. 1983, 'Cumulus parameterization and rainfall rates II', *Monthly Weather Review*, **111**, pp. 815-828.

Krueger, S. K., G. T. McLean and Q. Fu. 1995, 'Numerical simulation of the stratus-to-cumulus transition in the subtropical marine boundary layer. Part I: Boundary-layer structure', *Journal of the Atmospheric Sciences*, **52**, pp. 2839–2850.

Kubar, T. L., D. L. Hartmann and R. Wood. 2009, 'Understanding the importance of microphysics and macrophysics for warm rain in marine low clouds. Part I: Satellite observations', *Journal of the Atmospheric Sciences*, **66**, pp. 2953-2972.

Kumagai, T., T. M. Saitoh, Y. Sato, T. Morooka, O. J. Manfroi, K. Kuraji and M. Suzuki. 2004, 'Transpiration, canopy conductance and the decoupling coefficient in a lowland mixed dipterocarp forest in Sarawak, Borneo: dry spell effects', *Journal of Hydrology*, **287**, pp. 237-251.

Kuo, H. L. 1974, 'Further studies of the parameterization of the influence of cumulus convection on large-scale flow', *Journal of the Atmospheric Sciences*, **31**, pp. 1232-1240.

Lane, T. P., M. J. Reeder and T. L. Clark. 2001, 'Numerical modeling of gravity wave generation by deep tropical convection', *Journal of the Atmospheric Sciences*, **58**, pp. 1249-1274.

Lau, N.-C., and J. J. Ploshay. 2009, 'Simulation of synoptic- and sub-synoptic-scale phenomena associated with the East Asian summer monsoon using a high-resolution GCM', *Monthly Weather Review*, **137**(1), pp. 137–160.

Lau, K.-M., and C.-H. Sui. 1997, 'Mechanisms of short-term sea surface temperature regulation: Observations during TOGA COARE', *Journal of Climate*, **10**, pp. 465-472.

Lebsock, M. D., G. L. Stephens and C. Kummerow. 2008, 'Multisensor satellite observations of aerosol effects on warm clouds', *Journal of Geophysical Research*, **113**, D15205, doi:10.1029/2008JD009876.

L'Ecuyer, T. S., W. Berg, J. Haynes, M. Lebsock and T. Takemura. 2009, 'Global observations of aerosol impacts on precipitation occurrence in warm maritime clouds, *Journal of Geophysical Research*, **114**, D09211, doi:10.1029/2008JD011273.

Li, F., D. Rosa, W. D. Collins and M. F. Wehner. 2012, '"Super-parameterization": A better way to simulation regional extreme precipitation?', *Journal of Advances in Modeling Earth Systems*, **4**, M04002, doi:10.1029/2011MS000106.

Li, T., and G. Zhou. 2010, 'Preliminary results of a regional air-sea coupled model over East Asia', *Chinese Science Bulletin*, **55**(21), pp. 2295-2305, doi:10.1007/s11434-010-3071-1.

Liberti, G. L., F. Chéruy and M. Desbois. 2001, 'Land effect on the diurnal cycle of clouds over the TOGA COARE area, as observed from GMS IR data', *Monthly Weather Review*, **129**, pp. 1500-1517.

Lin, W. Y., and M. H. Zhang. 2004, 'Evaluation of clouds and their radiative effects simulated by the NCAR Community Atmospheric Model against satellite observations', *Journal of Climate*, **17**, pp. 3302-3318.

Lohmann, U., and E. Roeckner. 1996, 'Design and performance of a new cloud microphysics scheme developed for the ECHAM general circulation model', *Climate Dynamics*, **12**, pp. 557-572.

Lord, S. J. 1982, 'Interaction of a cumulus cloud ensemble with the large-scale environment. Part III: Semi-prognostic test of the Arakawa-Schubert cumulus parameterization', *Journal of the Atmospheric Sciences*, **39**, pp. 88-103.

Love, B. S., A. J. Matthews and G. M. S. Lister. 2011, 'The diurnal cycle of precipitation over the Maritime Continent in a high-resolution atmospheric model', *Quarterly Journal of the Royal Meteorological Society*, **137**, pp. 934-947.

Manfroi, O. J., K. Kuraji, M. Suzuki, N. Tanaka, T. Kume, M. Nakagawa, T. Kumagai and T. Nakashizuka. 2006, 'Comparison of conventionally observed interception evaporation in a 100-m^2 subplot with that estimated in a 4-ha area of the same Bornean lowland tropical forest', *Journal of Hydrology*, **329**, pp. 329-349.

Manton, M. J., and W. R. Cotton. 1977, *Formulation of approximate equations for modeling moist deep convection on the mesoscale*, Atmospheric Science Paper No. 266, Colorado State University, Fort Collins, 62 p.

Mapes, B. E., T. T. Warner and M. Xu. 2003, 'Diurnal patterns of rainfall in northwestern South America. Part III: Diurnal gravity waves and nocturnal convection offshore', *Monthly Weather Review*, **131**, pp. 830-844.

Marshall, J. S., and W. McK. Palmer. 1948, 'The distribution of raindrops with size', *Journal of Meteorology*, **5**, pp. 165-166.

Martin, G. M., M. A. Ringer, V. D. Pope, A. Jones, C. Dearden and T. J. Hinton. 2006, 'The physical properties of the atmosphere in the new Hadley Centre Global Environmental Model (HadGEM1). Part I: Model description and global climatology', *Journal of Climate*, **19**, pp. 1274-1301.

Martins, J. V., A. Marshak, L. A. Remer, D. Rosenfeld, Y. J. Kaufman, R. Fernandez-Borda, I. Koren, A. L. Correia, V. Zubko and P. Artaxo. 2011, 'Remote sensing the vertical profile of cloud droplet effective radius, thermodynamic phase, and temperature', *Atmospheric Chemistry and Physics*, **11**, pp. 9485-9501.

May, P. T., C. Jakob, J. H. Mather and G. Vaughan. 2008, 'FIELD RESEARCH: Characterizing oceanic convective cloud systems. The Tropical Warm Pool International Cloud Experiment', *Bulletin of the American Meteorological Society*, **89**, pp. 153-155.

May, P. T., and D. K. Rajopadhyaya. 1999, 'Vertical velocity characteristics of deep convection over Darwin, Australia', *Monthly Weather Review*, **127**, pp. 1056-1071.

McCaa, J. R., and C. S. Bretherton. 2004, 'A new parameterization for shallow cumulus convection and its application to marine subtropical cloud-topped boundary layers. Part II: Regional simulations of marine boundary layer clouds', *Monthly Weather Review*, **132**, pp. 883-896.

Mori, S., H. Jun-Ichi, Y. I. Tauhid, M. D. Yamanaka, N. Okamoto, F. Murata, N. Sakurai, H. Hashiguchi and T. Sribimawati. 2004, 'Diurnal land-sea rainfall peak migration over Sumatera Island, Indonesian Maritime Continent, observed by TRMM satellite and intensive rawinsonde soundings', *Monthly Weather Review*, **132**, pp. 2021-2039.

Neale, R. B., J. H. Richter, A. J. Conley, S. Park, P. H. Lauritzen, A. Gettelman, D. L. Williamson, P. J. Rasch, S. J. Vavrus, M. A. Taylor, W. D. Collins, M. Zhang and S.-J. Lin. 2010, 'Description of the NCAR Community Atmosphere Model (CAM 4.0)', *NCAR Technical Note NCAR/TN-485+STR*, National Center for Atmospheric Research, Boulder, Colorado.

Neale, R., and J. Slingo. 2003, 'The Maritime Continent and its role in the global climate: A GCM study', *Journal of Climate*, **16**, pp. 834-848.

Neelin, J. D., O. Peters, J. W.-B. Lin, K. Hales and C. E. Holloway. 2008, 'Rethinking convective quasi-equilibrium: observational constraints for stochastic convective schemes in climate models', *Philosophical Transactions of the Royal Society A*, **366**, pp. 2579-2602.

Nesbitt, S. W., and E. J. Zipser. 2003, 'The diurnal cycle of rainfall and convective intensity according to three years of TRMM measurements', *Journal of Climate*, **16**, pp. 1456-1475.

Neumann, J., and Y. Mahrer. 1974, 'A theoretical study of the sea and land breezes of circular islands', *Journal of the Atmospheric Sciences*, **31**, pp. 2027-2039.

New, M., M. Hulme and P. Jones. 1999, 'Representing twentieth-century space-time climate variability. Part I: Development of a 1961-90 mean monthly terrestrial climatology', *Journal of Climate*, **12**, pp. 829-856.

Newman, M., P. D. Sardeshmukh and J. W. Bergman. 2000, 'An assessment of the NCEP, NASA, and ECMWF reanalyses over the tropical west Pacific warm pool', *Bulletin of the American Meteorological Society*, **81**(1), pp. 41-48.

Nitivattananon, V., L. V. T. Noi and W. Lohpaisankrit. 2013, 'Chapter 39: Climate change vulnerability assessment: Case of coastal cities in South East Asia', *Climate Change and Disaster Risk Management*, W. Leal Filho (Ed.), Climate Change Management, Springer-Verlag Berlin Heidelberg, pp. 597-614.

O'Dell, C. W., F. J. Wentz and R. Bennartz. 2008, 'Cloud liquid water path from satellite-based passive microwave observations: A new climatology over the global oceans', *Journal of Climate*, **21**, pp. 1721-1739.

Pal, J. S., E. E. Small and E. A. B. Eltahir. 2000, 'Simulation of regional-scale water and energy budgets: Representation of subgrid cloud and precipitation processes within RegCM', *Journal of Geophysical Research [Atmospheres]*, **105(D24)**, pp. 579-594.

Pal, J. S., and Coauthors. 2007, 'Regional climate modeling for the developing world: The ICTP RegCM3 and RegCNET', *Bulletin of the American Meteorological Society*, **88**, pp. 1395-1409.

Peng, M. S., J. A. Ridout and T. F. Hogan. 2004, 'Recent modifications of the Emanuel convective scheme in the Navy Operational Global Atmospheric Prediction Scheme', *Monthly Weather Review*, **132**, pp. 1254-1268.

Ploshay, J. J., and N.-C. Lau. 2010, 'Simulation of the diurnal cycle in tropical rainfall and circulation during boreal summer with a high-resolution GCM', *Monthly Weather Review*, **138**, pp. 3434-3453.

Qian, J.-H. 2008, 'Why precipitation is mostly concentrated over islands in the Maritime Continent', *Journal of the Atmospheric Sciences*, **65**, pp. 1428-1441.

Ramage, C. S. 1968, 'Role of a tropical "Maritime Continent" in the atmospheric circulation', *Monthly Weather Review*, **96**(6), pp. 365-370.

Ramankutty, N. 1999, 'Estimating historical changes in land cover: North American croplands from 1850 to 1992', *Global Ecology and Biogeography*, **8**, pp. 381-396.

Randall, D., M. Khairoutdinov, A. Arakawa and W. Grabowski. 2003, 'Breaking the cloud parameterization deadlock', *Bulletin of the American Meteorological Society*, **November 2003**, pp. 1547-1564.

Rangno, A. L., and P. V. Hobbs. 2005, 'Microstructures and precipitation development in cumulus and small cumulonimbus clouds over the warm pool of the tropical Pacific Ocean', *Quarterly Journal of the Royal Meteorological Society*, **131**, pp. 639-673.

Rauber, R. M., and Coauthors. 2007, 'Rain in Shallow Cumulus over the Ocean: The RICO campaign', *Bulletin of the American Meteorological Society*, **88**, pp. 1912–1928.

Reid, J. S., P. V. Hobbs, A. L. Rangno and D. A. Hegg. 1999, 'Relationships between cloud droplet effective radius, liquid water content, and droplet concentration for warm clouds in Brazil embedded in biomass smoke', *Journal of Geophysical Research*, **104**(D6), pp. 6145-6153.

Reynolds, R. W., N. Rayner, T. Smith, D. Stokes and W. Wang. 2002, 'An improved in situ and satellite SST analysis for climate', *Journal of Climate*, **15**, pp. 1609-1625.

Roeckner, E., G. Baumi, L. Bonaventura, R. Brokopf, M. Esch, M. Giorgetta, S. Hagemann, L. Kornblueh, U. Schlese, U. Schulzweida, I. Kirchner, E. Manzini, A. Rhodin and A. Tompkins. 2003, 'The atmospheric general circulation model ECHAM5 Part 1: Model description', *Max Planck Institute for Meteorology Report No. 349*, Hamburg, Germany, 140 p.

Rogers, R. R., and M. K. Yau. 1989, *A Short Course in Cloud Physics*, Elsevier, 293 p.

Rondanelli, R., and R. S. Lindzen. 2008, 'Observed variations in convective precipitation fraction and stratiform area with sea surface temperature', *Journal of Geophysical Research*, **113**, doi:10.1029/2008JD010064.

Rosenfeld, D., and C. W. Ulbrich. 2003, 'Cloud microphysical properties, processes, and rainfall estimation opportunities', *Meteorological Monographs*, **30**(52), pp. 237-258.

Rosenfeld, D. and I. M. Lensky. 1998, 'Satellite-based insights into precipitation formation processes in continental and maritime convective clouds', *Bulletin of the American Meteorological Society*, **79**, pp. 2457-2476.

Rotstayn, L. D., B. F. Ryan and J. J. Katzfey. 2000, 'A scheme for calculation of the liquid fraction in mixed-phase stratiform clouds in large-scale models', *Monthly Weather Review*, **128**, pp. 1070-1088.

Rotstayn, L. D. 2000, 'On the "tuning" of autoconversion parameterizations in climate models', *Journal of Geophysical Research*, **105**(D12), pp. 15495-15507.

Saavedra, P., A. Battaglia and C. Simmer. 2012, 'Partitioning of cloud water and rainwater content by ground-based observations with the Advanced Microwave Radiometer for Rain Identification (ADMIRARI) in synergy with a micro rain radar', *Journal of Geophysical Research*, **117**, D05203, doi:10.1029/2011JD016579.

Saito, K., T. Keenan, G. Holland and K. Puri. 2001, 'Numerical simulation of the diurnal evolution of tropical island convection over the Maritime Continent', *Monthly Weather Review*, **129**, pp. 378-400.

Sakurai, N., M. Kawashima, Y. Fujiyoshi, H. Hashiguchi, T. Shimomai, S. Mori, J.-I. Hamada, F. Murata, M. D. Yamanaka, Y. I. Tauhid, T. Sribimawati and B. Suhardi. 2009, 'Internal structures of migratory cloud systems with diurnal cycle over Sumatera Island during CPEA-I campaign', *Journal of the Meteorological Society of Japan*, **87**(1), pp. 157-170.

Sakurai, N., F. Murata, M. D. Yamanaka, S. Mori, J.-I. Hamada, H. Hashiguchi, Y. I. Tauhid, T. Sribimawait and B. Suhardi. 2005, 'Diurnal cycle of cloud system migration over Sumatera Island', *Journal of the Meteorological Socieity of Japan*, **83**(5), pp. 835-850.

Seidel, D. J., Y. Zhang, A. Beljaars, J.-C. Golaz, A. R. Jacobson and B. Medeiros. 2012, 'Climatology of the planetary boundary layer over the continental United States and Europe', *Journal of Geophysical Research*, **117**, D17106, doi:10.1029/2012JD018143.

Shaffrey, L. C., and Coauthors. 2009, 'U.K. HiGEM: The new U.K. high-resolution global environment model-model description and basic evaluation', *Journal of Climate*, **22**(8), pp. 1861–1896.

Simmons, A. J., P. D. Jones, V. da Costa Bechtold, A. C. M. Beljaars, P. W. Kållberg, S. Saarinen, S. M. Uppala, P. Viterbo and N. Wedi. 2004, 'Comparison of trends and low-frequency variability in CRU, ERA-40, and NCEP/NCAR analyses of surface air temperature', *Journal of Geophysical Research*, **109**, D24115, doi:10.1029/2004JD005306.

Simpson, J. T., D. Keenan, B. Ferrier, R. H. Simpson and G. J. Holland. 1992, 'Cumulus mergers in the Maritime Continent region', *Meteorology and Atmospheric Physics*, **51**, pp. 73-99.

Singh, G. P., J.-H. Oh, J.-Y. Kim and O.-Y. Kim. 2006, 'Sensitivity of summer monsoon precipitation over East Asia to convective parameterization schemes in RegCM3', *SOLA*, **2**, pp. 29-32, doi:10.2151/sola.2006-008.

Slingo, J. M. 1989, 'A GCM parameterization for the shortwave radiative properties of water clouds', *Journal of the Atmospheric Sciences*, **46**, pp. 1419-1427.

Slingo, J., P. Inness, R. Neale, S. Woolnough and G.-Y. Yang. 2003, 'Scale interactions on diurnal to seasonal timescales and their relevance to model systematic errors', *Annals of Geophysics*, **46**(1), pp. 139-155.

Slingo, J., M. Blackburn, A. Betts, R. Brugge, K. Hodges, B. Hoskins, M. Miller, L. Steenman-Clark and J. Thuburn. 1994, 'Mean climate and transience in the tropics of the UGAMP GCM: Sensitivity to convective parameterization', *Quarterly Journal of the Royal Meteorological Society*, **120**, pp. 881-922.

Smith, R. N. B. 1990, 'A scheme for predicting layer clouds and their water content in a general circulation model', *Quarterly Journal of the Royal Meteorological Society*, **116**, pp. 435-460.

Sorooshian, S., X. Gao, K. Hsu, R. A. Maddox, Y. Hong, H. V. Gupta and B. Imam. 2002, 'Diurnal variability of tropical rainfall retrieved from combined GOES and TRMM satellite information', *Journal of Climate*, **15**, pp. 983-1001.

Squires, P. 1958, 'The microstructure and colloidal stability of warm clouds. Part II – The causes of the variation in microstructure', *Tellus X*, **11**, pp. 262-271.

Stephens, G. L., T. L'Ecuyer, R. Forbes, A. Gettlemen, J.-C. Golaz, A. Bodas-Salcedo, K. Suzuki, P. Gabriel and J. Haynes. 2010, 'Dreary state of precipitation in global models', *Journal of Geophysical Research*, **115**, D24211, doi:10.1029/2010JD014532.

Stephens, G. L. and J. M. Haynes. 2007, 'Near global observations of the warm rain coalescence process', *Geophysical Research Letters*, **34**, L20805, doi:10.1029/2007GL030259.

Stephens, G. L. and C. D. Kummerow. 2007, 'The remote sensing of clouds and precipitation from space: A review', *Journal of the Atmospheric Sciences*, **64**, pp. 3742-3765.

Stevens, B., and Coauthors. 2003, 'Dynamics and Chemistry of Marine Stratocumulus—DYCOMS-II', *Bulletin of the American Meteorological Society*, **84**, pp. 579–593.

Stull, R. B. 1988, *An Introduction to Boundary Layer Meteorology*, Kluwer Academic Publishers, 666 p.

Sudradjat, A., R. R. Ferraro and M. Fiorino. 2005, 'A comparison of total precipitable water between reanalyses and NVAP', *Journal of Climate*, **18**, pp. 1790-1807.

Sui, C.-H., X. Li, K.-M. Lau and D. Adamec. 1997, 'Multiscale air-sea interactions during TOGA COARE', *Monthly Weather Review*, **125**, pp. 448-462.

Sui, C.-H., and K.-M. Lau. 1992, 'Multiscale phenomena in the tropical atmosphere over the western Pacific', *Monthly Weather Review*, **120**, pp. 407-430.

Sun, L., F. H. M. Semazzi, F. Giorgi and L. Ogallo. 1999, 'Application of the NCAR regional climate model to eastern Africa. 1. Simulation of the short rains of 1988', *Journal of Geophysical Research*, **104**(D6), pp. 6529-6548.

Sundqvist, H., E. Berge and J. E. Kristjánsson. 1989, 'Condensation and cloud parameterization studies with a mesoscale numerical weather prediction model', *Monthly Weather Review*, **117**, pp. 1641-1657.

Sundqvist, H. 1988, 'Parameterization of condensation and associated clouds in models for weather prediction and general circulation simulation', in *Physically-Based Modelling and*

Simulation of Climate and Climatic Change, M. E. Schlesinger (Ed.), Kluwer Academic Publishers, Dordrecht, the Netherlands, pp. 433-461.

Suzuki, K., G. L. Stephens, S. C. van den Heever and T. Y. Nakajima. 2011, 'Diagnosis of the warm rain process in cloud-resolving models using joint CloudSat and MODIS observations', *Journal of the Atmospheric Sciences*, **68**, pp. 2655-2670.

Svensson, G., M. Tjernström and D. Koracin. 2000, 'The sensitivity of a stratocumulus transition: Model simulations of the ASTEX first Lagrangian', *Boundary-Layer Meteorology*, **95**, pp. 57–90.

Takahashi, H. G., T. Yoshikane, M. Hara, K. Takata and T. Yasunari. 2010, 'High-resolution modelling of the potential impact of land surface conditions on regional climate over Indochina associated with the diurnal precipitation cycle', *International Journal of Climatology*, **30**, pp. 2004-2020.

Teo, C.-K., T.-Y. Koh, J. C.-F. Lo and B. C. Bhatt. 2011, 'Principal component analysis of observed and modeled diurnal rainfall in the Maritime Continent', *Journal of Climate*, **24**, pp. 4662-4675.

Testud, J., S. Oury, R. A. Black, P. Amayenc and X. Dou. 2001, 'The concept of "normalized" distributions to describe raindrop spectra: A tool for cloud physics and cloud remote sensing', *Journal of Applied Meteorology*, **40**, pp. 1118-1140.

Tiedtke, M. 1993, 'Representation of clouds in large-scale models', *Monthly Weather Review*, **121**, pp. 3040-3061.

Tiedtke, M. 1988, 'Parameterization of cumulus convection in large-scale models', in *Physically-Based Modelling and Simulation of Climate and Climatic Change – Part 1*, M. E. Schlesinger (ed.), pp. 375-431.

Thompson, S. L., and D. Pollard. 1995, 'A global climate model (GENESIS) with a land-surface transfer scheme (LSX). Part I: present climate simulation', *Journal of Climate*, **8**, pp. 732-761.

Tombrou, M., D. Founda and D. Boucouvala. 1998, 'Nocturnal boundary layer height prediction from surface routine meteorological data', *Meteorology and Atmospheric Physics*, **68**, pp. 177-186.

Tompkins, A. M. 2001, 'Organization of tropical convection in low vertical wind shears: The role of cold pools', *Journal of the Atmospheric Sciences*, **58**, pp. 1650-1672.

Trenberth, K. E., J. T. Fasullo and J. Kiehl. 2009, 'Earth's global energy budget', *Bulletin of the American Meteorological Society*, **March 2009**, pp. 311-323.

Trenberth, K. E., A. Dai, R. M. Rasmussen and D. B. Parsons. 2003, 'The changing character of precipitation', *Bulletin of the American Meteorological Society*, **84**, pp. 1205-1217.

Trenberth, K. E., and C. J. Guillemot. 1998, 'Evaluation of the atmospheric moisture and hydrological cycle in the NCEP/NCAR reanalyses', *Climate Dynamics*, **14**, pp. 213-231.

Troccoli, A. and P. Kållberg. 2004, *ERA-40 Project Report Series No. 13: Precipitation correction in the ERA-40 Reanalysis*, European Centre for Medium Range Weather Forecasts, Reading, England.

Ulbrich, C. 1983, 'Natural variations in the analytical form of the raindrop size distribution', *Journal of Climate and Applied Meteorology*, **22**, pp. 1764-1775.

United States Geological Survey. 1997, *Global Land Cover Characterization*, [Available online at: http://edc2.usgs.gov/glcc/glcc.php].

United States Geological Survey. 1996, *Global 30-arc second elevation dataset (GTOPO30)*, [Available online at: http://eros.usgs.gov/#/Find_Data/Products_and_Data_Available/gtopo30_info].

Uppala, S. M., and Coauthors. 2005, 'The ERA-40 Re-Analysis', *Quarterly Journal of the Royal Meteorological Society*, **131**, pp. 2961-3012. [Dataset available online at: http://www.ecmwf.int/research/era/do/get/era-40].

Vermimmen, R. R. E., L. A. Bruijnzeel, A. Romdoni and J. Proctor. 2007, 'Rainfall interception in three contrasting lowland rain forest types in Central Kalimantan, Indonesia', *Journal of Hydrology*, **340**, pp. 217-232.

Verseghy, D. L. 1991, 'Class-A Canadian land surface scheme for GCMS. I. Soil model', *International Journal of Climatology*, **11**, pp. 111-133.

Vogelezang, D. H. P., and A. A. M. Holtslag. 1996, 'Evaluation and model impacts of alternative boundary-layer height formulations', *Boundary-Layer Meteorology*, **81**, pp. 245-269.

Wang, L., Y. Wang, A. Lauer and S.-P. Xie. 2011, 'Simulation of seasonal variation of marine boundary layer clouds over the eastern Pacific with a regional climate model', *Journal of Climate*, **24**, pp. 3190-3210.

Wang, Y., L. Zhou and K. Hamilton. 2007, 'Effect of convective entrainment / detrainment on the simulation of the tropical precipitation diurnal cycle', *Monthly Weather Review*, **135**, pp. 567-585.

Warner, T. T., B. E. Mapes and M. Xu. 2003, 'Diurnal patterns of rainfall in northwestern South America. Part II: Model simulations', *Monthly Weather Review*, **131**, pp. 813-829.

Warner, J. 1955, 'The water content of cumuliform cloud', *Tellus VII*, **4**, pp. 449-457.

Webster, P. J., C. A. Clayson and J. A. Curry. 1996, 'Clouds, radiation, and the diurnal cycle of sea surface temperature in the tropical western Pacific', *Journal of Climate*, **9**, pp. 1712-1730.

Weller, R. A., and S. P. Anderson. 1996, 'Surface meteorology and air-sea fluxes in the western equatorial Pacific warm pool during the TOGA coupled ocean-atmosphere response experiment', *Journal of Climate*, **9**, pp. 1959-1990.

Wentz, F. J., and R. W. Spencer. 1998, 'SSM/I rain retrievals within a unified all-weather ocean algorithm', *Journal of the Atmospheric Sciences*, **55**, pp. 1613-1627.

Wild, J., and J. K. Hall. 1982, 'Aspects of hydrology in the province of North Sumatra, Indonesia', *Proceedings of the Institute of Civil Engineers*, Part 2, **73**, pp. 85-108.

Winter, J. M., J. S. Pal and E. A. B. Eltahir. 2009, 'Coupling of Integrated Biosphere Simulator to Regional Climate Model Version 3', *Journal of Climate*, **22**, pp. 2743-2757.

Wu, P., J.-I. Hamada, M. D. Yamanaka, J. Matsumoto and M. Hara. 2009a, 'The impact of orographically-induced gravity waves on the diurnal cycle of rainfall over Southeast Kalimantan island', *Atmospheric and Oceanic Science Letters*, **2**(1), pp. 35-39.

Wu, P., M. Hara, J.-I. Hamada, M. D. Yamanaka and F. Kimura. 2009b, 'Why a large amount of rain falls over the sea in the vicinity of western Sumatra island during nighttime', *Journal of Applied Meteorology and Climatology*, **48**, pp. 1345-1361.

Xie, P., and P. A. Arkin. 1997, 'Global precipitation: A 17-year monthly analysis based on gauge observations, satellite estimates, and numerical model outputs', *Bulletin of the American Meteorological Society*, **78**, pp. 2539-2557.

Xu, K.-M., and Coauthors. 2005, 'Modeling springtime shallow frontal clouds with cloud-resolving and single-column models', *Journal of Geophysical Research*, **110**, D15S04, doi:10.1029/2004JD005153.

Xu, K.-M., and D. A. Randall. 1996, 'A semiempirical cloudiness parameterization for use in climate models', *Journal of the Atmospheric Sciences*, **53**(21), pp. 3084-3102.

Yang, S., and E. A. Smith. 2006, 'Mechanisms for diurnal variability of global tropical rainfall observed from TRMM', *Journal of Climate*, **19**, pp. 5190-5226.

Yang, G.-Y., and J. Slingo. 2001, 'The diurnal cycle in the tropics', *Monthly Weather Review*, **129**, pp. 784-801.

Yao, M.-S., and A. D. Del Genio. 1999, 'Effects of cloud parameterization on the simulation of climate changes in the GISS GCM', *Journal of Climate*, **12**, pp. 761-779.

Yu, T. W. 1978, 'Determining the height of the nocturnal boundary layer', *Journal of Applied Meteorology*, **17**, pp. 28-33.

Zeng, X., M. Zhao and R. E. Dickinson. 1998, 'Intercomparison of bulk aerodynamic algorithms for the computation of sea surface fluxes using TOGA COARE and TAO data', *Journal of Climate*, **11**, pp. 2628-2644.

Zhao, M., I. M. Held, S.-J. Lin and G. A. Vecchi. 2009, 'Simulations of global hurricane climatology, interannual variability, and response to global warming using a 50 km resolution GCM', *Journal of Climate*, **22**(24), pp. 6653–6678.

Zhou, L., and Y. Wang. 2006, 'Tropical Rainfall Measuring Mission observation and regional model study of precipitation diurnal cycle in the New Guinean region', *Journal of Geophysical Research*, **111**, D17104, doi:10.1029/2006JD007243.

Zilitinkevich, S. S. 1972, 'On the determination of the height of the Ekman boundary layer', *Boundary-Layer Meteorology*, **3**, pp. 141-145.

Zipser, E. J., and K. Lutz. 1994, 'The vertical profile of radar reflectivity of convective cells: A strong indicator of storm intensity and lightning probability', *Monthly Weather Review,* **122**, pp. 1751-1759.

Zipser, E. J., and M. A. LeMone. 1980, 'Cumulonimbus vertical velocity events in GALE. Part II: Synthesis and model core structure', *Journal of the Atmospheric Sciences,* **37**, pp. 2458-2469.

Zou, L., and T. Zhou. 2011, 'Sensitivity of a regional ocean-atmosphere coupled model to convection parameterization over western North Pacific', *Journal of Geophysical Research*, **116**, D18106, doi:10.1029/2011JD015844.

Zuidema, P. 1998, 'The 600-800 mb minimum in tropical cloudiness observed during TOGA COARE', *Journal of the Atmospheric Sciences*, **55**, pp. 2220-2228.